Mechanical and Optical Behavior of A Novel Optical Fiber Crack Sensor and An Interferometric Strain Sensor

by

Noah Gale Olson

B.S.E., Civil Engineering Systems (1995)
B.A., Design of the Environment (1995)
University of Pennsylvania

S.M., Civil and Environmental Engineering (1998)
Massachusetts Institute of Technology

Submitted to the Department of Civil and Environmental Engineering
in Partial Fulfillment of the Requirements for the Degree of
Doctor of Philosophy in Civil and Environmental Engineering

at the

Massachusetts Institute of Technology

September 2002

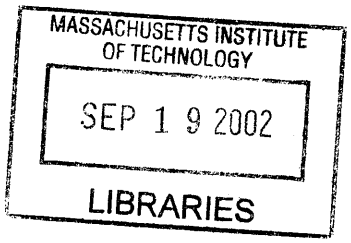

Signature of Author_____
Department of Civil and Environmental Engineering
August 9, 2002

Certified by _____
Christopher K. Y. Leung
Associate Professor of Civil and Environmental Engineering
Thesis Supervisor

Accepted by_____
Oral Buyukozturk
Professor of Civil and Environmental Engineering
Chairman, Departmental Committee on Graduate Studies

Mechanical and Optical Behavior of A Novel Optical Fiber Crack Sensor and An Interferometric Strain Sensor

by

Noah Gale Olson

Submitted to the Department of Civil and Environmental Engineering
on August 9, 2002 in Partial Fulfillment of the
Requirements for the Degree of Doctor of Philosophy in
Civil and Environmental Engineering

The proper interpretation of measurements from an optical fiber sensor requires a full understanding of its mechanical response to external action and the corresponding change in optical output. To quantify the mechanical behavior it is necessary to know the mechanical properties of the fiber coatings. A new method for measuring the coating stiffness directly on the fiber uses nano-indentation. Special sample preparation and testing procedures were developed for the measurement of very low modulus materials using the Nano Indenter II. Results are obtained for two different acrylate coated optical fibers, namely Corning SMF28 and 3M FS-SN-4228. These results are used in understanding the behavior of the novel crack sensor and of an interferometric strain sensor.

A distributed crack sensor that does not require prior knowledge of crack location and employs a small number of fibers to monitor a large number of cracks is developed. The basic design of the sensor is a polymer sheet containing an inclined fiber that is coupled to a structure. The sensor principle is that cracking in the structural member leads to cracking in the polymer sheet which induces fiber bending leading to signal loss. Monitoring the backscattered signal provides crack opening size and location. A theoretical model for optical fiber loss prediction is developed based on a combination of mechanical and optical analyses. Model prediction is found to be in relatively close agreement with experimental results. Model simulation can hence be carried out to provide guidelines for designing crack sensors for various applications.

The behavior of both coated and uncoated fibers for strain measurement applications is also examined. A theoretical assessment using a three-dimensional finite element model for both coated and uncoated optical fibers is presented. Results show that the coating stiffness can significantly affect the strain transfer from the member under load to the optical fiber. The three-dimensional finite element model can provide guidelines for the optimized design of strain sensors. A straightforward analytical solution shows good equivalence with the theoretical solution under certain conditions. Experiments using an interferometer were conducted to verify the results of the theoretical study and show good correspondence.

Thesis Supervisor: Christopher K. Y. Leung

Title: Associate Professor of Civil and Environmental Engineering

Table of Contents

List of Figures

CHAPTER 4

APPENDIX II

APPENDIX III

List of Tables

CHAPTER 2

CHAPTER 3

CHAPTER 4

APPENDIX II

Chapter 1

Introduction

As Civil structures age there arises a need to assess the safety of these structures. One way to accomplish this is by monitoring their condition and performance. Current practice uses only visual periodic inspections to monitor buildings. This could lead to a dangerous situation should a structural default occur in between the inspection intervals. Traditional sensors such as strain gages and accelerometers can provide useful information for such structures however optical fiber sensors offer some definite advantages. With low signal loss, optical fibers are suitable for remote sensing applications. The optical signal is immune to low-level electromagnetic noises commonly found in electrical instruments. Since the optical fiber does not carry electricity, the sensor and sensing system are not vulnerable to lightning attack, a problem faced by large bridges and dams in open areas. Also, with its small size and light weight, fiber optic sensors are unobtrusive when installed in buildings. Moreover, fiber sensors can be multiplexed to have a number of sensing points along a single fiber or designed to make distributed measurements. Such capabilities are beyond conventional electrical transducers and sensors.

The development of optical fiber sensors is relatively new. Many of the original sensors were developed for the aeronautical and military communities. Application of such sensors to Civil Engineering Systems has already started but requires additional study. This thesis investigates two different optical fiber sensors and how they mechanically behave as related to Civil Structures. The thesis also describes the development of a

novel optical fiber sensor that has the potential of measuring many crack openings with their corresponding locations.

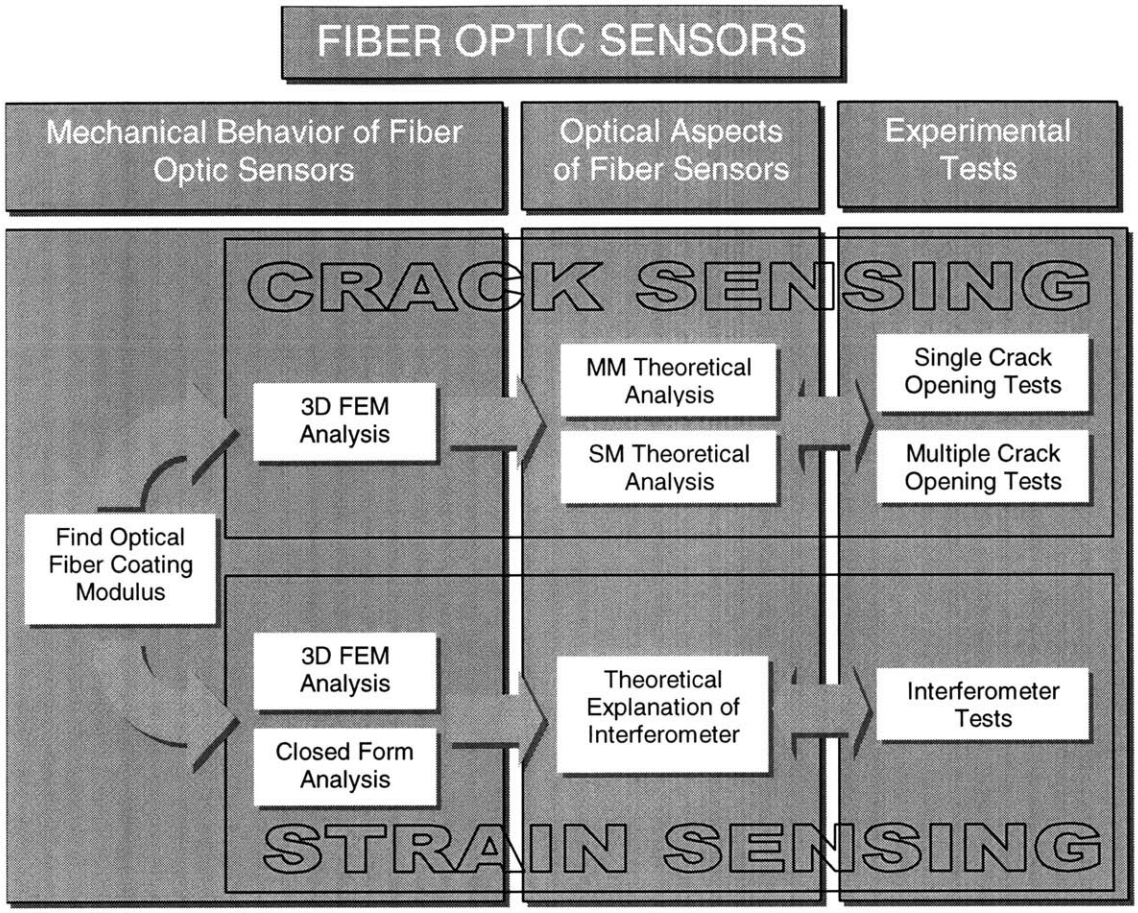

Figure 1: Visual outline of thesis

Figure 1 is a diagrammatic illustration of the different thesis components and how they are interrelated. There are two different types of optical fiber sensors that are investigated; namely crack sensors and strain sensors. Even though both sensors operate on different optical properties there are some similarities in looking at the sensors. These are extrinsic sensors which means that they have a mechanical interaction with the structure that physically changes the optical fiber. Understanding this mechanical change requires knowledge of the mechanical properties of the optical fiber and the manner in which it is connected to the structure. This is referred to as the "Mechanical Behavior of

Optical Fiber Sensors" in the figure. The "Optical Behavior of Optical Fiber Sensors" refers to the change in optical properties that occurs from the physical change of the fiber. The change in optical properties therefore alters the manner in which light passes through the fiber. In the case of the micro-bend crack sensor, the loss of light occurs due to leaky rays. For the strain sensor, the physical change in fiber length affects the amount of time it takes for the light to pass through the fiber. The final part of the figure "Experimental Tests" refers to the actual tests that were carried out in the lab to verify the theoretical analysis of the fiber sensors. Chapter 2 will discuss the manner by which to measure the mechanical properties of the optical fiber coating. Chapter 3 will look at the novel crack sensor and chapter 4 addresses the strain sensor. Chapter 5 will offer some conclusions and some ideas for future investigation.

Chapter 2

Stiffness Measurement of the External Polymeric Coating on an Optical Fiber

1. INTRODUCTION

When optical fibers are employed as mechanical sensors to monitor structural strain or cracking, the change in optical output is governed by the strain or deformation of the fiber, and this is related to the strain or damage state of the structure to which the fiber is coupled. The transfer of strain (or deformation) from the structure to the fiber strongly depends on the elastic property of the polymeric protective coating on the surface of the optical fiber. In many cases, the Young's modulus of the coating is required for the "calibration" of the sensor (i.e., to obtain the quantitative relation between optical signal change and changes in strain/cracking) and the proper interpretation of measurement results. The coating is typically about 62.5 microns in thickness and made of very soft polymeric materials. Determination of its elastic modulus is hence very difficult.

To measure the fiber coating stiffness, Nellen et al[1] developed an approach based on the testing of a torsional pendulum that consisted of an aluminum disc held by an optical fiber. Knowing the modulus of the glass fiber, the shear modulus of the coating can be found from the torsional frequency of the pendulum. This approach, while theoretically sound, is vulnerable to error when the coating is soft, as the additional stiffness contributed by the coating may be within the range of experimental error. Also, when the polymeric coating is produced as a dual layer (with a stiffer layer on the outside and a softer layer inside), the method is not applicable.

This chapter will explain a manner by which to measure the coating stiffness directly on the optical fiber using the nano-indentation technique. The principle of nano-indentation for the in-situ measurement of elastic properties is first described. A major focus of the chapter is on the specific specimen preparation technique to ensure successful execution of the indentation test. Also, since the modulus of the coating can be very low (on the order of several MPa), special procedures have to be followed in the testing. The required adjustments to the testing system and the proper interpretation of experimental results will be discussed. Experimental results for two types of acrylate coatings will be presented as examples to demonstrate the applicability of the testing approach.

2. THEORY-PRINCIPLE OF THE NANO INDENTER® II

NANO INDENTER® II, the machine used to measure the elastic moduli of the optical fiber coatings, was manufactured by NanoInstruments, Inc., a subsidiary of MTS. There are three main components of the machine, 1) the indenter, 2) an optical microscope and 3) a precision X–Y–Z table that moves the specimen. It is a load-controlled system capable of operating at loads in the microgram range. However, with feedback techniques it is able to run displacement-controlled experiments as well.

2.1 The Indenter

The indenter (see Figure 1) consists of a rod supported by leaf springs that confine it to move only in the vertical direction. The rod is attached to the middle plate of a special three-plate capacitive displacement sensor. Movement of the capacitor plate is used to measure the displacement of the indenter. The total movement possible (i.e., the physical gap of the capacitor) is 200μm. The theoretical depth resolution of the system is approximately ±0.04nm.

The tip of the indenter is a diamond tip. The tip used for the experiments was a standard three-sided diamond pyramid. The diamond is ground so that the sides of the pyramid make a 63.5° angle with the normal to the base. The resulting indent should look like an equilateral triangle with the length of a side approximately 7.4 times its depth.

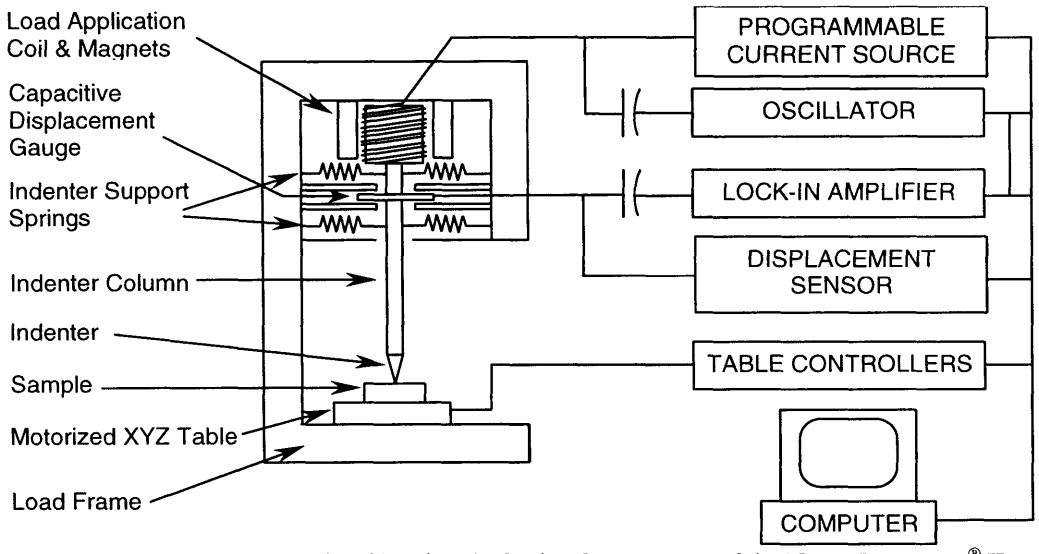

Figure 1: Schematic Drawing Showing the Major Components of the NANO INDENTER® II

A coil is attached to the top of the indenter rod and is held in a magnetic field. Thus, passage of a current through the coil can be used to apply a force to the indenter. For the coating stiffness tests the "Standard Head" was used. The load resolution for the "Standard Head" in the most sensitive range is approximately ±75 nN (±7.6 μgm). The different load ranges are in Table 1.

Table 1: Load Ranges for Standard Head

Load Range	mN	Grams
0	10	1
1	40	4
2	180	18
3	700	70

2.2 Principles for the determination of elastic modulus from indentation results

The NANO INDENTER® II with the Continuous Stiffness Method (CSM) option can measure the modulus of a sample in two different ways. The first is using pure indentation to measure the unloading stiffness and the second is by measuring the dynamic response of the material. Both methods will be examined.

2.2.1 Pure Indentation

The study of contact mechanics is thought to have formally started with the work of Hertz and Boussinesq in the early 1880s. The work of Hertz looked at the contact between two elastic spherical surfaces with different radii. His theory is restricted to perfectly elastic solids with no friction. Other researchers have expanded the theory since his time to include friction and nonelastic effects.[2,3] However, in regards to indentation it is known that the displacements recovered during unloading are primarily elastic and therefore the elastic frictionless assumptions made in Hertzian contact mechanics are valid. Thus, with an independent knowledge of the indenter contact area, the indenter modulus and the Poisson's Ratios for both the indenter and the material being tested it is possible to find the modulus of the material in question. The theory presented by Hertz has been used to develop the relationship between indenter depth and the corresponding force for different indenter geometries that have surfaces whose profiles are smooth and continuous. However, the common tips used in indentation tests are not smooth and continuous but rather they have sharp edges such as the Berkovich indenter used in the NANO INDENTER® II tests. G. M. Pharr, W. C. Oliver and F. R. Brotzen[4] have shown that there is a simple relationship between the contact stiffness, the contact area and the elastic modulus that is not dependent on the geometry of the punch. They further show that this methodology can be extended to geometries such as Berkovich indenters with

some small modifications as described by King.[5] They first start with the important contribution of Sneddon[6] who derived a general relationship between the load, displacement, and contact area for any punch that can be described as a solid of revolution of a smooth function.

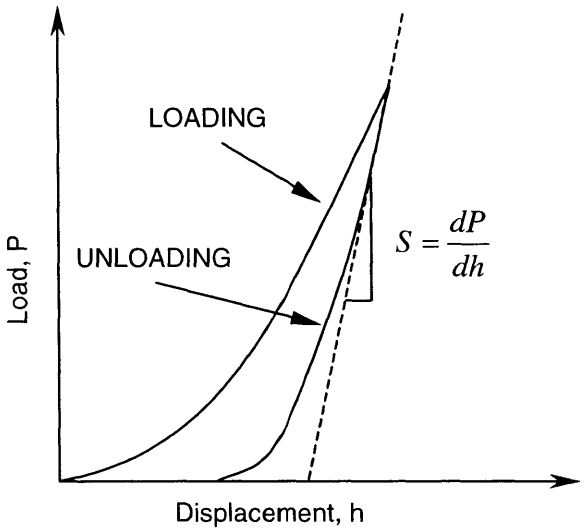

Figure 2: Load vs. Displacement Curve for Typical Indentation Test

The NANO INDENTER® II (using pure indentation) measures the stiffness of the specimen from the initial segment of the unloading curve as shown in Figure 2. This measurement assumes that during the initial period of unloading the displacements are elastic and that the contact area between the indenter and the specimen remains constant. With these assumptions it is possible to approximate the unloading behavior using the analysis for the indentation of a flat, cylindrical punch. Sneddon[6] carried out such an analysis and presented the results in the form:

$$P = \frac{4Ga}{1-\nu} h \qquad (1)$$

where a is the radius of the cylinder, G is the shear modulus, ν is Poisson's Ratio, h is the depth of the indentation and P is the load. Noting that the area of the contact circle is $A=\pi a^2$ and that $E=2G(1+\nu)$ Equation (1) can be rewritten as:

$$P = \frac{2E\sqrt{A}}{\sqrt{\pi}\left(1-\nu^2\right)}h \qquad (2)$$

Differentiating Equation (2) with respect to h yields:

$$\frac{dP}{dh} = \frac{2}{\sqrt{\pi}}\sqrt{A}\frac{E}{\left(1-\nu^2\right)} \qquad (3)$$

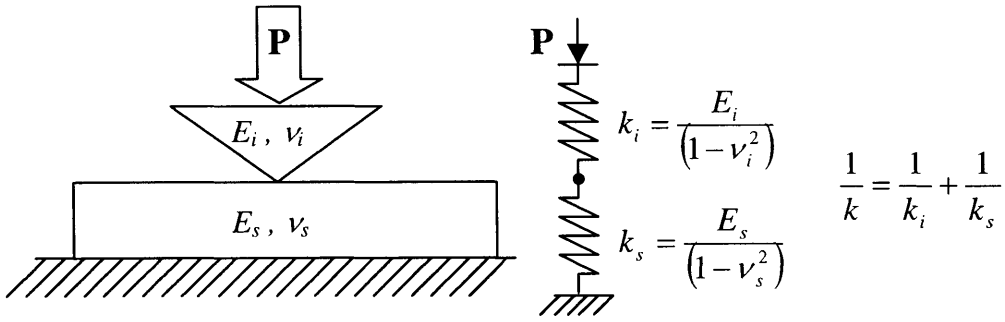

Figure 3: Explanation for the Reduced Modulus

Since the indenter and the specimen both contribute to the deformation of the system it is good to show the contributions of both materials in the measurement of the modulus. One common way to model the behavior of elastic materials is to think of them like springs as illustrated in Figure 3. In this case, one spring would represent the indenter, k_i, and the other spring, k_s, would represent the specimen being tested. When these two materials are in contact they are behaving like two springs in series. To find an equivalent stiffness for the two springs one would use the equation $\frac{1}{k} = \frac{1}{k_i} + \frac{1}{k_s}$. For an elastic material the spring stiffness, k, is the elastic modulus, E. However, since this

analysis has been done with a plane strain assumption, actually the plain strain modulus, $E/(1-\nu^2)$, should be used.[3] The plane strain assumption has been used since the thickness of the solid being measured is large compared to the width of the loaded region. Therefore, the equivalent modulus that represents the modulus of the indenter and specimen is called the reduced modulus, E_r, and is calculated by

$$\frac{1}{E_r} = \frac{\left(1-\nu^2\right)}{E} = \frac{\left(1-\nu_i^{\,2}\right)}{E_i} + \frac{\left(1-\nu_s^{\,2}\right)}{E_s} \qquad (4)$$

It follows then that Equation (4) can also be written in the form

$$E_r = \frac{E}{\left(1-\nu^2\right)} = \frac{E_i E_s}{\left(1-\nu_i^{\,2}\right)E_s + \left(1-\nu_s^{\,2}\right)E_i} \qquad (5)$$

where ν_i and E_i are the indenter elastic constants and ν_s and E_s are the elastic constants of the specimen. Substituting the reduced modulus into Equation (3) yields:

$$\frac{dP}{dh} = \frac{2}{\sqrt{\pi}}\sqrt{A} \times E_r \qquad (6)$$

Remembering that $S=dP/dh$, and rearranging Equation (6) leads to:

$$E_r = \frac{\sqrt{\pi}}{2\sqrt{A}} S \qquad (7)$$

Equation (7) holds only for flat cylindrical punches. The indenter head used in the NANO INDENTER® II for the tests is a Berkovich shaped indenter, which is a triangular based pyramid and therefore not like a flat cylindrical punch. Nevertheless, Pharr et. al.[4] have shown that not only is Equation (6) valid for any indenter whose geometry can be

described as a revolution of a smooth function, it is also the same general relationship that describes the connection between contact stiffness, contact area and elastic modulus regardless of indenter geometry. Therefore, even though the Berkovich Indenter cannot be described by the revolution of a smooth function, Equation (6) still has application with only a small modification.

King[5] investigated flat-ended punches with circular, square and triangular cross sections using finite element analysis. The triangular flat-ended punch is the flat-ended equivalent of the Berkovich indenter.[4] He found that for all three indenters the unloading stiffness is given by

$$\frac{dP}{dh} = \beta\sqrt{A} \times E_r \qquad (8)$$

where β represents a correction factor to make the equation right for the corresponding geometry. The values for the three different geometries are shown in Table 2. Additionally, it is nice to put Equation (8) in a form similar to Equation (6) leading to

$$\frac{dP}{dh} = \beta\frac{2}{\sqrt{\pi}}\sqrt{A} \times E_r \qquad (9)$$

Table 2: Values for β

Geometric Shape	β by King[5] for Equation (8)	β by Pharr et. al.[4] for Equation (9)
Circular	1.129	1.000
Triangular	1.142	1.034
Square	1.167	1.012

The constant β has the value of 1.034 for the Berkovich tip.

2.2.2 Continuous Stiffness Method

The Continuous Stiffness Method allows the machine to do two things, first, it can help in determining the surface of the specimen and second, it can determine the modulus of the material being tested. In order to understand this, a brief overview of the dynamic theory for the NANO INDENTER® II will be presented. Then, a discussion about the ways that it can help with determining the surface and the modulus will follow.

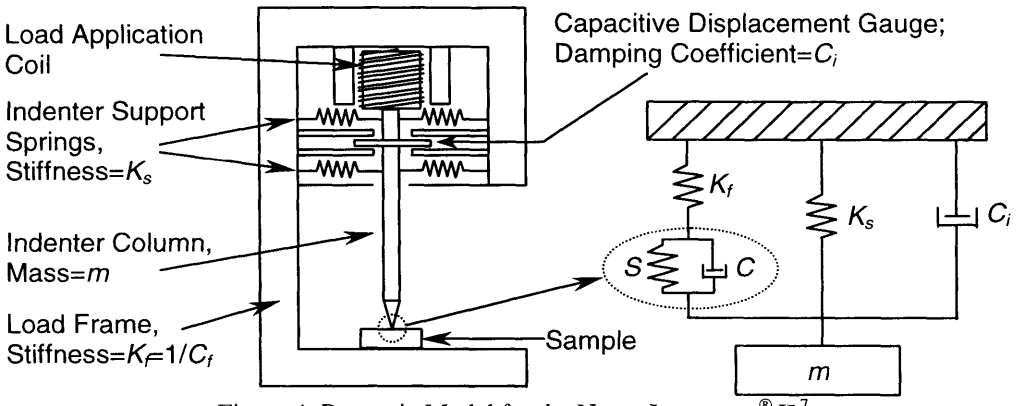

Figure 4: Dynamic Model for the NANO INDENTER® II [7]

A dynamic model of the indenter head presented by Lucas, et. al.[7] for the NANO INDENTER® II is shown in Figure 4. The load application coil and the magnets create the force to push the indenter into the specimen. With a DC signal it creates a quasi-static indent. If the Continuous Stiffness Method is used, a harmonic component is added to the DC signal to force the indenter into a vibration. The additional force amplitude is small in comparison to the pure indentation so that the deformation is not significantly effected. The system can measure displacements as small as 0.0001nm using frequency specific amplification. The system can also measure the harmonic force amplitude as well as the phase difference between the displacement and force signals. The dynamic model and analysis will look at this behavior.

Before the indenter makes contact the system can be simplified to a system with a mass, spring and damper as seen in Figure 5.

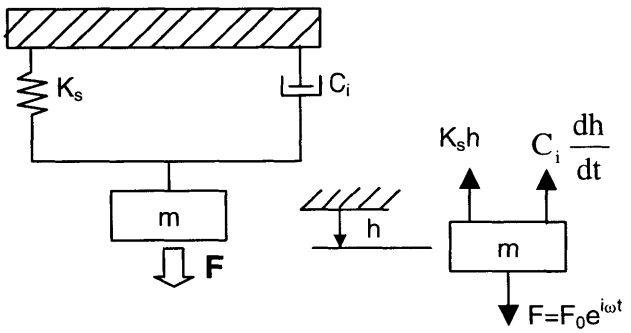

Figure 5: NANO INDENTER® II dynamic model before sample contact

The differential equation for the motion of the system shown in Figure 5 is easier to understand by first assuming that the forcing function is $F=F_0\sin(\omega t)$. Then the differential equation would be (see Thomson[8] and Norton[9] for more details)

$$m\frac{d^2h}{dt^2}+C_i\frac{dh}{dt}+K_sh=F_0\sin(\omega t) \qquad (10)$$

However, since the forcing function is $F=F_0(\cos\omega t + i\sin\omega t)$ it is necessary to look at the complex frequency response. Using complex algebra and substituting $h(t)$ with $\mathbf{H}e^{i\omega t}$ and $F_0\sin(\omega t)$ with $\mathbf{F_0}e^{i\omega t}$ into Equation (10) yields

$$(-m\omega^2+C_i\omega+K_s)\mathbf{H}e^{i\omega t}=\mathbf{F}e^{i\omega t} \qquad (11)$$

It is important to note that only the imaginary part of Equation (11) is relevant. Furthermore, the general solution to this equation consists of the complementary solution, which represents the transient nature of the system, and of the particular solution, which is the steady state solution. Since this system is in a steady-state condition when running the tests that is the solution that is wanted. For the system shown above, the output

displacement amplitude, H, is obtained by multiplying Equation (11) by its complex conjugate which leads to

$$\left|\frac{F_0}{h_0}\right| = \sqrt{\left(K_s - m\omega^2\right)^2 + \omega^2 C_i^2} \qquad (12)$$

The phase angle between the applied force and the resulting displacement is given by

$$\tan\phi = \frac{C_i\omega}{K_s - m\omega^2} \qquad (13)$$

To understand the response of the system once it has come into contact with the specimen it is necessary to look at the more complicated model as shown in Figure 4. The solution to this is understood by looking at the graphical vector representation in Figure 6. Remember that in the harmonic motion the acceleration is 180° ahead of the displacement while the velocity is 90° ahead of the displacement.

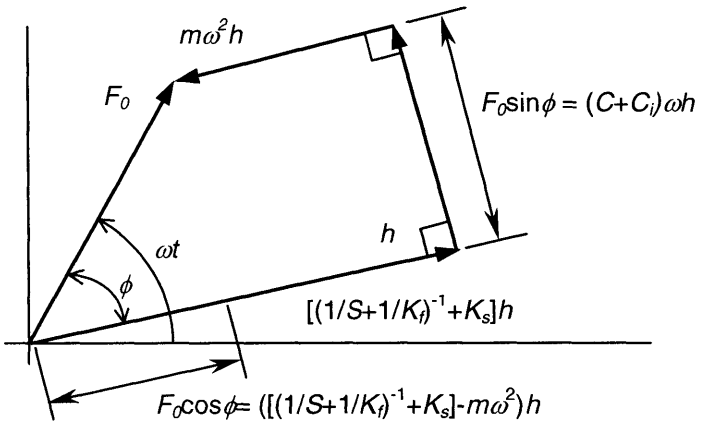

Figure 6: Graphical Representation of the dynamic response of the system after contact with specimen

The spring stiffness is associated with the displacement (in a translation system $F=kx$) and is represented by the equivalent stiffness of $k_{eq}=[(1/S+1/K_f)^{-1}+K_s]$. The mass, m, is associated with the acceleration ($F=ma$) and therefore it is 180° out of phase with the

displacement. Finally, the damping is associated with the velocity ($F=bv$) which is 90° out of phase with the displacement and the equivalent damping is $C_{eq}=(C+C_i)$. It follows then that the equations describing the performance of the system are

$$\frac{F_0}{h_0}\cos\phi = \left[\frac{1}{S}+\frac{1}{K_f}\right]^{-1} + \left(K_s - m\omega^2\right) \qquad (14)$$

$$\frac{F_0}{h_0}\sin\phi = \left(C + C_i\right)\omega \qquad (15)$$

From Figure 6 the phase angle can be found as

$$\tan\phi = \frac{\left(C + C_i\right)\omega}{\left[\frac{1}{S}+\frac{1}{K_f}\right]^{-1} + \left(K_s - m\omega^2\right)} \qquad (16)$$

The final consideration is the calculation of the modulus from the frequency specific indentation. Referring to Figure 7 the Δh is described by Equation (17).

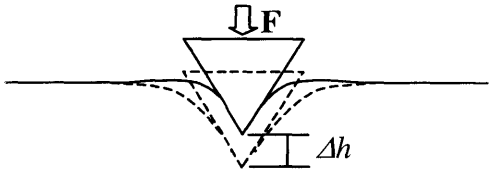

Figure 7: Modulus measurement with the Continuous Stiffness Method

$$\Delta h = \frac{F}{E}\frac{\sqrt{\pi}}{2\sqrt{A}} \qquad (17)$$

Rearranging Equation (17) by solving for the modulus (compare to Equation (7))

$$E = \frac{F}{\Delta h}\frac{\sqrt{\pi}}{2\sqrt{A}} \qquad (18)$$

Furthermore, since the testing machine can be fully characterized meaning that values for K_f, K_s, C_i and m can be found, it is possible to determine the stiffness (S) and damping (C) properties of the material under test. This can be seen by rearranging Equations (14) and (15).

$$S = \left[\frac{1}{\frac{F_0}{h_0}\cos\phi - \left(K_s - m\omega^2\right)} - \frac{1}{K_f} \right]^{-1} \qquad (19)$$

$$C\omega = \frac{F_0}{h_0}\sin\phi - C_i\omega \qquad (20)$$

2.3 Characterization of NANO INDENTER® II

As mentioned previously, it is necessary to know the different parameters of the system so that measurement of the modulus can be made. These parameters along with typical values are shown in Table 3.

Table 3: Parameters to Characterize the NANO INDENTER® II

Symbol	Quantity	Typical Value(s)
A	Area of the indenter	$24.5h^2$+...
E_i, ν_i	Indenter elastic constants	E_i = 1141 GPa, ν_i = 0.07
β	Geometric Berkovich tip factor	1.034
K_s	Indenter support springs	46.63 N/m
K_f=1/C_f	Load Frame Stiffness	7.86×10^6 N/m
m	Indenter mass	6.579g
C_i	Damping of Capacitive Displ. Gage	5 N/m/s

Some of the values summarized in Table 3 have already been discussed in regards to how they are obtained. However, a discussion about how the area of the Berkovich tip and the load frame compliance will be discussed now. These two parameters are important to

ensuring that precise values of the specimen modulus are measured. Therefore, precise calibration methods have been developed.

For a perfectly shaped Berkovich indenter tip the contact area is described by

$$A(h) = 24.5h^2 \qquad (21)$$

Yet, in reality the Berkovich tip is not perfectly sharp, rather it is rounded, thus it is necessary to calibrate each tip by approximating the shape with

$$A(h) = 24.5h^2 + C_1h^1 + C_2h^{1/2} + C_3h^{1/4} + \ldots + C_8h^{1/128} \qquad (22)$$

where C_1 to C_8 are constants to be found. In the past the area function was determined by imaging a series of large indentations. However, imaging methods are either not effective for small indentations (such as optical imaging) or they are very time consuming and expensive (such as TEM). Oliver et. al.[2] have devised a reliable method for calibrating the area function without imaging. Their method for determining the area function is also done in conjunction with the measurement of the load frame compliance.

The calibration technique that they advise uses two calibration samples, one is well-annealed, high purity aluminum and the other is fused quartz. These two materials are chosen since they both have well known elastic moduli that are not depth dependent and they both are elastically isotropic.

Since the calibration indentations are carried out in pure indentation mode, the load frame and specimen can be modeled as two springs in series. Remembering that the compliance is the inverse of the stiffness the combined compliance can be written as

$$C = \frac{1}{K_f} + \frac{1}{K_s} = C_f + C_s \qquad (23)$$

where C_f is the load frame compliance and C_s is the specimen compliance. Combining Equation (23) with Equation (7) gives

$$C = C_f + \frac{\sqrt{\pi}}{2E_r}\frac{1}{\sqrt{A}} \qquad (24)$$

The above formula can be further simplified since the elastic constants for aluminum are known to be E=70.4GPa and ν=0.347. Combining this information with the elastic constants of the diamond indenter (see Table 3) the value of E_r can be calculated (Equation (5)) and therefore Equation (24) can be simplified. The system can measure the total compliance, C, and the displacement, h, of the indenter. This is all the information that is available to calibrate the area function and find the load frame stiffness. To start, a series of large indents are made in the aluminum. For the two largest indents, as an initial guess, Equation (21) is used to calculate the contact areas. Next, an estimate of C_f is made from a plot of C versus $A^{-1/2}$. Then the contact areas for all of the indents is made by rearranging Equation (24) to be

$$A = \frac{\pi}{4E_r^2}\frac{1}{\left(C - C_f\right)^2} \qquad (25)$$

A graph of A versus h is used to obtain an initial guess for the area function as expressed in Equation (22). Since the area function influences the value of C_f, it is not finished with just one step. It is necessary to iterate the process until convergence is reached. Once convergence is reached, it will be noticed that on a plot of (C-C_f) versus $A^{-1/2}$ the

data are linear and that at $A^{-1/2} = 0$, $(C\text{-}C_f) = 0$. This is what should happen when the appropriate values of the load compliance and area function have been found. When the frame stiffness is found, the area function can be completely determined. The aluminum sample is good for large indents since it has low hardness however for small indents it is not good for the same reason. For that reason, the fused quartz specimen (E=72 GPa and ν=0.170) that has a high hardness is used to make small indents. The constants for the area function (Equation (22)) are found by fitting the data for both the large and small indents.

Oliver et. al.[2] assessed the capability of the aforementioned calibration procedure by testing six different materials. After creating the indentations the contact areas were determined through SEM imaging. These values were compared with the calculated values from the procedure above and the agreement was very good.

3. SAMPLE PREPARATION FOR THE NANO-INDENTATION TEST

With an explanation of the physics for the NANO INDENTER® II now in place, it is possible to look at the specifics of the indentation tests for the optical fibers.

Sample preparation for the NANO INDENTER® II is very important if accurate results are to be obtained. For successful tests, the sample should be smooth and flat at an 800X magnification. The samples need to be 38mm (1.25in) diameter cylinders to fit into the holder of the indentation system (shown in Figure 8).

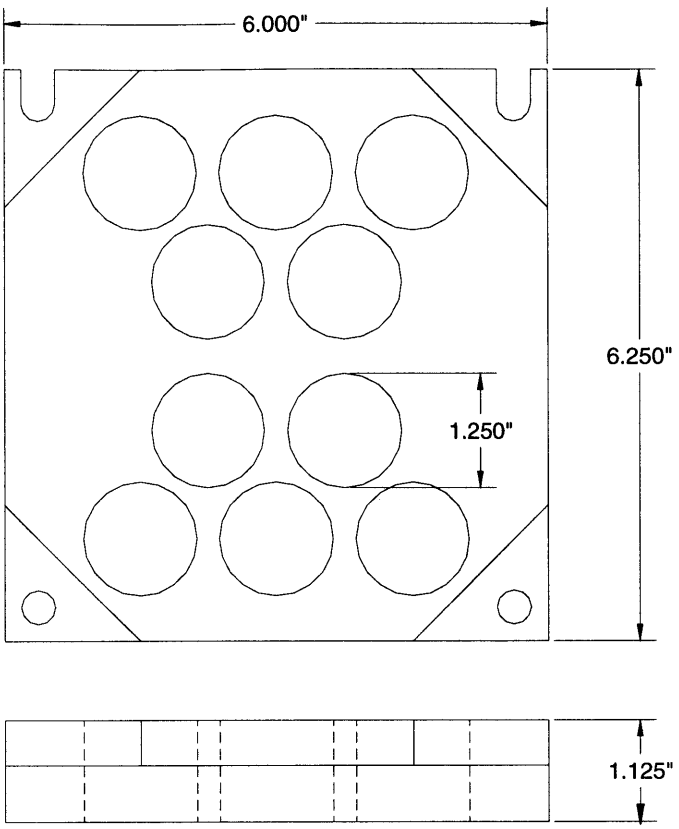

Figure 8: sample Holder for the NANO INDENTER® II

3.1 First Attempt at Sample Preparation

In the initial attempt to prepare specimens, optical fibers were aligned vertically in a cylindrical mold that was later filled with epoxy. The cylinder was cut in the horizontal (or transverse) plane with the fibers lying perpendicular to the plane. It is customary for the samples to be metallographic samples that can be polished using standard established techniques. However, the optical fiber presents some very special requirements that do not allow for standard preparation. In fact, the sample preparation was very difficult and a solution was found only after much trial and error. The reason for the difficulty has to do with the optical fiber itself. Since the optical fiber is composed of at least two materials with very different elastic moduli the polishing becomes very difficult. The silica core has an elastic modulus of around 72 GPa whereas the coatings on the optical fiber have an elastic modulus from about 4MPa to 1GPa (100 to 20,000 times less stiff

than glass). This creates an obvious problem in preparing a good smooth surface for use in the NANO INDENTER® II. The first attempt to make the sample was by casting the optical fiber in an epoxy mold. These samples were made with EpoFix epoxy and the optical fiber. Once the epoxy had cured the sample was cut with a diamond saw into sizes that would fit into the sample holder (less than 1.125"). Then one side of the sample was polished to obtain a smooth surface. To obtain this the samples were placed in a Buehler Mechanical Polish/Lapping machine. First the sample was polished with a 600-grit size (14μm nominal grain diameter) paper and then an 800-grit size (10μm nominal grain diameter) paper and finally a 1200-grit size (5μm nominal grain diameter). After this a polishing pad with alumina was used. The crystal sizes for the alumina were 3μm and on down to less than 1μm. The problem with this method was that the coating around the silica core was severely damaged and not smooth. In fact the more that it was polished the worse it became as it would start rounding. Since the coatings are so soft compared to the glass the coating material is removed much faster than the silica. To make things even worse, the silica as it grinds off gets embedded in the soft coating which then completely destroys the coating and makes it entirely unacceptable for tests. After attempting to make the sample this way it became clear that a different approach was necessary.

3.2 Failed alternative sample preparation methods

Attempts to prepare samples using a rotary and sliding microtome with glass and diamond cutting blades did not yield good results. Freezing the optical fiber with liquid nitrogen while using the microtome did not help. These different approaches did not give

a good sample surface that could be used in the tests. Finally a method was found that created an acceptable surface for testing.

3.3 Final sample preparation method

Failure of the above approaches made it clear that the very stiff silica core needed to be avoided as much as possible. Consequently, it was decided that the optical fiber should be placed on its side and polished from the side as opposed to the circular cross-section. Furthermore, the polishing would only be performed until the coatings had been exposed and only a minimal amount of the glass was uncovered. This would require very careful supervision of the polishing procedure since there is only about 62.5μm of coating thickness (Figure 9). To improve the prospects for success many fibers were embedded onto the same aluminum plate. Figure 10 shows a diagram of the final sample layout with the optical fibers to be tested embedded in epoxy on top of an aluminum plate.

The polishing procedure has to be carefully chosen to yield acceptable results. In general, it was found that there is a certain point at which more polishing makes the sample worse. Indeed, things would go from good to bad very quickly with excessive polishing. Once the epoxy was cured the sample was loaded into a Buehler Mechanical Polish/Lapping Machine with a 600-grit size paper. Close monitoring was necessary to ensure that once the surface of the optical fiber was reached, polishing was stopped so that it did not progress deep into the fiber. This could be a matter of a few minutes depending on the thickness of the epoxy on top of the fibers. Once the fibers were reached it would be just a matter of minutes before the optical fibers were completely polished away. Vigilance was essential. When the optical fiber was exposed the polishing paper was changed to an 800-grit size paper. This was done for about a minute

and then it was changed to a 1200-grit size paper that was run for just a few more minutes before the whole process was completed. During this process the sample was checked under a microscope to see that it was progressing well. As mentioned above, the sample should be smooth and flat at an 800X magnification. Excessive polishing beyond the process described above always led to rounded samples that would not work for the tests.

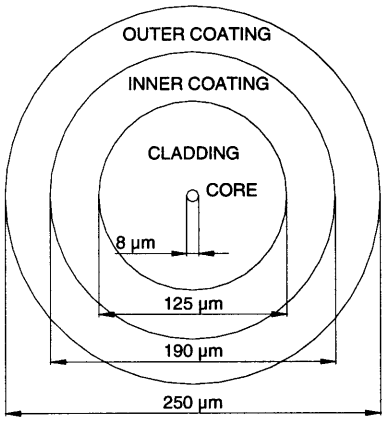

Figure 9: Typical Optical Fiber Geometry

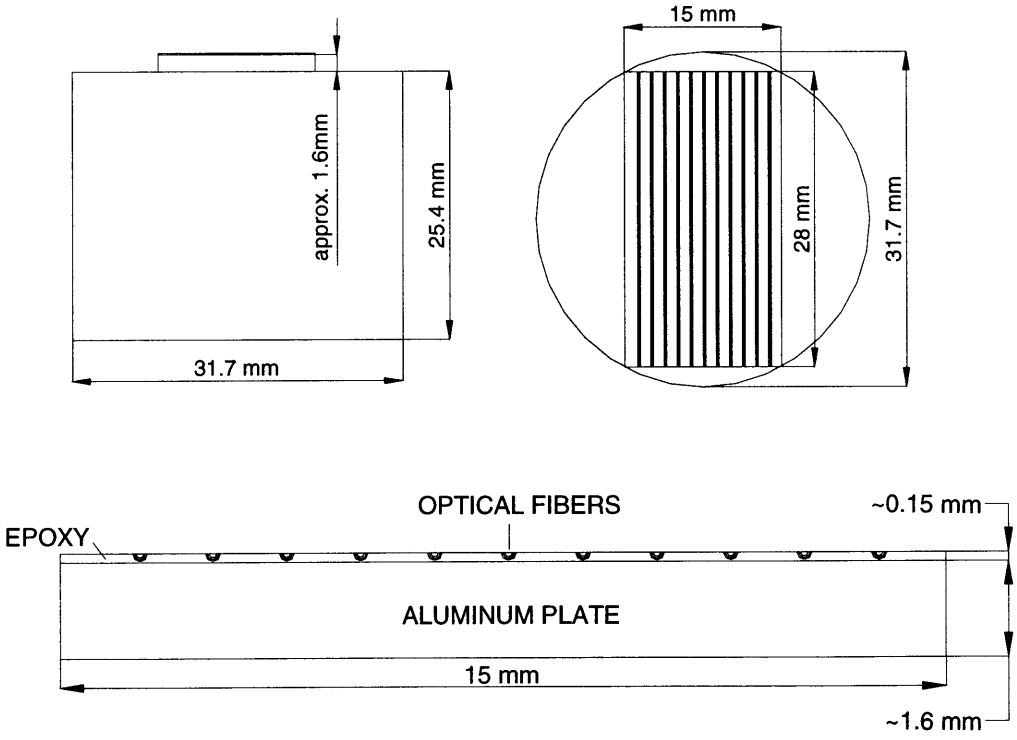

Figure 10: Final Sample for NANO INDENTER® II

4. THE NANO INDENTER® II TESTING PROCEDURE

4.1 Preliminary Considerations

Before the tests even begin it is necessary to determine whether the machine has the capability to measure the desired modulus and if it can which procedure will best suit this purpose. The NANO INDENTER® II has very impressive measuring capabilities as mentioned earlier nonetheless, these capabilities need to be used judiciously if an accurate measurement is to be obtained. For soft materials this is especially true since the machine and the testing procedures were originally focused on testing stiff materials. Nevertheless, as will be shown the machine has the capability to measure materials with low stiffness when proper attention is paid to some important details. One of the critical details is the ability of the system to detect the contact stiffness of the surface.

The dynamic model presented in Section 2.2.2 provides a framework by which to assess whether the machine and/or the proposed testing procedure are capable of determining the desired stiffness. As mentioned previously, the Continuous Stiffness Method can be used to not only find the modulus of the material but to also find the surface of the material. In order to find a minimum discernible contact stiffness the dynamic compliance of the system can be calculated for the frequency at which the tests will be conducted. Figure 11 shows the dynamic compliance of the NANO INDENTER® II system over a wide range of frequencies. The plot was created using Equation (12) along with the representative values found in Table 3.

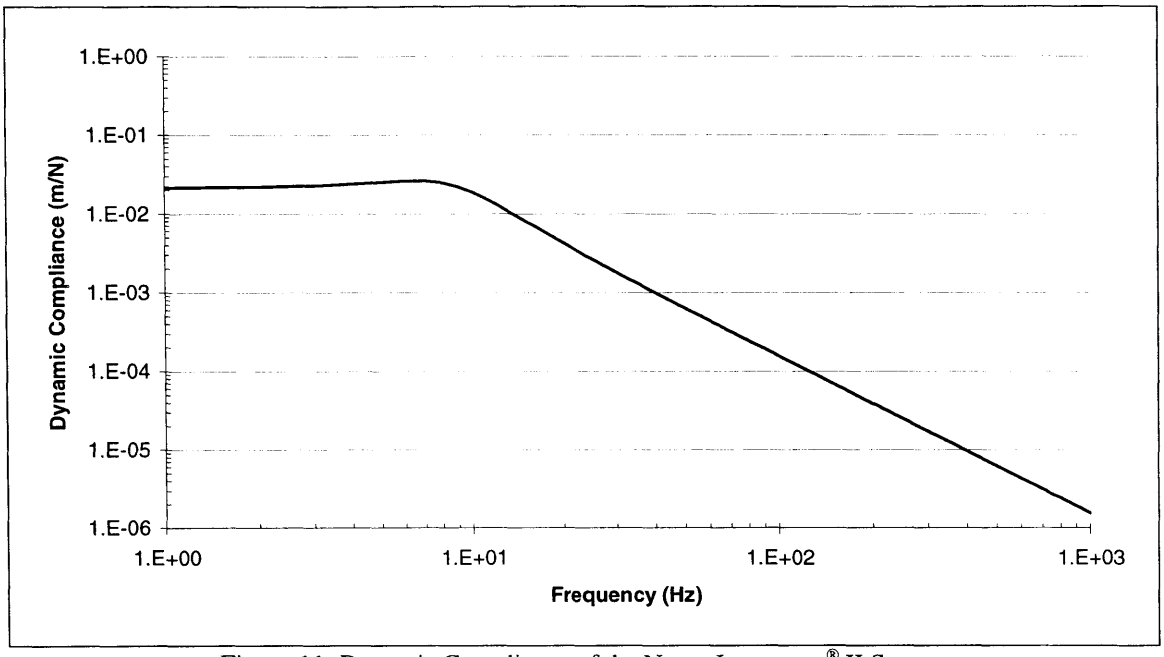

Figure 11: Dynamic Compliance of the NANO INDENTER® II System

The experiments carried out here were done at a frequency of 10Hz since the desired modulus measurements were done for a quasi-static system (the crack sensor is for static measurements of cracks). The dynamic stiffness (the inverse of the compliance) of the system at 10Hz is 53N/m. This value represents the combined effects of the indenter rod mass and the leaf springs. For the contact stiffness to be accurately measured, the change in stiffness on contacting the specimen must be significant compared to the initial indenter stiffness contributed by the leaf springs alone. According to Lucas et al[7], the contact stiffness should be at least 10% of the indenter stiffness. Given that the contact stiffness depends on the contact area, which increases with penetration depth, an initial analysis can be carried out to find the required penetration depth, h, for S to be sufficiently high. Recalling Equation (7), the stiffness of the sample is directly related to the contact area and the stiffness of the specimen. Equation (22) shows that the contact area is directly related to the indenter displacement h. Combining this information makes it possible to create Figure 12. This graph shows the contact depth

necessary to measure several different moduli. The horizontal line in Figure 12 represents 10% of this value, which is the lowest contact stiffness that can be accurately measured. The trend is that the lower the modulus to be measured the greater the need to have a greater contact depth. For example, since one of the tests was to measure a coating modulus suspected to be around 1MPa, a contact depth of at least 1,000nm (1μm) should be used in the tests.

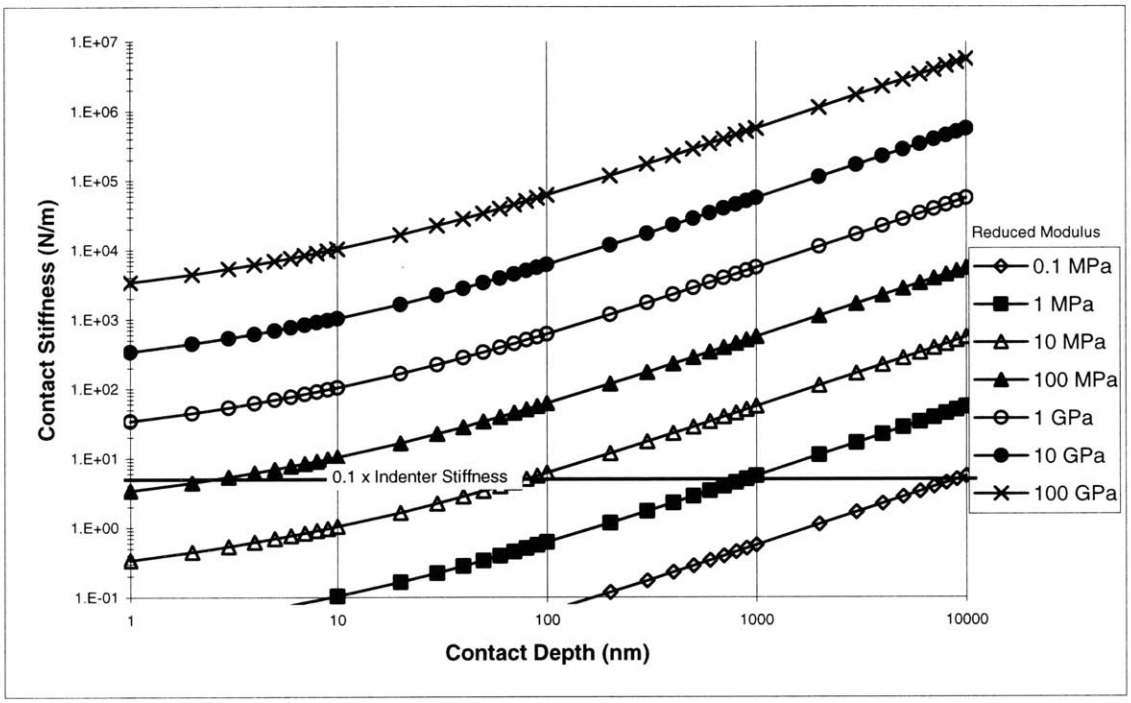

Figure 12: Theoretical plot of contact stiffness versus depth for different material moduli (The horizontal lines show the minimum measurable stiffness which is 10% the indenter stiffness)

One may suggest employing a very high contact depth (say 10,000 nm) for any test, to ensure sufficient contact stiffness for the sample. However, there are other considerations that will limit the indenter penetration depth. For the optical fiber polished from the sides, the exposed polymeric coating is on top of epoxy resin. Also, for fiber with a dual coating, the inner coating is lying on top of the outer coating. Depending on the location of the indent, the coating/epoxy interface or inner/outer

coating interface may not be very far away from the sample surface. The deeper the indenter penetration, the higher is the chance to have the contact stiffness affected by properties of the underlying or adjacent material. Therefore, the specification of very high contact depth may not be practical. In the coating tests, a specified contact depth of 3,000nm was found to be a good compromise that produced consistent results.

4.2 Finding the Sample Surface

The previous discussion spoke about the importance of the contact area in finding the modulus of a material. For an accurate measurement of the contact area it is necessary to have an accurate value for the displacement h as seen in Equation (22) in addition to having a good calibration for the Berkovich indenter tip. The system has very good displacement resolution (±0.04nm) and therefore the limiting factor is to know when to start measuring the displacement. In other words finding the surface of the sample is very important. For soft materials, initial contact is associated with a small force that is quite difficult to determine. The default values used by the NANO INDENTER® II in the surface search were found to be inadequate. Experience has shown that the system will automatically pick the surface point after the indenter has already entered into the sample a considerable amount. Therefore, the contact area is underestimated which means that the modulus is overestimated. Hence it is necessary to understand the function of the surface search and how to modify it to work for soft materials.

As was mentioned previously, the NANO INDENTER® II has amazing measuring capabilities that have originally been set-up to test stiff materials, albeit the system can be modified to better suit the needs of testing low stiffness materials. The Continuous Stiffness Method (CSM), which is used in finding the surface after the initial rough find,

can be modified to better accommodate searching on a polymer surface. When the modulus of the material is very small, the stiffness or mechanical transfer function is by definition going to be very small, that is, the force required for a given oscillation size is going to be small. To overcome these types of problems the voltage divider in the oscillator output line can be changed. A reduction in the voltage going into the oscillator will give a better discretization in the excitation at the smaller contacts. An increase in the in-line resistance of the oscillator output effectively reduces the amplitude of the signal being sent to the indenter head. This increases the resolution of the oscillator at small amplitudes. The default resistor (in the NANO INDENTER® II it is 15 kΩ) used for this divider circuit is located in the blue box in the BNC coaxial cable coming out of the oscillator. This can be changed to a higher value of resistance. Then it is necessary to re-run step 2 of the dynamic calibration (the step that creates the look-up table for the modulation) to get the calibration for the new set-up. Different values of resistance were tried and finally a resistance value of 200kΩ was settled on. One way to know that this change is necessary is shown in Figure 13. The jumps in the Amplitude voltage (it should be smooth and not have jumps) occur at the steps taken in the Excitation voltage (the voltage driving the oscillation). Decreasing the jumps in the Excitation voltage by increasing the resistance in the divider circuit helps to reduce the unwanted jumps. If the resistance is changed it needs to be done before any tests are run since a new calibration file needs to be found.

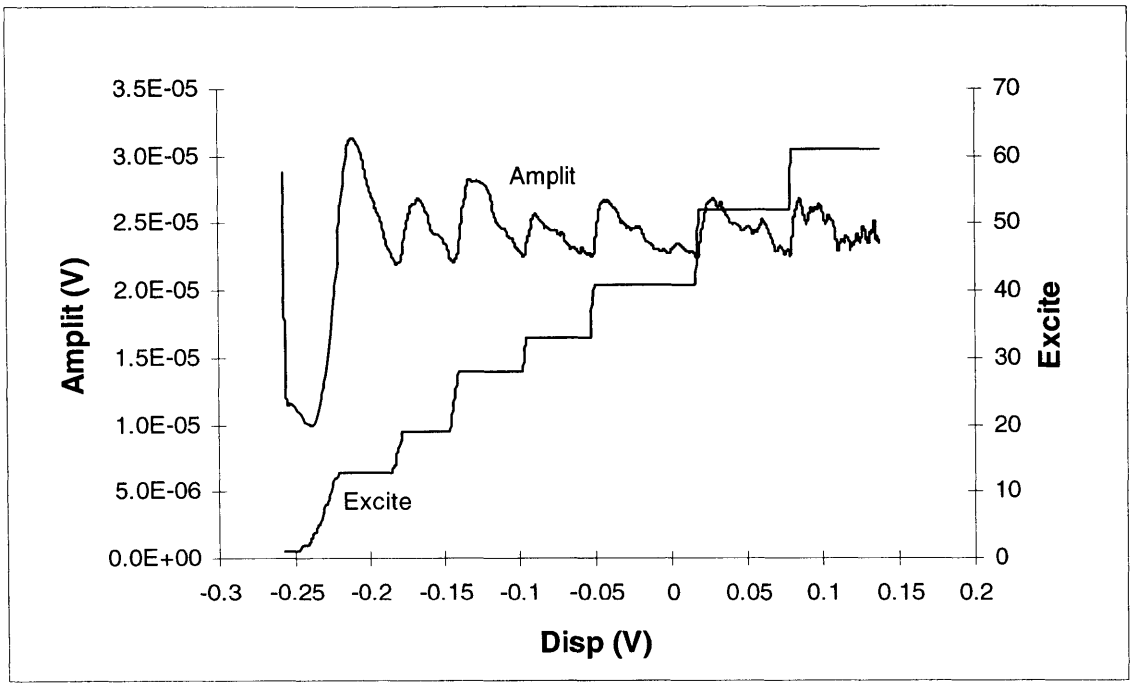

Figure 13: Illustration of the influence of the voltage excitation levels in CSM on testing soft materials

Once the system is set-up, the specimens are ready and in place, and the operator is setting up the tests there is one more available choice to make concerning the CSM. The system will ask if the user wishes to use "Constant Displacement or Constant Force Oscillation (D/F)?". The "Constant Displacement" method controls the amplitude of the oscillation to the prescribed amount by using a loop to find the correct force. The "Constant Force" method controls the force of the oscillation and does not require a loop since it is a force controlled system. It was found that the "Constant Force" method worked best in testing the optical fiber coatings. The system also allows one to choose the force to be used. A load of 3μN worked best for the tests.

The surface find of the NANO INDENTER® II involves several different steps some of which are summarized in Figure 14.

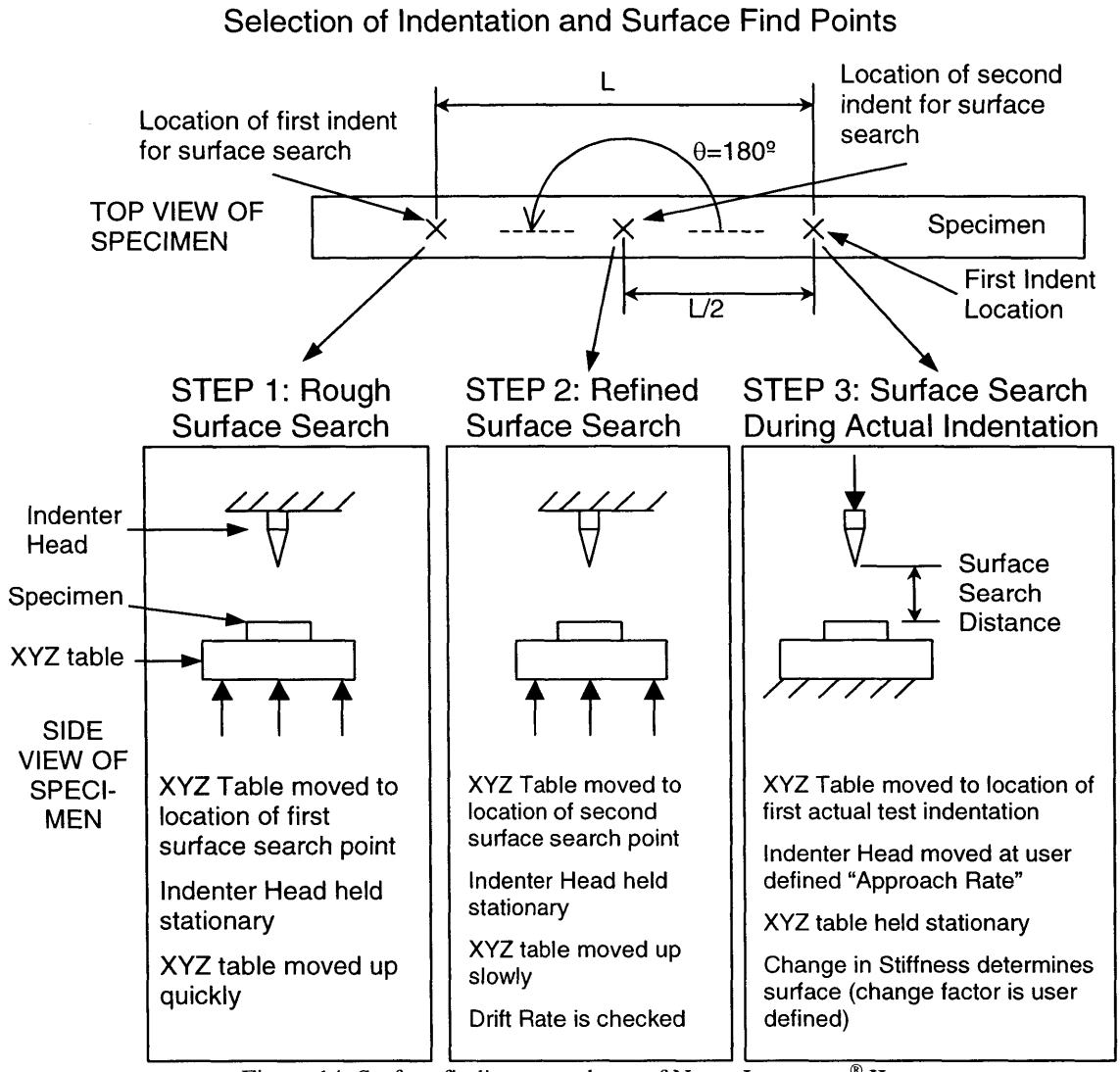

Figure 14: Surface finding procedures of NANO INDENTER® II

It is important to carefully select the points that will be used for the indentation so that the first two preliminary indents that are done automatically to find the surface are carried out in a good location. The default values for the initial surface searches were used, which are L=50μm and θ=180° (referring to Figure 14). Of course these could be changed, however the user should select points such that the surface searches occur on a surface at the same level as the actual indents that will be tested.

The first surface search is a rough surface approximation (STEP 1 in Figure 14) and is done by quickly raising the XYZ table to cause an indent in the sample. This quick movement will give a rough estimate of the surface height. Next, (STEP 2 in Figure 14) the table is moved to a new location where it is slowly raised until the surface is found. At this point the displacement gage reads near zero displacement. This procedure produces the best estimate of the surface location that can be made by moving the tables only.

During this second surface finding indent, the drift rate of the indenter while in contact with the specimen is monitored. The actual indentation test will only start when the drift rate is sufficiently low, so thermal and/or vibration effects on the test results are minimized. Once the drift rate becomes smaller than the user prescribed maximum the displacement of the indenter is recorded which establishes the initial estimate of the elevation of the sample surface. The default value for the drift is 0.05nm/s however a drift value of 0.1nm/s worked best in the tests conducted for the optical coatings moduli.

With an estimate for the surface, the indenter moves to the specified location for the first indentation (STEP 3 in Figure 14). The indenter moves down into a position that is located above the estimated surface location by a distance specified as the "Surface Search Distance" that is usually 1000 to 2000nm. Measuring soft polymers as found on the optical fibers required a larger "Surface Search Distance". A value of 3000-5000nm was found to work fine. Once the indenter is in place, it is set to approach the sample while the displacement and corresponding load are recorded. When the indenter reaches the surface, an increase in stiffness is sensed by the change in the stiffness of the system, which reflected initially in the stiffness of the very flexible leaf springs that support the

indenter shaft. The system defines the surface as the point at which the stiffness reaches a magnitude that is a certain factor times the stiffness of the springs. By default, this factor is set to 4. It was found in the testing that using the default value of 4 is not good for finding the surface of soft polymers. This is due to the fact that the soft material introduces very little force on the indenter tip on initial contact, resulting in a very small stiffness increase. For various coatings, different factors were identified by trial and error. A value of 1.25 worked fine for the inner coating of the SMF28 Corning Fiber, a value of 2 for its outer coating and 1.75 for the single acrylate coating on the 3M FS-SN-4224 optical fiber.

One of the ways to tell if the system is detecting the surface correctly is to look at the "Approach Curve". This is a graph of the Load (or Phase) versus Displacement as the indenter approaches the sample surface during the "Surface Search Distance" mentioned earlier. The approach curve should have a very definite jump or "knee" when it touches the surface (see Figure 19 for an example). The system generally does a good job finding the surface of stiff materials like fused silica. However, since the system is not really tuned to test soft materials it is necessary to adjust it to work as desired. There are two main factors to be adjusted so that a good approach curve can be constructed. Those two factors are the "Surface Search Distance" and the number of points to save from the approach curve. Their importance is illustrated in Figure 15. The search distance is important since it determines how much above the location of the surface (what the system thinks is the surface) the indenter should start to approach the surface. As Figure 15 illustrates, in a worse case scenario using the default settings, this could mean that the indenter starts to approach the surface when it actually is already inside the specimen.

Obviously, in this situation the surface will never be found. The other main factor to consider is that the system does not automatically save all of the information from the approach segment; it is necessary to tell the system how many points it should save. By definition, the number of points that are saved is counted starting from where the system thinks is the surface going backwards. Once again referring to Figure 15 the default setting only saves the last 50 points which is most likely less than the total approach segment (in the worse case scenario case it does not matter since the approach segment is already inside the material). However, this is important because, even if the search distance is increased so that the approach segment of the indenter starts outside the specimen (as shown in the improved part of Figure 15) if only the last 50 points are saved the important part of the approach curve, that is the actual point of contact, will be lost. Hence, it is important to prudently adjust both factors so that the actual surface of the specimen is found.

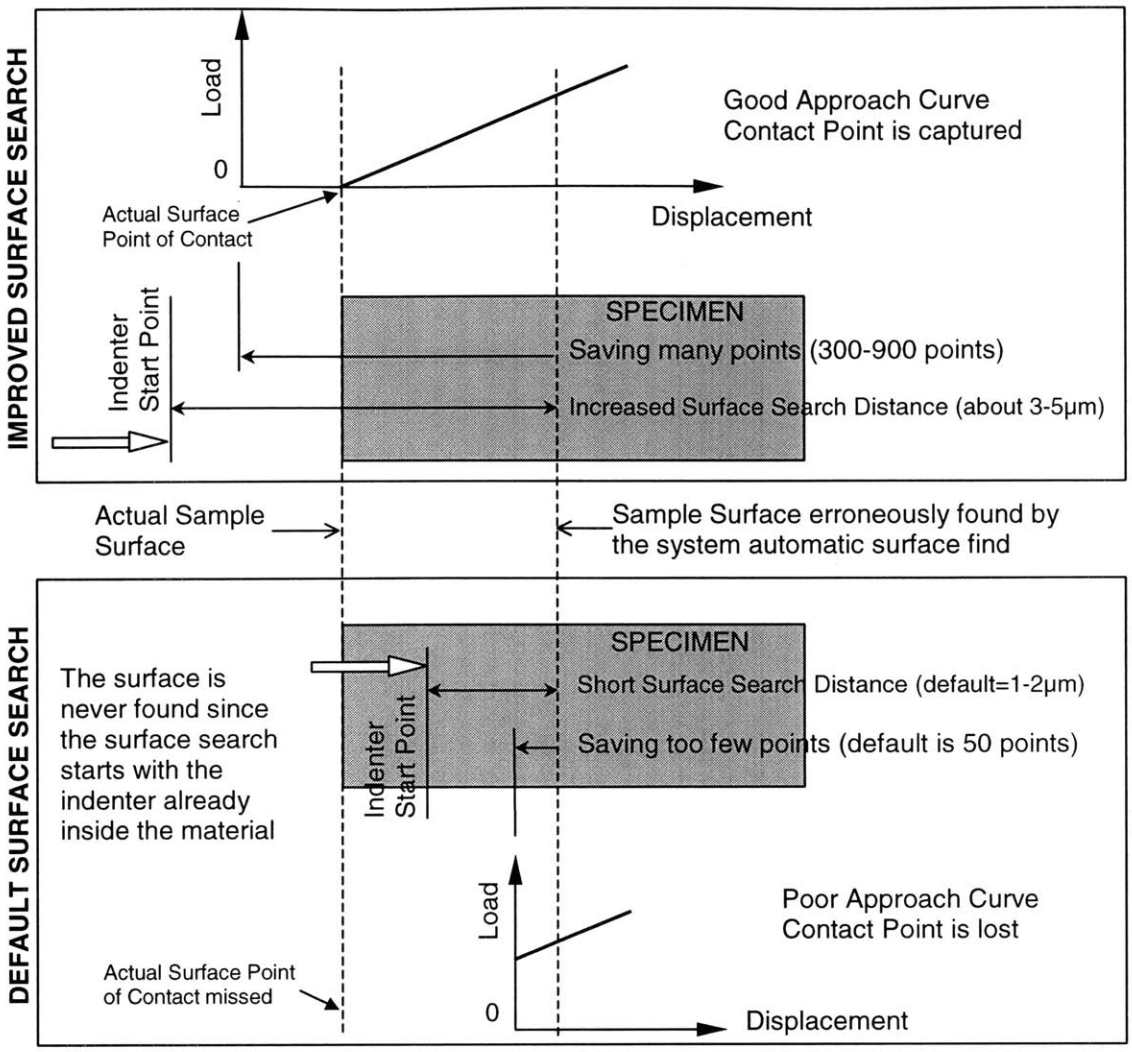

Figure 15: Factors in obtaining good Approach Curves

For completeness, it should be mentioned that there are some additional factors that may need to be considered in order to find the surface. Those factors are the approach rate, the data logging rate and the maximum number of points that the system can save. The system saves one data point per second and therefore if the approach rate is very fast the number of points that are saved will be very low (the system will save the specified number of data points if there are enough, if not it will save less). Conversely, if the approach rate is very slow, the number of points saved may not be sufficient. The system can only save a maximum number of points (typically it can only save less than 1,000

points). One option is to specify that the system save data points at a slower rate, say one data point every two seconds. Of course, another consideration in determining the approach rate is that it be good for finding the surface and that it be a good indentation rate. Since the system is usually lost and it is already indenting into the material before it stops the "Approach Segment", then the approach rate that is indicated will actually be the initial indentation rate. The default approach rate is 10nm/s which worked fine for the tests that were run for the optical fiber coatings.

Finding the correct surface search distance, the right number of points to save, and the correct approach rate all require experience and therefore it takes some iteration to find the correct values. The approach curves give good insight about whether these different parameters have been chosen correctly. Table 4 summarizes the values that were useful in finding the surfaces for the optical fibers.

Table 4: Summary of Recommended Values for Surface Search Parameters

Parameter	Material	Value
Surface Search Distance	Default	1,000-2,000nm
	SMF28–Inner Coating	3,000-5,000nm
	SMF28–Outer Coating & 3M	2,000-3,000nm
Number of Points to Save	Default	50 points
	SMF28–Inner Coating	500-900 points
	SMF28–Outer Coating & 3M	300 points
Approach Rate	Default	10mn/s
	SMF28–Inner Coating	5-10nm/s
	SMF28–Outer Coating & 3M	10mn/s
Data logging	Default	1 point/second
	SMF28–Inner Coating	1 point/s or 1 point/2s
	SMF28–Outer Coating & 3M	1 point/second
Factor change in Stiffness to determine surface	Default	4.00
	SMF28–Inner Coating	1.25
	SMF28–Outer Coating	2.00
	3M	1.75

To manually determine the correct point of contact, one can look at the Load versus Displacement relation for the approach curve (i.e. the part of the load vs displacement curve before and right after contact takes place). A typical example of such a curve is given in Figure 16. When the indenter is approaching the sample surface, small attractive forces may result from surface charges, leading to negative force. Then, when the indenter starts to penetrate the sample surface, the force will start to increase. For the purposes of these experiments the initial contact was assumed to occur at the point when the load is zero on the continuously rising part of the Load versus Displacement curve. This may not be the exact value, as contact may have already occurred before the point of zero load. However, this provides an objective way to find the surface, and the approach is found to give consistent modulus results in the tests.

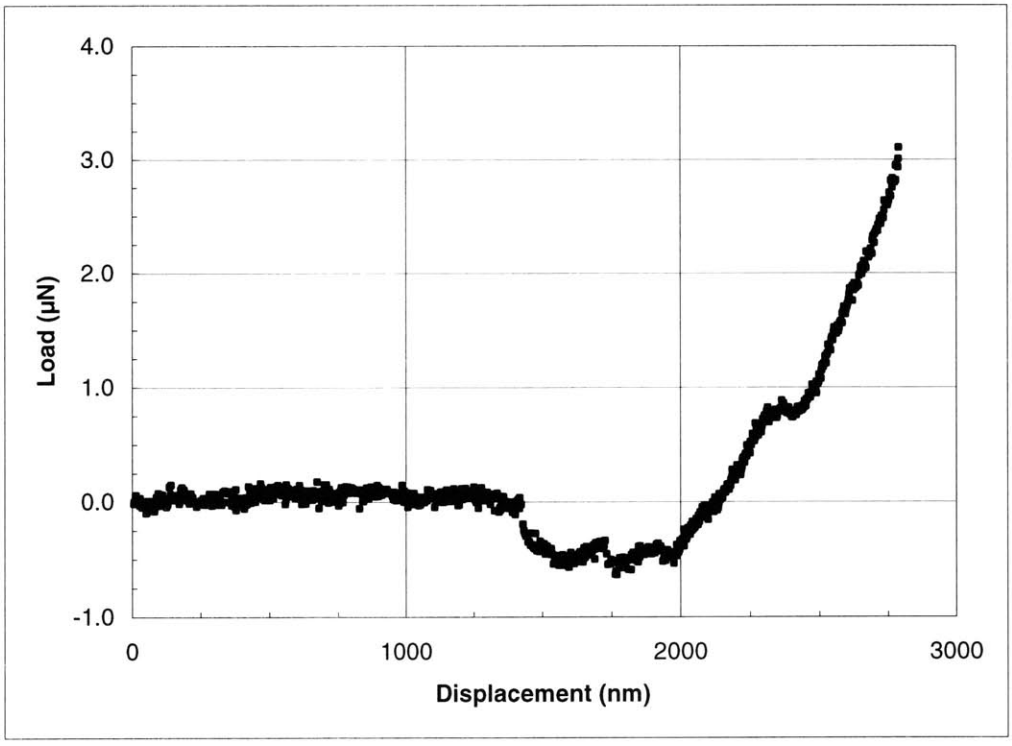

Figure 16: Approach Curve for Inner Optical Coating on Corning SMF28 Fiber

In some cases, the Load versus Displacement curve is much more "noisy" than the one in Figure 16, and cross the point of zero load several times. It is then hard to obtain the initial contact point.

The Continuous Stiffness Method offers a different approach for finding the surface. As previously described CSM has the ability to measure the modulus of the material at various depths. The CSM system can measure the harmonic force, harmonic displacement amplitude and the phase angle between the force and displacement. The ability to measure the phase angle is helpful in finding the sample surface. Recalling the dynamic model before contact (Figure 4) and after contact with the sample (Figure 5), it is evident that when the indenter contacts the sample there are additional damping and stiffness components from the sample that are now part of the model. Comparing the equations for the phase angle before contact (Equation (13)) and after contact (Equation (16)) this influence is obvious. To illustrate the point, Equation (16) can be further simplified by assuming that the damping of the specimen is zero (like Oliver, et. al.[2] have done) then the equation becomes

$$\tan\phi = \frac{C_i\omega}{\left[\frac{1}{S}+\frac{1}{K_f}\right]^{-1}+\left(K_s - m\omega^2\right)} \qquad (26)$$

With this simple equation it is possible to plot the phase angle before and after contact as seen in Figure 17 and Figure 18. These graphs show the dramatic change in phase angle that takes place once the indenter makes contact. Since the graphs do not take into consideration the damping of the material, they are not intended to predict the phase angle change exactly, rather just to show the trend. Figure 17 shows the influence of the

specimen modulus in the phase angle with the excitation frequency held at ω=10Hz. The contact depth is taken to be just h=10nm, so it is just touching.

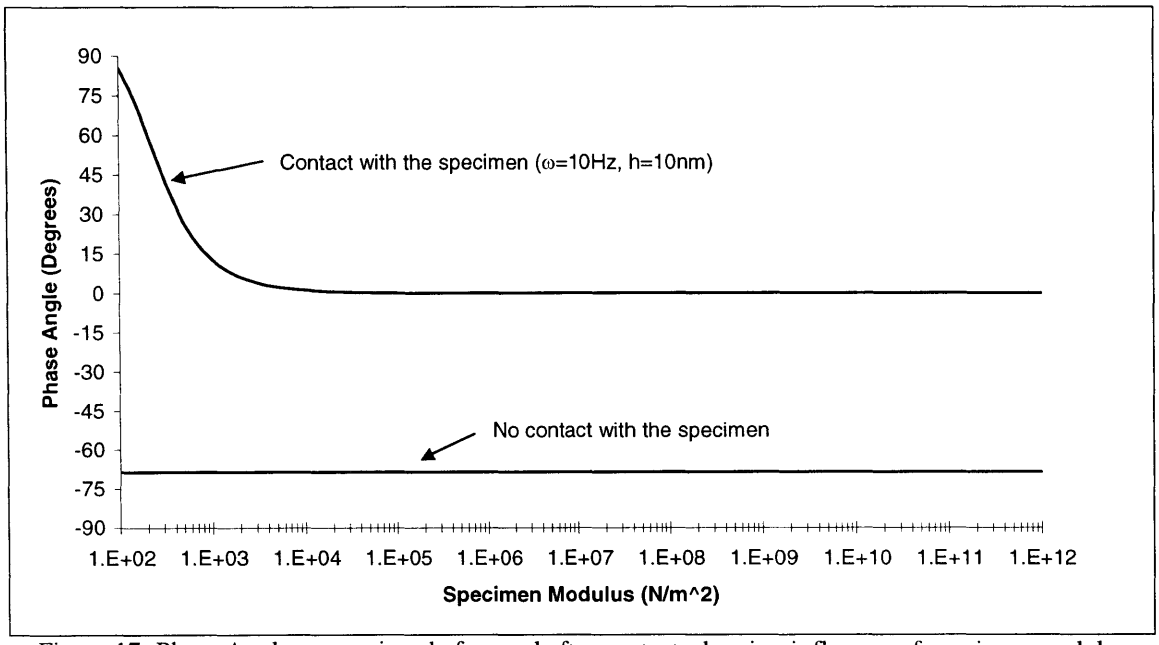

Figure 17: Phase Angle comparison before and after contact, showing influence of specimen modulus

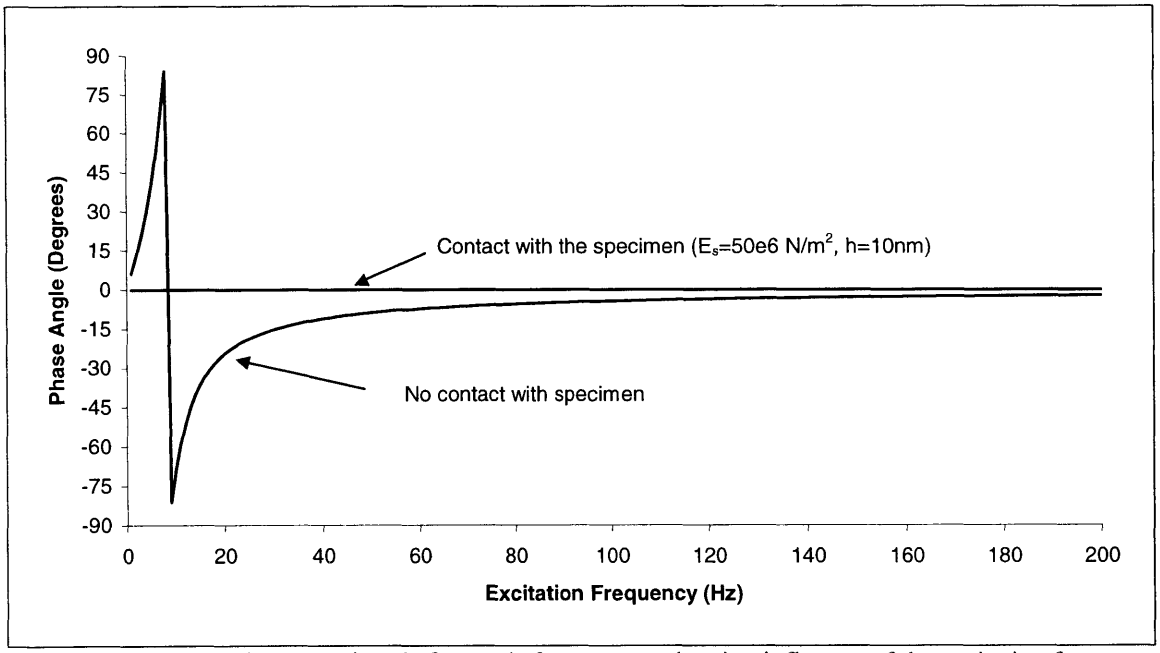

Figure 18: Phase Angle comparison before and after contact, showing influence of the excitation frequency

Figure 18 on the other hand shows the influence of the excitation frequency on the phase angle. In this situation, the sample modulus is taken to be E_s=50MPa, just like the 3M optical fiber coating, and the contact depth is once again taken to be h=10nm.

The oscillatory load was very helpful in identifying the sample surface of the stiffer optical fiber coatings. A typical approach curve showing phase versus approach distance is shown in Figure 19. A sudden change of phase can be clearly observed. The phase change signifies initial contact between the indenter and the sample.

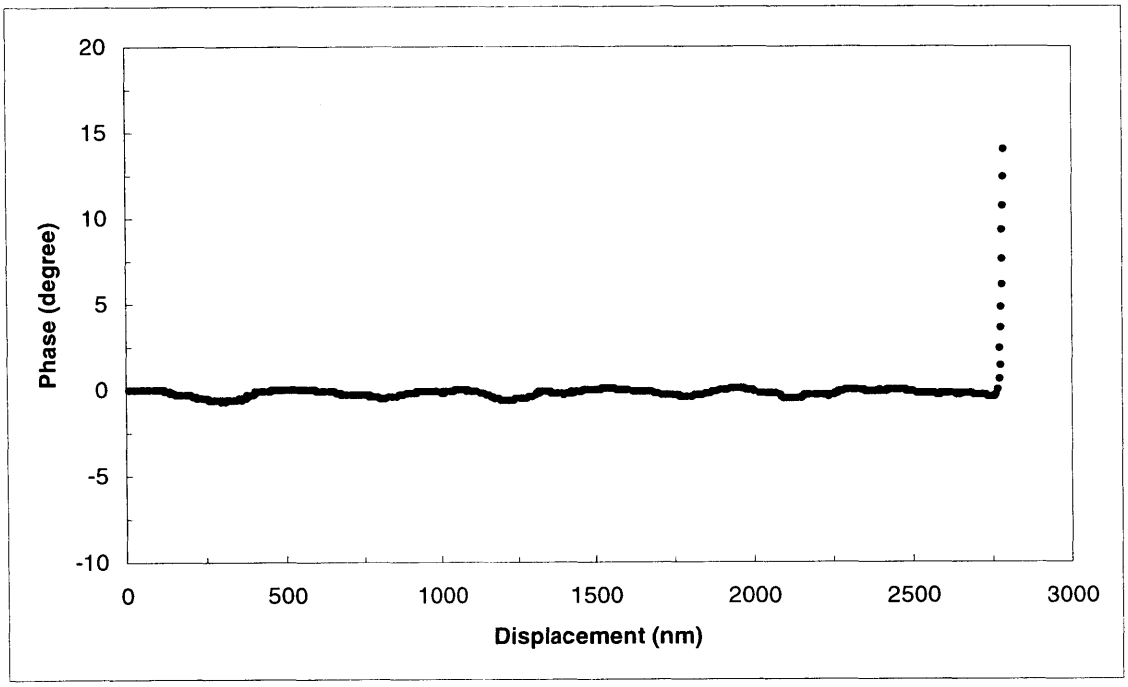

Figure 19: Approach curve for optical coating on 3M FS-SN-4224 Fiber

4.3 The Actual Indentation Process

With the surface properly identified it is possible to obtain good results in measuring the modulus of these materials. As explained previously, the modulus can be measured using the pure indentation technique or the CSM. The actual indentation procedure followed more routine procedures. In Figure 16, only the initial part of the load versus displacement curve (the approach curve) is shown. A curve starting from the manually

determined point of contact is given in Figure 20. A "Constant Loading Rate Loading Segment (LL)" is most precise since the NANO INDENTER® II is designed as a load controlled instrument. Therefore the "LL" segment was used in the tests carried out for the optical fiber coatings. The "Constant Displacement Rate Loading Segment (LD)" was sometimes used to find an appropriate load limit for the tests to reach a desired displacement.

The depth of the indentation is important for good results and therefore should be selected wisely. This has been discussed previously and a depth of 3,000nm was found to work well.

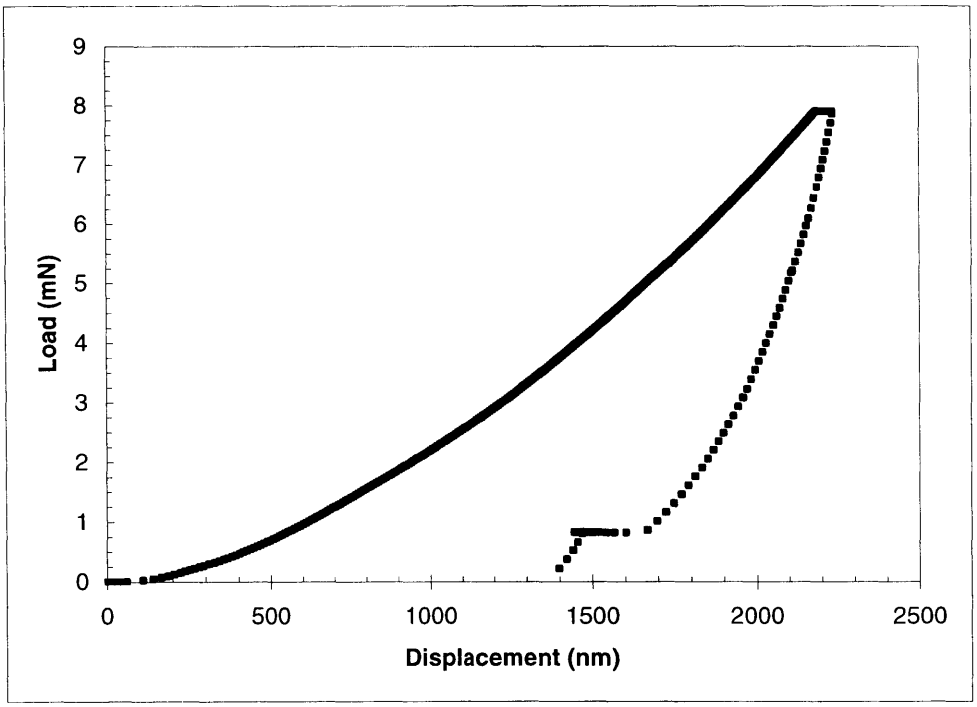

Figure 20: A Typical Loading/Unloading Curve

5. RESULTS

From the tests that were conducted, the pure indentation tests gave the most reliable and consistent results. Given that the crack sensor and strain sensors are studied in static

situations, the results from the pure indentation tests are more representative of the desired material properties. Still, some results from the CSM tests will be shown for comparison and then results from the pure indentation will be discussed.

5.1 Continuous Stiffness Method-Results

Figure 21 shows a sample of the CSM data from a test run on the inner coating of the Corning SMF28 optical fiber. In the beginning the modulus looks rather high and then the modulus quickly drops to a near steady state value. The reason for this behavior in the beginning could be explained by a couple of things. First, since the sample is made by polishing the surface it is possible that some debris particles from the sample or from the polishing materials became embedded in the surface of the very soft material. Certainly steps were taken to minimize this damage, however it is not possible to completely avoid it. Another reason for this behavior is that since the Berkovich indenter tip is not perfectly sharp, but rather it is rounded, at very shallow depths there is much greater likelihood for error in the contact area calculation.

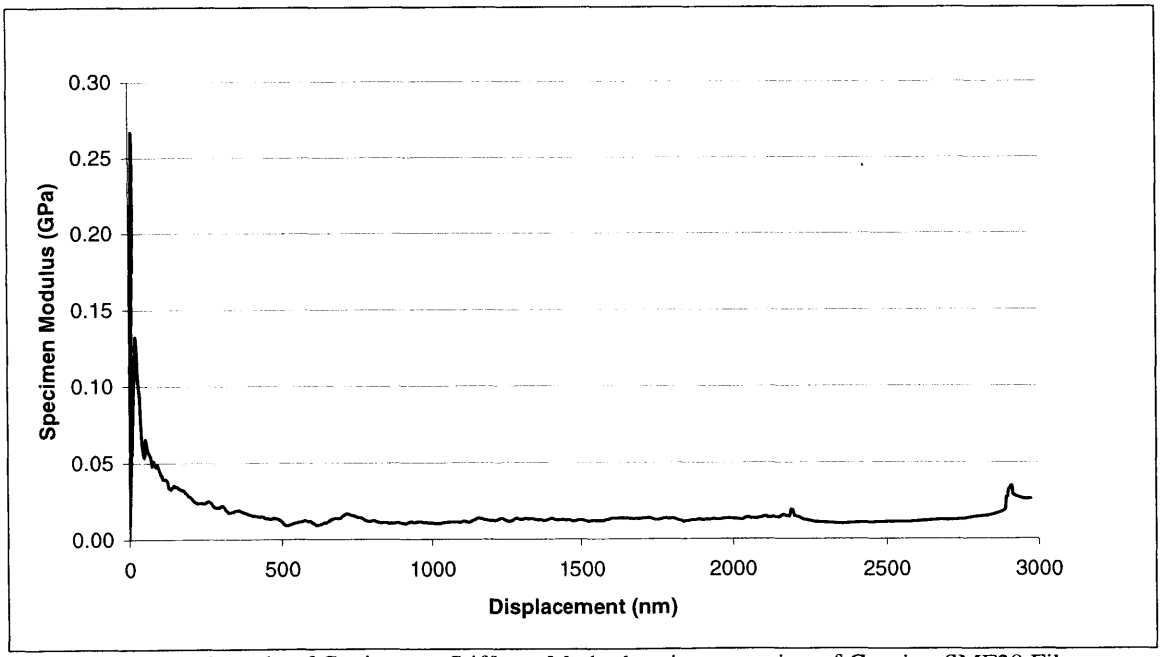

Figure 21: Sample of Conintuous Stiffness Method on inner coating of Corning SMF28 Fiber

Since the scale in Figure 21 is rather high it is difficult to see what happens once the steady-state value is reached. Figure 22 shows a closer view of the CSM results from three different indentations on the inner coating of the SMF28 fiber. Looking at the results in this region shows that there is some noise even at a near steady-state region. Table 5 shows the CSM results from three indentations made on the inner coating of the SMF28 optical fiber run at a frequency of 10 Hz.

Table 5: CSM Results for Corning SMF28 Inner Coating (ω=10Hz)

Indent	Modulus within stead-state region	
	Average	Standard Dev.
1	11.07	1.85
2	10.12	1.07
3	12.54	0.97
Average for all indents	**11.24**	**1.21**

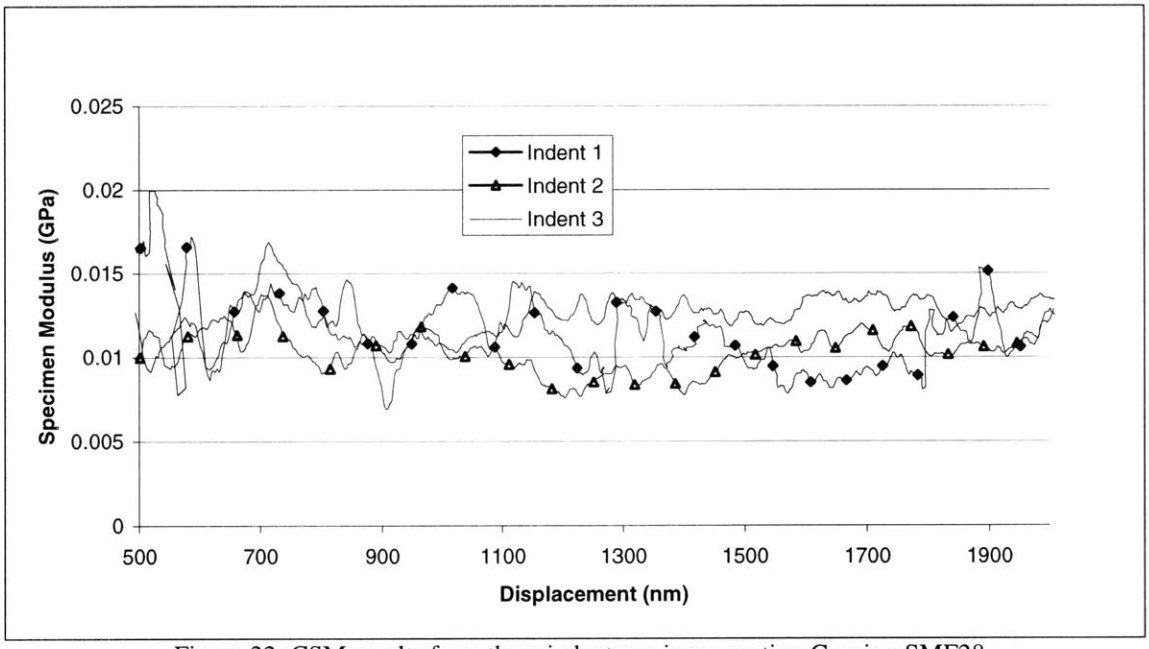

Figure 22: CSM results from three indents on inner coating Corning SMF28

5.2 Pure Indentation Method-Results

Finding the modulus from the unloading curve of an indentation proved to be the best method. Three materials were tested, they are the inner and outer coatings of the Corning SMF28 dual coated fiber and the single coating on the 3M FS-SN-4224 fiber. Both fiber

coatings are made with an acrylate polymer. For each coating, a significant number of indentation tests have been performed. In calculating E_s, the Poisson's ratio was taken to be 0.5. Table 6 shows the results for the tests done on the outer coating of the Corning SMF28 fiber. A total of 5 different tests were carried out with 3 indents in each test, thus a total of 15 different indents were done. To explain further, each time a test is started a number of separate indents can be selected by the user. The indents are different locations on the specimen however they are generally close, like 50μm away. The reason that the points are close is that the indents should be at the same surface height, in other words the surface should stay in focus (at 800X magnification) moving from one indent to another. Given the difficulty in producing a flat specimen as discussed previously, the polished optical fiber only has a flat surface area that allows for a few points to be chosen at that height. For that reason only a few indents were done for each test. Additional tests were carried out so that more data could be collected. One will notice that the measured modulus for each indent in the same test is very close to each other and consequently has a low standard deviation. However, comparing indents from different tests can sometimes lead to greater deviation. Even though the same testing procedures were used there are different factors that could account for this variance. One reason may be that the sample material is not perfectly homogenous. Additionally, the surface preparation may affect one part of the sample slightly differently than another location. The environment of the testing room, including mechanical vibrations, temperature and humidity changes can also influence the testing results and could account for some of the differences in the results. Certainly, efforts were made to minimize these different

influences (except for the possibility of material inhomogeneity) albeit it is not possible to completely eliminate all the factors.

Since the inner coating of the SMF28 fiber is very soft it is difficult to find the surface and it is also difficult to find good locations on the sample to run the tests. Nonetheless, many tests were carried out and the results tabulated in Table 7.

Table 6: Corning SMF28 Outer Coating Modulus results from pure indentation (all results in GPa)

Test \ Indent	1	2	3	Statistics Per Test	
				Average	Stand. Dev.
1	1.1150	1.0644	1.1321	1.1038	0.0352
2	0.9829	0.9574	0.9373	0.9592	0.0228
3	0.9046	0.9644	0.9746	0.9478	0.0378
4	0.7710	0.7499	0.7039	0.7416	0.0343
5	0.7930	0.7675	0.7458	0.7688	0.0237
Statistics for all tests and indents				**0.9042**	**0.1410**

Table 7: Corning SMF28 Inner Coating Modulus results from pure indentation (all results in MPa)

Test \ Indent	1	2	3	4	Statistics Per Test	
					Average	Stand. Dev.
1	2.545	3.219	None	None	2.882	0.477
2	3.744	4.340	4.272	None	4.119	0.326
3	5.507	6.607	6.893	6.935	6.486	0.668
4	3.427	4.030	4.076	4.829	4.090	0.574
5	2.703	3.489	4.729	5.380	4.075	1.205
6	2.291	3.590	3.494	3.746	3.280	0.667
7	3.160	4.278	4.454	4.590	4.121	0.653
8	3.025	3.849	3.854	4.231	3.740	0.509
9	3.141	3.979	4.050	4.472	3.911	0.557
10	3.535	3.742	4.385	4.497	4.040	0.473
11	4.716	None	None	None	4.716	–
12	4.780	4.691	None	None	4.736	0.063
13	3.171	4.169	4.076	4.560	3.994	0.587
14	4.063	3.901	4.685	None	4.216	0.414
15	3.504	4.840	4.188	3.750	4.070	0.586
16	4.676	4.749	4.211	3.847	4.371	0.423
17	4.093	4.635	3.848	4.034	4.152	0.338
Statistics for all tests and indents					**4.174**	**0.888**

Finally, Table 8 shows the results from the 19 different indents that were done for the 3M fiber. Since this material is stiffer than the inner coating of the SMF28 fiber the surface find was not as difficult and therefore not as many tests were required.

Table 8: 3M Coating Modulus results from pure indentation (all results in MPa)

Test \ Indent	1	2	3	4	Statistics Per Test	
					Average	Stand. Dev.
1	65.828	68.945	71.738	None	68.837	2.956
2	43.254	43.635	43.940	None	43.610	0.344
3	32.512	33.401	34.114	None	33.342	0.803
4	47.984	44.158	41.381	43.167	44.173	2.789
5	59.013	59.074	58.706	None	58.931	0.197
6	44.243	42.861	45.647	None	44.250	1.393
Statistics for all tests and indents					**48.611**	**11.793**

When this work was started, the fiber coating moduli were not available from Corning and 3M. Recently, Corning released values of coating stiffness for the SMF28 fiber, which was 650-950 MPa for the outer coating and 1 to 1.7 MPa for the inner coating. The outer coating stiffness is in good agreement with the data shown here. The inner coating stiffness is lower than the results of the tests, but considering the difficulties in measuring small stiffness values of only several MPa, the agreement is quite satisfactory. The comparisons verify the applicability of the proposed experimental procedure for coating stiffness measurement. These values are summarized in Table 9.

Table 9: Modulus of coatings measured using the NANO INDENTER® II and from manufacturer

Manufacturer	Coating (Material)	Measured		Manufacturer	
		Modulus (MPa)	Poisson's Ratio	Modulus (MPa)	Poisson's Ratio
Corning SMF 28 (Dual Coating)	Inner–Acrylate	3.29-5.06	0.5	1-1.7	0.47-0.50
	Outer–Acrylate	763-1045	0.5	650-950	0.42-0.46
3M FS-SN-4224	Single–Acrylate	36.8-60.4	0.5	Not avail.	Not avail.

6. CONCLUSIONS

Optical fiber sensors are increasingly being used to measure structural quantities such as strain and cracking condition. To properly interpret sensor results, it is essential that there be an understanding of the mechanical properties of the coating materials. In this investigation, special sample preparation techniques and testing procedures to measure the in-situ fiber coating properties were developed. With the proposed procedure, very low modulus values can be measured. Since fiber coating properties are often not measured or reported by optical fiber manufacturers, the measurement technique is useful for researchers and engineers interested in the development of fiber optic mechanical sensors.

7. REFERENCES

1. Nellen, Ph.M., Frank, A., Mauron, P. and Sennhauser, U., "Lifetime and Reliability of Embedded Optical Fibers", in Fiber Optic Sensors for Construction Materials and Bridges, ed. F. Ansari, Technomic Pub., Lancaster, PA, pp. 183-193, 1998.
2. Oliver, W.C. and Pharr, G.M. "An improved technique for determining hardness and elastic modulus using load and displacement sensing indentation experiments", J. Mater. Res., Vol. 7, No. 6, pp. 1564-1583, 1992.
3. K. L. Johnson, *Contact Mechanics*, Cambridge University Press: Cambridge, 1985.
4. G. M. Pharr, W. C. Oliver and F. R. Brotzen, "On the generality of the relationship among contact stiffness, contact area, and elastic modulus during indentation," J. Mater. Res., Vol. 7, No. 3, pp. 613-617, 1992.
5. R. B. King, "Elastic Analysis of some punch problems for a layered medium," Int. J. Solids Structures, Vol. 23, No. 12, pp 1657-1664, 1987.
6. Ian N. Sneddon, "The relation between load and penetration in the axisymmetric Boussinesq problem for a punch of arbitrary profile," Int. J. Engng. Sci., Vol. 3, No. 47, pp. 47-57, 1965.
7. Lucas, B., Oliver, W. C. and Swindeman, J. E., "The Dynamics of Frequency-Specific, Depth-Sensing Indentation Testing," MRS Proceedings, Volume 522, Fundamentals of Nanoindentation and Nanotribology, pp. 3-14, 1998.
8. William T. Thomson, *Theory of vibration with applications*, Prentice Hall: Englewood Cliffs, NJ, 1988.
9. M. P. Norton, *Fundamentals of noise and vibration analysis for engineers*, Cambridge University Press: Cambridge, 1989.

Chapter 3

Novel Crack Sensor

1. INTRODUCTION

Safe, durable and efficient structures are in the public's best interest. Certainly designers, engineers and building managers strive to achieve these objectives in facilities that they design, build and maintain. However, even well designed structures need to be well cared for and regularly inspected to ensure that they are successfully meeting the demands that the users and environment place on them. One effective method in determining the "health" of concrete structures is by detecting and monitoring cracks. Crack openings beyond 0.2 to 0.4 mm (depending on environmental exposure) may lead to durability problems associated with steel reinforcement corrosion. Large openings beyond 1 to 2 mm, which may be caused by overloads during natural hazards, is a sign of severe damage and requires immediate closing of a facility. Presently, this sort of crack monitoring is carried out with regular visual inspections. An efficient, less costly and reliable method will be presented here.

1.1 Previous work in fiber optic crack sensors

Various non-destructive techniques, including the impact-echo method,[2] ground probing radar,[3] infrared thermography[4] and acoustic emission[5] have been proposed to assess the condition of concrete structures. All these techniques attempt to detect cracking or discontinuities in concrete structures, but none can provide quantitative measurement of crack opening. Also, besides acoustic emissions, all the other measuring techniques are

insensitive to cracks perpendicular to the structure surface (e.g. flexural cracks) which are instrumental in increasing concrete permeability (and accelerating steel corrosion).

The application and major advantages of fiber optic sensors in the monitoring of civil structures have been discussed in Ansari[6] and Culshaw.[7] Various crack sensors have been developed with optical fibers, but most of them are rather limited in their applications. Sensing based on fiber breakage in Rossi and LeMaou,[8] and Huston et al.[9] can distinguish between the presence or absence of cracking but cannot provide information on gradual structural degradation. The sensor developed by Ansari et al.[10] is a "point" sensor, which means that it can detect and monitor the opening of a crack only if the crack passes through a small sensor loop 31.75mm in size. While the sensor is useful in experimental fracture mechanics, where crack location can be controlled, its application to real concrete structures is very limited. Voss and Wanser[11] created a crack sensor by gluing an inclined optical fiber at two points on opposite sides of a crack. As the crack opens, fiber bending at the glued spots induces signal loss. This sensor again relies on the prior knowledge of crack location. Wolff and Meisseler's crack sensor[12] is an optical fiber sensing system attached to the exterior surface of concrete structures for the monitoring of displacement between the points of attachment. If the attachment points are too close, a crack may not pass through the sensing system. If the points are too far apart, sensitivity will be low and it is not possible to distinguish between the presence of a harmful widely opened crack or several narrow ones (which may be harmless).

Gu et al.[13] developed a multi-gauge crack sensor by splicing together lengths of cleaved fiber. By monitoring the Fresnel reflection at each splice between two pieces of fiber, the

average strain within each piece can be obtained. Based on the strain reading, the severity of cracking within a certain region can be assessed. While this technique is very robust, it is measuring averaged behavior. If the splices are far apart, the sensor suffers similar limitations to that of Wolff and Meissler's[12]. If the splices are placed very close to one another, cost will be high and also the forward signal may drop rapidly with distance (due to the presence of many reflection points), making the sensor inapplicable to real structures where a long sensing length is required. Brown et al.[14] and Oka et al.[15] worked on a new technique for distributed strain sensing in concrete structures. By measuring the strain-induced frequency change of Brillouin backscattered light as a function of time, the strain distribution along a fiber can be derived. For a fiber inside concrete, high local strain will be induced at a concrete crack. In theory, the crack can hence be detected. In practice, however, the fiber will either break due to the high strain concentration, or debond to allow "averaging" of the localized high strain over the debonded length. For cracks with relatively large openings, their presence is indicated by high averaged strain values.[15] However, since averaging removes the "peaks" in the strain distribution, the number of cracks, and their respective locations and openings, cannot be determined. For cracks with small openings, it is questionable if the resulting small increase in averaged strain can reveal their presence. Hence, the method may not work for the detection of cracks with 0.2-0.4mm opening, which is certainly small but able to facilitate water/salt penetration and steel corrosion.

2. NOVEL CRACK SENSING CONCEPT

The crack sensing method presented here can determine crack location and magnitude without prior knowledge of crack location. The principle of the sensor is illustrated in

Figure 1 and is discussed below. Knowledge of the crack opening direction is sufficient for the proper design and application of this sensor. The sensor design along with Optical Time Domain Reflectometry (OTDR) makes it possible to monitor a large structure with a few optical fibers.

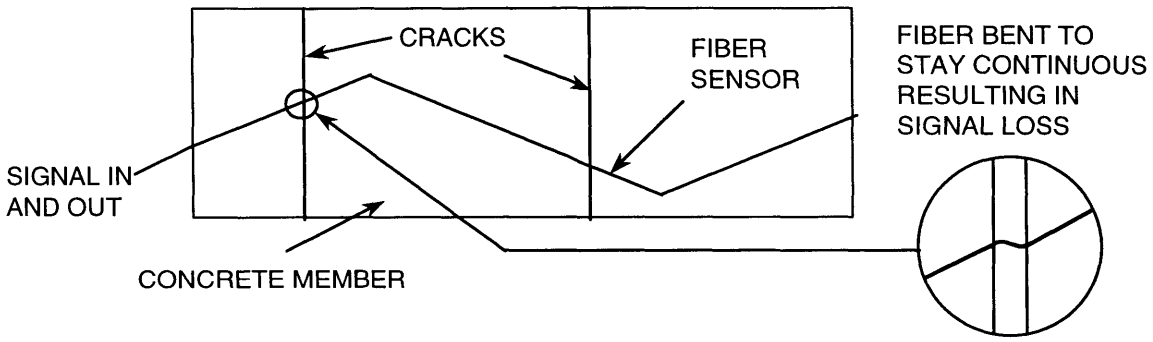

Figure 1: Novel crack sensor concept

2.1 Principle of the Sensor

The fundamental principle of the crack sensor is a bend in the fiber. A bend, especially a tight one, creates a loss in optical power that results in a reduction in he back–scattered signal. If a fiber is placed at an angle to a crack like in Figure 2, when the crack opens the optical fiber must bend in order to remain continuous.

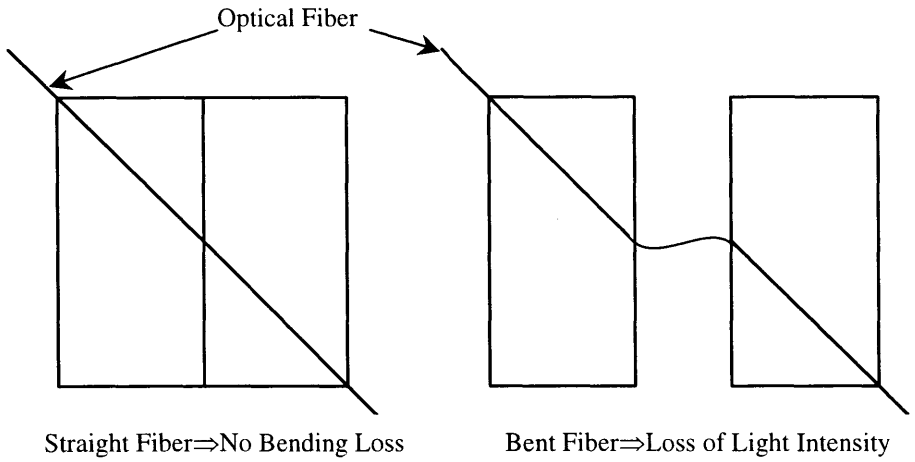

Figure 2: Principle of Sensor

The optical, mechanical and geometric properties of the optical fiber determine the loss corresponding to each bend. In the simplest of terms, the reason that an optical fiber loses light intensity when bent is understood from examination of the optical fiber. An optical fiber consists of three major parts as seen in Figure 3. The core is where the lightwave travels down the fiber. The cladding with a slightly different refractive index helps to keep the light in the core with internal reflections. Any light that leaks into the cladding is quickly dispersed. The jacket protects the fiber from external environmental damage.

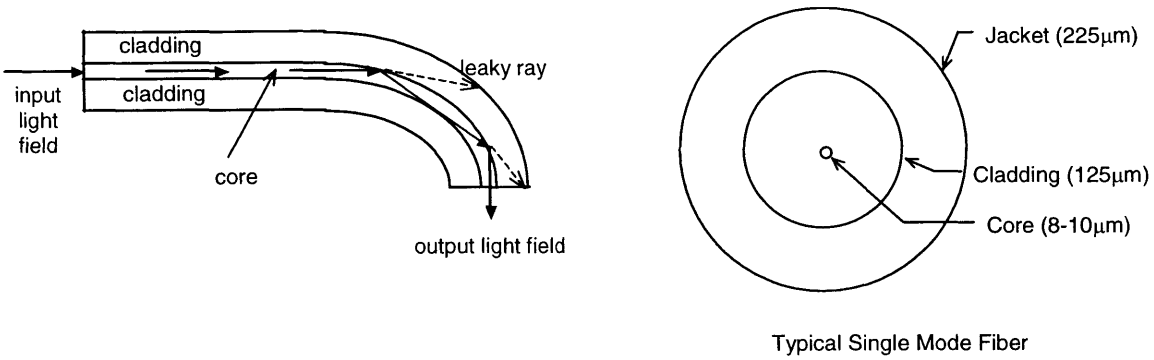

Figure 3: Geometry of an optical fiber

When the optical fiber is bent sharply the lightwave hits the core-cladding interface at an angle smaller than the critical angle and consequently perfect internal reflection is violated. Hence part of the light is leaked into the cladding and is lost. A power meter can monitor the loss in forward power intensity. However, if only forward power is measured, the crack location cannot be found. The backscattered light, which is a small fixed portion of the forward light, is also reduced at the bend. In addition to loosing intensity, part of the lightwave is sent back down the fiber to the source. Optical Time Domain Reflectometry (OTDR) can be used to detect this backscattered wave. By the time of flight information one can determine the location of the bend. The intensity loss

of the signal can also be found and can be correlated to crack size. Crack sensors designed using the aforementioned principles need to create a fiber bend where the crack forms. There are different ways in which this can be accomplished and some of the different approaches will be reviewed further on.

2.2 Sample Design

A crack simulating specimen was designed to understand the mechanical and optical behavior of the crack sensor and to later verify the theory developed to explain the phenomena. The specimen size was chosen to be 2"×2"×$^3/_8$". Figure 4 shows the molds that were created to make the specimens.

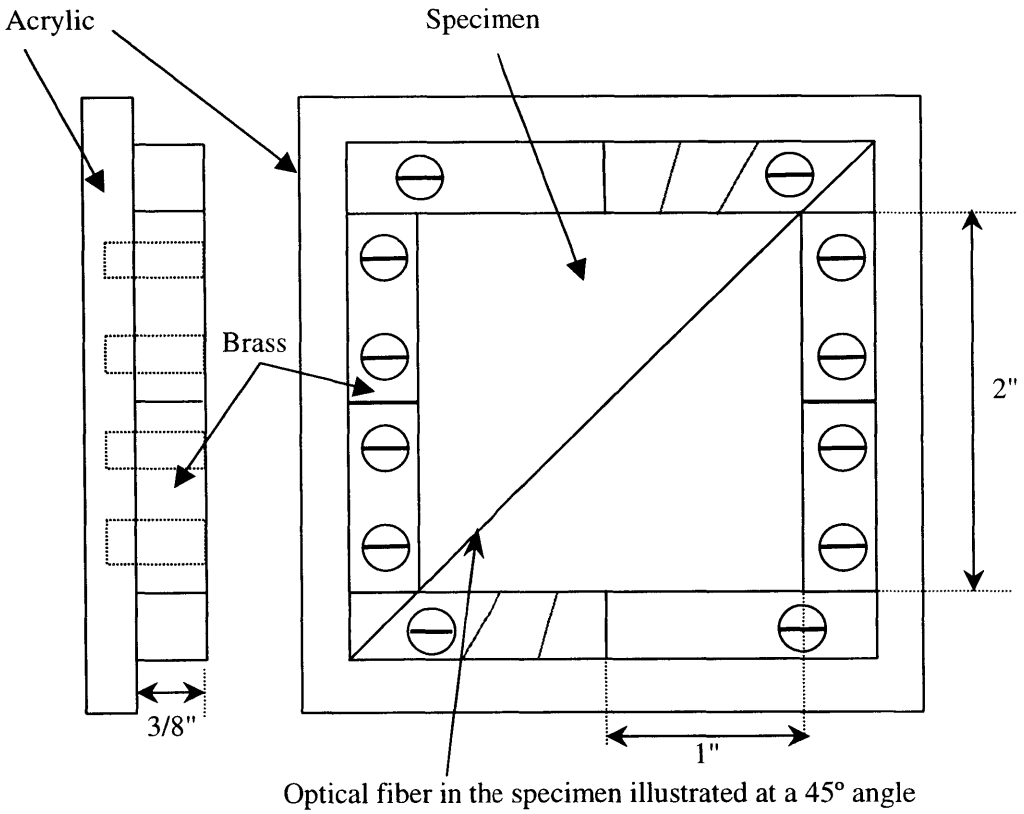

Figure 4: Mold for Experimental Specimen

Note that there are three holes drilled into the molds, which allows for an optical fiber to be passed through the mold at 15°, 30° and 45° angles from the crack separator. The

mold pieces were made of brass since it can be easily machined and is durable. The base was made of acrylic so that the specimens could easily be removed from the mold. However, when the specimens are cast it is necessary to use the proper releasing agent to facilitate easy removal from the molds. Vacuum grease (silicone) or specialized releasing agent was used for epoxy and polyester casting.

2.3 *Epoxy Block* Creation

Experimental verification of the crack sensor was carried out with *Epoxy Blocks*. Using the aforementioned specimen mold, a 254μm diameter steel wire, coated with releasing agent, is placed in the mold at the desired angle (see Figure 5). Next epoxy is cast into the mold and allowed to cure.

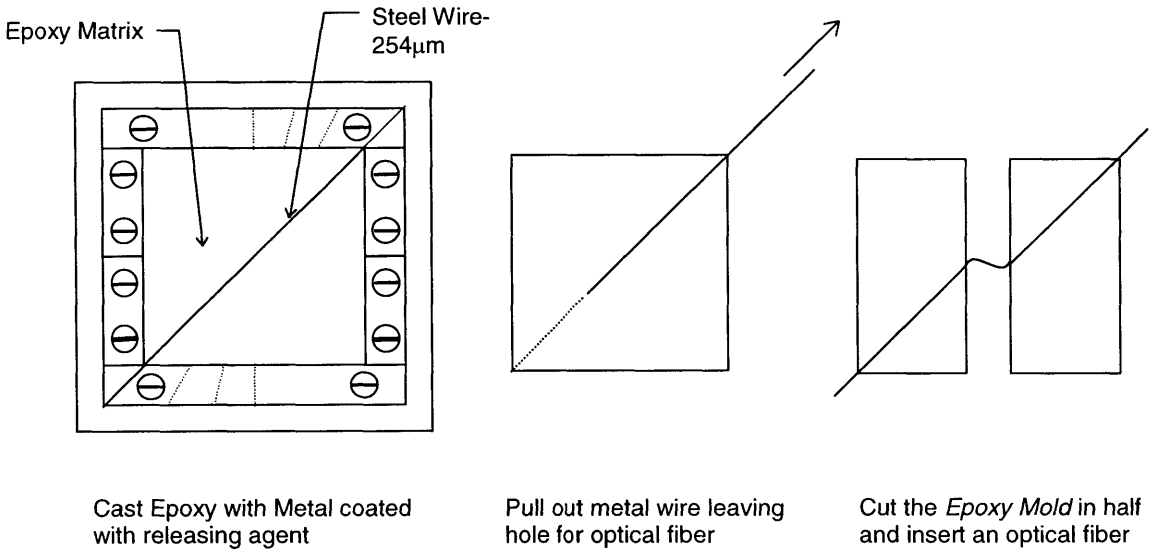

Figure 5: *Epoxy Block* Creation

Once the epoxy is fully cured it is removed from the mold. The steel wire is removed and then the epoxy is cut in half. Now an optical fiber can be placed into the hole left by the steel wire. This can simulate the crack sensor and allow for repeated opening and closing of the crack sensor using the same optical fiber.

2.4 Design of Test Fixture

To properly test the sensing concept with the crack-simulating specimen some requirements needed to be met. The simulated crack opening had to be controlled and repeatable. In order to accomplish this, a machine was specially designed which could test the sensor principle in a controlled manner. The machine was designed so that the crack opening could be measured using a Linear Variable Differential Transformer (LVDT) in a very accurate fashion. It was also important that the testing stage be very stable and precisely level. Furthermore, the machine had to accommodate measurement of the optical power so that it could be compared with the crack opening. The final design of the machine is shown in Figure 6.

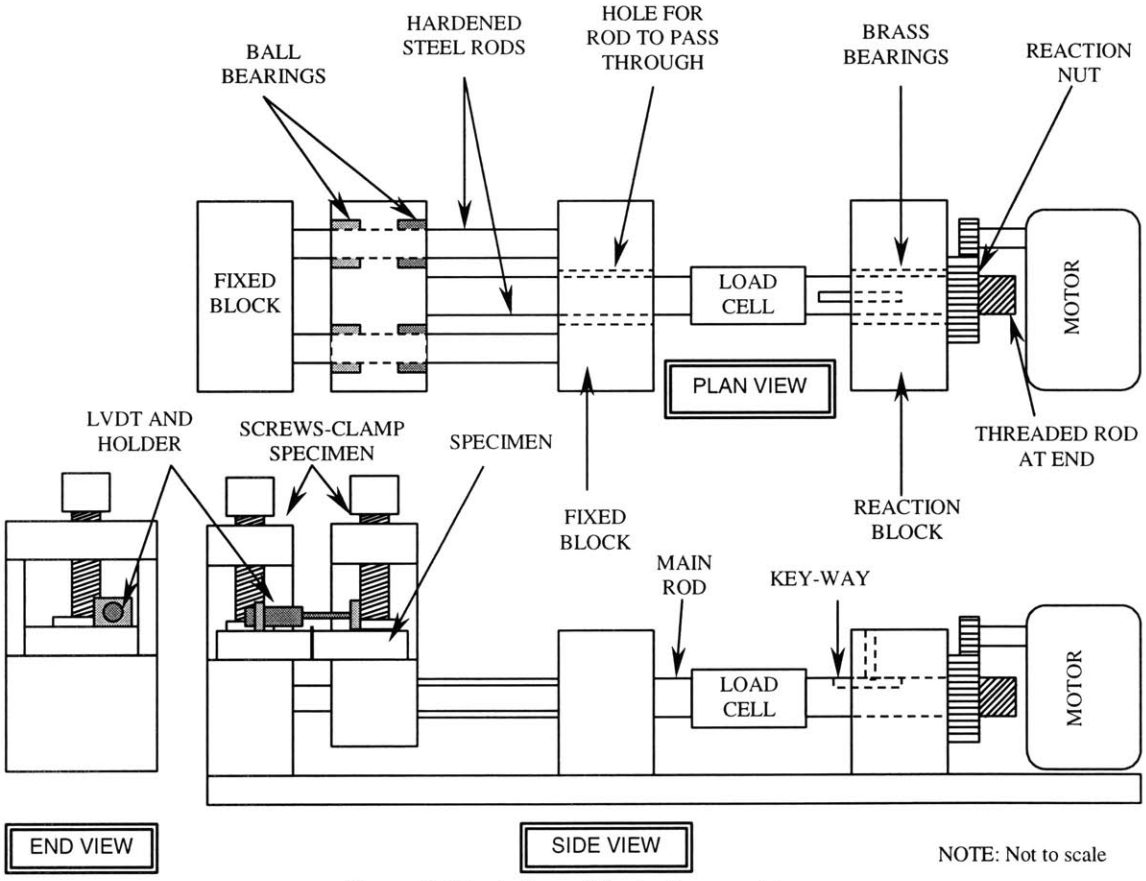

Figure 6: Illustration of the testing machine

Referring to Figure 6, the testing stage has a fixed part and a moving part. The moving part rests on two hardened steel rods and has four precision ball bearings to keep it aligned and moving with very little friction. The specimen is clamped onto the stage by tightening the screws. The motor turns the reaction nut that moves against the reaction block and therefore pulls the main rod that opens the testing stage. Note that the main rod is keyed to ensure that the motion is purely linear without rotation. The machine has been used for many tests and has performed well.

2.5 Polyester Sensor Sheet Mold Design

Crack sensor design depends on the type of structure to be monitored. A new bridge could have the sensor placed inside it while it is built. It would be very difficult to do this to an existing structure. Therefore, a method for applying the sensor to existing structures as well as new buildings was developed and is called the *Sensor Plate*. A graphical illustration of the *Sensor Plate* can be found in Figure 7. The *Sensor Plate* is designed to be a distributed crack sensor. The principle is that once a crack forms in a beam, the polymeric plate will crack along with the beam. The fiber will slide in the polymeric plate in order to remain continuous across the crack. For the fiber to slide unrestricted there are loops of fiber that provide the necessary free length.

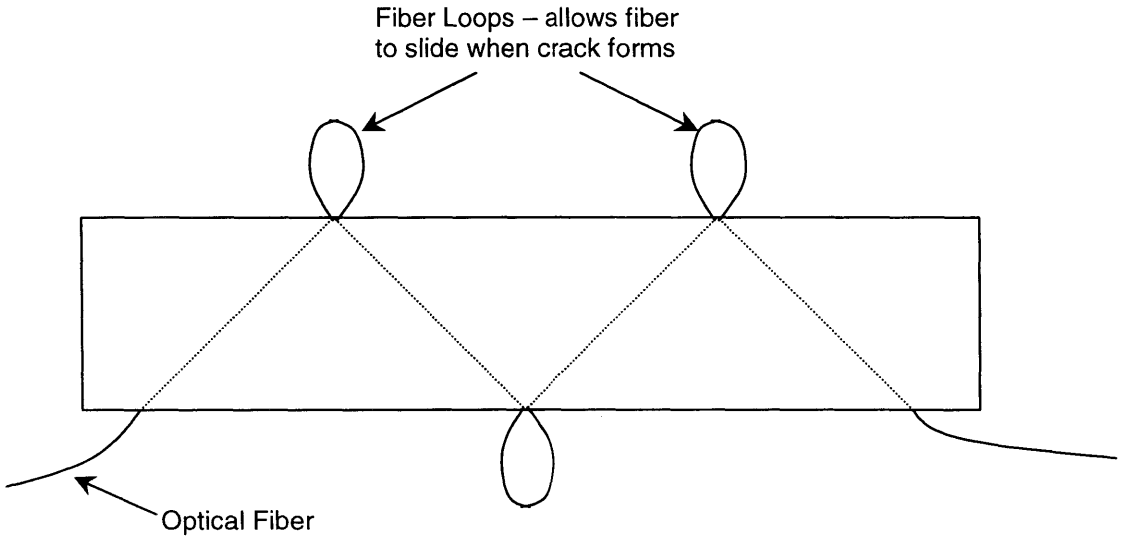

Figure 7: *Sensor Plate* for Distributed Crack Sensing

The fiber loops are made large enough so that the bending loss is minimal and allow for some sliding when a crack forms. With the zigzag placement of the fiber it is possible for the plate to go on infinitely and maintain the same desired angle. Cracks could be effectively measured anywhere along the plate length with the exception of the loop location. Figure 8 shows a possible remedy for this issue with two overlapping fibers.

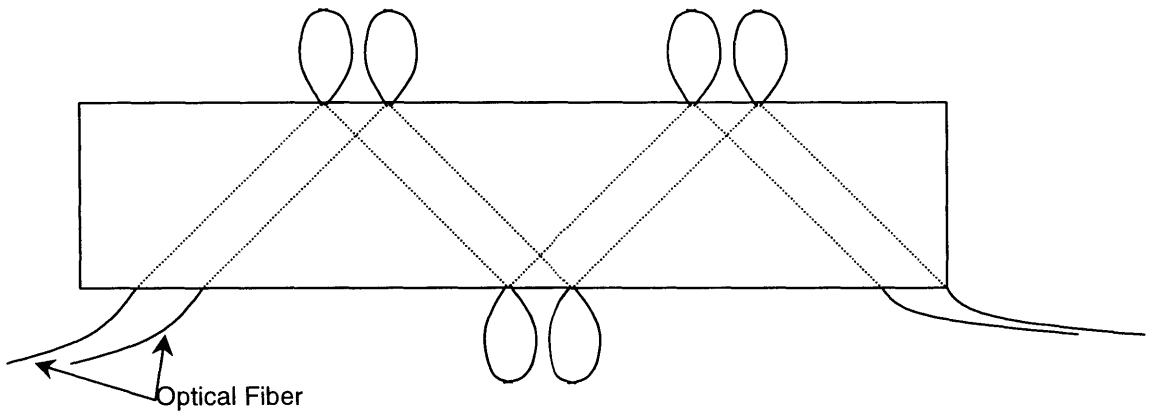

Figure 8: *Sensor Plate* for Distributed Crack Sensing with Double Fiber

2.6 Sensing Plate Fabrication

An off-site factory fabrication is though to be better for the *Sensor Plate*. The process can be seen below in Figure 9 with detailed drawings of the mold found in Appendix 1. It will be noticed that the mold is made of polypropylene to facilitate removal of the

Sensor Plate after it has cured. The optical fiber is wrapped around the pegs in zigzag fashion. There are slits in the polypropylene around the pegs so that the optical fiber is about in the middle of the polymeric sheet. Vacuum grease (silicone) is placed around the slits so that the mold is sealed. Once the fiber is securely in place and the mold is sealed a polymer is poured into the mold and allowed to cure.

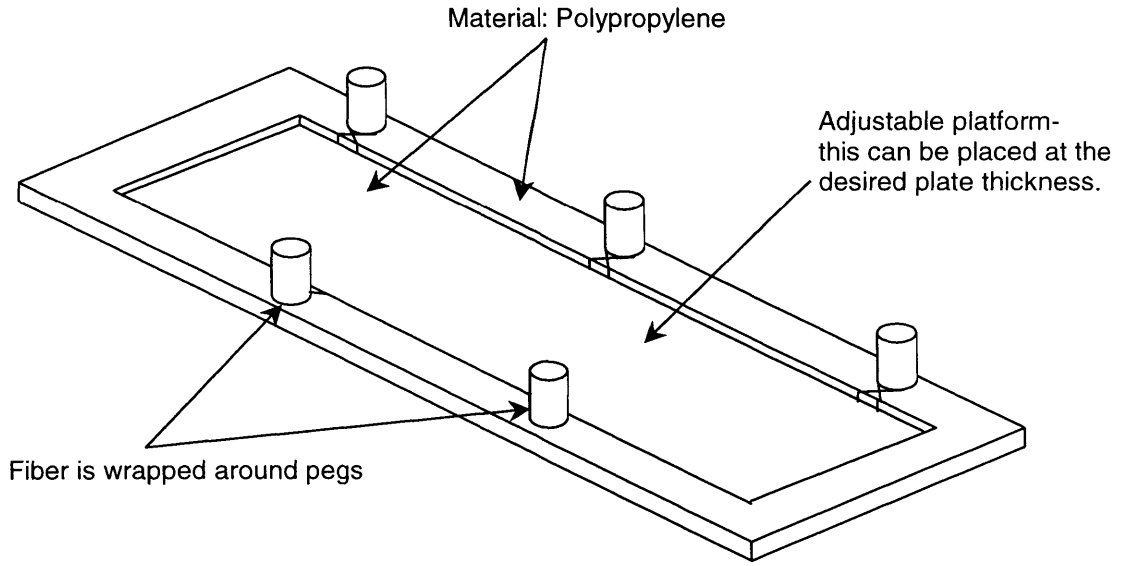

Figure 9: Mold for Sensor Plate Fabrication

One advantage to making the sensor this way is that it allows for the sensor to be made precisely as specified off-site. This avoids having to employ specially trained people in the field to ensure that the sensor is made properly on site. Another advantage is that standardizing the production will reduce prices. Since many of the applications would be similar in nature standardization should be possible. Popular standard sizes and lengths could be made. Different segment lengths could be joined together for long sections by fusion splicing the free fiber coming out of the plate. Although, if an application required customized pieces that could also be accommodated by making new molds to the desired size (which would be more expensive).

2.6.1 Material Issues for making the *Sensor Plate*

The matrix of the *Sensor Plate* is critical to the success of the sensor. The matrix needs to be brittle so that it cracks with the concrete. Further, it needs to bond well with the surface of the monitored structure so that it does not delaminate when under load. Moreover, the matrix-fiber jacket interface needs to allow the fiber to slide. Finally, the matrix must be durable and able to withstand environmental attacks that could include chemical attack from pollution, severe cold and ice or desert heat.

Thermosets like epoxy and polyester are good candidates for the matrix. Marine polyester was found to work best after trying different thermosets. The polyester when applied to concrete adheres well and cracks with the structural member. The durability of the polymer has been tested for many years in the harsh conditions of the sea similar to the conditions of a bridge over a waterway. For the experimental tests shown later in the chapter polyester was used.

2.7 Experimental Set-up

Once the machine and molds were developed, it was necessary to set-up the rest of the equipment so that the necessary measurements could be made. The experimental set-up can be seen in Figure 10 with a listing of the equipment tabulated in Table 1. It will be noticed that this set-up is monitoring the crack opening using forward power transmission (as opposed to OTDR). An OTDR set-up is shown in Figure 11.

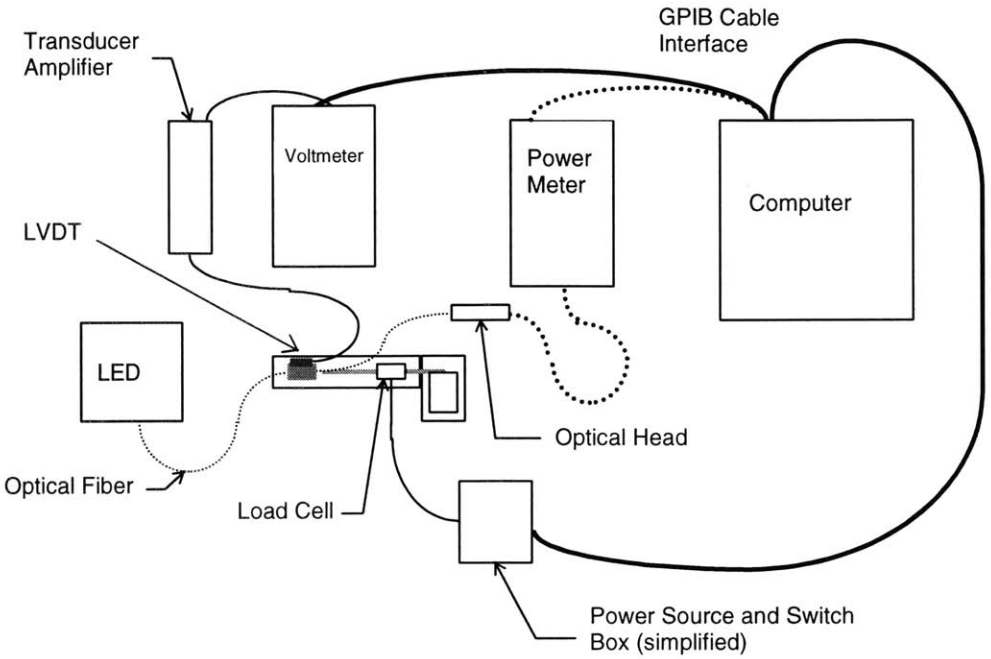

Figure 10: Experimental Set-up for verification tests

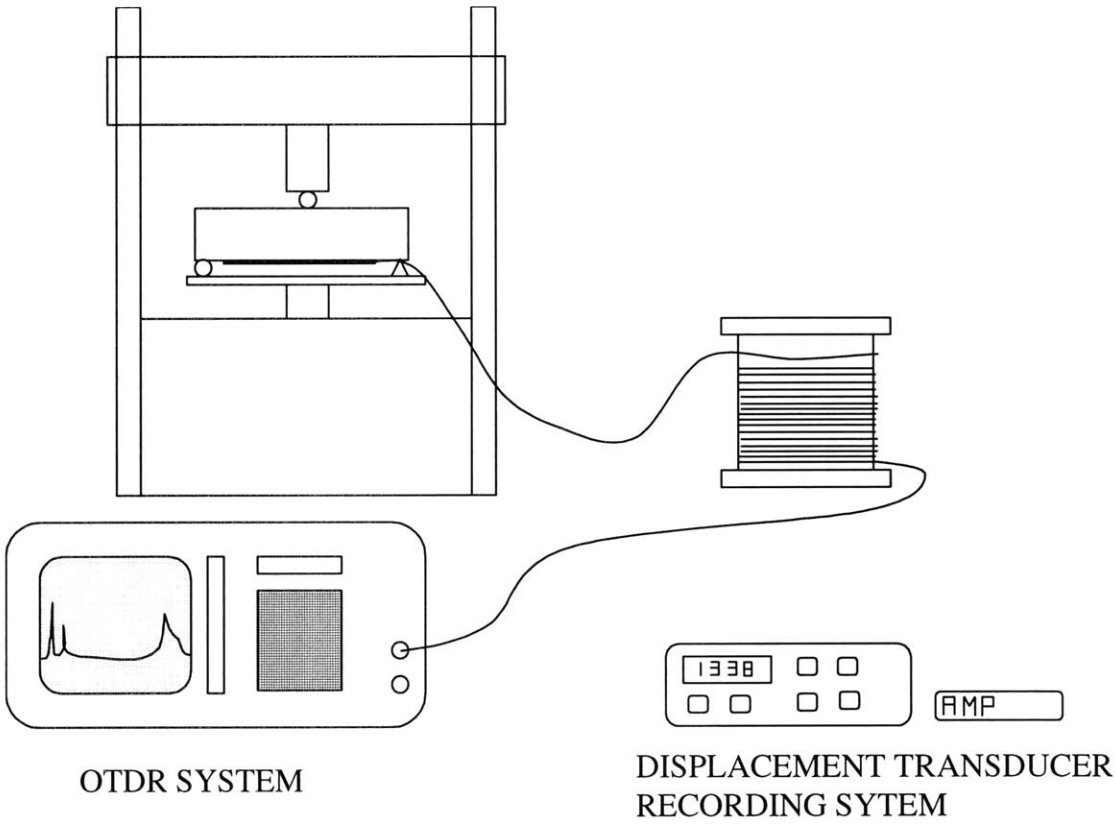

Figure 11: OTDR Experimental Set-up for distributed crack sensing

Table 1: List of testing equipment

ELEMENT	DESCRIPTION	COMPANY
OPTICAL MEASUREMENT PATH		
Laser	Stabilized Light Source MG9001A (LD850nm)	Anritsu
LED	850nm LED with controller made in-house	–
Optical Head	Optical Head 0.38 to 1.15μm (MA9412A)	Anritsu
Power Meter	Optical Power Meter Model ML9001A	Anritsu
OTDR	OFM 20	Opto-Electronics
Optical Fiber	Various types as described in the text	
DISPLACEMENT MEASUREMENT PATH		
Transducer Amplifier	ATA-101-Analog Transducer Amplifier	Lucas Schaevitz
LVDT	100-MHR	Lucas Schaevitz
Voltmeter	Multi-meter 45-05 (GPIB interface)	Fluke
OTHER ITEMS		
Bare-Fiber Adapter	FC-PC (125μm) (MA9013A)	Anritsu
Fiber Cleaver	FCP-22L Ultra Compact Precision Cleaver	Sumitomo Electric
Computer	Pentium 1, 166MHz	PC Compatible
LabVIEW	Version 4 and 5 for the PC	National Inst.
GPIB Board	PCI-1200	National Inst.

Three measurements are possible with the forward power configuration. The opening of the testing stage can be measured with an LVDT, the power loss resulting from the crack opening can be measured and the required load to pull the specimen apart can also be recorded. In this investigation, the LVDT measurement and the power loss measurement are of primary interest. The optical power loss measurement path is in dashed lines and gray shading. The displacement measurement path is the other path with the exception of the load cell path. All of the measurement data is gathered in digital form in the computer. The optical measurement path is controlled through a GPIB interface using LabVIEW. The LVDT path (and load cell path) could be controlled using an analog to digital converter or a GPIB interface (both have been used successfully). The LabVIEW interface controls the GPIB and A/D cards as well as collects the data from them. The LabVIEW program has been customized so that it not only collects the data but also performs simple operations on the data making them more representative of the desired

measurements. Results from the tests done with the *Epoxy Blocks* will be shown later. The OTDR system configuration is used in the experimental test discussed further on.

2.8 Crack Sensor Trends-Epoxy Mold Tests

Once the testing machine and the *Epoxy Molds* had been created tests were carried out to understand the behavior of the crack sensor. The tests carried out provide important information such as the optical power loss trend, minimum detectable crack size, and the eventual asymptotic power loss. The creation of the *Epoxy Molds* and testing machine as well as the experimental set-up have just been described in detail in the preceding sections. To run the tests, *Epoxy Blocks* are placed into the loading machine (Figure 6) where the blocks are pulled apart in a controlled manner while the crack opening and the optical signal loss are recorded. The crack opening with the corresponding light signal loss can be plotted.

Two commercially available optical fibers were studied in depth. The first is 3M single-mode optical fiber at 850nm (FS-SN-4224) and the second is Corning SMF28 at 1550nm wavelength with Table 2 containing the optical properties of the fibers. The fibers were tested at the two different angles of inclination, namely 30° and 45°. An LED light source at the appropriate wavelengths was used for the tests because it was found to have less noise than LD light sources. The results are shown as the absolute value of optical power loss in decibels versus the crack opening in millimeters. The reason for this display is that it readily describes the absolute power loss that corresponds to a certain crack size, and could easily be used to back figure a crack size from the power loss as intended.

Table 2: Optical Properties of Optical Fibers used in Tests

Characteristic	3M (FS-SN-4224)	Corning SMF 28
Wavelength	850nm	1550nm
Cut-Off Wavelength	<780nm	<1260nm
Mode Field Diameter	5.5μm	10.4μm ± 0.8μm
Geometric Core Diameter	2.215μm*	8.3μm
Core refractive index	1.458	1.4505
Cladding Diameter	125μm ± 2μm	125μm ± 1μm
Cladding refractive index	1.453	1.4447
Jacket Diameter	250μm ± 15μm	245μm ± 5μm
Jacket Material	Acrylate	Acrylate
Attenuation Maximum	5dB/km	0.25dB/km

*This value is calculated as shown below since the manufacturer could not provide the information (see Equation (12))

Figure 12 shows the optical power loss versus crack size for the Corning SMF28 optical fiber for both angles and Figure 14 shows the same thing for the 3M optical fiber. The power loss for a 30° inclination is noticeably less than the 45° inclined fiber as would be expected. The lower angle creates less of a tight bend on the optical fiber which correlates to less optical light loss. As the fiber approaches the 2.0mm crack opening size the rate of optical power loss is decreasing and is starting to reach an asymptotic value. As mentioned previously, it is desirable to measure and monitor cracks less than 1 mm while large cracks require immediate action to repair the structure. Since the crack sensor loss decreases after the cracks become large (> 1mm), the larger cracks will not significantly decrease the total number of cracks that can be monitored with one fiber by using up the limited dynamic range of the system.

Comparing the two different fibers one sees that the Corning fiber looses much more light than does the 3M fiber. Finally, the pick-up point where the crack sensor starts to measure a loss is also visible in the two graphs. These trends need to be reflected in the theoretical model of the loss prediction for the crack sensor. The mechanical and optical

properties of the fibers are those parameters in addition to the crack sensor parameters (angle of inclination and matrix properties) which determine the sensor performance.

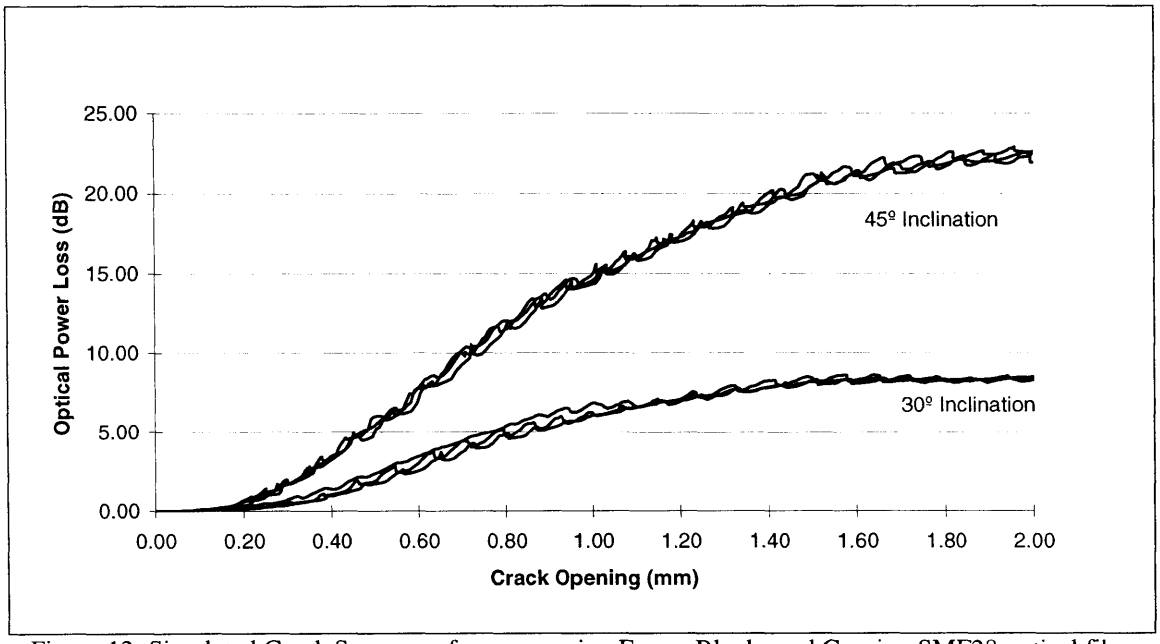

Figure 12: Simulated Crack Sensor performance using Epoxy Blocks and Corning SMF28 optical fiber with a 1550nm LED light source

As mentioned in the introduction to this section, the light source found best suited to the needs of the sensor was an LED light source. Tests were also carried out with the *Epoxy Blocks* using an LD light source and a representative example of the results is shown in Figure 13. These results are for a Corning SMF 28 fiber at 1550nm wavelength with a 45° angle of inclination. Comparing the graphs in Figure 12 and Figure 13, which have a similar scale, shows that the sensor power by a LD source has a lot more fluctuations in the light loss. One possible explanation for this phenomenon is modal noise created by the cladding modes interfering with the lightwaves in the core when the fiber is bent. It is something that is not desirable in the crack sensor so it is advisable to use an LED source which not only performs better but is also cheaper.

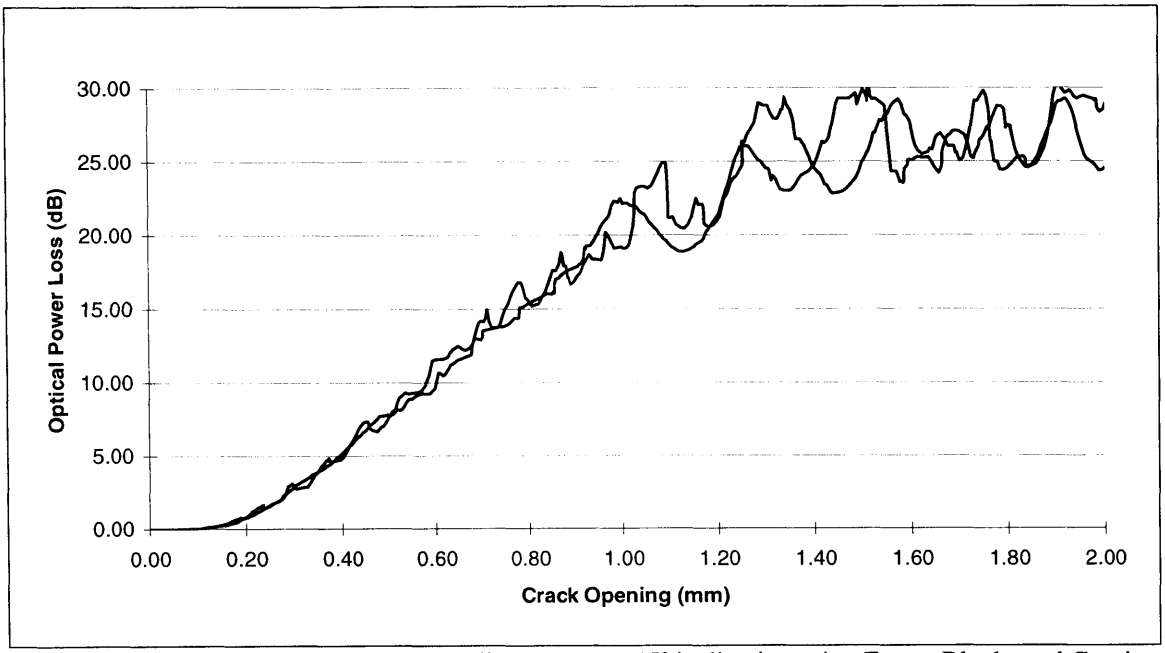

Figure 13: Modal Noise using 1550nm LD light source at 45° inclination using Epoxy Blocks and Corning SMF28 optical fiber.

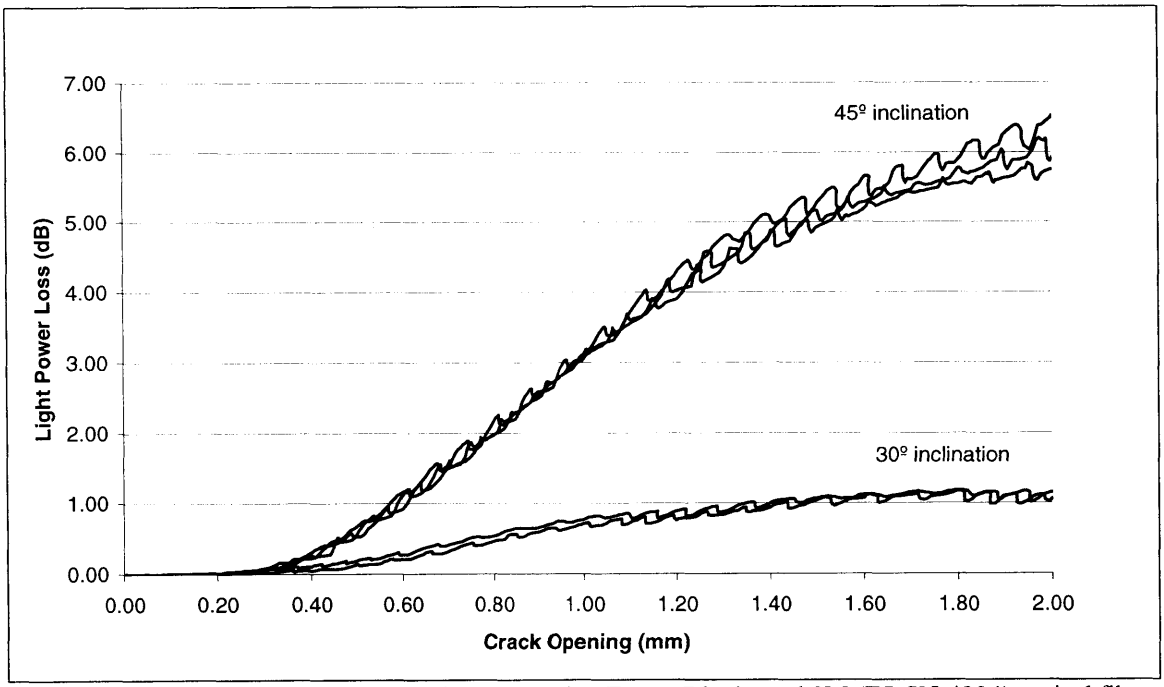

Figure 14: Simulated Crack Sensor performance using Epoxy Blocks and 3M (FS-SN-4224) optical fiber with a 850nm LED light source

3. EXPERIMENTAL TEST TO ILLUSTRATE SENSING CONCEPT

Actual experimental testing illustrates the novel distributed sensing concept to be viable. The *Sensor Plate* was fabricated with polyester and a single-mode optical fiber (as

explained previously). Figure 15 illustrates the sensor configuration. The optical fiber is positioned in a forty-five degree "zigzag" orientation along the sensor. A forty-five degree fiber inclination was chosen since it produces a high optical signal loss while still allowing the fiber to slide as required for the sensor to function properly. The loops of fiber seen at the corners of the "zigzag" transitions serve a dual purpose since they allow for a smooth transition that does not degrade the signal and they also allow for the fiber to slide freely once a crack opens. To facilitate fiber sliding within the polyester a releasing agent was applied to the fiber before casting the polyester. Polyester was applied once the optical fiber was in place.

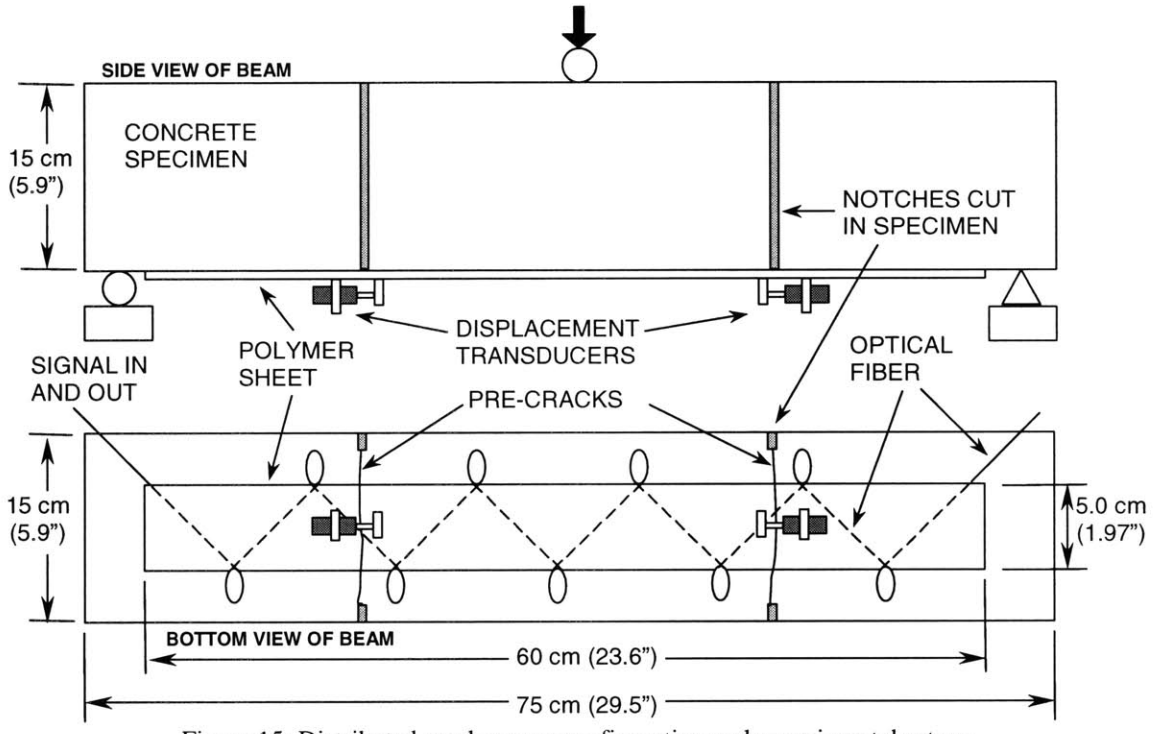

Figure 15: Distributed crack sensor configuration and experimental set-up

The testing specimen was a concrete beam reinforced with steel rebar as well as steel fiber. The beam was 75cm long, 15cm wide and 15cm in height. The steel fiber was included to ensure a more ductile response once the beam cracked. The concrete beam

was cut with notches so that the crack locations were known which enabled the crack openings to be monitored with displacement transducers. It should be noted that the illustrated sensor configuration is not final but only used in this experiment. Multiple fibers should be used in the final configuration to ensure that the crack does not elude detection if the beam by chance cracks at a corner transition point in the "zigzag" configuration.

Close attention was given to the attachment of the sensor to the concrete beam. Proper sensor performance requires that the sensor sheet crack at the same time and location as the beam crack. Delamination of the sensor from the beam is obviously something that needs to be avoided. Attaching the sensing sheet to the concrete beam with a thin layer of epoxy and then before the epoxy hardens, applying pressure to the sensor to remove any air-bubbles from the epoxy layer was found to be successful in meeting the aforementioned criteria. Care was taken to keep the fiber loops free from the adhesive so that they could perform their function unhindered.

Figure 16 shows the OTDR screen when there are no cracks present in the beam/sensor. The OTDR was linked to the sensor sheet with a spool of fiber between the OTDR bulkhead and the sensor to avoid loosing the crack signals due to the strong reflection created at the bulkhead connection (Figure 11). As a result, the beam and hence the cracks are located over 20 meters from the bulkhead. The sharp peak at the beginning of the chart is the strong reflection created when connecting the optical fiber to the OTDR system. The last large peak at the end of the chart is the large reflection created by the cleaved end of the fiber. In between the large peaks the signal is level with minimal noise. In Figure 17 the same beginning and ending large peaks are present however there

is also a small dip in the signal near the end of the fiber where the two cracks have formed (as it is marked on the figure).

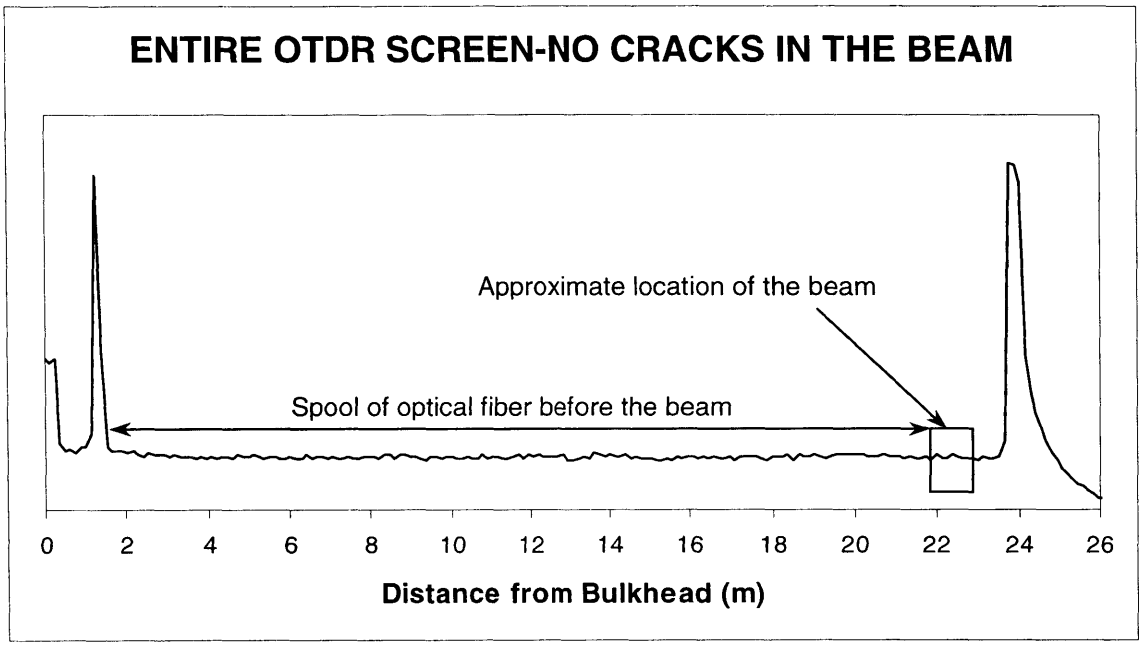

Figure 16: OTDR screen capture showing no cracks in the beam

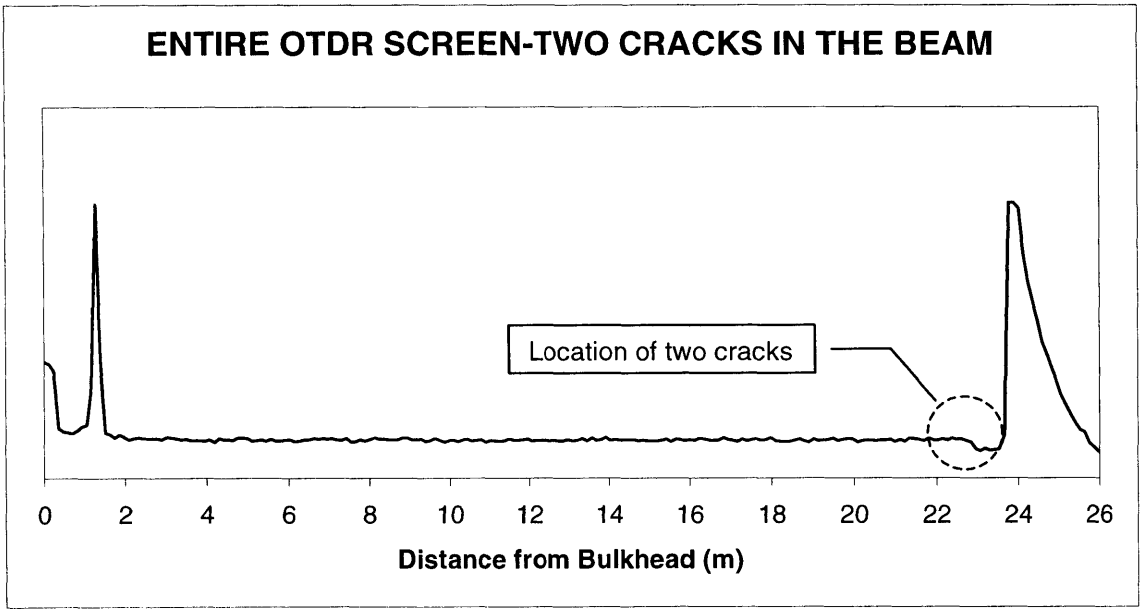

Figure 17: OTDR screen capture showing cracks in the beam

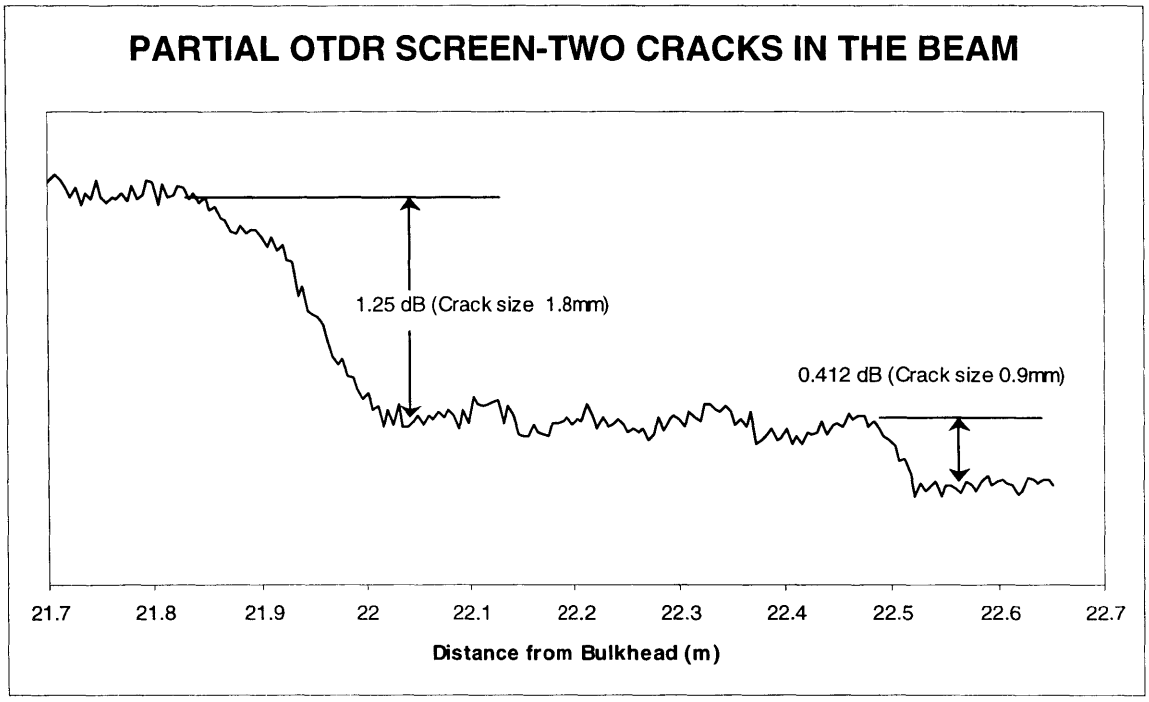

Figure 18: OTDR screen capture zooming in on two cracks

If this small area is expanded the OTDR window will look like Figure 18. In this figure the two distinct cracks are visible. It is possible to use the OTDR system in Rayleigh mode to measure the loss from each bend. This is done by measuring a length of fiber before the bend and saving that as a reference. Then a length of fiber after the bend is measured and compared to the reference which leads to a measurement of the loss in dB as shown in Figure 18. The crack sizes shown in the figure are from the displacement transducers. Additionally, the OTDR provides the location of the cracks along the optical fiber as shown along the x-axis in the figure.

4. MECHANICAL MODEL

To optimize the design of the crack sensor an understanding of the mechanical and optical behavior of the sensor is useful. Since it is desirable to detect small cracks the sensitivity needs to be sufficiently high. However, to detect many cracks requires that the sensitivity not be too high because that would limit the number of cracks that could be

detected since the dynamic range of an OTDR system is not unlimited. There are many different design parameters that influence the sensor performance such as optical fiber size and fiber orientation to the crack, mechanical properties of the optical fiber and matrix as well as the optical properties of the fiber. A thorough analysis can take these design parameters into consideration and therefore aid in the optimal selection of each parameter for the specific sensor application. The analysis of the optical power loss in the crack sensor involves two major steps. First, a mechanical analysis of the bend in the fiber caused by the crack opening and second, an optical analysis of the bend loss caused by the crack.

There are a number of different modeling approaches that were tried in order to find which ones best simulate the loss characteristics of the crack sensor. Figure 19 demonstrates the different ways to simulate the crack opening and is labeled "Displacement Method"; additionally the 3D FEM analysis can be carried out either as linear or nonlinear and is labeled "Analysis Method" and finally the method for calculating the radii from the FEM analysis is labeled "Radius Calculation Method" in the diagram. Each one of these important steps will be discussed in depth later.

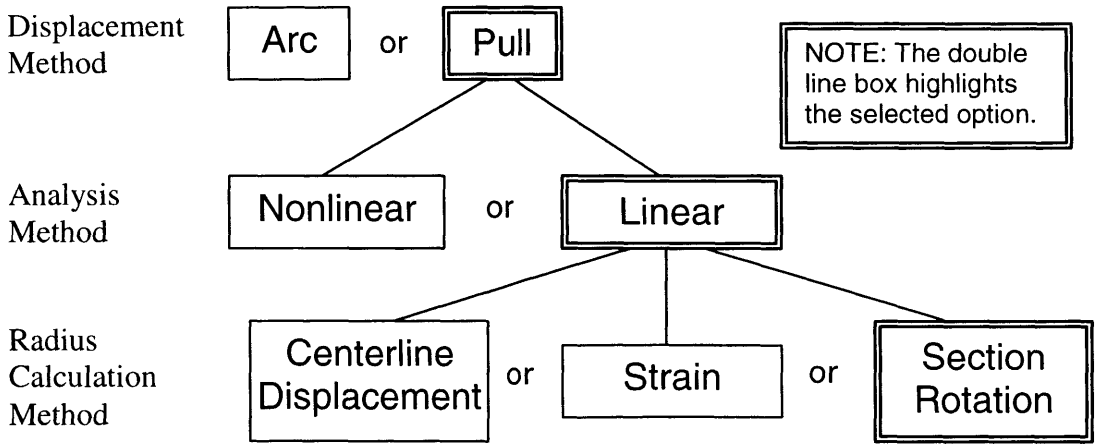

Figure 19:Different Calculations Considerations for Mechanical Analysis

4.1 Mechanical model

Mechanical analysis is an important first step in understanding the behavior of the crack sensor. Modeling the crack sensor required that some assumptions be made as illustrated in Figure 20. A single crack is shown in *Part A* of the illustration. It is assumed that the influence of the matrix surrounding the optical fiber can be taken at five fiber diameters from the fiber center. This is found to be sufficient to simulate a matrix of infinite extent. The fiber length is taken to be about 36 times the fiber diameter which is adequate for the fiber to reach a near steady-state straight fiber condition. The dotted lines in *Part A* illustrate that section of the matrix which is used in the three-dimensional finite element model (3D FEM). *Part B* demonstrates the input model for the 3D FEM analysis. While one piece of the sensor matrix is held stationary the other piece is displaced to the position representing the crack opening. *Part C* illustrates the 3D FEM output representing the final position of the crack opening. The curvature of the bent optical fiber can be calculated using the output information from the 3D FEM file.

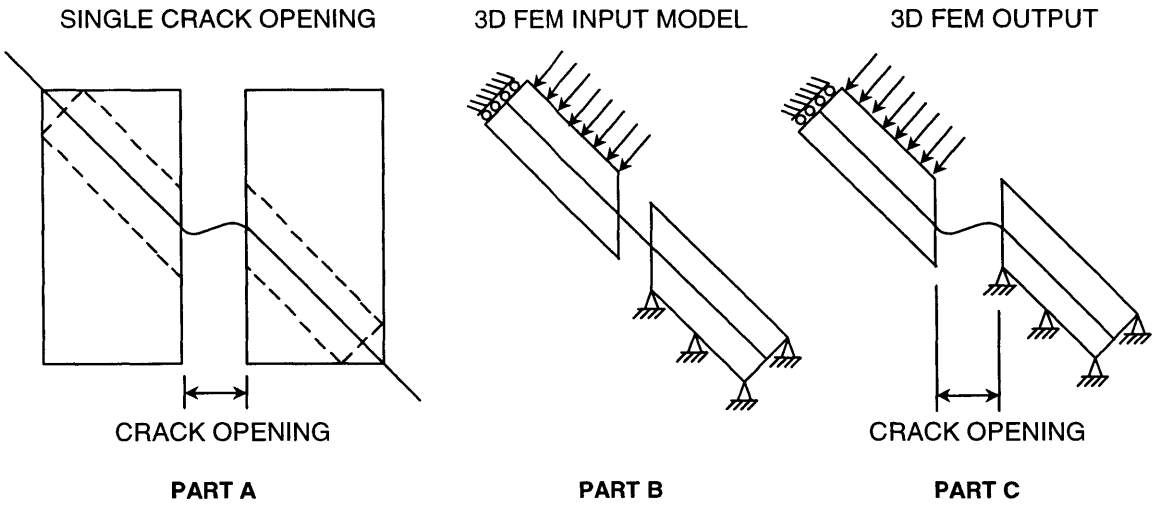

Figure 20: Diagram of the mechanical model for the crack sensor

4.1.1 Boundary Conditions

The boundary conditions for the 3D FEM model are shown in Figure 21. The assumptions for making the model are shown in Figure 20. The boundary conditions reflect the assumptions made in the model. The model has been cut in half to save calculation time by greatly reducing the number of elements used. The plane of the split which cuts the optical fiber in half does not allow for y-translation. To ground the model, one side of the crack is held stationary and does not allow x, y or z translations while the other side of the model is displaced to represent the crack opening.

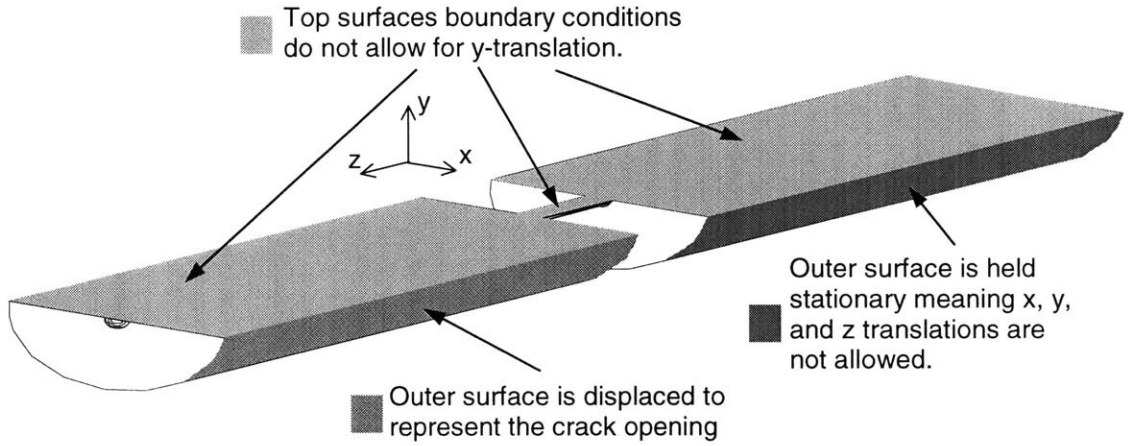

Figure 21: Boundary conditions for the 3D FEM model of the crack sensor

Figure 22 shows a close-up view of part of the FEM model pointing out the different material components of the model.

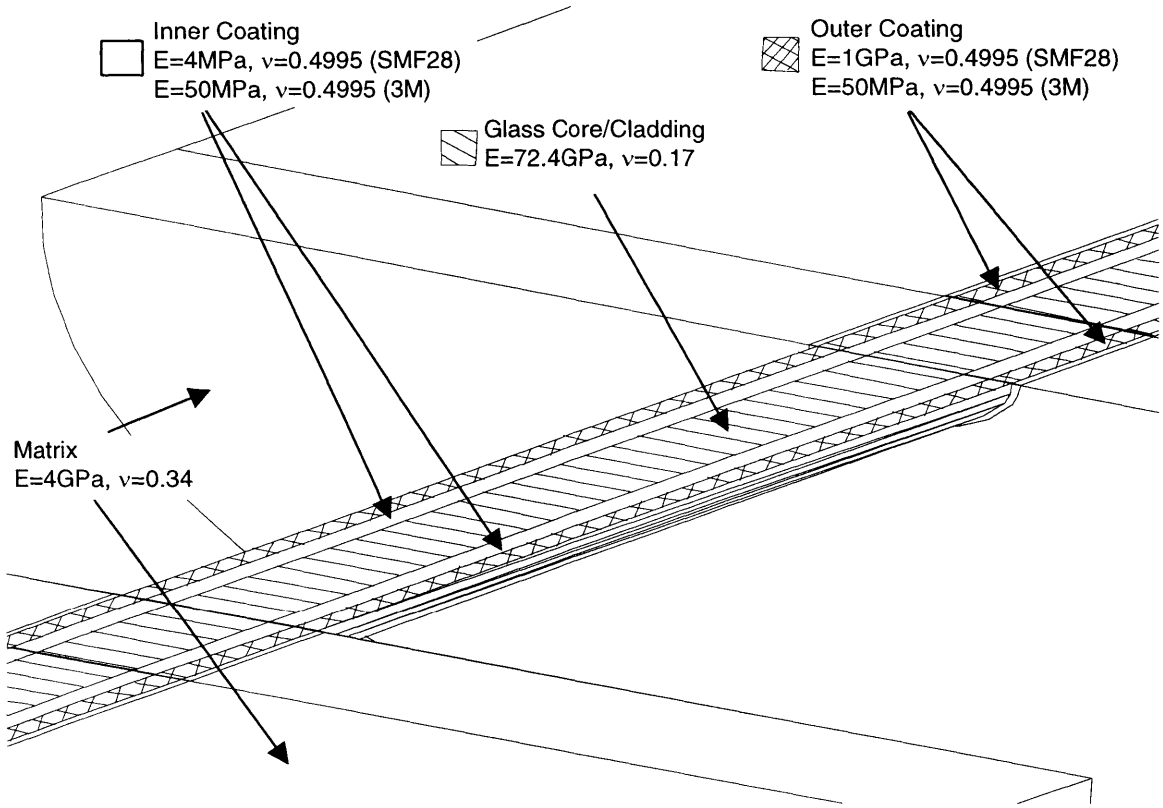

Figure 22: Illustration showing different components for the 3D FEM model of the crack sensor

4.1.2 Displacement models

When modeling the crack sensor different approaches to how the crack opening forms were tried to see which would best simulate the loss of the optical sensor. The two major methods that were looked at can be called the "arc" method and the "pull" method. Both methods are illustrated in Figure 23.

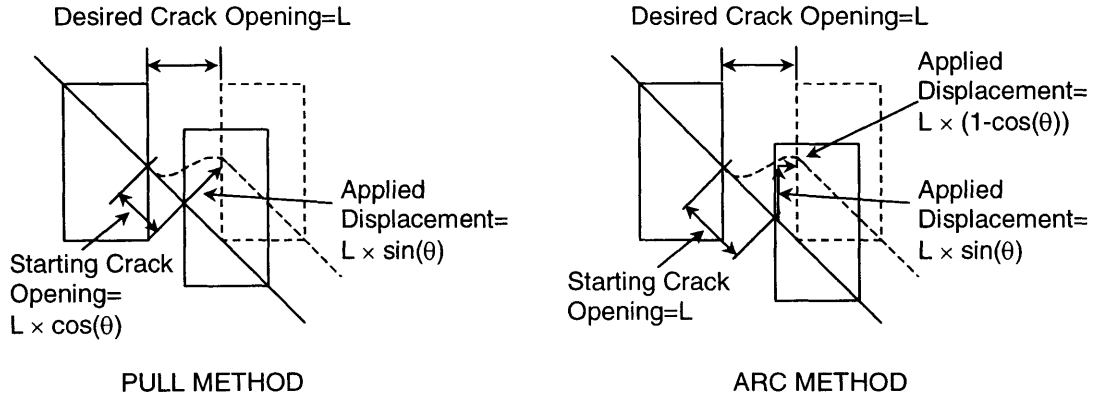

Figure 23: Diagram of the different displacement models for the crack sensor

While the two methods yield similar results the trends are different. The pull model rises with an almost flat like a line trend while the arc model trend raises more rounded like a circle. These trends will be compared and discussed later by looking at the radius profiles and then the actual optical signal loss diagrams.

4.1.3 Separation zone

In the analysis, twenty-node three-dimensional solid elements are employed to model the fiber, the matrix as well as the polymeric coating (or jacket) around the fiber. Figure 24 shows the finite element mesh near the crack opening. Note that a thin layer of material is removed from the tension zone of the fiber-matrix interface and is marked as "Separation Zone" in Figure 24. This zone allows for the separation of the fiber from the matrix as it is bent away. There is no need for a separation zone when the fiber is pressed against the matrix and that is why the separation zone is only on one side of the fiber. The extent of such a layer (along the fiber direction) can be obtained through iteration. It is necessary to adjust the length of the zone for each computation of a different crack opening. Figure 25 shows an example of the iteration process that was followed to arrive at the correct separation zone.

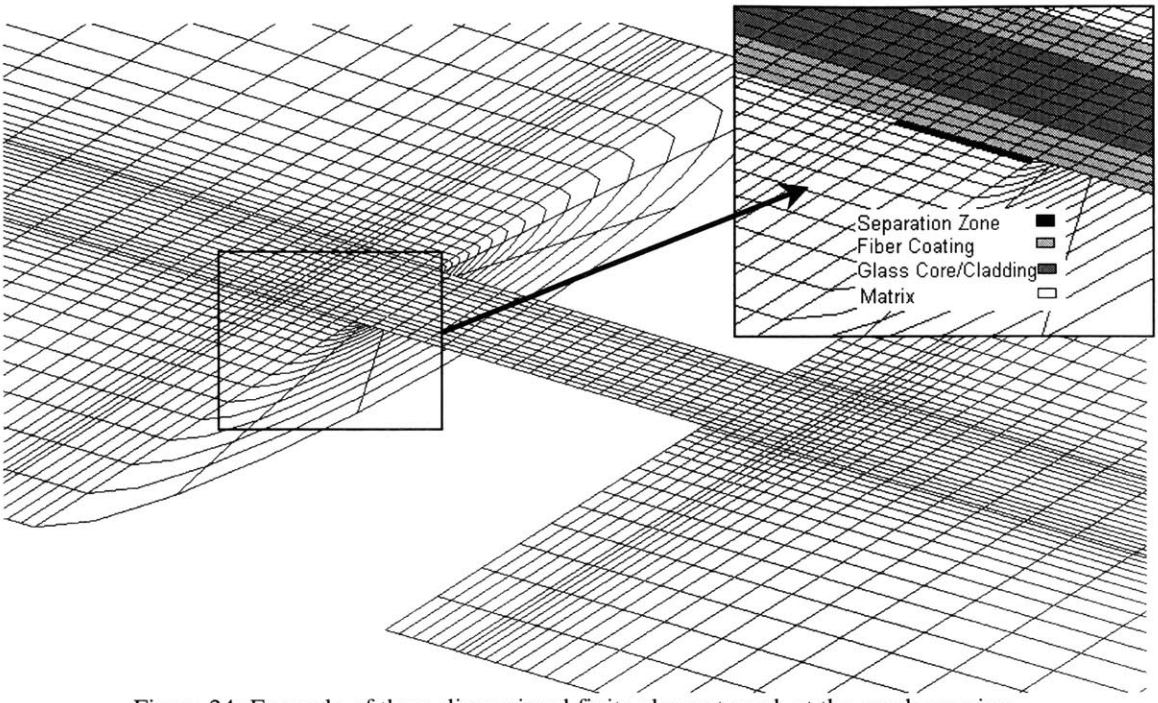

Figure 24: Example of three-dimensional finite element mesh at the crack opening.

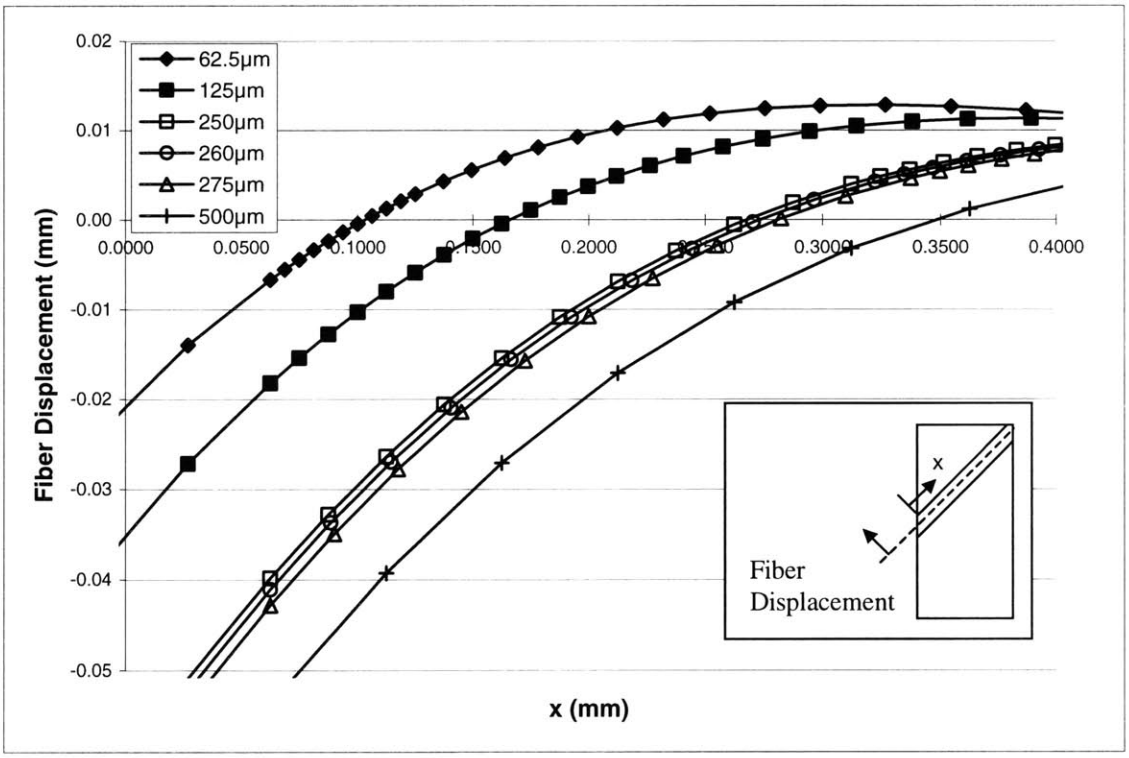

Figure 25: Iterative process for finding the appropriate separation zone length

4.1.4 FEM Model

The 3D finite element model analysis used a total of 8,400 20-node solid elements. The ADINA finite element program was used for the computation. As mentioned previously a linear and nonlinear approach were used to make the analysis. In the end, the linear method was chosen for reasons that will now be discussed.

Given the large displacements in the analysis a large displacement-small strain geometric non-linear analysis was carried out. Solving the non-linear problem using ADINA was not simple. The different available searching algorithms, Modified Newton iterations with and without line searches, BFGS (Broydeb-Fletcher-Goldfarb-Shanno) method, and the Full Newton iterations with and without line searches were all tried. The Full Newton Method with line searching was the only one that converged given the convergence criteria. While this analysis takes into consideration the large displacements, which more accurately depict the actual sensor performance, there are some issues with the analysis that ultimately made it not suitable for the purposes of the work. Given the unpredictable nature of solving non-linear problems, even if the convergence occurred quickly, the computation time was at least 1000 times longer than a linear analysis on the same model. If the convergence takes many steps to occur it may take 10,000 times longer than a linear model and finally sometimes it just simply does not converge and the analysis fails. For comparison, on a 1.4GHz Pentium 4 with 220Mb allocated memory running Windows 2000, the linear analysis typically took about 10 minutes whereas the non-linear problem running on the same computer took just under 13,000 minutes if it converged quickly. The purpose of the theoretical model is to help find an optimal sensor configuration for a specific application. Actual calibration of the sensor would need to be done with experiments. In order to simulate different sensor configurations efficiently,

and quickly, the linear model was thought to be the best selection in regards to speed. In regards to finding the correct trend of the crack sensor the linear model was much closer than the non-linear model. This is rather surprising and one possible explanation for this is that the convergence criterion for the non-linear model is not correct for some of the points. Even though the FEM program may have arrived at a result that does not mean that it is the correct result. Such is the nature of non-linear problems. In the end, it is yet another reason why the non-linear analysis was not used.

4.2 Radius Profile: Comparison Between Different Mechanical Model Attributes

The objective of the mechanical model is to create a representative radius profile of the bent fiber so that the optical analysis can calculate the corresponding optical power loss. The radius profile is very directly related to the optical power loss for a crack opening and therefore a good representation of the expected power loss. As one would expect, a smaller bend radius will result in much greater light loss. Since the optical analysis, which will be looked at later, does not distinguish between positive and negative radii the radius profiles shown later in this section are the absolute values of the radii. Furthermore, since the mechanical analysis shows that the radius profiles are symmetric about the crack sensor centerline, which one would expect, only half of the profile is shown. Moreover, as the radii become large the influence on signal loss becomes negligible and therefore for illustration purposes the scale of radius profile is cut off to show the smaller radii which greatly influence the power loss. One final note, once the optical analysis has been discussed, graphs of the optical power loss versus crack opening will be shown to further collaborate the comparisons.

In order to compare the different methods charts of the radius profile will be shown for three different crack openings. Crack openings in the range of 0.2mm to less than 1mm are the sizes of interest in monitoring Civil Structures. The crack simulations were carried out to 2mm crack openings in order to see the effect of larger cracks. The analysis was done using 0.2mm increments. Crack openings of 0.2mm, 0.8mm and 2.0mm were selected to make the comparisons between different analysis parameters. These sizes were selected because they show the trend of the crack sensor without having to show the radius profiles for each crack opening.

4.2.1 Bend radius calculation

Calculating the behavior of the model with the ADINA FEM software package only provides the stresses, strains and displacements of the sensor components. It is necessary to take this information and manipulate it to be useful for the optical analysis. To analyze the signal loss due to bending, the curvature along the fiber is required. There are three different means by which to calculate the bend radius information. One method is using the strain values another is using the displacement information to find the section rotation and a final one is to use the displacement information of the centerline (Figure 26).

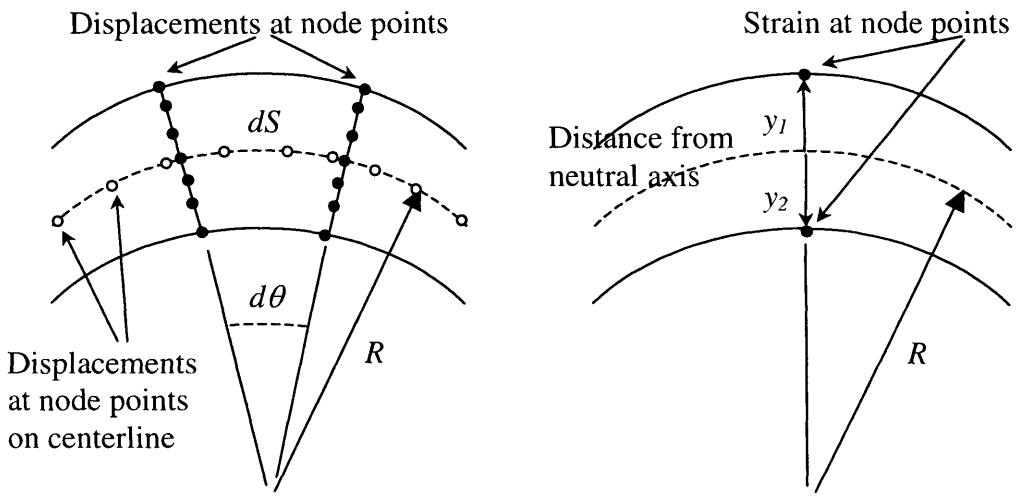

Figure 26: Calculating the radius of curvature from FEM data.

4.2.1.1 Bend radius calculation-Spline Fit to Centerline Displacement

The displacement values that are available in the FEM model are the most reliable when compared to the strains. The first method used to do the calculations was to look at the displacement values from the centerline of the optical fiber. These data points could be used to find the radius from the well-known relationship shown in Equation (1).

$$r = \frac{\left(1+\left(\frac{dy}{dx}\right)^2\right)^{3/2}}{\frac{d^2y}{dx^2}} \qquad (1)$$

The data points that are available for the analysis are not sufficient for the spacing that is needed (usually 2μm). Reducing the FEM mesh to accommodate the required spacing is not plausible since it would be very computationally expensive. To obtain the necessary data points a cubic spline was used to interpolate the required values. From these values the numerical derivatives dy/dx and d^2y/dx^2 could be calculated and then used in Equation (1) to find the corresponding radius. This sort of analysis is straightforward and relatively quick however calculating the derivatives introduces noise into the calculated

radius profile as seen in Figure 33. Furthermore the trend that it produces is not consistent with experimental results. Comparing the radius profiles for 0.8mm and 2.0mm as in Figure 27, it is clear that the loss is very similar which is not like the actual experimental results.

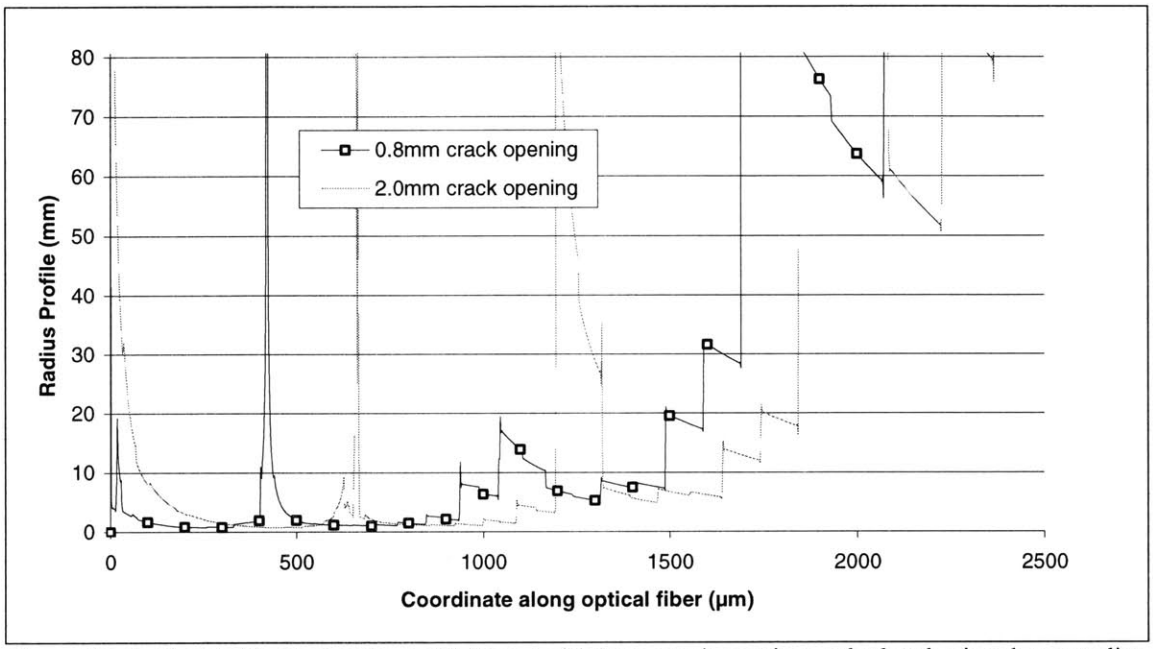

Figure 27: Radius Profile Comparison of 0.8mm and 2.0mm crack openings calculated using the centerline displacements and along with a linear FEM analysis with a "pull" displacement model.

4.2.1.2 Bend radius calculation-Section Rotation

Using the displacement values it is possible to calculate the rotation of the glass cross-section along the fiber. The process is done as shown in Figure 28. Looking at the displacement of the face and calculating the corresponding angle can find the rotation of a section of the glass fiber. Once the rotation angle is known the radius can be calculated as $R = \frac{d\theta}{ds}$ where the Central Difference Method is used to calculate $\frac{d\theta}{ds}$. The FEM mesh is only fine enough to obtain accurate results. Increasing the mesh beyond that is very computationally costly even though additional points are desired for the optical analysis. To find the additional points that are required a linear interpolation was used.

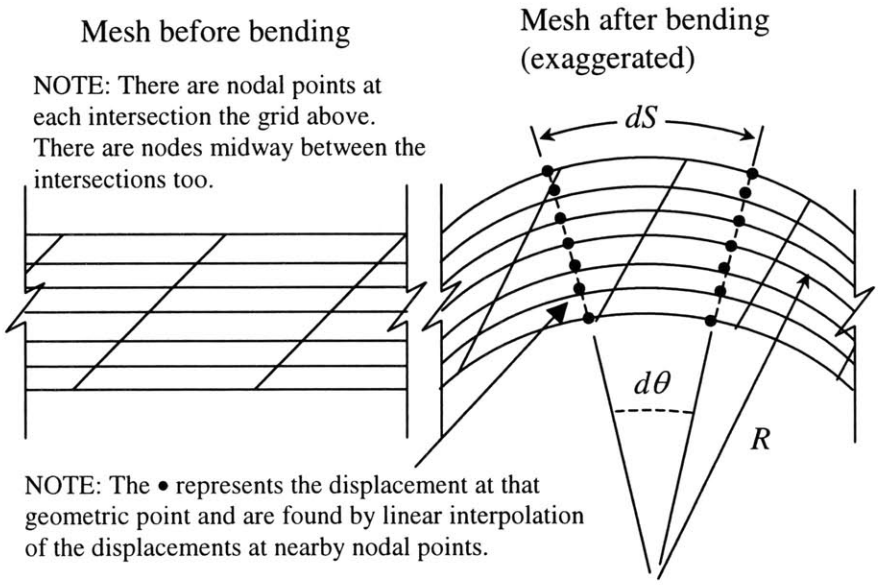

Figure 28: Diagram of finding the bend radius from displacement information.

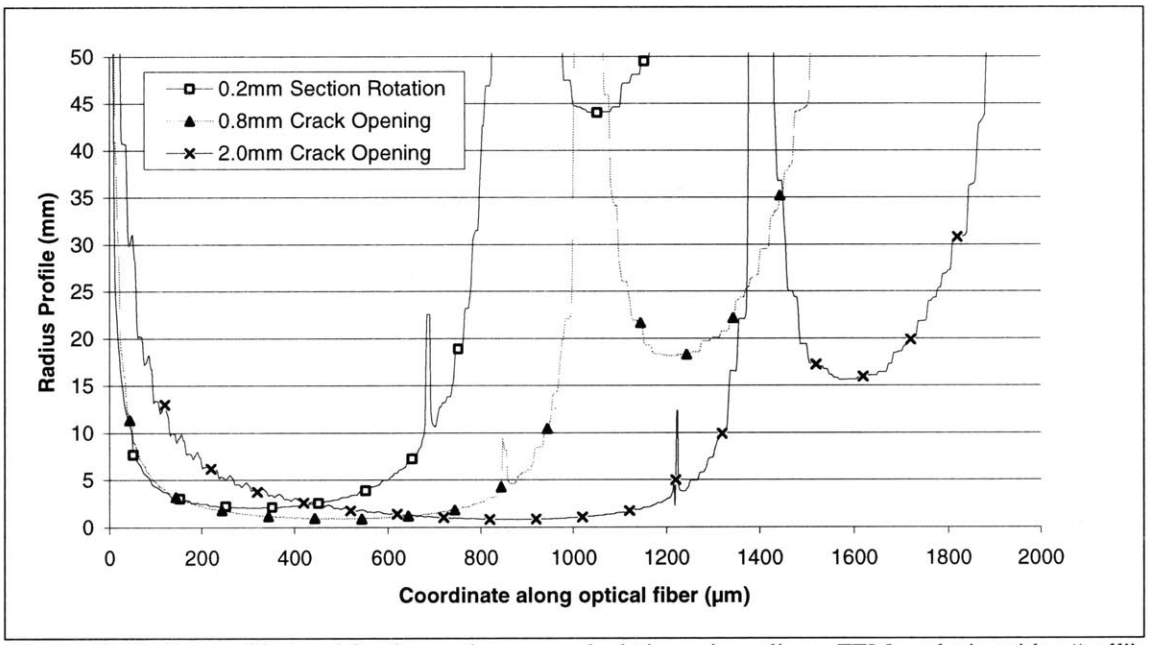

Figure 29: Radius profile trend for the crack sensor calculation using a linear FEM analysis, with a "pull" displacement and section rotation method of radius calculation.

This method is not as noisy as the previous method using the centerline displacements however it is not as smooth as the next method, the strain method. The trend of the loss is more as expected as seen in the radius profile comparison found in Figure 29. A larger

part of the fiber is bent to small radii as the crack opening increases, but the rate of increase at least qualitatively seems to decrease as the crack size increases.

4.2.1.3 Bend radius calculation-Strain Method

Calculation of the bend radius using the strain values was also carried out. This method looked at the strains (along the length of the fiber) on opposite sides of the bent glass fiber divided by the distance between the two points or $R = \frac{d}{\varepsilon_1 - \varepsilon_2}$.

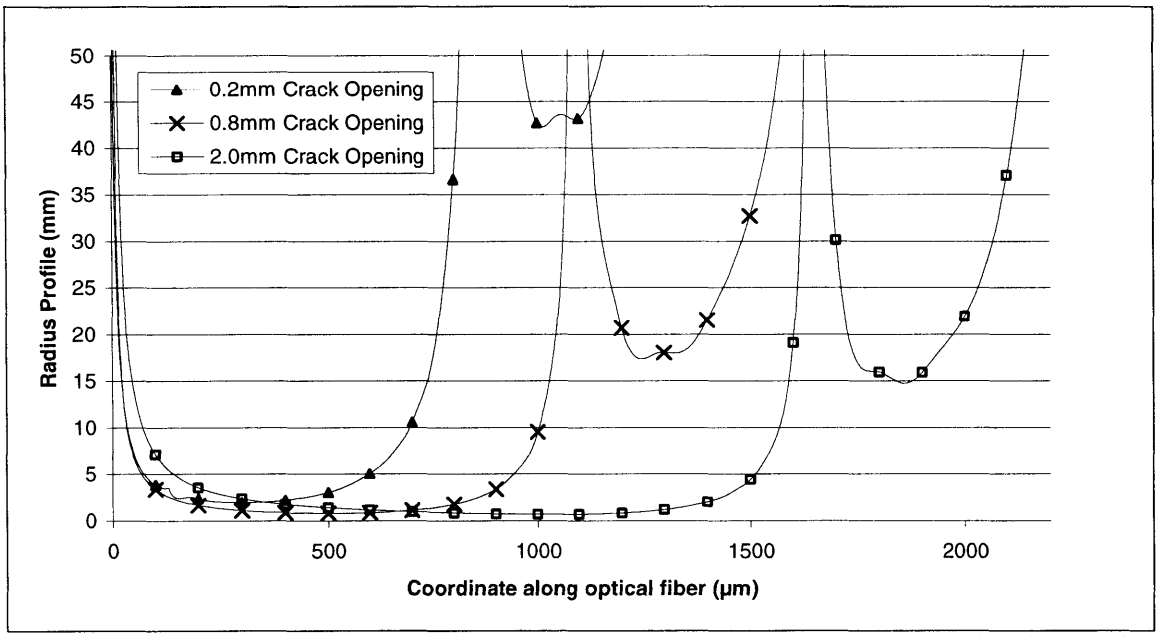

Figure 30: Radius profile trend for the crack sensor calculation using a linear FEM analysis, with a "pull" displacement and strain method of radius calculation.

The calculation using the strain values has the least amount of numerical noise since it is not necessary to carry out many calculations such as finding derivatives. The trend also looks to be good as in Figure 30, the increasing crack size corresponds to a larger number of small radii which will result in more power loss as would be expected.

The calculation of the radii using this method makes the assumption that the neutral axis is in the middle of the bent fiber which is not always the case. This could lead to errors

in the calculations. Additionally, since the fiber is displaced quite a significant amount the value of the strain in the direction of the global coordinates is probably not the correct value to use. Strain values in the new coordinate system after the fiber section rotates cannot be obtained directly from the program. To find the values would require additional calculations along with making some assumptions such that the values would become less accurate. Therefore, using the displacement values was the most direct way to find the bend radius.

4.2.1.4 Bend radius calculation-Comparison of different methods

Looking at Figure 31, one can compare the three different methods and come to some preliminary conclusions about which method best suits the needs of the analytical model. At a 0.2mm crack opening the section rotation and strain methods are very similar while the centerline displacement method shows a significant increase in the number of small radii. Moving to 0.8mm the trend is again similar with the centerline displacement method having a larger number of small radii than the similar strain and section rotation methods. At a 2.0mm crack opening the trend changes with the strain method showing many more small radii followed by the centerline displacement method and then the section rotation method with slightly less. Since there is such a strong correlation between bend radii and optical power loss it can be seen that the power loss from the strain and section rotation methods would start up slowly and then lose light similarly until about 0.8mm at which point the strain method loses light faster than the section rotation method. Whereas, the centerline displacement method loses light quickly at first and rises rather quickly in loss to 0.8mm crack opening at which point it kind of levels out with similar levels until 2.0mm crack opening.

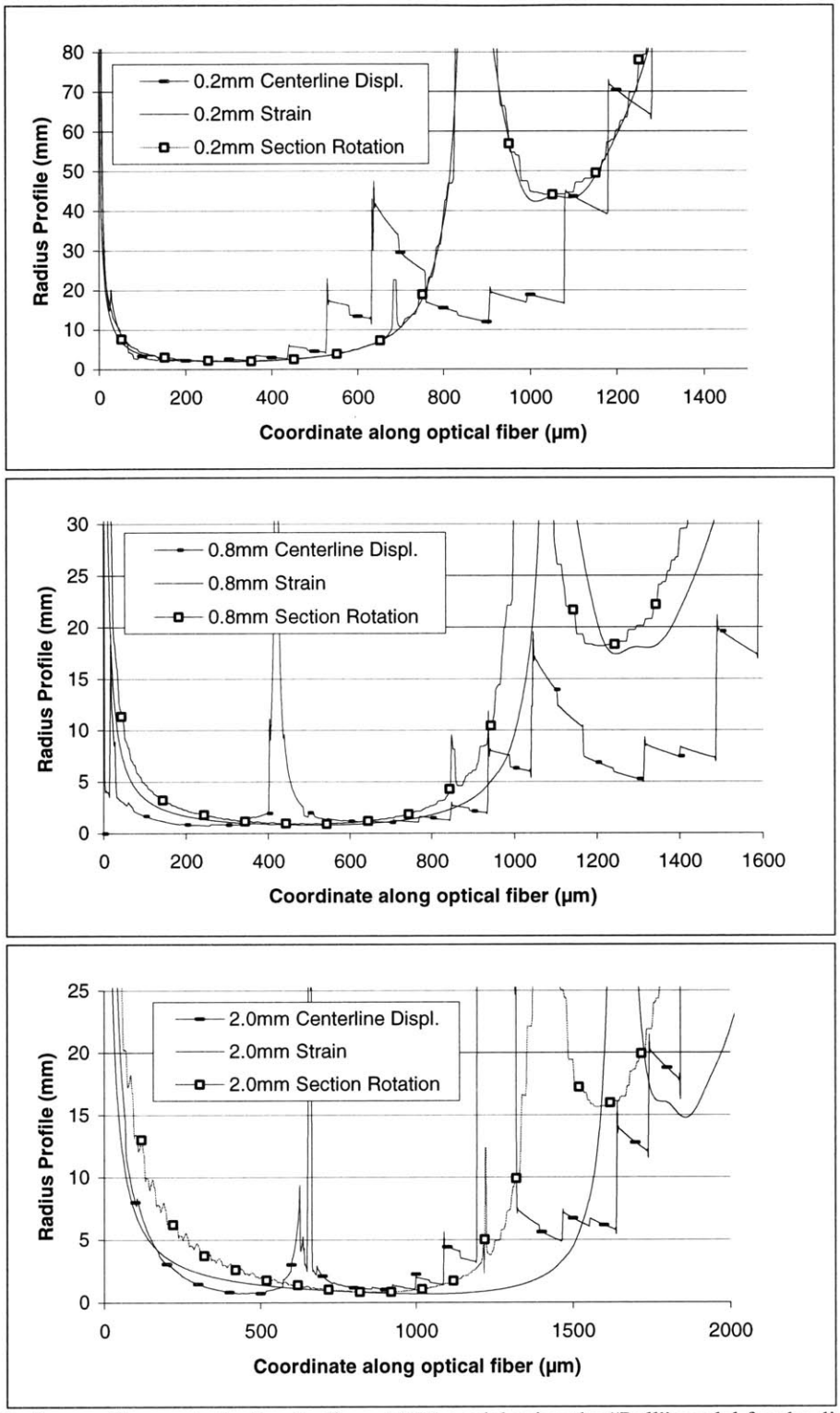

Figure 31: Radius profiles created using the linear FEM model using the "Pull" model for the displacement. Comparison shows the differences between different ways for finding the radius profile with a "Centerline Displacement" or using the "Strain" or "Section Rotation".

After the optical analysis it will be possible to make final comments on the selected method for the mechanical analysis. However, it would appear that the strain and section rotation methods better resemble the experimental results.

4.2.2 Displacement Models

The two methods yield similar results however the trends are different. The pull model rises with an almost flat like a line trend while the arc model trend raises more rounded like a circle. These trends can be seen in the comparison of the two different models later in Figure 36. However, Figure 32 compares the different radius profiles for the two different models at 0.2mm, 0.8mm and 2.0mm crack openings. For this comparison, the "displacement method" is varied while the "analysis method" used was a linear 3D FEM and the "radius calculation method" used was the strain. If other calculation approaches are used such as nonlinear analysis or section rotation to calculate the radii, comparable trends are seen. In general it was found that the "pull" model predicted smaller radii compared to the "arc" model. A higher loss is hence expected in the optical analysis. Looking at the different charts in Figure 32 this can be seen. For a 0.2mm crack opening the radii profile are very close, with a 0.8mm crack opening the "pull" model has a more pronounced influence of smaller radii and this becomes even more evident for the 2.0mm crack opening. This supports another observation when comparing the two methods, which is that the "arc" model shows a reduction in optical power loss as the crack opens which is not as evident in the "pull" model. Sometimes this dip becomes very pronounced and the experimental data does not show such a quick reduction in power loss. Since the "pull" model best represents the experimental trends it was chosen as the method for carrying out the theoretical analysis.

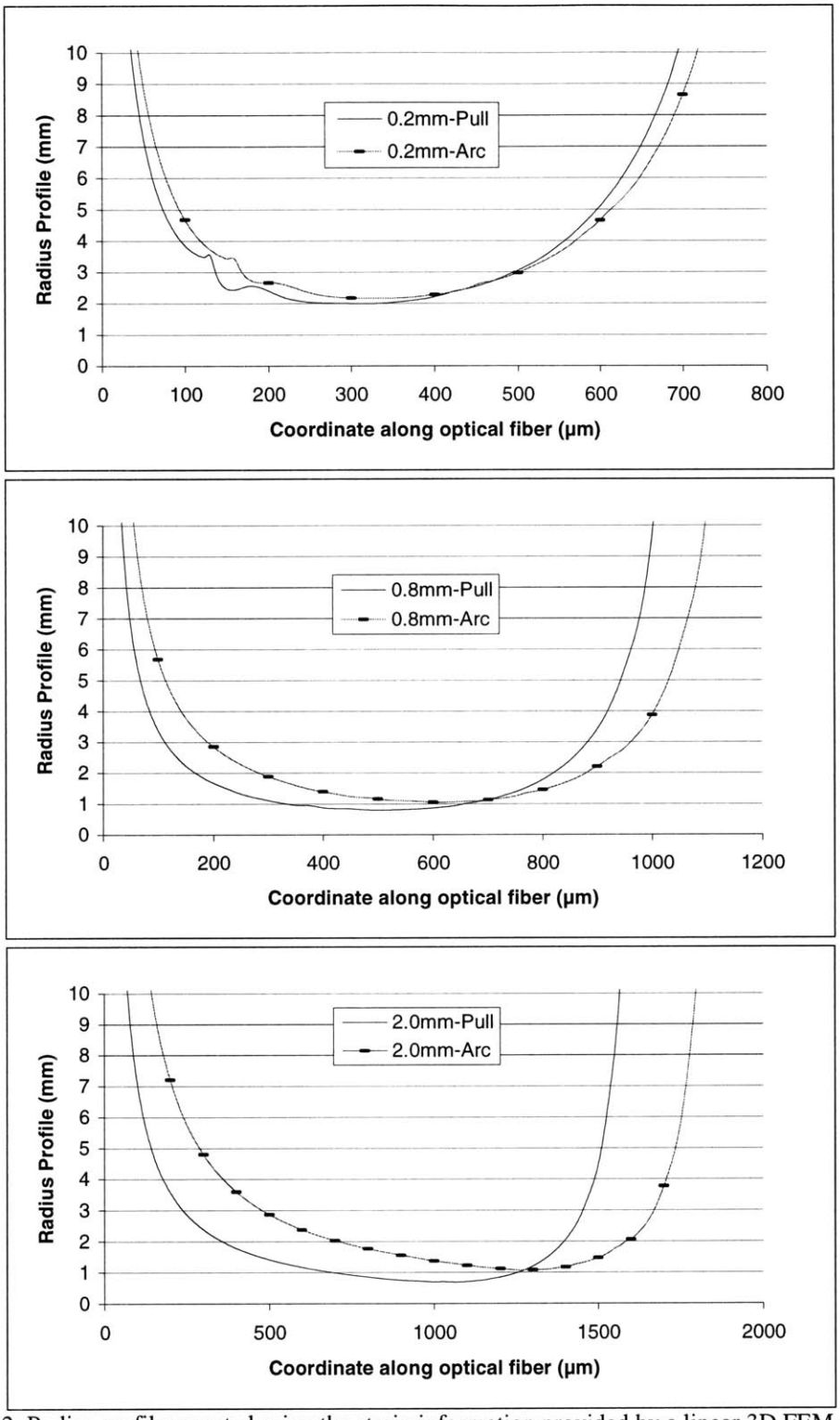

Figure 32: Radius profiles created using the strain information provided by a linear 3D FEM analysis. Comparison shows the difference between "Arc" and "Pull" model performance.

4.2.3 FEM Model

The radius profiles comparing the linear and nonlinear analysis approaches in Figure 33 use a pull "displacement method" along with section rotation as the "calculation method to find the radius".

The radius profile for all three illustrated crack openings has less tight bends than the linear model and therefore would have a lower optical power loss. The other trend that can be seen from Figure 33 as well as Figure 34 is the power loss trend corresponding to the crack opening. For the linear analysis the amount of small radii present in the profiles which corresponds to a higher optical power loss increases with each crack size. However, for the nonlinear analysis the influence of small radii is very similar for both 0.8mm and 2.0mm crack openings as shown in Figure 34 where the 2.0mm radius profile has been shifted left to make the comparison more clear. This would translate to a similar optical power loss which is not the trend observed in the tests.

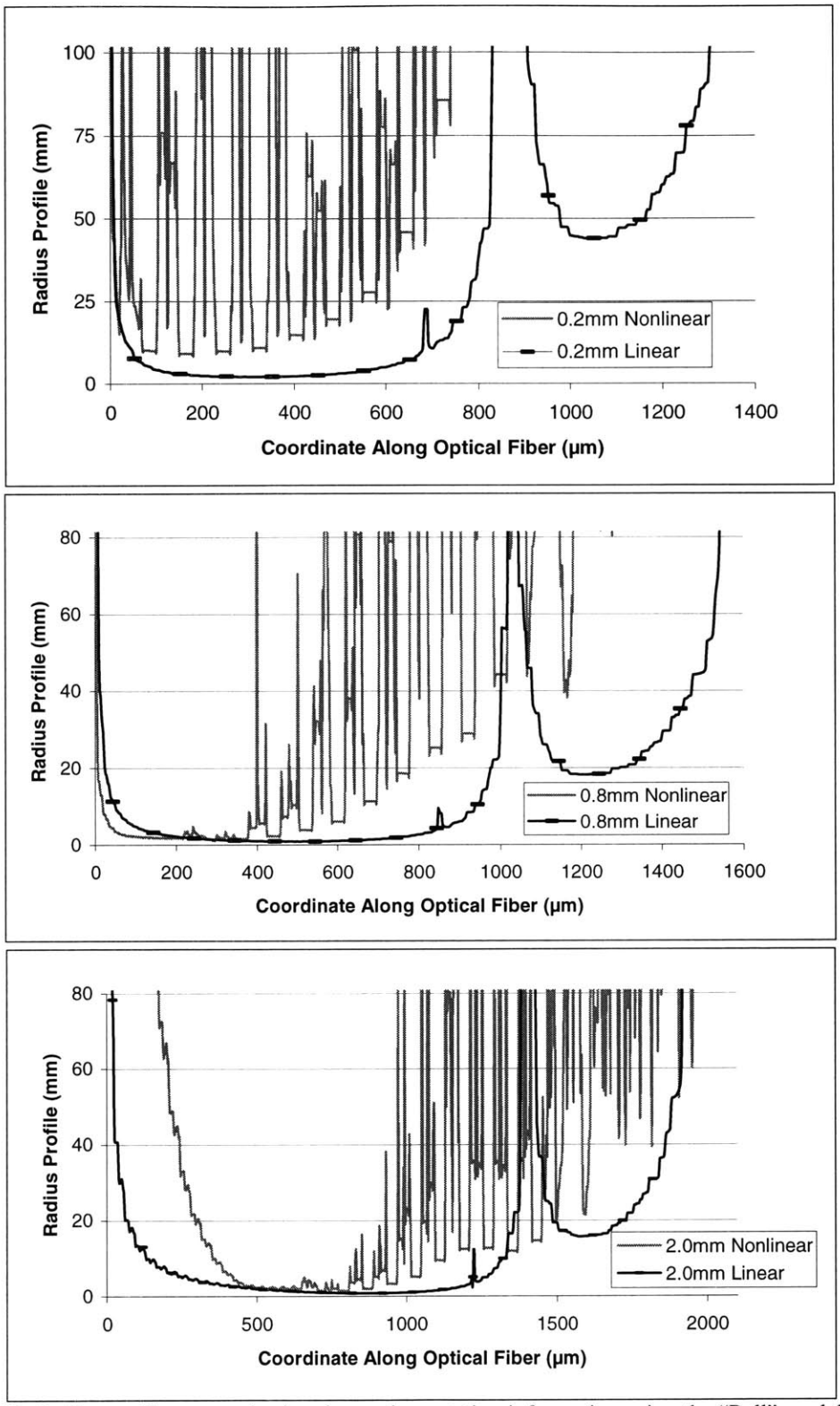

Figure 33: Radius profiles created using the section rotation information using the "Pull" model for the displacement. Comparison shows the difference between "Linear" and "Nonlinear" model performance.

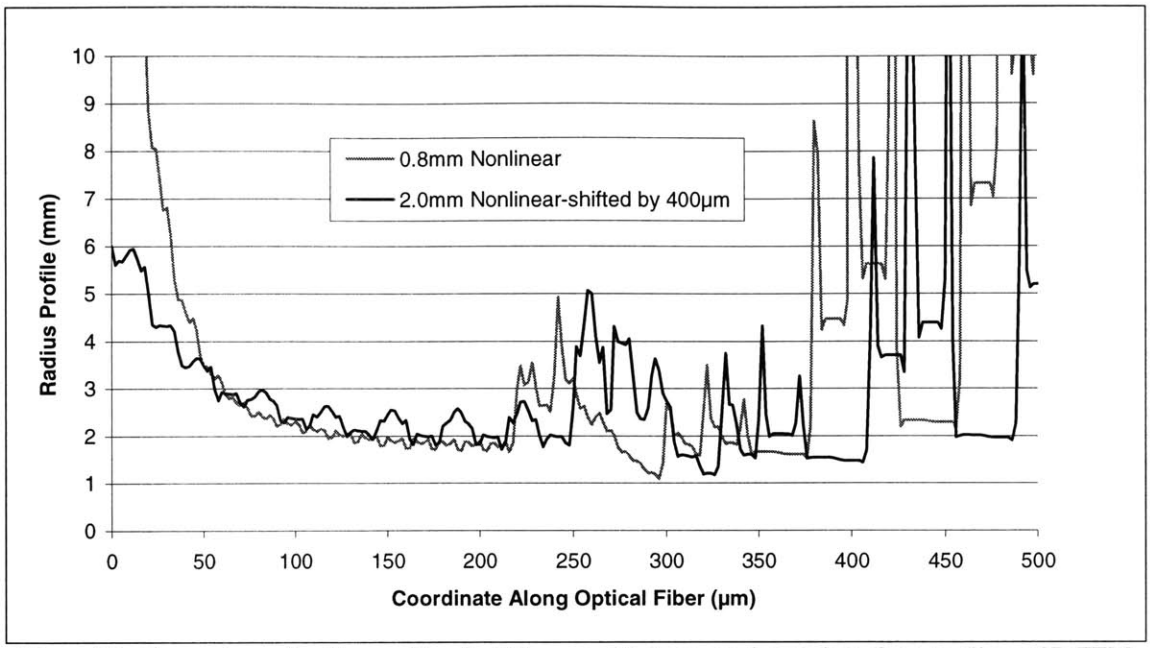

Figure 34: Comparison of radius profiles for 0.8mm and 2.0mm crack openings for a nonlinear 3D FEM "pull" displacement analysis using section rotation for radius calculation.

5. SINGLE-MODE OPTICAL ANALYSIS

Calculation of the bending loss can now be carried out with the radius of curvature profile obtained from the mechanical analysis. It is important to remember that the purpose of this theoretical model is to aid in the design of the fiber optic sensor for specific applications. The actual calibration of the sensor is carried out through experiments. The optical calculations that are carried out for the bend sensor need to be good but relatively quick. Simple bend loss equations have been put forth by many authors which could be used to solve for the power loss. However, these calculations are generally just related to the pure bend loss and do not account for the transition loss. The Beam Propagation Method (BPM) does take into consideration the transition and pure bend loss mechanisms but it is more computationally intensive and fiber bending violates the paraxial condition. In this section, a close examination of the different available calculation methods for optical power loss will be taken.

5.1 Simple Pure Bend Loss Equation

Several authors, such as Marcuse[20,21] and Snyder et. al.[19] to name a few, have derived a simple formula that describes the power loss of a bent optical fiber due to pure bend loss. After many years of tests, the pure bend loss formula has been widely accepted as correct. Since it is derived in many places the results will be shown here as presented by Marcuse.[20] The simple curvature loss formula can be expressed as:

$$2\alpha = \frac{\sqrt{\pi}\kappa^2 \exp\left[-\frac{2}{3}\left(\gamma^3/\beta_g^2\right)R\right]}{e_\nu \gamma^{3/2} V^2 \sqrt{R} K_{\nu-1}(\gamma a) K_{\nu+1}(\gamma a)} \qquad (2)$$

where e_ν=2 since ν=0 because for this analysis the LP_{01} mode is used. The R is the bend radius of the fiber. It should also be noted that the 2 in front of the α is necessary since α is defined as the amplitude-loss coefficient of the guided wave. The other parameters in the equation will be discussed below. "An Introduction to Fiber Optics" by Ajoy Ghatak and K. Thyagarajan[18] is very useful in understanding the propagation characteristics of a step index optical fiber. First, a few important optical fiber parameters are defined in Table 3.

Table 3: Optical Analysis Definitions

a	core radius
λ	wavelength of light
n_1	core refractive index
n_2	cladding refractive index
k	$\frac{2\pi}{\lambda}$
V	$ka\sqrt{n_1^2 - n_2^2}$
J_ν	Bessel function of the first kind
K_ν	Modified Bessel function of the second kind

With the above information it is now possible to find the normalized propagation constant b by solving the following transcendental equation for the LP_{0l} mode:

$$V(1-b)^{1/2} \times \frac{J_{l-1}\left|V(1-b)^{1/2}\right|}{J_l\left|V(1-b)^{1/2}\right|} = -Vb^{1/2} \times \frac{K_{l-1}\left|Vb^{1/2}\right|}{K_l\left|Vb^{1/2}\right|} \qquad (3)$$

Once b has been determined, the other propagation characteristics can be determined as listed below in Equations (4), (5) and (6).

$$\beta = k \times \sqrt{n_2^2 + b\left(n_1^2 - n_2^2\right)} \qquad (4)$$

$$\kappa = \sqrt{n_1^2 k^2 - \beta^2} \qquad (5)$$

$$\gamma = \sqrt{\beta^2 - n_2^2 k^2} \qquad (6)$$

To apply this formula to the calculation for the bend sensor, it is necessary to numerically integrate the formula for each of the bend radii along the fiber. For convenience, the bend radii are found in the previous step at equal spacing, dz. From experience, a spacing of dz=2μm has been found to work well. Since the α is a loss coefficient in units of loss/distance, the cumulative loss is therefore added up for each step by applying the following formula:

$$P_c(i) = P_c(i-1) \times \left(1-\alpha(i)\right)^{(dz/1\mu m)} \qquad (7)$$

With the final loss for the entire fiber expressed in dB as:

$$P_{final} = 10\log_{10} P_c(final) \qquad (8)$$

Calculating the optical power loss in this manner over-estimates the loss when compared to the experimental results. Many researchers use this formula for bend loss calculation since the bend radii in their studies are quite large compared to the crack sensor radii. Generally the other studies do not look at radii smaller than 10mm but for the crack sensor the bend radii in some parts can be as small as 1mm. Marcuse developed another formula, which takes into consideration the field deformation due to the bend in the fiber[21], and it is more accurate for smaller bends. He notes that the difference between the conventional loss formula and his new formula are not very great for large bend radii however for small bend radii the conventional loss formula overestimates the loss significantly. Hence, in the analysis for the crack sensor the new loss model was used. The loss formula is:

$$2\alpha = \frac{2\kappa^2 \exp[-2\gamma a]}{e_\nu \sqrt{\pi}\gamma^{5/2} R^{3/2} V^2 \left|H_\mu^{(2)}(\xi)\right|^2 K_{\nu-1}(\gamma a) K_{\nu+1}(\gamma a)} \qquad (9)$$

The optical quantities defined for the previous Marcuse analysis, Equation (2) still apply. The only addition is that H refers to the Hankel function with,

$$\xi = n_2 \times k \times (R(i) + a) \qquad (10)$$

$$\mu = \beta \times R(i) \qquad (11)$$

The $R(i)$ refers to the specific radius in the radius profile at index i.

The cumulative loss can also be found in the same manner as shown previously (Equations (7) and (8)). The optical loss from this formula better matches the loss of the crack sensor.

5.2 Calculation of the geometric core radius

Some manufacturers of single-mode optical fibers only provide the mode field diameter (MFD) in the specifications for their fiber. Furthermore, the manufacturer may not even measure the actual core diameter and therefore cannot provide the information. The bend loss calculation is sensitive to the core radius and therefore it is important to know the value. Marcuse[22] found an empirical formula that relates the MFD to the actual core diameter for step index single-mode fibers.

$$\frac{w}{a} \approx 0.65 + \frac{1.619}{V^{3/2}} + \frac{2.879}{V^{6}};\ 0.8 \le V \le 2.5 \qquad (12)$$

where a and V were defined previously (Table 3)and w is the MFD divided by two. This empirical formula is within 1% of actual values if the V is within the listed range. From this formula it is possible to calculate the geometric core radius.

5.3 BPM Analysis

The Beam Propagation Method (BPM)[16,17] can be used to calculate the bending loss along an optical fiber with arbitrary curvature. The BPM method not only considers the pure bending loss like the bending formula in Equation (9), but the transition loss as well. The details of the analysis follow.

In order to satisfy the paraxial condition of BPM, the curved waveguide can be mapped into an equivalent straight waveguide with a modified refractive index profile if the bending radius R is much larger than the core radius (as it is in this analysis):

$$n_{new} = n_{old} \cdot \left(1 + 2r\cos\phi / R\right)^{1/2} \qquad (13)$$

Based on this refractive index transformation, BPM can be applied directly to a bent fiber.

If $E(\omega, x, y, z)$ is the transverse component of the electric field and ω is the circular frequency of the light, by ignoring the time dependence $\exp(i\omega t)$, E can be expressed in the form:

$$E(x, y, z) = \Phi(x, y, z) \cdot \exp(-ikz) \tag{14}$$

where

$$k = (n_0 \omega / c) \tag{15}$$

The propagating beam solution can be generated by repeated application of the expression in symmetrical split operator form:

$$\begin{aligned} \Phi(x, y, z + \Delta z) = \exp\left\{\frac{-i\Delta z}{2}\left[\frac{\nabla_\perp{}^2}{\left(\nabla_\perp{}^2 + k^2\right)^{1/2} + k}\right]\right\} \exp(-i\Delta z \chi) \\ \times \exp\left\{\frac{-i\Delta z}{2}\left[\frac{\nabla_\perp{}^2}{\left(\nabla_\perp{}^2 + k^2\right)^{1/2} + k}\right]\right\} \times \Phi(x, y, z) + O(\Delta z)^3 \end{aligned} \tag{16}$$

where $\chi = k\left[(n / n_0) - 1\right]$ and $\nabla_\perp^2 = \nabla_x^2 + \nabla_y^2$. The above equation can be calculated step-by-step using a Fourier transformation algorithm.[17]

One concern when using BPM is the field that propagates to the edge of the computational window in the transverse plane. This field should be absorbed to avoid reflection to the opposite edge of the window. The absorber function used in this analysis to attenuate the field is:

$$\text{Absorb(x)} = \begin{cases} 0.5\left[1+\cos\pi\left\{\left(x+x'_a\right)/\left(x'_a-x'_b\right)\right\}^{\gamma}\right] & -x'_b < x < -x'_a \\ 1 & -x'_a < x < x_a \\ 0.5\left[1+\cos\pi\left\{\left(x-x_a\right)/\left(x_b-x_a\right)\right\}^{\gamma}\right] & x_a < x < x_b \end{cases} \quad (17)$$

In the function, x_a and x'_a denote the inner edge of the absorber while x_b and x'_b are the outer edge. The parameter γ is chosen from empirical experience to be 3. The same absorber function with respect to y is also used to attenuate the field.

For example, the BPM analysis that was carried out for the 3M optical fiber and is shown in Figure 39 was done with a 256 × 256 computational grid. The sampling points were $\Delta x = \Delta y = a/6 = 0.45833$ (a=2.75μm) which means that the parameters for the absorber function were $x_a = x'_a = 29.33$, $x_b = x'_b = 58.67$, $y_a = y'_a = 29.33$, $y_b = y'_b = 58.67$. The longitudinal spacing was Δz=2μm.

It should be noted that in the paper of Yamauchi et. al.[17], the authors are able to obtain results that match well with the simple pure bend loss equation however; the bending radii that they are using are in the range of 17.5mm to 30mm. When implementing the BPM for the crack sensor analysis, which has radii in the 1mm range, it was found to overestimate the loss (see Figure 39). Since the BPM model is also computationally expensive compared to the simple bend equation, it was not used for the analysis of the crack sensor.

5.4 Correction Factor

Nagano et. al,[24] have shown that the refractive index of an optical fiber changes due to the influence of external forces. These authors conducted experiments bending optical fibers under controlled conditions and made some important observations. They

observed that the optical fiber could be mechanically treated as a homogeneous circular rod. Additionally, there is no stress concentration at the core-cladding interface. Also, the amount of change in the refractive index is proportional to the tensile force and to the curvature of the fiber. Finally, they suggested that the change in the refractive index due to pure bending stress could be seen as an equivalent reduction in the geometrical bending curvature. Hence, a correction factor making the geometric radius of the bend larger could compensate for the changes in refractive index. Valiente[25] suggested that this correction factor be found as the best match between theory and experiment. That is also the procedure that R. C. Gauthier and C. Ross followed in their analysis.[23] They used two different fibers in their experiments and used a different correction factor for each fiber. Their correction factors were 1.22 and 1.29. One important difference is that they were dealing with a constant curvature whereas the crack sensor presented here has many different segments of constant curvature. To keep the analysis straightforward and simple for the crack sensor, a constant correction factor for each fiber was used. This however, could explain part of the discrepancy between the experimental results and the theoretical analysis.

6. THEORETICAL SIMULATIONS AND EXPERIMENTAL VALUES

Now that the mechanical and optical models have been examined in full it is possible to combine them and find out which methods best match the experimental data (see Figure 35).

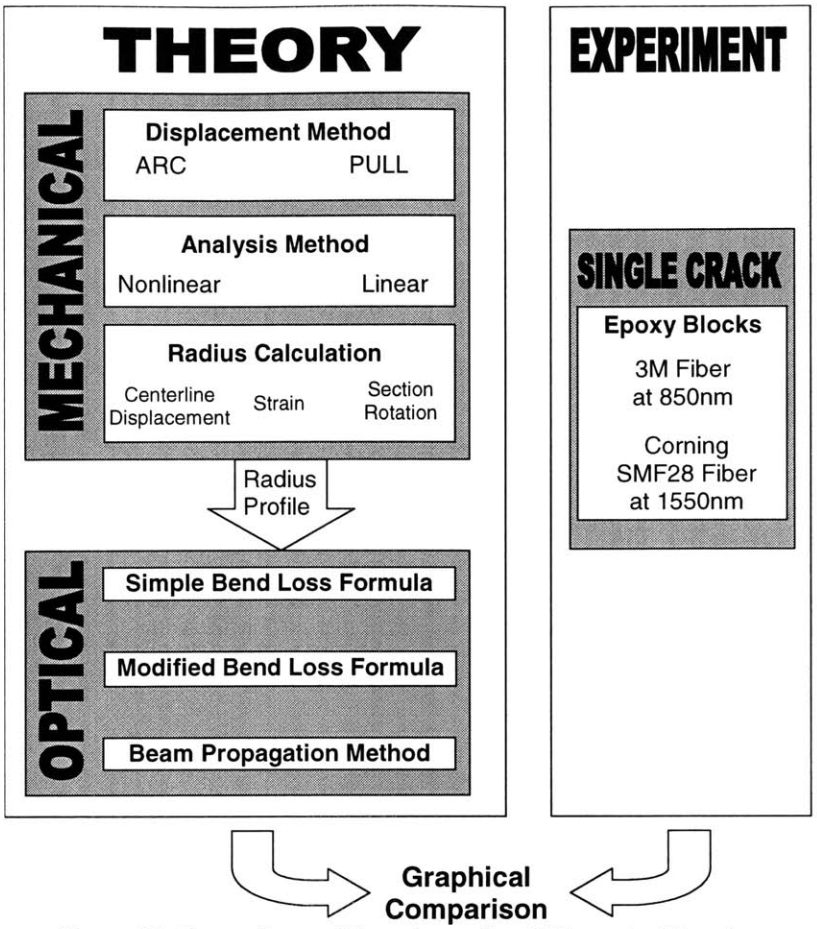

Figure 35: Comparisons of Experimental and Theoretical Results.

6.1 Mechanical Considerations

The radius profiles have been looked at previously and were used to discuss the manner in which they would influence the optical analysis (see Figure 31, Figure 32, Figure 33). Now that the optical analysis has been reviewed it is possible to look at the manner in which the different options influenced the optical analysis. The optical analysis used for all of the comparison is the modified bend formula proposed by Marcuse (Equation (9)). No correction factors were used in these comparisons. Finally all of the comparisons in this section are for a 3M optical fiber at a 45° angle of inclination.

When looking at the two different "Displacement Method" approaches, namely the "arc" and "pull" models, the radius profiles indicated (Figure 32) that there would be some differences. Figure 36 demonstrates that these indications were correct.

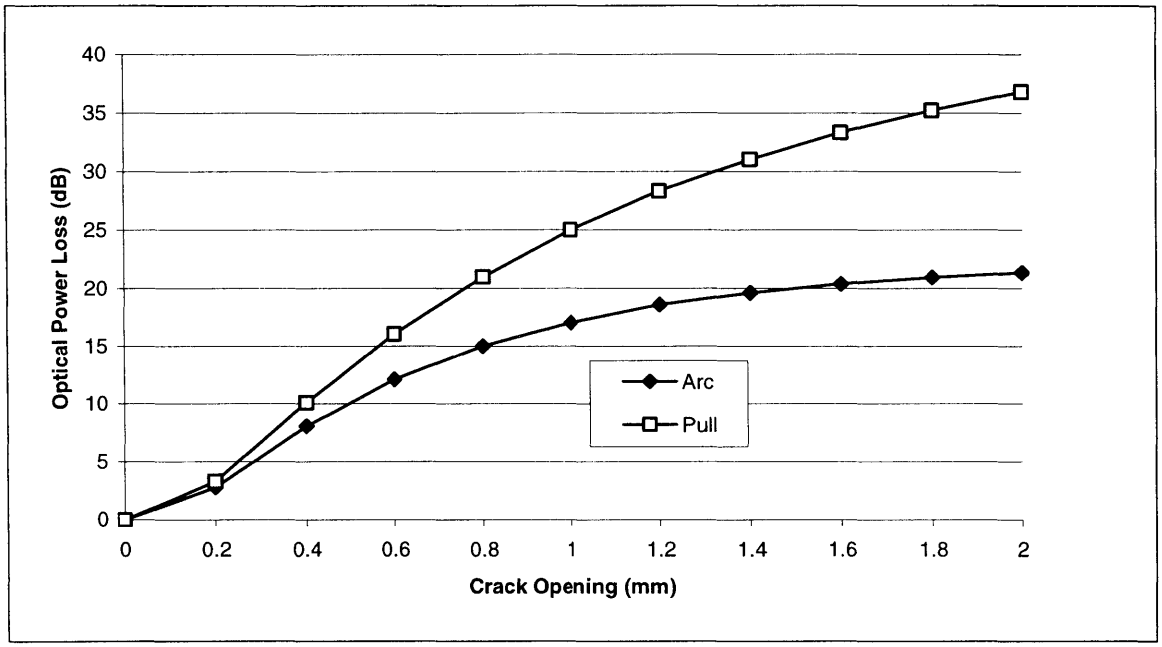

Figure 36: Comparison of the "pull" and "arc" method using the same radii profiles made using the strain information provided by a linear 3D FEM analysis.

The "arc" and "pull" models both start out very similar however the "pull" model continues to increase while the "arc" model starts to level out. In some other simulations there is a much more pronounced drop with the "arc" method even decreasing. The *Epoxy Blocks* experimental tests showed a trend more like the "pull" method.

The nonlinear and linear analyses each have pros and cons. They both predict a different power loss trend as shown in Figure 37. This radius profiles (Figure 33) used to calculate the curves were found by analyzing the section rotation from a "pull" model displacement. The modified bend formula was used for the optical analysis.

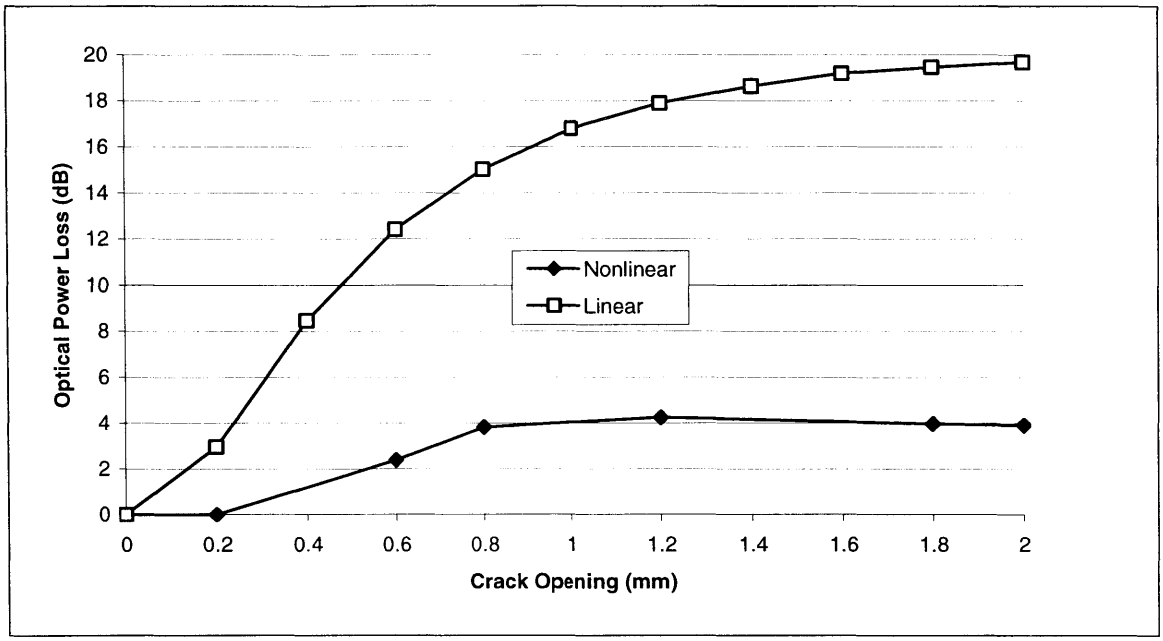

Figure 37: Comparison of the "linear" and "nonlinear" method of analysis. The radius profiles were made using the section rotation information provided by the 3D FEM analysis.

The trends of the nonlinear and linear models are quite different. The nonlinear method starts out with a very low loss and then quickly climbs to an almost steady loss for the rest of the crack openings. The linear model on the other hand gradually climbs in optical power loss much more like the trend seen in the actual experimental data. Since the trends match better and given the much better computational performance of the linear model it was chosen as the one to use. Figure 37 only shows 6 data points for the nonlinear model instead of 10 data points for the linear model. The reason for this is that the nonlinear model could not converge on a solution for the 4 other points which is just another reason why the nonlinear model was not chosen.

The final mechanical consideration is the radius calculation method. Three different approaches were discussed previously, two methods used the displacement information provided by the FEM analysis and the other used the strain information. The data points

in Figure 38 which compares the three different methods, were created using a linear 3D FEM analysis with a "pull" model displacement describing the crack opening.

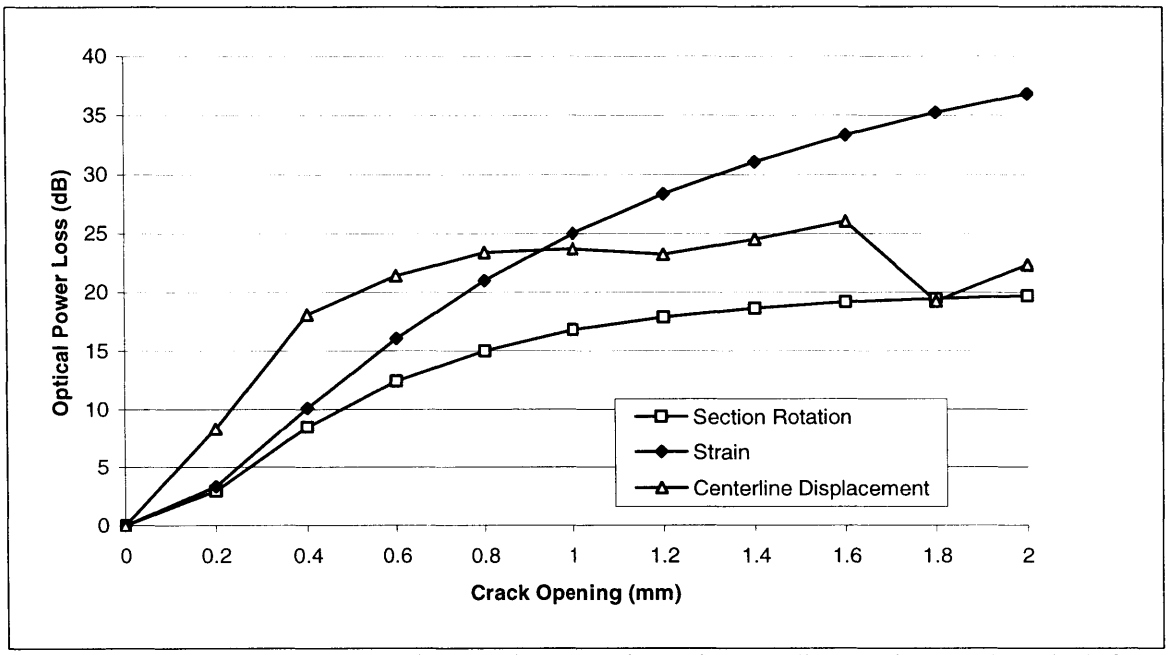

Figure 38: Comparison of the "Section Rotation", "Strain" and "Centerline Displacement" methods for calculating the radius profile. A linear 3D FEM analysis using the "pull" model for displacement was used for the calculation.

The trends that are visible in Figure 38 are similar to those seen in the radius profiles looked at previously. The "Centerline Displacement" method is very noisy and the optical analysis shows a jumpy behavior especially as the crack size becomes large. Additionally, this method predicts a high loss in the beginning and then levels out fairly quickly. This is not in good agreement with the experimental results. The "Strain" method and the "Section Rotation" method both start out rather closely however the "Strain" method continues to predict a high optical power loss while the "Section Rotation" method starts to level off. The experimental data more closely resemble the "Section Rotation" trend and therefore it was the one chosen.

6.2 Optical Considerations

There are three different optical analysis approaches that have been discussed at length previously. When these different approaches are used to analyze the radius profile information given by the mechanical analysis the results can be compared to the experiments directly.

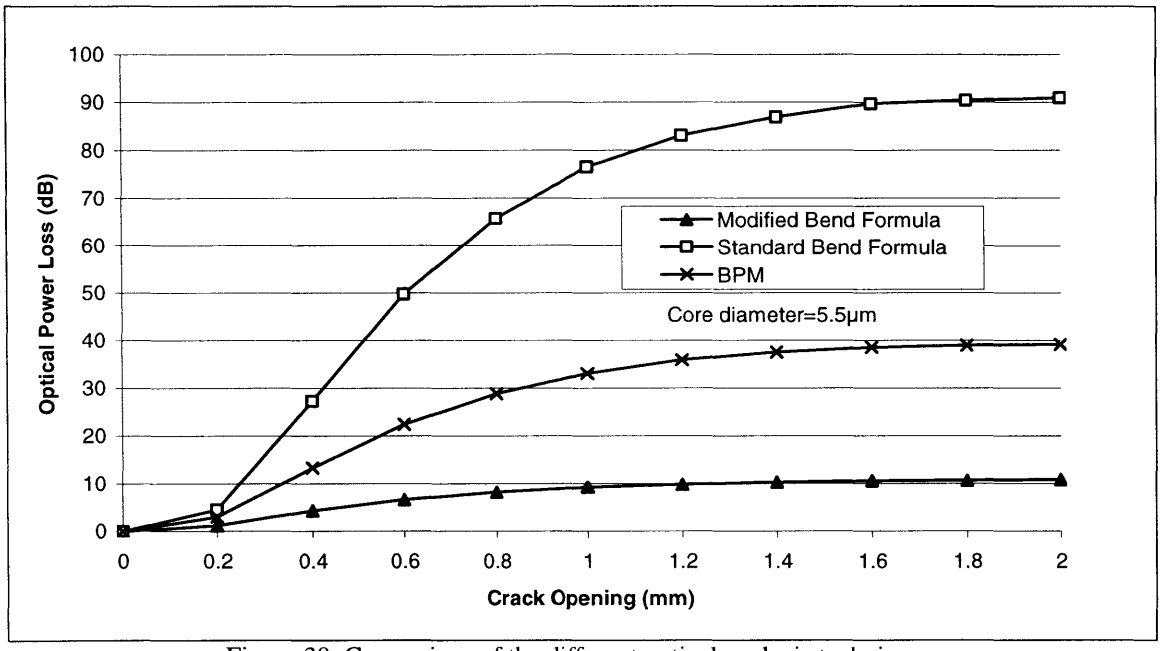

Figure 39: Comparison of the different optical analysis techniques.

In Figure 39 the three different optical analyses are compared using the same radius profiles (Figure 33). In this case the radius profiles are a simulation for a crack sensor with a 3M optical fiber at a 45° angle. The radii were calculated from the section rotation found from the displacement information from the linear 3D FEM model which was using the "pull" model to replicate the crack opening. The modified bend formula predicts the least amount of optical power loss while the standard bend formula predicts the most loss. The BPM model predicts a loss in between the two bend formulas. The reasons for the different amount of loss has been discussed previously and therefore to

choose the method that will best predict the optical power loss it is necessary to compare the results to the experimental results.

6.3 Comparisons to Experimental Values

Combining the mechanical radius profile with the optical analysis leads to the simulated results. In doing the comparisons it is necessary to take into consideration the "correction factor" as mentioned before. Figure 40 has combined all of these things together to make a comparison. This comparison uses results from the *Epoxy Blocks* with 3M optical fiber at a 45° angle. The radius profile was created using the section rotation method. The figure compares the experimental results with the simulations that are done with nonlinear and linear FEM analyses using both the "pull" and "arc" methods for displacement to simulate the crack opening. Many of the characteristics of the different analysis techniques mentioned previously are evident here. The nonlinear analysis generally predicts a lower optical loss as seen in the lower "correction factor" used however the very quick jump in optical loss that then levels out is also apparent. Furthermore, the nonlinear analysis does not have as many data points since a solution could not be found for all crack openings. The linear case while it predicts a higher optical loss always finds a solution; there are no convergence issues. The "arc" method has a clear drop in optical loss at 2.0mm opening while the "pull" does not. Since the "pull" model using a linear analysis matches the experimental values best, it was chosen as the technique to use.

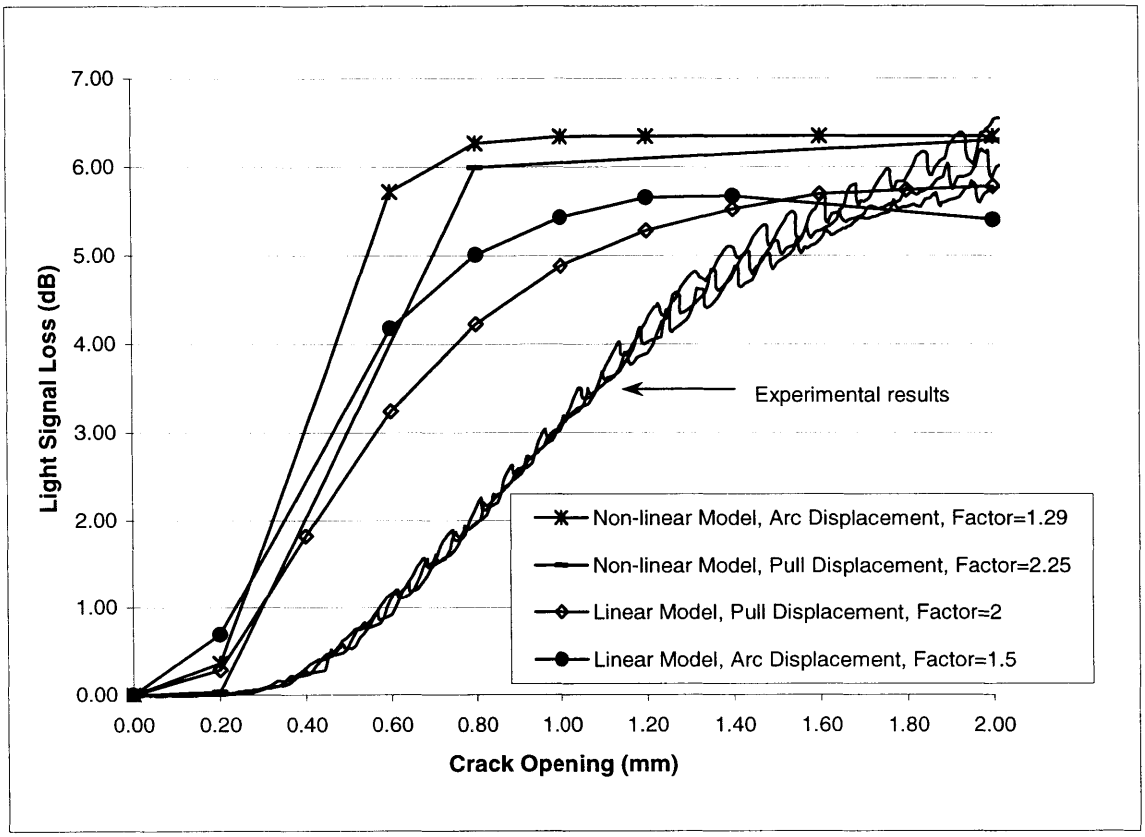

Figure 40: Compares non-linear and linear mechanical analysis 3M single-mode fiber at 45° inclination

6.4 Discussion of theoretical prediction and experimental results

The comparison of the theoretical prediction and the experimental results in Figure 41 and Figure 42 is relatively close considering the objective of the analysis. The purpose of the theoretical model is to help optimize the design of the sensor for each individual application. It is not intended to take the place of actual calibration of the sensor. Once the final design for an application has been decided, empirical tests to calibrate the sensor would need to be carried out. Hence, it is not necessary that the theoretical prediction be extremely precise in forecasting the power loss in order for it to be useful.

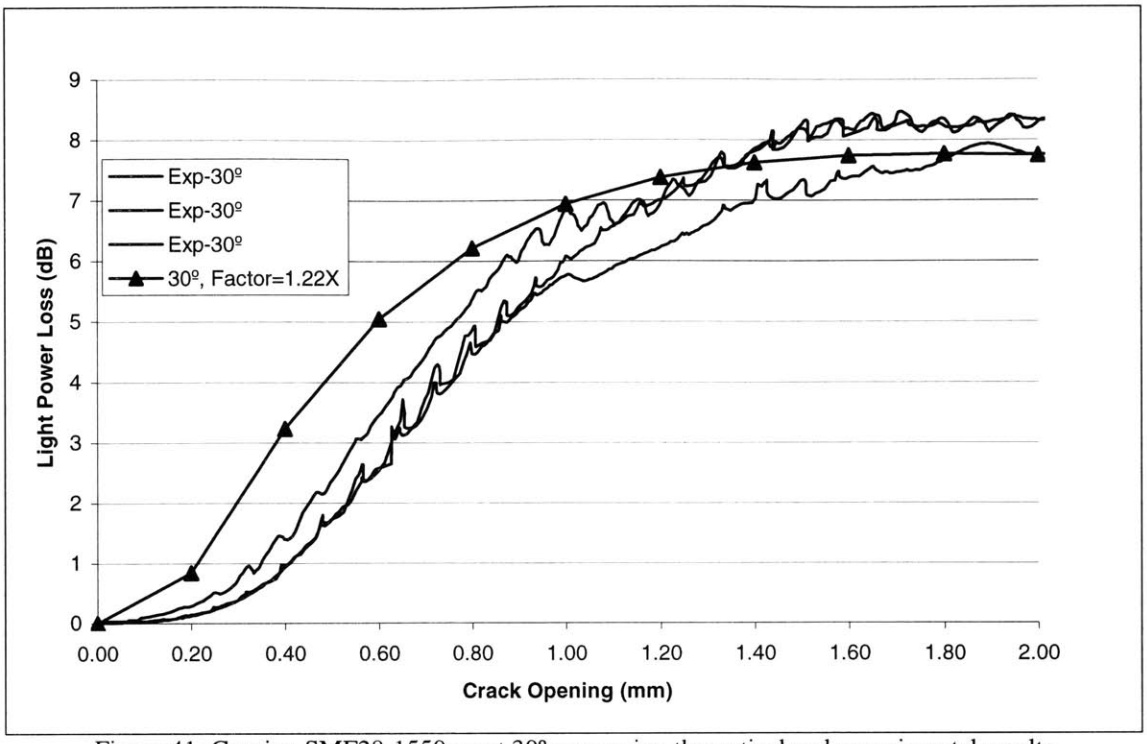

Figure 41: Corning SMF28-1550nm at 30° comparing theoretical and experimental results

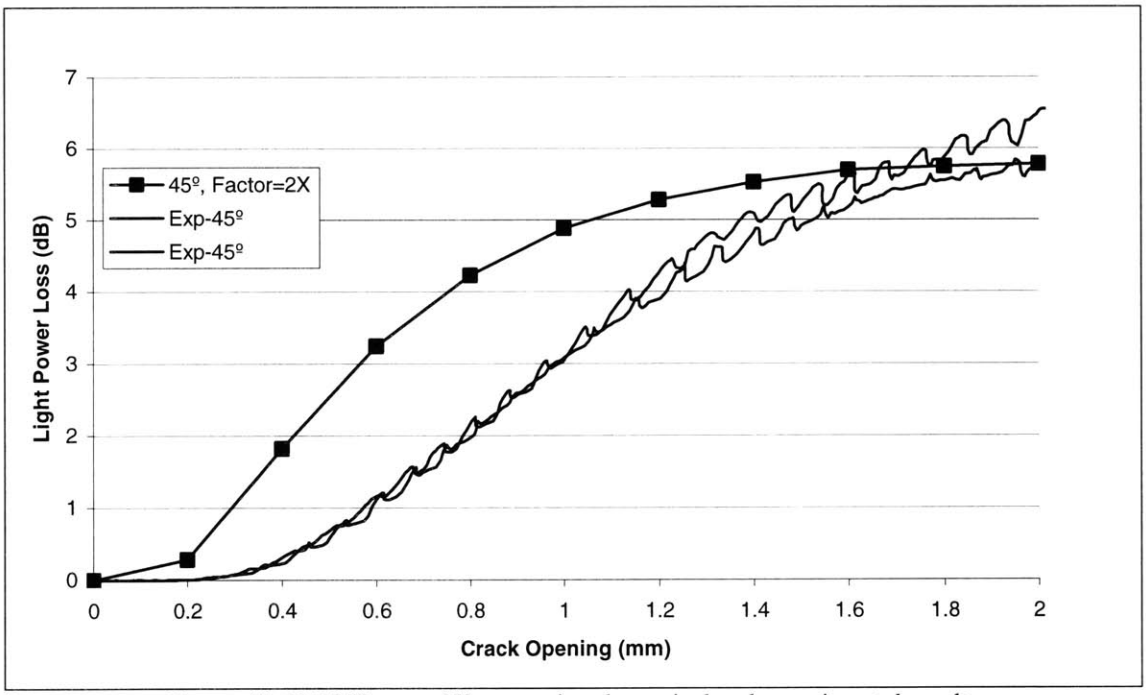

Figure 42: 3M-850nm at 45° comparing theoretical and experimental results

However, Figure 43 and Figure 44 show that the theoretical model is not a perfect prediction tool as mentioned previously. It can catch the trends and help in designing the sensors as will be shown in the next section.

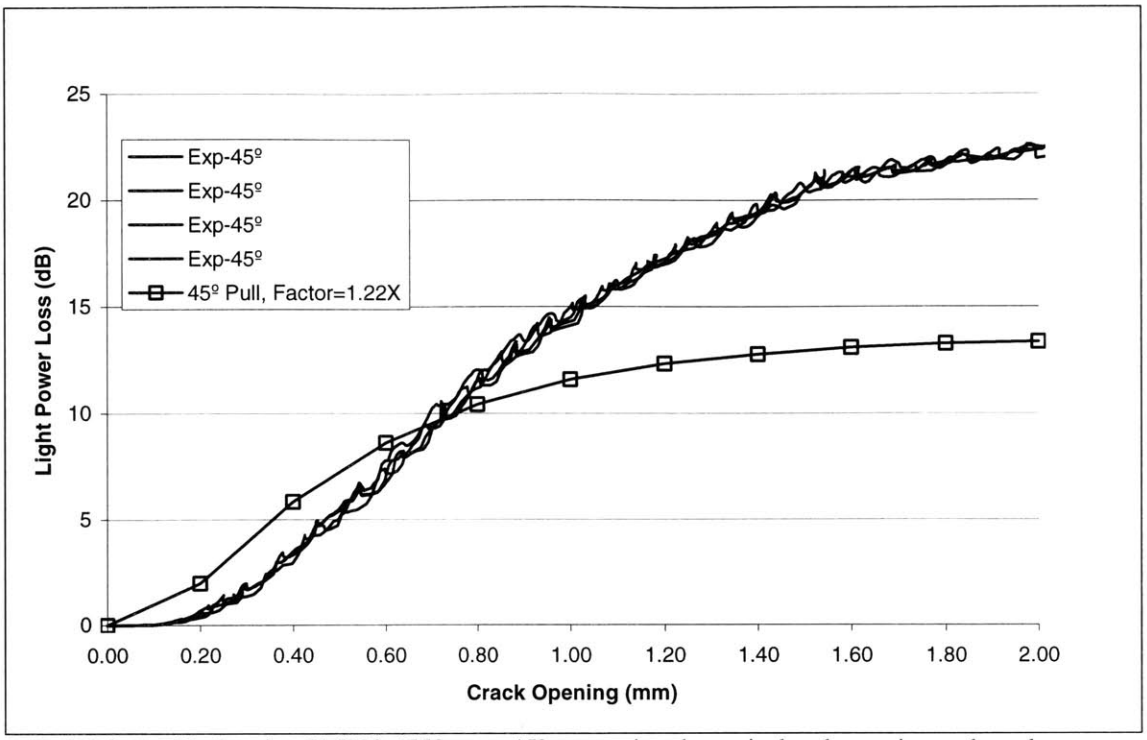

Figure 43: Corning SMF28-1550nm at 45° comparing theoretical and experimental results

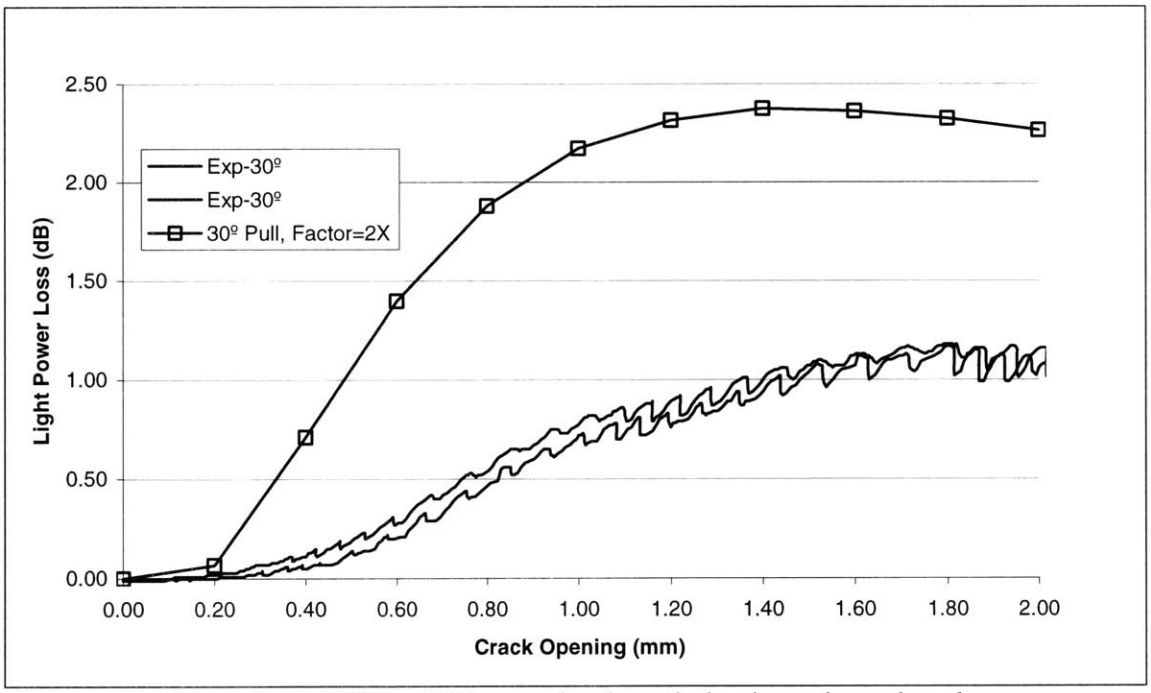

Figure 44: 3M-850nm at 30° comparing theoretical and experimental results

7. DESIGNING WITH THE THEORETICAL MODEL

The objective of the theoretical model is to help in the optical design of the crack sensor for specific applications. The model can take into consideration the geometric layout of the sensor, the mechanical properties of the sensor matrix, the mechanical properties of the optical fiber and the optical properties of the fiber. Each one of these properties can influence the performance of the sensor. The previous sections have discussed the selection of the analysis methodology, therefore using this methodology the following comparisons can be made. In review, the mechanical analysis is done with the "pull" displacement method using a linear 3D FEM analysis. Displacement values are then extracted from the FEM model and used to determine the radius profile from the section rotation. The modified bend formula proposed by Marcuse is then used to carry out the optical analysis. As shown above, to obtain the actual loss for the bent fiber, a correction factor should be applied and this factor is fiber dependent and could change from fiber to fiber. Practically speaking, in order to determine the correction factor, at least one set of test results for a given fiber needs to be obtained. In this section, the major purpose is to illustrate how the theoretical model can provide guidelines for sensor design. In order not to complicate the issue, the correction factor is not considered in the analysis. The theoretical results will then be higher than actual values, but the trend can still provide insight to the designer of sensors.

The notation in the legends of the graphs follows the same conventions used in the previous analysis with a couple of additional definitions that have been summarized in Table 4. Since the investigation here looks at varying optical properties it is important to keep them within reasonable bounds and to make sure that they describe a singlemode

optical fiber. It is well known that an optical fiber with a waveguide parameter V less than 2.41 is singlemode.

Table 4: Definitions for Comparisons

a	Core radius
λ	Wavelength of light
n_1	Core refractive index
n_2	Cladding refractive index
k	$\frac{2\pi}{\lambda}$
V	$ka\sqrt{n_1^2 - n_2^2}$
NA	$\sqrt{n_1^2 - n_2^2}$
θ	Fiber angle inclination in crack sensor
$3M$	The radius profile from the 3M fiber was used and λ is 850nm
SMF	The radius profile from the Corning fiber was used and λ is 1550nm

The first comparison in Figure 45 looks at the influence of the core radius on optical power loss using the 3M optical fiber coatings with λ=850nm. The trend is that as the core radius increases the optical power loss decreases. Thinking about this with simple ray tracing methods it makes sense. If the only loss mechanism is assumed to be at the core/cladding interface, then the more often that a light ray comes in contact with the interface the more chance for loss. Comparing two fibers, one with a radius larger than the other but with the same numerical aperture, the large radius core will have less contact with the core/cladding interface than the small radius core in order to travel the same distance. Therefore, there would be less loss of optical light.

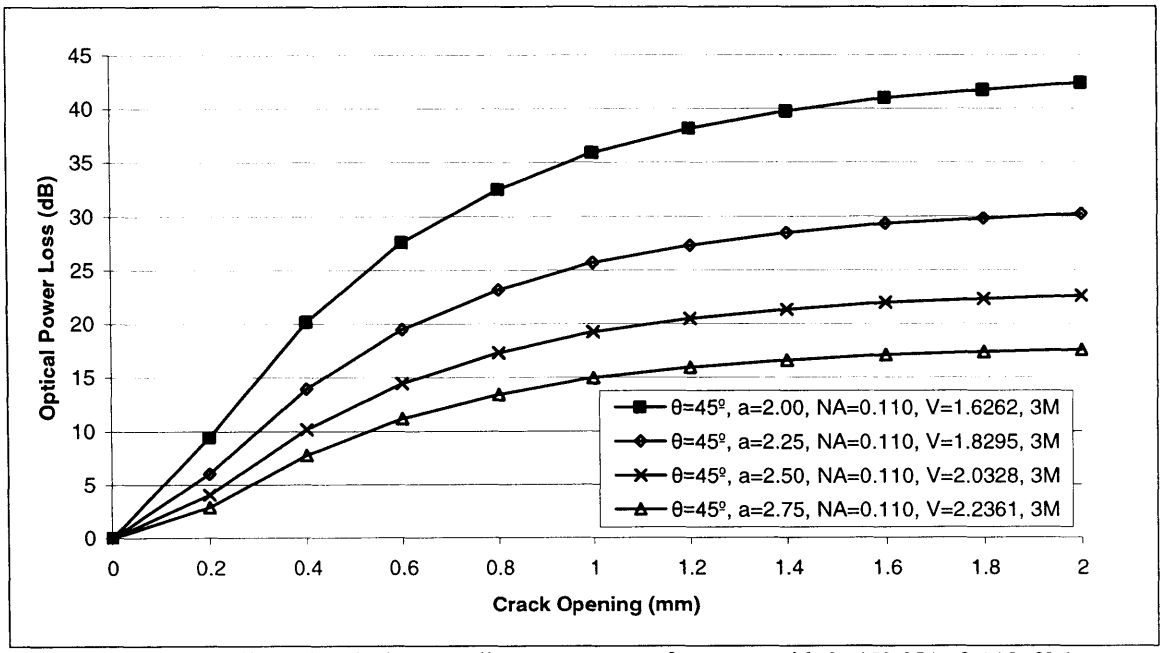

Figure 45: Effect of optical core radius on sensor performance with θ=45°, NA=0.110, 3M

The next comparison in Figure 46 shows the effect of the numerical aperture on the loss of optical signal. As the numerical aperture increases so does the loss of optical light. Once again looking at simple ray tracing methods to understand the loss the trend seems reasonable. Using Snell's Law it is possible to define which rays will be bound rays, those that have no signal loss, and which will be refracting or tunneling rays, those which loose some light. The definitions are shown in Table 5 along with the formula for calculating the complement of the critical angle, θ_c. The definitions for refracting and tunneling rays will be discussed later. It will be noticed that as the numerical aperture increases so does θ_c which means that a greater number of the rays are bound rays. Hence, more of the rays have total internal reflection and do not loose any light than do optical fibers with a lower *NA*.

Table 5: Classification of Rays

Bound Rays	$0 \leq \theta_z < \theta_c$
Ray angle being examined	θ_z
Complement of the critical angle	$\theta_c = \cos^{-1}\left(\frac{n_1}{n_2}\right)$

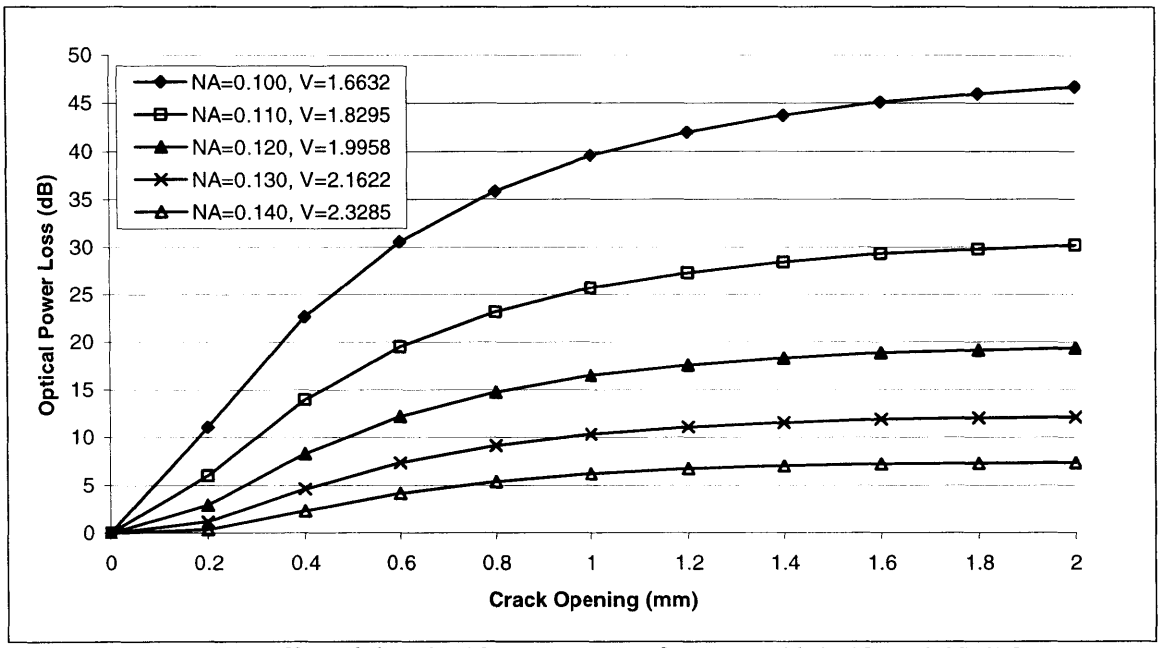

Figure 46: Effect of changing NA on sensor performance with θ=45°, a=2.25, 3M

The angle of inclination has a definite influence on the signal loss as shown in Figure 47. The higher the angle the higher is the loss. The reason for this behavior is that when the sensor angle of inclination is higher as the crack opens the fiber bridging the crack opening needs to bend more to be continuous across the crack. The sharper bends that are necessary lead to a higher optical power loss.

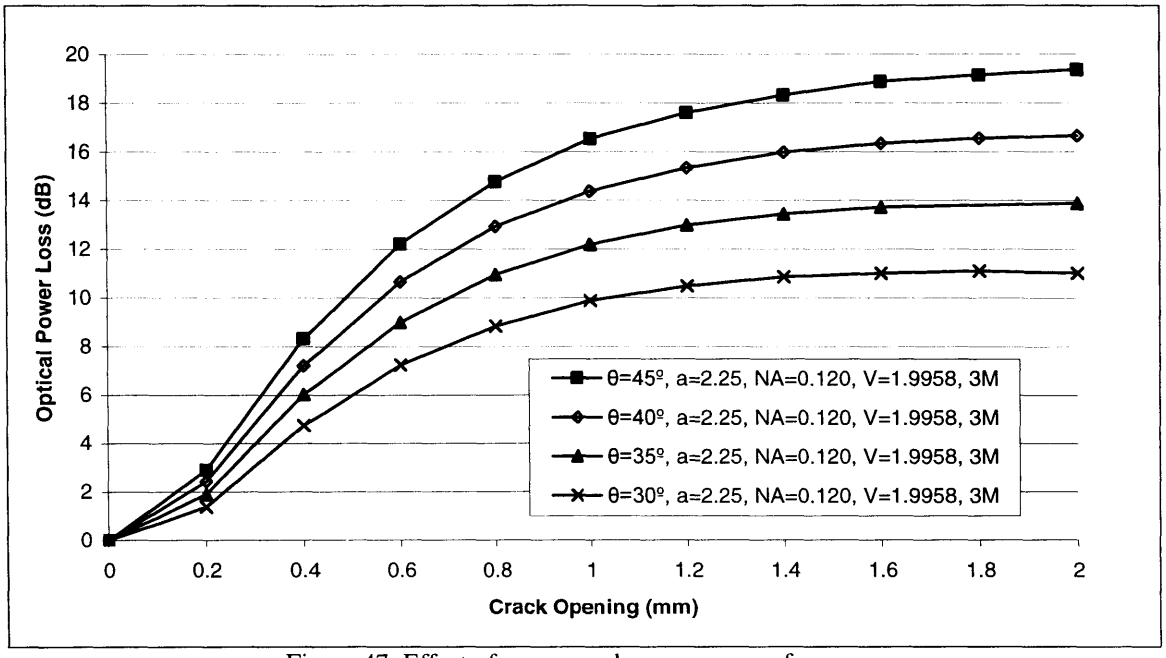

Figure 47: Effect of sensor angle on sensor performance

As the previous charts show, changing the core radius, numerical aperture and the inclination of the optical fiber change the behavior of the crack sensor. When designing the crack sensor, these different parameters could be used to manipulate the sensor performance. For example, in some cases it may be desirous to measure small cracks that are less than 1mm in opening while any increase beyond 1mm may not be as important to measure. The reason for this may be that if the crack forms any larger than 1mm it needs to be repaired regardless of how large it becomes and therefore measuring the crack size accurately over 1mm may be a waste of limited optical signal. In this situation, it would be important to have the sensor detect small crack sizes quickly and then reach an asymptotic value soon after 1mm. Figure 48 illustrates such a scenario. The top curve that is at a 45° angle continues to lose light even after 1mm crack opening, however there are two different curves shown that present an attractive alternative. The second highest curve which is at a 30° incline with a=2.25μm has almost the same optical loss at 0.2mm crack opening but at 2.0mm crack opening the loss is much less than the 45° curve. The

final curve with θ=30° and a=2.00μm has a slightly less optical loss at 0.2mm crack opening while the loss at 2.0mm is much less with a 2dB savings when compared to the 45° curve. A savings of more than 2dB signal loss adds up quickly when many curves are being measured.

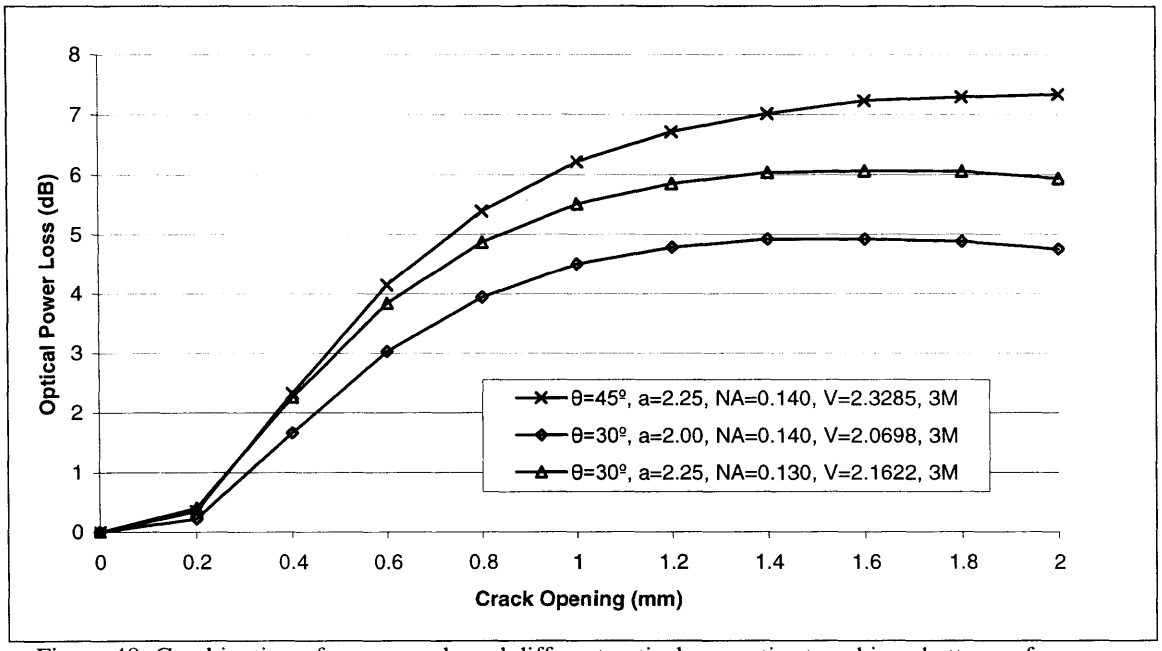

Figure 48: Combination of sensor angle and different optical properties to achieve better performance.

The previous example accomplished the desired output by manipulating the optical parameters and the fiber angle. Another available approach is to change the optical fiber which then changes the optical parameters as well as the coating parameters. Figure 49 shows how a similar thing can be accomplished without changing the angle of incline and just changing the optical fiber parameters or the optical fiber. In this case the three curves that are shown all have very similar loss characteristics at 0.2mm opening however at 2.0mm crack opening the loss difference between the top one (a=2.00μm, 3M) and the two lower ones (a=2.50μm, 3M and a=3.50μm, SMF28) is about 2dB.

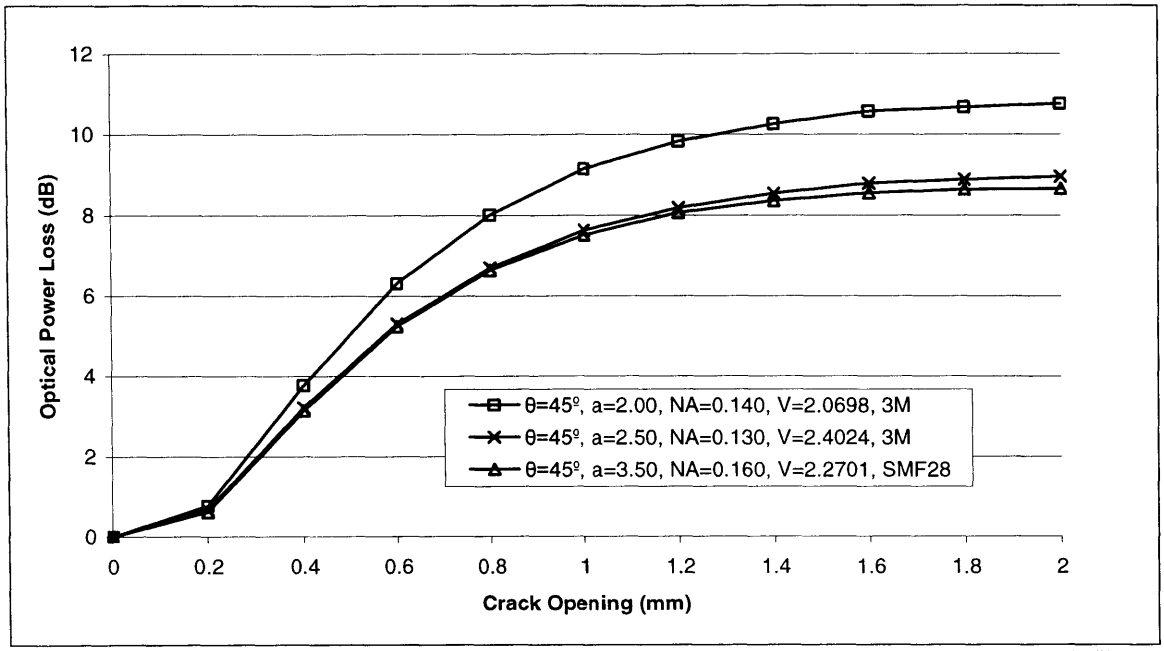

Figure 49: Different optical fibers with same angle of inclination give different performance. Both fibers start out with almost the same loss in the beginning however the amount of loss at large crack openings is different.

8. MULTIMODE OPTICAL ANALYSIS

Up until this point the discussion has been about single-mode fibers. However, multimode fibers can also be used in the crack sensor. Since multimode optical fibers can carry much more light than single-mode fibers, the number of distributed cracks along a fiber that could be measured can be increased. A description of the theoretical analysis used in analyzing the crack sensor using multi-mode fibers follows. The approach described previously for the singlemode optical fiber analysis is followed here. In other words, the mechanical model is needed to create the radius profile which is then analyzed with an optical analysis. The exact same mechanical model as described earlier is used here since the optical fibers that are used have very similar geometric and mechanical properties. Any change in mechanical or geometric properties could be properly addressed with the proposed mechanical model. However, the optical analysis

for the multimode fiber has to be different than the singlemode analysis and therefore it will be addressed here.

The objective for the multimode analysis is the same as for the singlemode analysis which is to provide a good design tool for crack sensors. To fulfill this mission it should be relatively fast and fairly accurate. The model that has been chosen for the multimode analysis is a geometric optics model put forth by Snyder and Love.[19] There are more complicated models that could be used however they would be very computationally expensive and the improved accuracy would not be worth the extra resources. It is expected that the final design would need to be calibrated with experiments. This analysis is to be an aid to the designer.

8.1 Analysis background

Classical geometric optics can describe light propagation in an optical fiber fairly well if the refractive index does not vary much over a distance comparable to the wavelength of light. The analysis in this section approximates the loss by assuming that the fiber is a step-index slab. In this model there are three classes of light rays, bound rays, refracting rays and tunneling rays. Bound rays do not loose light and are totally reflected at each reflection. On the other hand, refracting and tunneling rays loose light at each reflection. By using Snell's Law it is possible to find the critical angles which classify the different types of rays. When a waveguide is bent there are no bound rays which means that each light ray loses some energy at each reflection point either through refraction or tunneling. The power loss through a bend can be calculated by using geometric optics to determine the path of the leaky ray and then apply the appropriate power transmission coefficient.

To understand the reason for refracting and tunneling rays one can look at a step-profile planar waveguide. In this configuration there are just bound and refracting rays as shown in Figure 50.

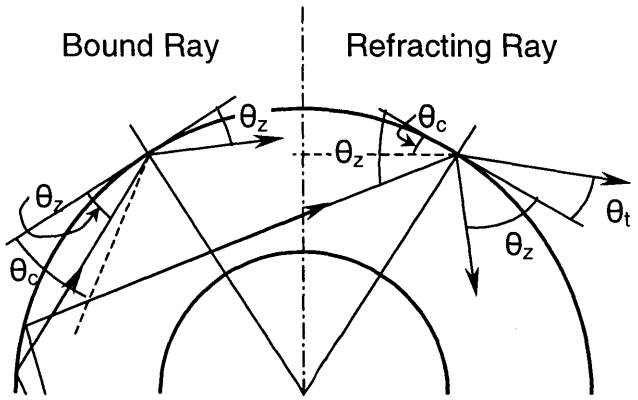

Figure 50: Examples of Bound Rays and Refraction Rays in a planar waveguide.

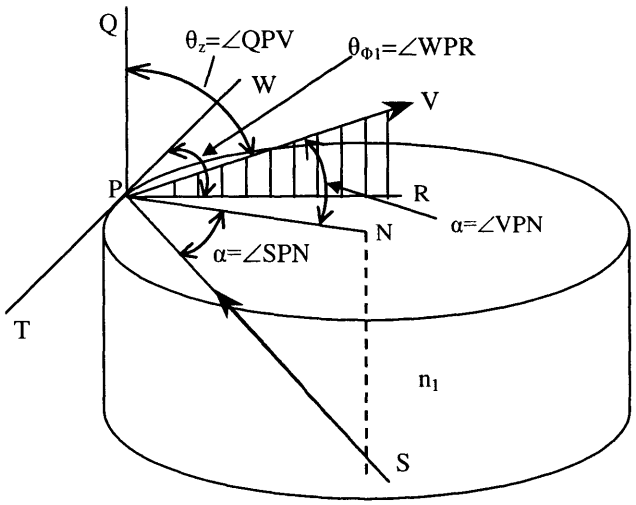

Figure 51: Explanation for angles in describing refracting and tunneling rays in a step-index slab.[19]

A step-index slab is modeling a circular fiber in three dimensions in which an additional ray path is possible when compared to a planar waveguide that is only modeled in two dimensions. In a circular fiber there are rays which cross the fiber axis between reflections that are called meridional rays, and there are rays which do not cross the fiber axis between reflections that are called skew rays. In order to know the direction of the skew ray it is necessary to introduce another angle, α defined in Figure 51. It is then

possible to classify which rays are bound rays and which are refracting and tunneling rays as shown in Table 6.

Table 6: Classification of Rays for Step-index Slab

Bound Rays	$0 \le \theta_z < \theta_c$
Refracting Rays	$0 \le \alpha < \alpha_c$
Tunneling Rays	$\theta_c \le \theta_z \le \pi/2$ and $\alpha_c \le \alpha \le \pi/2$
Ray angle being examined	θ_z
Complement of the critical angle	$\theta_c = \cos^{-1}\left(\frac{n_1}{n_2}\right)$ $\alpha_c = \sin^{-1}\left(\frac{n_1}{n_2}\right)$

With this background information it is now possible to look at the multimode analysis for a bent step-index slab.

8.2 Bending loss with constant curvature radius

The analysis makes the following assumptions making reference to Figure 52. The fiber is modeled as a step-profile slab and has a large V (V>50). Furthermore, before the fiber bend of fixed radius R there is a long straight section of length d. Diffuse source S (Figure 52) illuminates the slab waveguide at z=0 and excites all bound and refracting rays. The length of straight section d is assumed to be sufficiently long so that the light power is stable and all higher order leaky rays have been lost. Once the fiber bend is reached, it is only necessary to consider bound rays from the straight slab waveguide. Once in the bend all the rays are leaky rays (refracting and tunneling) and there are no bound rays.[19, 26] Thus, every ray path in a bent guide necessarily loses some power when it is reflected either from the core-cladding interface or from the outer caustic. Such loss

can be expressed in terms of a power transmission coefficient T, also known as a *loss coefficient*, defined as:

$$T = 1\text{-(power in the reflected ray)/ (power in the incident ray)} \qquad (18)$$

In other words, a fraction T of ray power is transmitted across the interface or outer caustic.

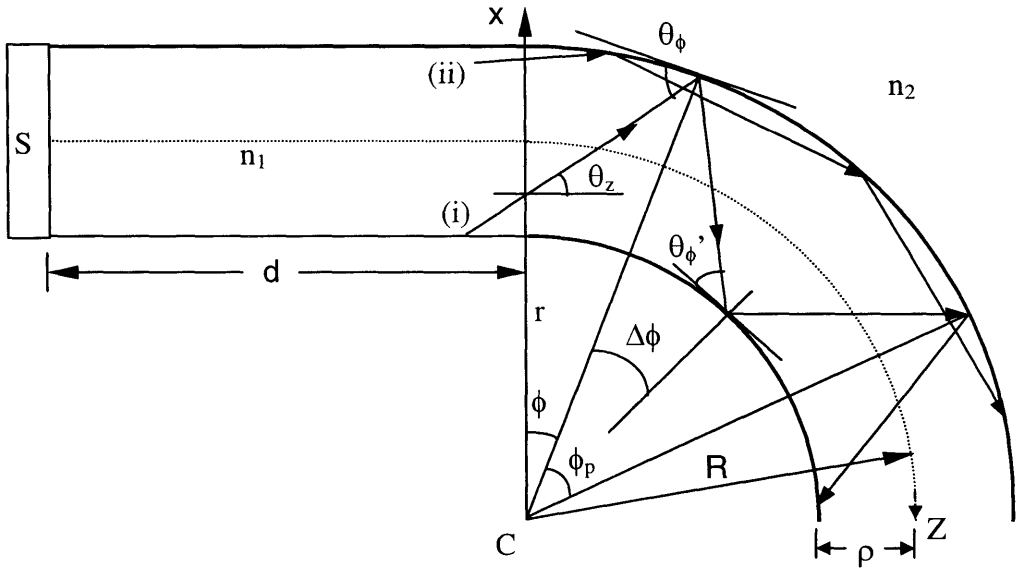

Figure 52: Ray paths on a bent step-profile planar slab waveguide.

To describe the attenuation from the bend, the *power attenuation coefficient* of a ray is defined as:

$$\gamma(\phi) = \frac{\sum_{i=1}^{N} T_i}{\sum_{i=1}^{N} \Delta\phi_i} = \frac{T}{\phi_p} \qquad (19)$$

with T_i being the fraction of ray incident power lost by reflection, $\Delta\phi_i$ is the angular separation between successive reflections, N is the total number of reflections, and T is

the average ray power attenuation coefficient over the angular separation ϕ_p (see Figure 52). Therefore, $\gamma(\phi)$ is the rate of power loss per unit angle which for a circular bend is constant. The power remaining after one reflection in the length of fiber under consideration can be expressed in terms of the initial power of the light ray $P(0)$ as

$$P(\phi) = P(0)(1-\gamma\phi) \tag{20}$$

Now for N reflections in a section of fiber, the remaining power could be described in the following manner

$$P(\phi) = P(0)\left(1-\frac{\gamma\phi}{N}\right)^N = P(0)\exp(-\gamma\phi) \tag{21}$$

Since $(1-\gamma\phi/N)^N$ quickly converges to (exp(-$\gamma\phi$)) it is expressed in the latter form.

The total ray power $P_s(\phi)$ at angle ϕ around the bend is found by adding together the power loss for all of the light rays over the entire core cross-section. Integrating Equation (21) does this.

$$P_s(\phi) = P(0)\int_{R-\rho}^{R+\rho}\int_{-\theta_c}^{\theta_c}\exp(-\gamma(r,\theta_z,R)\phi)d\theta_z dr \tag{22}$$

where θ_c is the complement of the critical angle and θ_z is the angle between the path and the axial direction at radius r at the beginning cross-section of the bend. In the straight fiber, the range of values of θ_z for bound rays is $0\leq\theta_z\leq\theta_c$. Since the ray power attenuation coefficient γ varies with r, θ_z and R it is expressed as a function of these parameters. In the bent slab waveguide with fixed radius R, every ray with different r and θ_z has

different complement of incident angle θ_ϕ at the outer interface and θ_ϕ' at the inner interface, which results in a different loss coefficient T and different power attenuation coefficient γ. The geometric relationship between r, θ_z and θ_ϕ, θ_ϕ' is:

$$r\cos\theta_z = (R+\rho)\cos\theta_\phi = (R-\rho)\cos\theta_\phi' \qquad (23)$$

If $\frac{\pi}{2} > \theta_\phi$ (or θ_ϕ')$> \theta_c$, the ray refracts at the interface, and the equation for the loss calculation coefficient T is:

$$T = \frac{4\sin\theta_\phi(\sin^2\theta_\phi - \sin^2\theta_c)^{\frac{1}{2}}}{\left\{\sin\theta_\phi + (\sin^2\theta_\phi - \sin^2\theta_c)^{\frac{1}{2}}\right\}^2} \qquad (24)$$

If $0<\theta_\phi<\theta_c$, the light ray tunnels, and the corresponding T is given as:[26, 27]

$$T = \frac{4\sin\theta_\phi}{\sin\theta_c}\left[1-\left(\frac{\sin\theta_\phi}{\sin\theta_c}\right)^2\right]^{\frac{1}{2}} \exp\left[-\frac{2}{3}\frac{n_{co}k(R+\rho)}{\cos^2\theta_\phi}(\sin^2\theta_c - \sin^2\theta_\phi)^{\frac{3}{2}}\right] \qquad (25)$$

However, T is always simplified as:

$$T = \frac{4\sin\theta_\phi}{\sin\theta_c}\left[1-\left(\frac{\sin\theta_\phi}{\sin\theta_c}\right)^2\right]^{\frac{1}{2}} \exp\left[-\frac{2}{3}n_{co}k(R+\rho)(\theta_c{}^2 - \theta^2{}_\phi)^{\frac{3}{2}}\right] \qquad (26)$$

On a bent step-profile slab, the ray path follows straight lines between reflections from inner and outer interfaces, as shown in Figure 52. Path (i) reflects alternately from the inner and outer interfaces, and path (ii) reflects only from the outer interface and is

known as a *whispering-gallery ray.* From Equation (23), if rays satisfy $\cos\theta_\phi > (R-\rho)/(R+\rho)$, θ_ϕ' does not exist and the ray cannot reach the inner interface, it is a *whispering-gallery ray.*

For calculating the ray power attenuation coefficient γ, we use Equation (19). The angular separation ϕ_p for the paths (i) and (ii) in Figure 52 is given according to geometry:

For path (i): $$\phi_p = 2(\theta_\phi - \theta_\phi') \quad (27)$$

For path (ii): $$\phi_p = 2\theta_\phi \quad (28)$$

Up to now, the total ray power $P_s(\phi)$ through the bend can be calculated by Equation (22) as long as the angular displacement ϕ is known.

8.3 Bending losses with arbitrarily curved multimode optical fiber

The analysis thus far has been concerned only with a constant curvature bend. The crack sensor does not have a constant curvature hence it is necessary to adjust the model to work for the sensor analysis. The *S* bend shape of the fiber resulting from the crack is shown diagrammatically in Figure 53. The bend radius of curvature is not constant, but the radius profile for the entire crack opening can be obtained from the mechanical analysis described in detail in preceding sections. Figure 53 shows the bent fiber divided into *M* sections. At any section *m*, the angle displacement ϕ_m and the curvature radius R_m are calculated by the mechanical analysis. If the initial angle θ_{zm} of the ray and the initial radius r_m where the ray accesses section *m* can be determined, then the ray power attenuation coefficient $\gamma_m(r_m, \theta_{zm}, R_m)$ can be found according to the prior discussion.

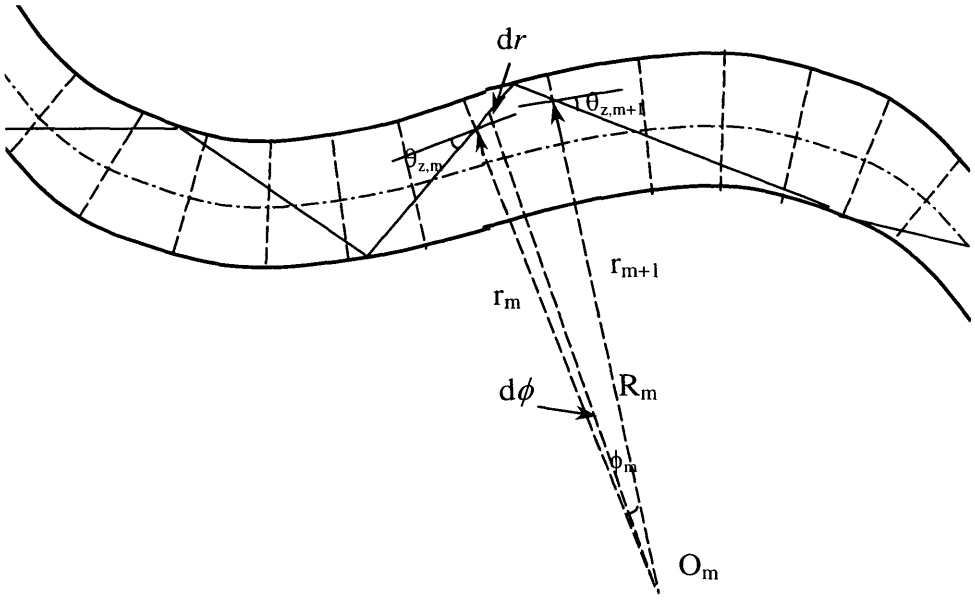

Figure 53: Bent slab waveguide with arbitrary curvature radius

The total loss of the rays going through this bent slab waveguide is given as:

$$\frac{P_{out}}{P_{in}} = \frac{\int_{R-\rho}^{R+\rho} \int_{-\theta_c}^{\theta_c} \exp(-\sum_{m=1}^{M} \gamma(r_m, \theta_{zm}, R_m)\phi_m) d\theta_z dr}{\int_{R-\rho}^{R+\rho} dr \int_{-\theta}^{\theta_c} d\theta_z} \qquad (29)$$

where P_{out} is the output light power from the bent slab waveguide and P_{in} is the input power.

To numerically calculate Equation (29), the integration operation is replaced by a summation operation. At the beginning of the bent slab waveguide, if we divide the diameter of the fiber 2ρ into I sections and $2\theta_c$ into J sections, the input light is divided into IxJ rays. The radius location r_1 for each rays is $R-\rho$, $R-\rho+\frac{2\rho}{I}$,

$R-\rho+\frac{2\rho}{I}x2,\ldots,R+\rho-\frac{2\rho}{I}$. The initial angle θ_{z1} for each rays is $-\theta_c$, $-\theta_c+\frac{2\theta_c}{J}$, $-\theta_c+\frac{2\theta_c}{J}x2,\ldots,\theta_c-\frac{2\theta_c}{J}$ as is shown in Figure 54.

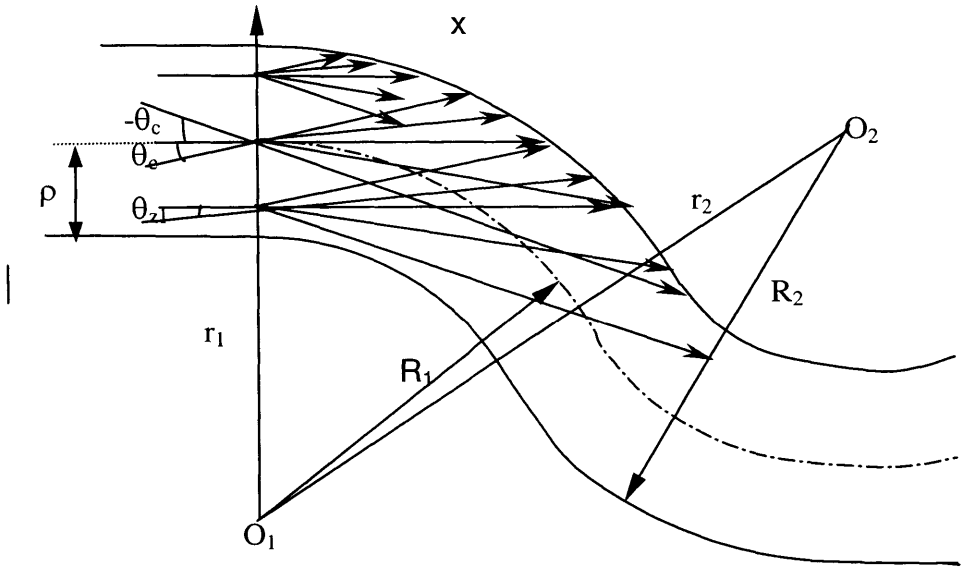

Figure 54: Input light is divided into I×J rays

Then the power loss for one section of the bent slab is:

$$\frac{P(\phi_1)}{P_{in}}=\frac{\sum_1^I\sum_1^J \exp(-\gamma(r_1,\theta_{z1},R_1)\phi_1)D\theta_z Dr}{\sum_1^I\sum_1^J D\theta_z Dr} \qquad (30)$$

The equation for the total loss of the bent slab (Equation (29)) becomes:

$$\frac{P_{out}}{P_{in}}=\frac{\sum_1^I\sum_1^J \exp(-\sum_{m=1}^M\gamma(r_m,\theta_{zm},R_m)\phi_m)D\theta_z Dr}{\sum_1^I\sum_1^J D\theta_z Dr} \qquad (31)$$

where, $D\theta_z = \frac{2\theta_c}{J}$, and $Dr = \frac{2\rho}{I}$, providing that r and θ_z at each section of the bend are known.

Now the only remaining problem to be solved is how to determine the initial angle of the ray with the axis θ_z and the initial radius r at each section.

Referring to Figure 53, in section *m*, we can get r_{m+1} and $\theta_{z,m+1}$ in terms of r_m, $\theta_{z,m}$ and ϕ_m by the equation:

$$d\phi = \frac{dr}{r\tan(\theta_z)} \qquad (32)$$

where $d\phi$ is the change of angle coordinate and dr is the change of radius. So θ_z and r at every section can be acquired since the initial condition r_1 and θ_{z1} have already been determined.

8.4 Experimentation

The experimentation for this section is carried out using the specially designed loading stage with *Epoxy Blocks* that can provide well-controlled bending to the fiber.

It is important to discuss the influence of the light source on the experimental results. The above analysis assumes that the light source equally excites all modes in an optical fiber. If this condition is not satisfied, the experimental results will not match the theoretical analysis.

The light source used in this experiment is an LED. There are two kinds of LEDs in common use. One is a surface launching LED where light comes from the surface of the

PN junction as shown in Figure 55(a), another is the edge launching LED where light comes from the edge of the PN junction shown is Figure 55(b). The surface launching LED has a much broader launch angle α and β than the edge lunching LED. For example, α is always larger than one hundred degrees (e.g. 120°) for a surface launching LED, and only several tens of degrees (e.g. 50°) for an edge launching LED. The β is always several tens of degrees for a surface launching LED and is smaller (e.g. 15°) for an edge launching LED.

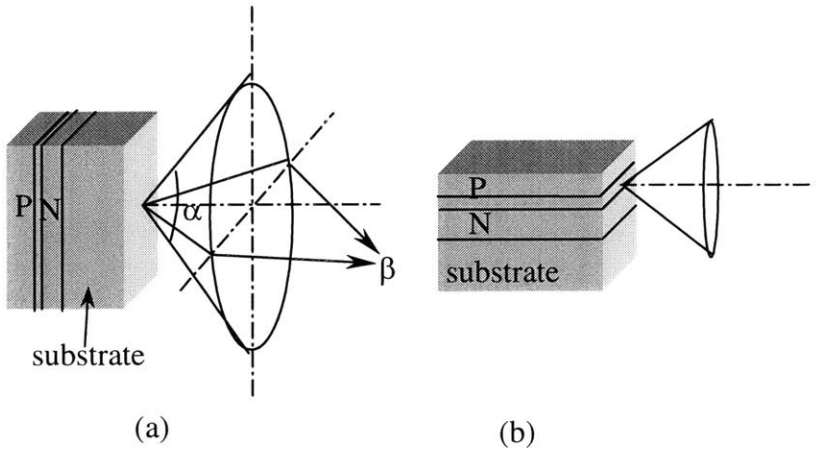

Figure 55: LED with different launching plane.

When the LED is used to excite modes in a multimode fiber, the source size, the launch angle and the distance between source and fiber will influence the power distribution of the modes.

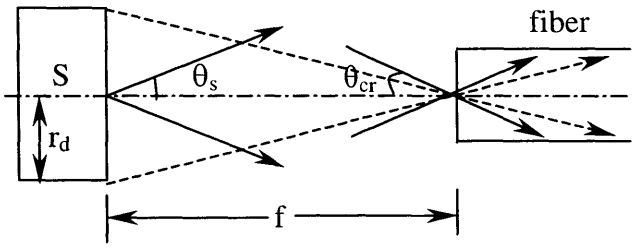

Figure 56: Fiber excited condition.

Referring to Figure 56, if the launch angle of the LED is smaller than the critical angle of the fiber, or the distance f between the source and the end-face of the fiber is large in comparison with the source size r_d and the fiber core, less higher modes will be excited and the lower modes will be abundant. In the present experimentation, it is desirable that all bound modes be excited equally. Therefore it is necessary to choose an LED with a launch angle θ_s larger than the critical angle θ_{cr} and to put the optical fiber close to the source.

The multimode fiber that was used first, was a 3M multimode fiber (FG-050-GLA) with NA=0.3513, n_1=1.49, and n_2=1.448. The critical angle θ_{cr} is 20.57°. The light source is an LED at 850nm purchased from mainland China (referred to here as Number 44 Institute or simply LED850). This LED has been fixed with a fiber connector adapter (FC/PC), so the light can be coupled to the testing fiber easily. As a fiber source, to insure high coupling efficiency, this LED must be an edge launching LED and consequently has a relatively small launch angle θ_s. The size of the launch angle is not known. However, if it is smaller than θ_{cr}, the higher modes in the fiber cannot be excited and the testing results of the bend loss must be lower than the theoretical analysis (see Figure 57 for the experimental data, and Figure 58 for the simulated resutls).

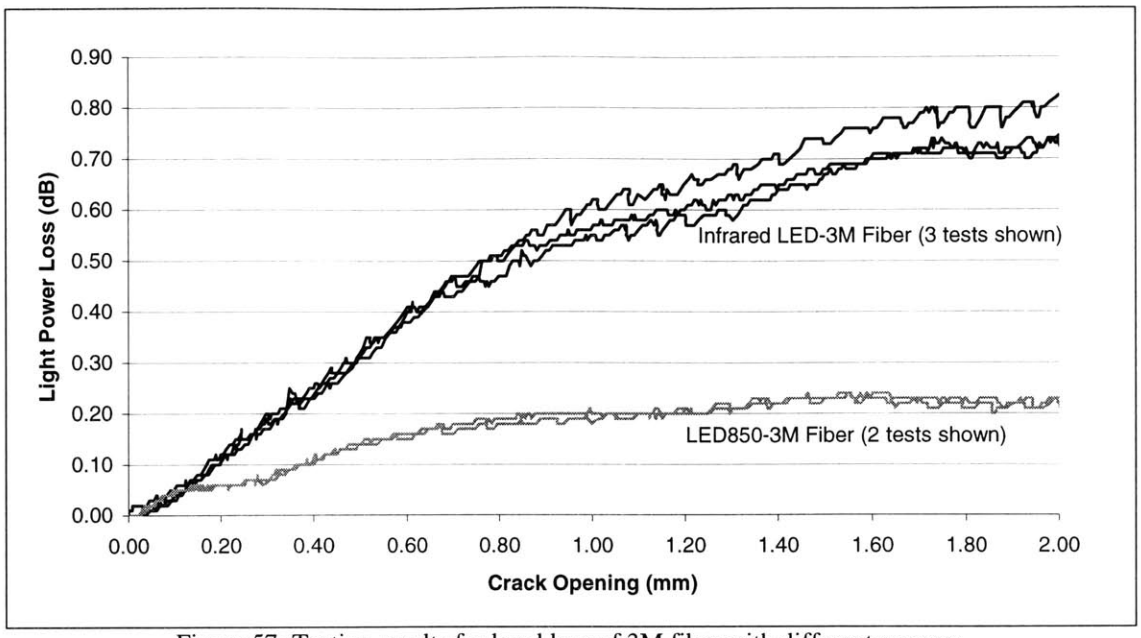

Figure 57: Testing results for bend loss of 3M fiber with different sources.

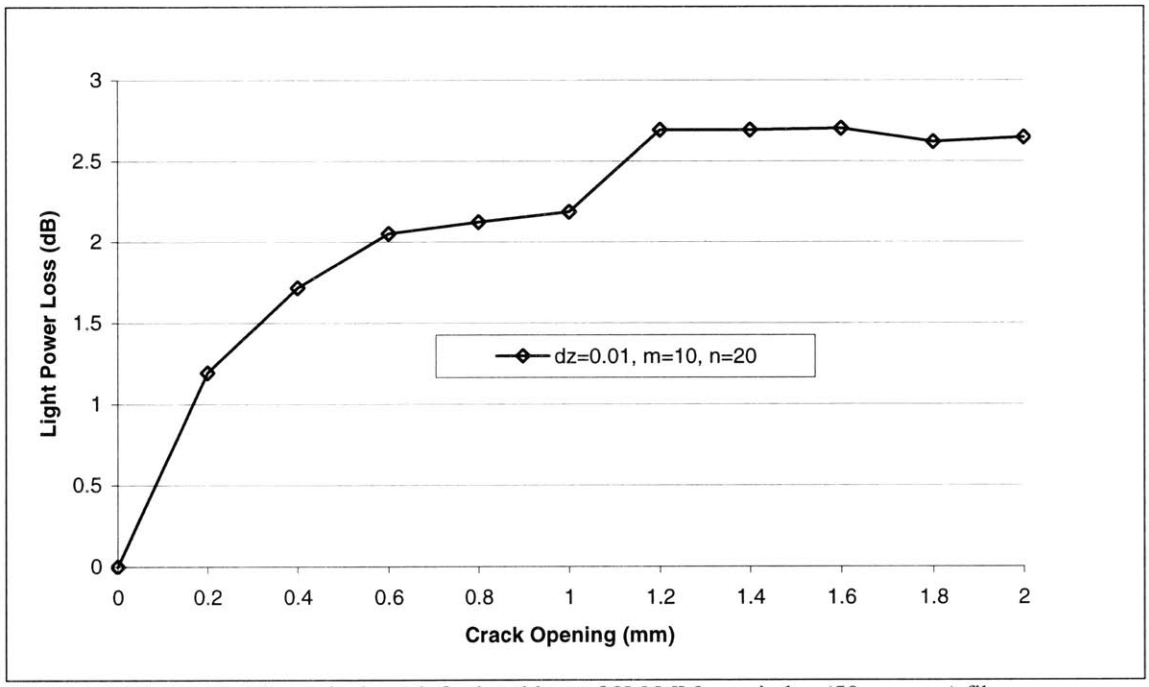

Figure 58: Theoretical result for bend loss of 3M MM step index (50μm core) fiber.

A surface launching cheap LED (named 'Infrared LED' in Figure 57) was used in place of the previous source from Number 44 Institute (LED850). The result is that the bend loss becomes higher in Figure 57. Because it is difficult to put the fiber very close to the cheap surface launching LED ('Infrared LED'), it is difficult to say if all the high bound

modes in the fiber are excited. Hence, there is still a large difference between testing and theoretical results.

Another type of multimode fiber with a lower *NA* (0.22) was also used for the tests (purchased from Beijing Glass Research Institute). The critical angle θ_{cr} of this fiber is 12.7°. When this fiber was tested with both of the light sources, there was little difference between the results (Figure 59). That means that both light sources can excite all of the modes in this fiber. The bend loss is a little higher with the surface launching cheap LED ('Infrared LED') as the source because some higher modes that exceed the bound rays remain in the fiber and go through the bent section and are lost.

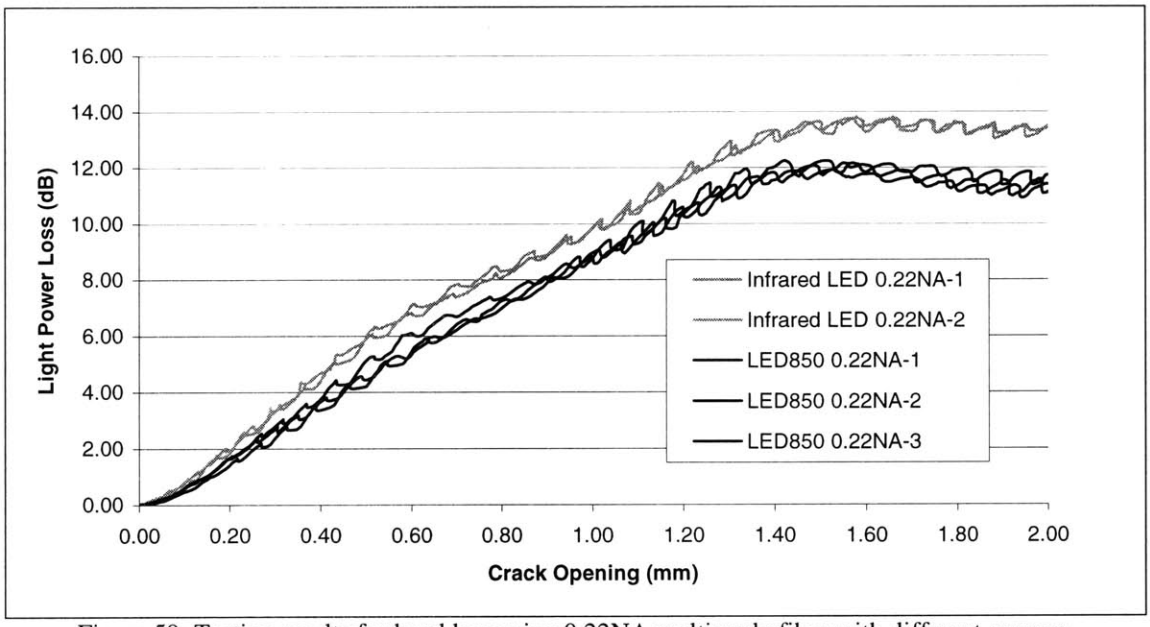

Figure 59: Testing results for bend loss using 0.22NA multimode fiber with different sources.

The manufacturer of the 0.22*NA* fiber did not provide information about the plastic coating materials on the optical fiber. However, since Acrylate is a common coating material, it would be a reasonable assumption that it is similar to the 3M optical fiber

mechanical properties. If this assumption is made and the optical analysis is run the theoretical prediction is very close to the testing results (Figure 60)

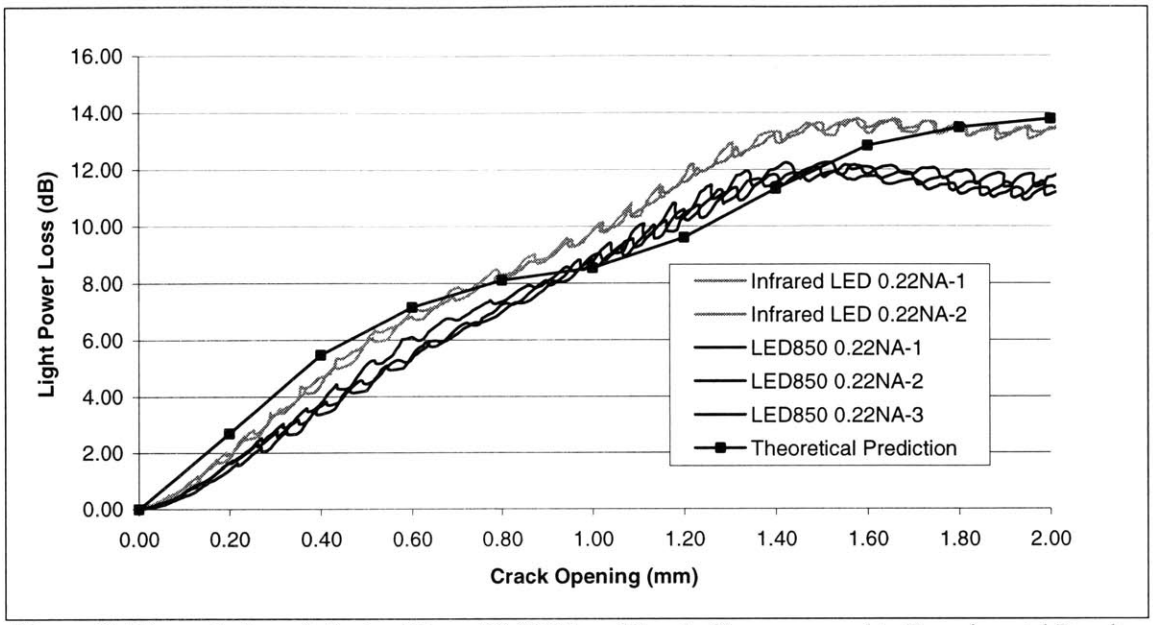

Figure 60: Theoretical result for bend loss of 0.22NA multimode fiber compared to Experimental Results.

The multimode analysis presented in this section is straightforward and computationally fast to run. The results that it predicts also seem reasonable, although more tests would be good. It therefore meets the objective that it serve as a guide tool to the crack sensor designer.

9. CONCLUSIONS

The novel distributed optical fiber crack sensor has the potential to be an important tool in monitoring the health of concrete structures thus aiding in improving their safety and durability. The sensor is able to detect cracks with no a-priori knowledge of crack locations (although crack direction needs to be known) using a small number of fibers to detect and monitor a large number of cracks. The sensor capability for detecting multiple cracks has been demonstrated in a concrete beam using an OTDR system.

The theoretical analysis presented for both the singlemode and multimode fibers provides a way for the engineer to design the crack sensor. Even though the prediction may not be perfect, it is sufficiently good in forecasting the signal loss. Albeit, actual calibration of the sensor would still need to be carried out before the sensor could be implemented.

10. REFERENCES

1. C. K. Y. Leung, N. Elvin, N. Olson, T. F. Morse, and Y. He, "A novel distributed optical crack sensor for concrete structures," *Engrg. Fract. Mech.* 65, pp. 133-148, 2000.
2. M. Sansalone and N. J. Carino, "Transient Impact Response of Plates Containing Flaws," *Journal of Research of the National Bureau of Standards* 92, No.6, pp. 369-381, 1987.
3. T. Cantor and C. Kneeter, "Radar as Applied to Evaluation of Bridge Decks," *Transportation Research Record,* No.853, TRB, Washington, D.C., pp. 27-32, 1982.
4. G. J. Weil, "Detecting the Defects," *Civil Engineering Magazine* 59, No. 9, pp. 74-77, 1989.
5. A. T. Moczko, A. Pszonka, and P. Stroeven, "Acoustic Emission as a useful technique for Reflecting Cracking Behavior of Concrete Composites," in *Non-Destructive Testing in Civil Engineering*, edited by G. Schickert and H. Wiggenhauser, pp. 805-812, 1995.
6. F. Ansari, "Theory and Applications of Integrated Fiber Optic Sensors in Structures," in *Intelligent Civil Engineering Materials and Structures*, edited by Ansari, Maji and Leung, pp. 2-28, 1997.
7. B. Culshaw, "Monitoring Systems and Civil Engineering – Some Possibilities for Fiber Optic Sensors," in *Fiber Optic Sensors for Construction Materials and Bridges*, edited by F. Ansari, pp. 29-43, 1998.
8. P. Rossi and F. LaMaou, "New Method for Detecting Cracks in Concrete using Fiber Optics," *Materials and Structures (RILEM)* 22, No.132, pp. 437-442, 1989.
9. D. Huston, P. Fuhr, P. Kajenski and D. Snyder, "Concrete Beam Testing with Optical Fiber Sensors," in *Nondestructive Testing of Concrete Elements and Structures*, edited by S. Sture and F. Ansari, pp. 60-69, 1992.
10. F. Ansari and R. K. Navalurkar, "Kinematics of Crack Formation in Cementitious Composites by Fiber Optics," *ASCE J. Eng. Mech.* 119, No.5, pp. 1048-1061, 1993.
11. K. F. Voss and K. H. Wanser, "Fiber Sensors for Monitoring Structural Strain and Cracks," *Proceedings, 2nd European Conference on Smart Materials and Structures*, pp. 144-147, 1994.
12. R. Wolff and H. Miesseler, "Monitoring of Prestressed Concrete Structures with Optical Fiber Sensors," *Proceedings, 1st European Conference on Smart Structures and Materials*, pp. 23-29, 1992.
13. X. Gu, Z. Chen, and F. Ansari, "Method and Theory for a Multi-Gauge Distributed Fiber Optic Crack Sensor," *Journal of Intelligent Material Systems and Structures* 10, pp. 266-273, 1999.
14. A. W. Brown, J. P. Smith, X. Bao, M. D. DeMerchant, and T. Bremner, "Brillouin Scattering Based Distributed Sensors for Structural Applications," *Journal of Intelligent Material Systems and Structures* 10, pp. 340-349, 1999.
15. A. Oka, et al. "Fiber Optic Distributed Sensor for Structural Monitoring," in *Smart Structures and Systems*, edited F.K. Chang, pp. 672-679, 1999.
16. M. D. Feit and J. A. Fleck Jr., "Light Propagation in Graded-Index Fibers," *Appl. Optics* 17, No. 24, pp. 3990-3998, 1978.
17. J. Yamauchi, M. Ikegaya and H. Nakano, "Analysis of bent step-index optical fibres by the beam propagation method," *IEE Proceedings-J* 139, No. 3, pp. 201-207, 1992.

18. A. Ghatak and K. Thyagarajan, *An introduction to fiber optics*, New York: Cambridge University Press, 1998.
19. A. Snyder and J.D. Love, "Optical Waveguide Theory," New York: Chapman & Hall Medical, 1983.
20. D. Marcuse, "Curvature loss formula for optical fibers," J. Opt. Soc. Am., Vol. 66, No. 3, 216-220, 1976.
21. D. Marcuse, "Field deformation and loss caused by curvature of optical fibers," J. Opt. Soc. Am., Vol. 66, No. 4, 311-320, 1976.
22. D. Marcuse, "Loss Analysis of Single-Mode Fiber Splices," Bell System Technical Journal, Vol. 56, No. 5, 703-718, 1977.
23. R. C. Gauthier and C. Ross, "Theoretical and experimental considerations for a single-mode fiber-optic bend-type sensor," Appl. Opt. Vol. 36, No. 25, 6264-6273, 1997.
24. K. Nagano, S. Kawakami, and S. Nishida, "Change of the refractive index in an optical fiber due to external forces," Appl. Opt. 17, 2080-2085, 1978.
25. I. Valiente and C. Vassallo, "New formalism for bending losses in coated single-mode optical fibers," Electron. Lett. 25, 1544-1545, 1989.
26. C. Winkler, J. D. Love, A. K. Ghatak, "Loss calculation in bent multimode optical waveguides", *Optical and Quantum Electronics,* 11(1979) pp 173-183
27. A. W. Snyder and John D. Love, "Reflection at a curved dielectric interface-electromagnetic tunneling", *IEEE* Transactions on Microwave Theory and Techniques, Vol. MTT-23, No. 1, January 1975.

Chapter 4

Optical Fiber Strain Sensors

1. INTRODUCTION

Civil engineers are constantly looking for ways to improve the durability and safety of structures. Regular inspection of a facility can help evaluate its performance in the real environment under the actual loads. Sensors can perform this inspection in a consistent manner providing valuable information about the "health" of the structure. Strain, defined as the change in length divided by the original length ($\Delta L/L$), can provide valuable information about the condition of a structure when it is measured in critical areas. Strain measurements can be modified to find the load, torque, pressure, vibration or other physical quantities of a structural element. However, one of the most useful quantities that strain can help measure is the stress. The measured strain (ε) combined with the modulus of elasticity (E) for the material being measured can be used to find the stress (σ) of the structural element by $\sigma=E\varepsilon$. Engineers can use the stress information to determine if a building is behaving in a safe manner.

The measurement of strain with the exception of photo-elastic measurement is by deformation of a sensor material over a short gage length or measurement base. The strain sensor measurement represents the average strain of the structure over the gage length (Figure 1). If the gage length is very short compared to the structure it can be seen as a point measurement of the strain. Whether the average strain of the sensor is representative of the total average strain of the structure depends on the loading

conditions and the geometry of the structural member and therefore requires engineering judgment when assessing the meaning of the reading.

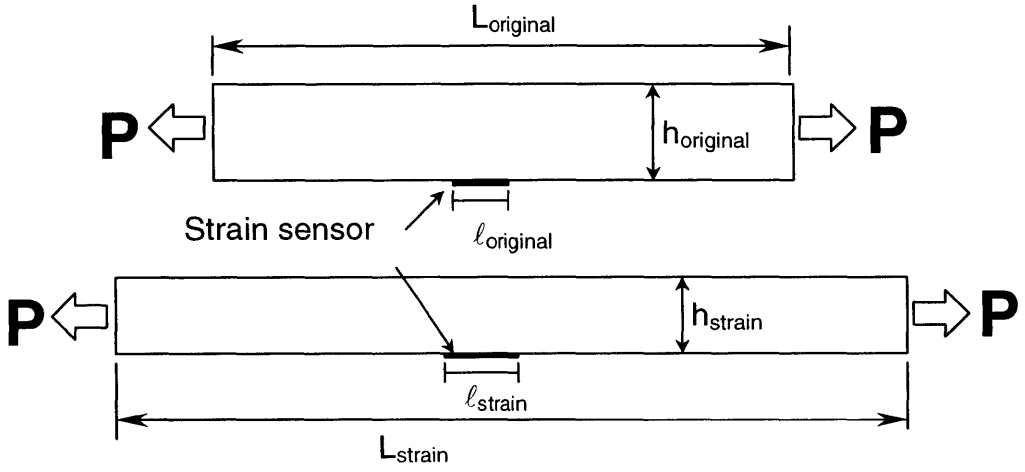

$$\varepsilon_{total\_average} = \frac{L_{strain} - L_{original}}{L_{original}} = \varepsilon_{total\_average} \qquad \varepsilon_{sensor\_average} = \frac{\ell_{strain} - \ell_{original}}{\ell_{original}}$$

$$\varepsilon_{transverse} = \frac{h_{strain} - h_{original}}{h_{original}} \qquad \nu = -\frac{\varepsilon_{transverse}}{\varepsilon_{longitudinal}}$$

Figure 1: Different definitions for strain

While traditional electrical sensors like resistive strain gages have proven to be effective in measuring some structural parameters, optical fiber sensors offer additional benefits that have been discussed in general in the introduction. More specifically, optical fiber strain sensors, such as interferometric strain sensors and Fiber Bragg Gratings, can have high resolution (less than one micro-strain) and are also easily adapted to distributed sensor configurations. These two common optical fiber strain-sensing techniques will be discussed briefly.

Interferometric strain sensors can be very sensitive at measuring strains. The operating principle of the sensor is shown in Figure 2. The strain in the sensing arm of an

interferometer induces a change in the phase of a lightwave propagating along a single-mode optical fiber.

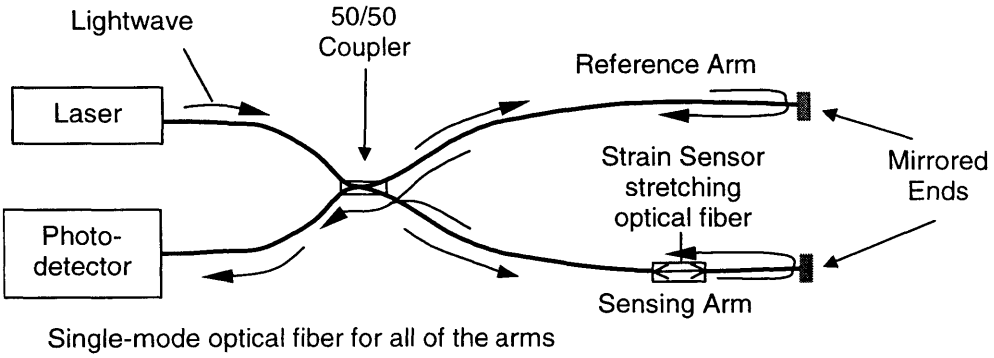

Figure 2: Schematic Illustration of a fiber optic strain sensor using a Michelson Interferometer

A 50/50 coupler divides the light from the highly coherent laser so that light travels down both the sensor arm and the reference arm of the interferometer as shown in Figure 2. The mirrors at the ends of the two arms reflect the light back towards the coupler where it is again divided and part is sent to the photo-detector. Once the light is split at the coupler it is in phase while traveling down the two arms of the interferometer. If there were no perturbation of either reference or sensing arm, the light would return and be in phase with each other. However, if the sensing arm were to be stretched (strained), the reflected light signal would return with a phase difference in relation to the reflected light of the reference arm. The phase difference, $\Delta\phi$, is directly proportional to the differences in optical paths shown by

$$\Delta\phi = 2kn_0\left(L_{sensor} - L_{reference}\right) \qquad (1)$$

where k is the free-space propagation constant, n_0 is the refractive index of the core of the optical fiber, L_{sensor} and $L_{reference}$ are the lengths of the interferometer arms. In this sensor configuration the gage length would be the entire length of the bonded fiber.

Another common strain sensing fiber optic sensor is the Fiber Bragg Grating (FBG). The FBG is a periodic variation in the index of refraction written into the core of an optical fiber. The first grating was made in 1978[1] by launching a very intense laser into an optical fiber. Today Fiber Bragg Gratings can be created using a two beam interferometer set-up or with an intense laser and a phase mask. Different gratings can be created which allows for different central wavelengths. The different grating wavelengths are useful when creating distributed sensing configurations.

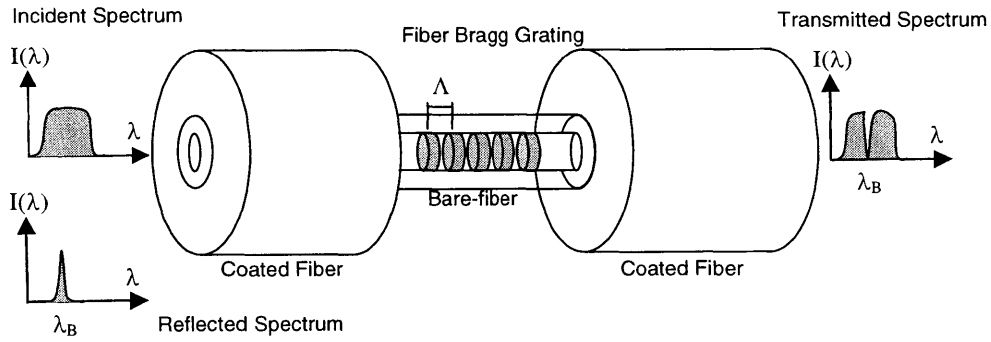

Figure 3: Schematic Drawing of Fiber Bragg Grating

When a broadband light source is sent into the FBG, the gratings scatter some of the light creating a narrowband reflection. The Bragg wavelength, λ_B, is the center wavelength of the reflected signal and is related to the grating period, Λ, and the mean core index of refraction n_0 by

$$\lambda_B = 2n_0\Lambda \qquad (2)$$

If the FBG is strained there is a linear shift in the Bragg wavelength. The shift in the Bragg wavelength can be correlated to the corresponding strain with very high accuracy if a good demodulation scheme is utilized. There are different ways of evaluating the wavelength shift as well as different ways that FBGs can be set-up in distributed strain

measuring systems. R. M. Measures[2] and K.O. Hill et. al.[3] provide good background on the subject. Additionally, there are commercially available systems that can be purchased to calculate the strain directly from one or more FBGs. The gage length for the FBG is the bonded length of the grating not the entire bonded length of the optical fiber.

Some optical sensors are embedded directly into concrete while others are attached to the structural body with adhesives. How well these sensors perform depends on different factors. Leung and Darmawangsa[4] have studied the effect of environmental conditions such as wet curing, wetting/drying and freezing/thawing on jacketed optical fibers in a cementitious environment. A more specific effect on sensor performance has been examined in Leung, Wang and Olson[5]. These studies were for optical fibers with a protective jacket. When optical fibers with no jacket are embedded into materials they can be easily damaged since bare-fiber is very fragile. Generally the optical fiber is coated with a protective plastic jacket to make it much less fragile. It is much more practical to use these jacketed fibers in sensors since they are less prone to damage.

Regardless of how the sensor is attached to or embedded in a structure, in order for the sensor to work a stress transfer needs to occur. The optical fiber undergoes a change which can then be correlated to a strain measurement[6]. Figure 4 graphically illustrates that there is a shear lag in transferring the strain from the measured body into the optical fiber sensor. This means that the strain in the fiber may not be the same as in the monitored structure. Since only a portion of the strain is transferred it is convenient to express this as a *calibration factor* that is defined as

$$Calibration\ Factor = \frac{Average\ Fiber\ Strain}{Applied\ Strain} \qquad (3)$$

Ansari and Yuan[7] have looked at the issue of strain transfer in fiber sensors and have made some important observations about the mechanics involved. This chapter further investigates this matter by (i) using a three-dimensional finite element model (3D FEM) to study the transfer, (ii) investigating the limitations of a simple analytical model to describe the shear transfer, and (iii) looking more closely at the influence of the mechanical strain on the optical fiber by using the photo-elastic strain-optic coefficients. Experimental results will also be shown to validate the mechanical model.

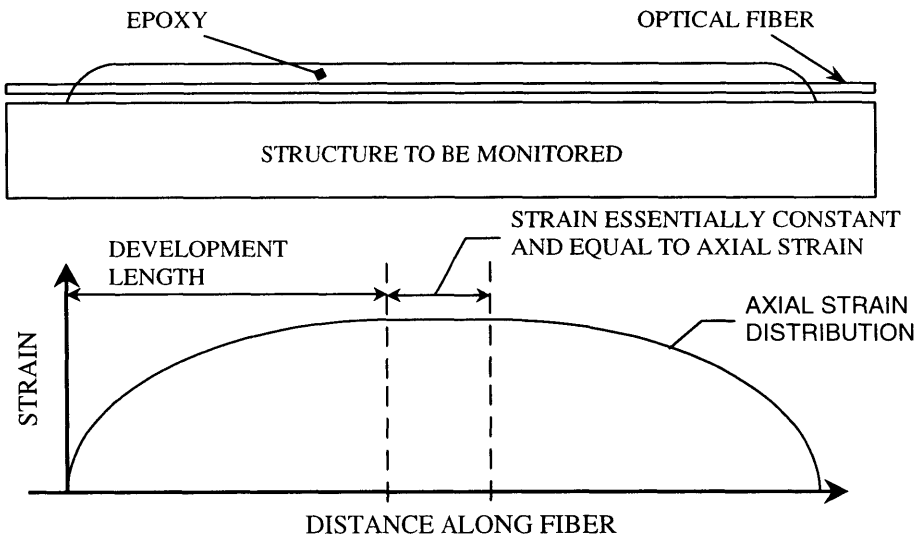

Figure 4: General Principal of the Strain Sensor with Shear Lag

2. MECHANICAL ANALYSIS

2.1 Three-dimensional finite element analysis

The 3D FEM investigation was a first step to understanding the strain transfer in the sensor. Figure 5-Figure 8 show the way in which the sensor was modeled. The geometry of the model was taken from the sensors themselves. A sensor was taken and cut with a diamond saw along the cross-section perpendicular to the axis of the optical fiber and

then observed under an optical microscope. The shape of the epoxy adhesive was found to be elliptical and therefore the 3D FEM model uses the same shape.

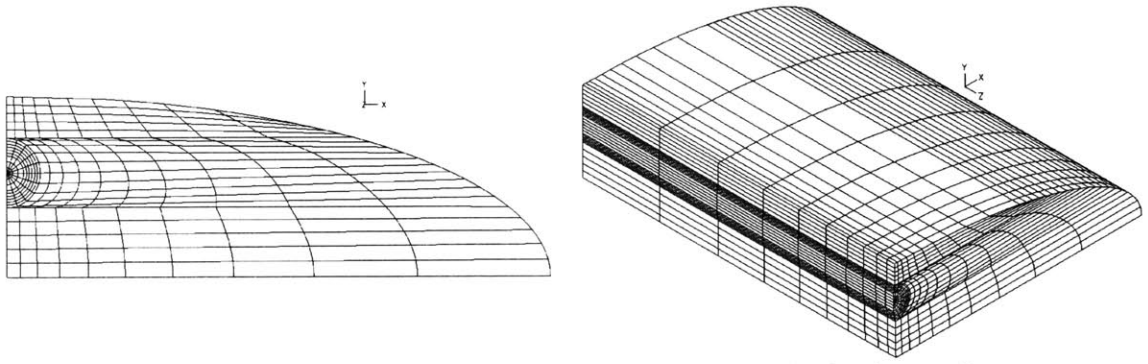

Figure 5: Example of three-dimensional finite element mesh of strain transfer

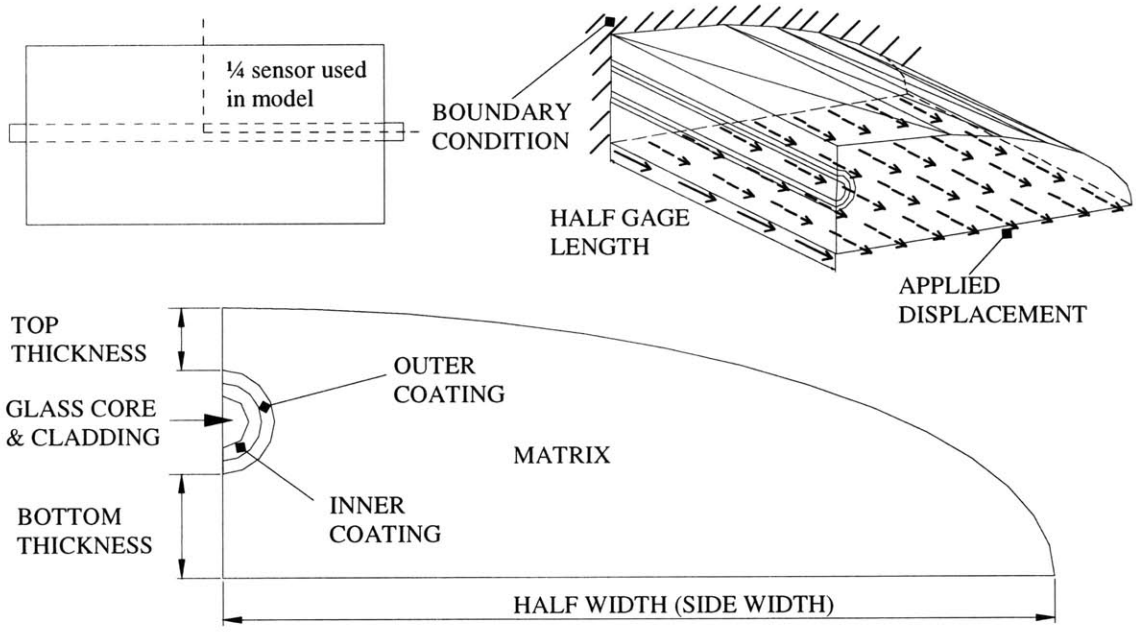

Figure 6: Diagram explaining important characteristics of the 3D FEM model of the strain transfer

Due to the geometric and loading symmetry of the analysis, it was only necessary to use one quarter of the sensor for the model. If a non-uniform loading condition were to be analyzed or if the geometry of the sensor were asymmetrical these simplifying assumptions could not be made. The boundary conditions also reflect these assumptions as illustrated in Figure 7. The center-line along the axis of the optical fiber is not allowed

to move in the x-direction (please note the coordinate system in Figure 7), however the other degrees of freedom are not restricted. The bottom surface of the adhesive is not allowed to move in the y-direction while the x and z-directions are allowed. Finally, the centerline of the sensor going perpendicular to the axis of the optical fiber is not allowed to move in the z-direction.

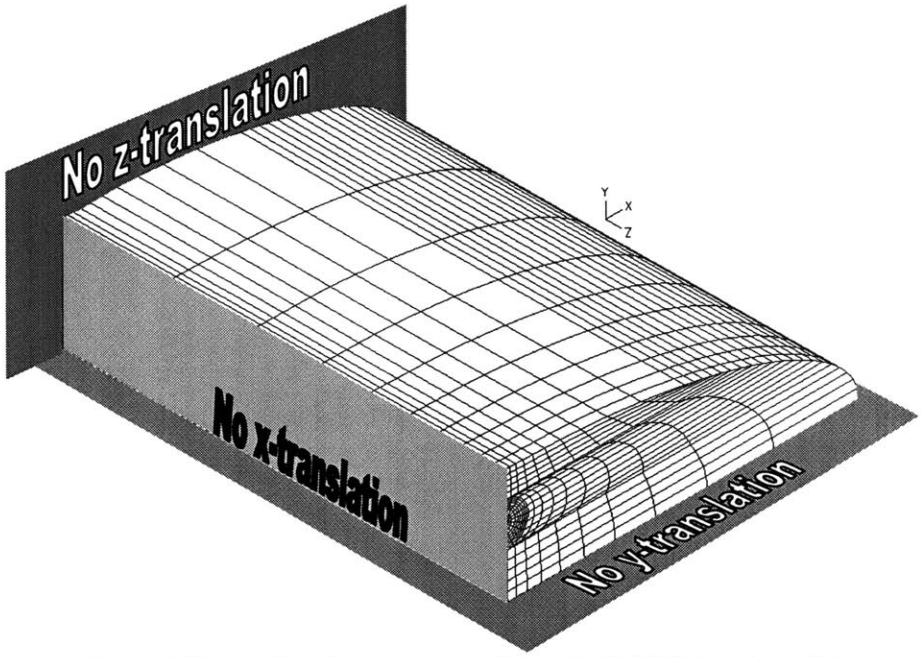

Figure 7: Illustration of boundary conditions for 3D FEM strain model

The FEM model places displacement values directly onto the nodal points on the bottom of the model (the bottom of the adhesive, Figure 6). This can be done since the sensor is assumed to have an inappreciable effect on the structure being measured and the displacement in the structure can be easily obtained through integration of the strain field. The former assumption is valid since the size of the sensor is very small and much less stiff when compared to the civil structures that it would be measuring (for example a large steel beam). By placing displacements directly onto the nodal points, the number of elements used in the model was greatly reduced. Additionally, a graded mesh was used

so that more elements could be placed where the high rate of strain transfer would be expected. Figure 5 shows a sample of the mesh that was employed in the analysis. The displacements that were placed onto the nodal points depend on the strain field as well as the specific finite element mesh. Calculating the correct displacements for a uniform strain field was done with a MATLAB program that calculated the length of each element by using the same geometric progression as the ADINA meshing program. Specifically, the size of elements is graded from one side of the mesh, where the strain transfer rate is high, to the other side of the mesh following a geometric progression. Details are given below. The appropriate displacement can be found for each node from the following relationship,

$$d_n = S_n * R * \varepsilon_{desired} \tag{4}$$

with $\varepsilon_{desired}$ as the strain acting on the sensor from the structure being monitored. The explanation for the rest of the terms makes frequent reference to Figure 8. The term R is the ratio of the total length of the FEM mesh (l_{mesh}) divided by the summation of the geometric series for the entire length of the FEM mesh (S_{mesh}), which is

$$R = \frac{l_{mesh}}{S_{mesh}} \tag{5}$$

The S_n term is the summation of the geometric series up to the point, n, which is the nodal point of the mesh for which the displacement is being calculated. It is calculated by the well-known relationship

$$S_n = \left(1 - r^n\right) / \left(1 - r\right) \tag{6}$$

In order to use Equation (6) it is necessary to figure out the correct value for the ratio r. This ratio is related to the geometric ratio used in the FEM program (r_{mesh}) to find the lengths of the individual elements. The relationship is expressed as

$$r = r_{mesh}^{(1/(n\_mesh-1))} \qquad (7)$$

The *n_mesh* refers to the total number of elements in the mesh (in Figure 8 *n_mesh* =10). The r_{mesh} is a constant ratio of the lengths of adjacent elements as expressed by

$$r_{mesh} = \frac{l_2}{l_1} = \frac{l_n}{l_{n-1}} \qquad (8)$$

Finally, once all of the main nodal point displacements have been found the intermediate nodal points can be found as the average of the two surrounding displacements

$$d_{ave} = \frac{d_n + d_{n+1}}{2} \qquad (9)$$

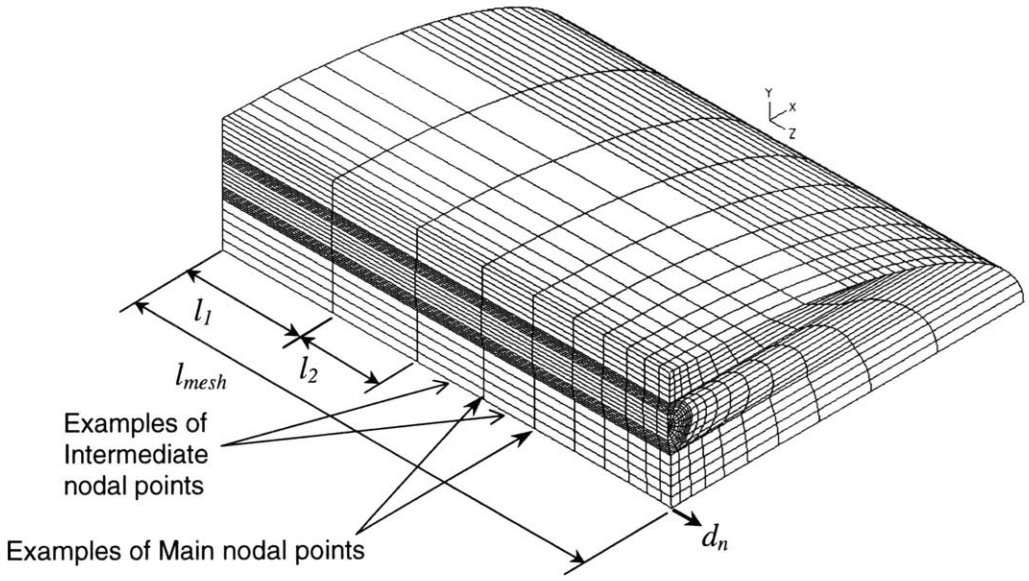

Figure 8: Illustration of 3D mesh and explanation for finding nodal displacements

The analysis used three-dimensional twenty-node solid elements. The number of elements used depended on the length of the sensor being studied however the number was generally around 3,000 elements. The ADINA Finite Element System, which is commercially available software, was used for all of the analysis.

The analysis and experimental work done in the rest of this chapter refer to interferometric sensing. Therefore, the average strain (as defined in Figure 1) is what would be measured and therefore is the focus of the analysis.

In order to carry out a valid mechanical analysis it is essential to have reliable values for the modulus of the coating materials on the optical fiber. The manufacturers of optical fibers generally will disclose what material has been used to coat the optical fiber however they do not reveal the modulus of the material. Different materials such as acrylate, silicone and even some metals can be used to coat optical fibers. Acrylate is a very common coating material, however, the mechanical properties of acrylate can vary quite a bit as seen in chapter 2. Table 1 shows the mechanical properties that were used in the strain analysis found in this chapter.

Table 1: Modulus of coatings used in 3D FEM analysis found from testing

Manufacturer	**Coating**	**Modulus** (MPa)
Corning SMF 28	Dual Acrylate Coating–inner layer	4
	Dual Acrylate Coating–outer layer	1000
3M FS-SN-4224	Single Acrylate Coating	50

2.2 Analytical solution

The time required to input, run and post-process a full 3D FEM analysis is quite significant. However, if an analytical solution for the problem could be found it would greatly reduce the amount of time required for the computation. Here, a simple analytical

model is proposed. The model assumes that (i) there is no axial stress acting on the polymeric fiber coating and that only shear stress is carried, (ii) the matrix material outside the fiber coating is considered to be rigid and having a strain equal to the strain in the underlying structure and (iii) the fiber does not debond at all. Following is a derivation of the model.

Given the assumptions that only shear stress is carried in the polymer coating and that the matrix is considered to be rigid, the shear stress $\tau(x,r)$ at any point in the fiber coating is related to the shear stress $\tau_f(x)$ at the glass/polymer interface by

$$\tau(x,r) = \tau_f(x) r_f / r \qquad (10)$$

where r_f is the radius of the glass fiber; x represents the coordinate along the fiber axis; and r is the radial distance from the fiber center. The displacement of the glass fiber relative to the rigid matrix defined as u_f can be obtained through integration of the shear strain within the polymer coatings. The result is given by

$$u_f - u_m = \tau_f r_f \left(\frac{1}{G_c} \ln \frac{r_c}{r_f} + \frac{1}{G_{c2}} \ln \frac{r_{c2}}{r_c} \right) = \tau_f \cdot a_0 \qquad (11)$$

where G_c and G_{c2} are the shear moduli of the two different coatings, u_m is the axial displacement in the matrix and the rest of the values are defined in Figure 9. Please note that for simplicity, $\tau_f(x)$ is denoted as τ_f, and both u_f and τ_f are understood to be functions of x.

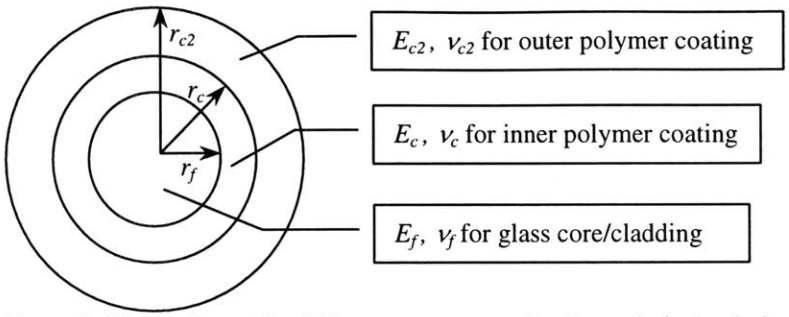

Figure 9: Illustration of the different parameters for the analytical solution

If Equation (11) is differentiated and combined with $\sigma_f = E_f du_f / dx$ and using the identity of $\varepsilon_m = du_m / dx$, the governing equation is obtained as

$$\frac{d^2\sigma_f}{dx^2} - \alpha^2\sigma_f = -\alpha^2 E_f \varepsilon_m \qquad (12)$$

where

$$\alpha^2 = \frac{2}{E_f r_f a_0} \qquad (13)$$

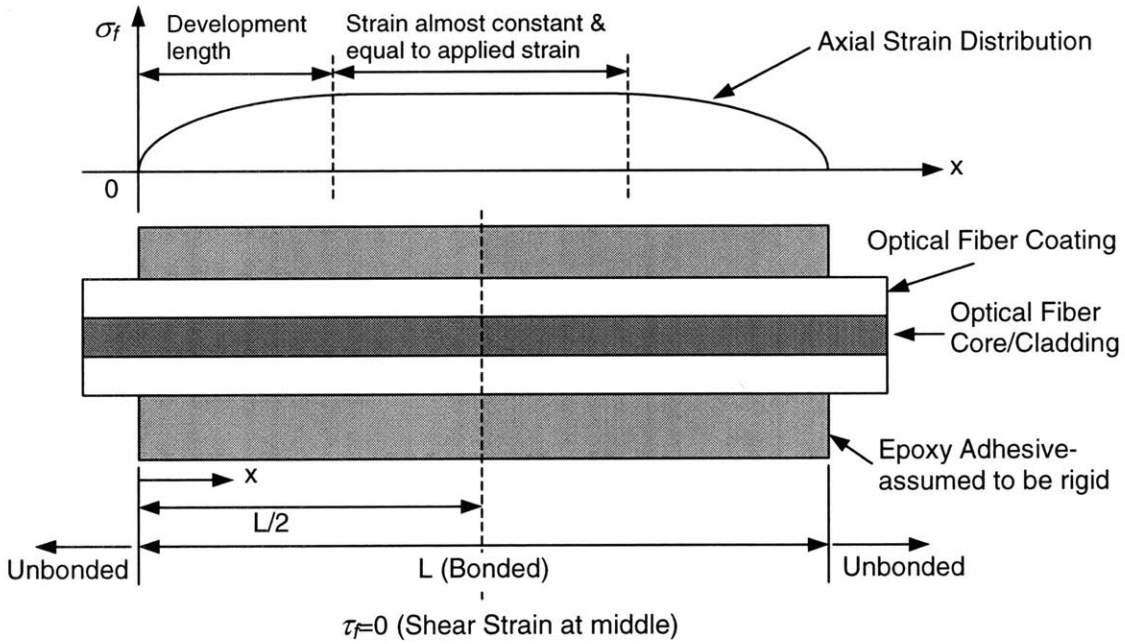

Figure 10: Boundary Conditions for Analytical Strain Transfer Model

The boundary conditions that are used to solve this equation are (see Figure 10):

1. $\sigma_f = 0$ at $x = 0$ because there is no stress transfer in the unbonded part of the fiber
2. $\tau_f = 0$ at $x = L/2$ due to the symmetry at the middle of the bonded region.

With these boundary conditions the solution for σ_f is found as

$$\sigma_f = E_f \varepsilon_m \left(1 + \tanh\left(\frac{\alpha L}{2}\right)\sinh(\alpha x) - \cosh(\alpha x)\right) \qquad (14)$$

with α defined in Equation (13) and $a_0 = r_f\left(\frac{1}{G_c}\ln\frac{r_c}{r_f} + \frac{1}{G_{c2}}\ln\frac{r_{c2}}{r_c}\right)$ and $G_c = \frac{E_c}{2(1+\nu_c)}$

(G_{c2} is found using E_{c2} and ν_{c2}). For a single coated optical fiber $a_0 = r_f\left(\frac{1}{G_c}\ln\frac{r_c}{r_f}\right)$.

Finally, it will be noted that the soft coating that surrounds the glass cladding/core makes the transfer of the radial stress very ineffective. The 3D FEM model shows the radial stress to be essentially zero which verifies this assumption. Therefore by neglecting the influence of the radial stress it is possible to calculate the strain along the fiber by dividing the axial stress by the Young's modulus.

For a bare-fiber there is no coating and the above analysis would not work. Albeit, to obtain approximate results for a bare fiber, it was assumed that shear transfer occurs over the epoxy surrounding the bare fiber up to a radial distance similar to the typical fiber coating thickness of 62.5 microns.

2.3 Importance of sensor geometry examined using 3D FEM

As Figure 6 illustrates, there are four different geometric aspects that can be examined to evaluate the impact that it has on the sensor performance or *calibration factor*, they are:

i.) Bottom thickness, that is the thickness of the adhesive between the structure and the optical fiber; ii.) Top thickness, the thickness of the adhesive on top of the optical fiber; iii.) Side width, the width of the adhesive on the side of the optical fiber and finally iv.) Gage length which is the length of the fiber bonded in the adhesive connecting it to the structure. The effect that these different geometric parameters have is looked at in order to guide one in the proper design of the sensor.

2.3.1 Side Width

Experience has shown that the amount of adhesive on the side of the optical fiber is usually very large compared to the diameter of the optical fiber. Therefore, one might wonder if it is safe to assume that it is almost infinitely large and of little consequence to the transfer. Figure 11 graphically shows the effect on the strain transfer for the dual coated Corning SMF28 optical fiber by maintaining the bottom thickness fixed at 100μm and the top thickness constant at 150μm. Table 2 which also maintains the bottom thickness at 100μm and top thickness constant at 150μm, shows the effect on the transfer for SMF28 and 3M optical fibers as well as for bare-fiber. As expected, the width of the adhesive on the side of the optical fiber does not have much of an influence on the performance of the optical fiber sensor. It will be noted that the more wide the adhesive the less (albeit not much less) the strain transfer. It would seem that the wider adhesive is more compliant and the transfer is not as efficient, especially when compared to the completely rigid analytical solution. The column entitled "% Change from previous width" which compares the current value with the value from the previous row, shows that the effect of the increasing width on the side of the optical fiber diminishes which fits well with expectations.

Table 2: Effect of Matrix side width (bottom=100μm and top=150μm)

Matrix side width (mm)	Corning SMF28			3M (FS-SN-4224)			Bare-fiber		
	Ave. strain in fiber/ applied strain (%)	% Different from Analytical	% Change from previous width	Ave. strain in fiber/ applied strain (%)	% Different from Analytical	% Change from previous width	Ave. strain in fiber/ applied strain (%)	% Different from Analytical	% Change from previous width
Analy.	15.695	–	–	53.044	–	–	94.475	–	–
0.5	14.982	4.539	4.645	50.975	3.900	3.977	86.083	8.883	9.295
1	14.955	4.712	0.181	50.940	3.966	0.069	86.009	8.960	0.086
2	14.929	4.878	0.174	50.861	4.116	0.156	85.881	9.096	0.149
5	14.913	4.978	0.106	50.823	4.186	0.074	85.860	9.118	0.024

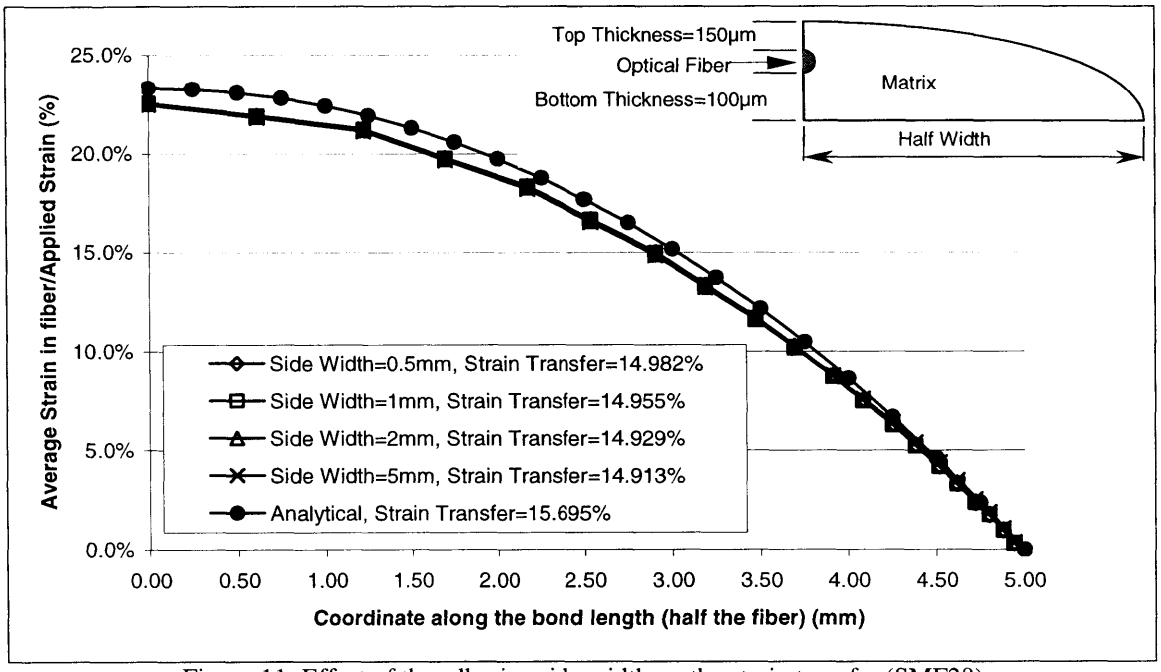

Figure 11: Effect of the adhesive side width on the strain transfer (SMF28)

2.3.2 Top Thickness

The thickness of the adhesive on top of the optical fiber does not influence the sensor performance dramatically as seen in Figure 12, with the side width fixed at 500μm and the bottom thickness constant at 100μm. The chart lines almost stack on top of each other since the transfer rates are very similar.

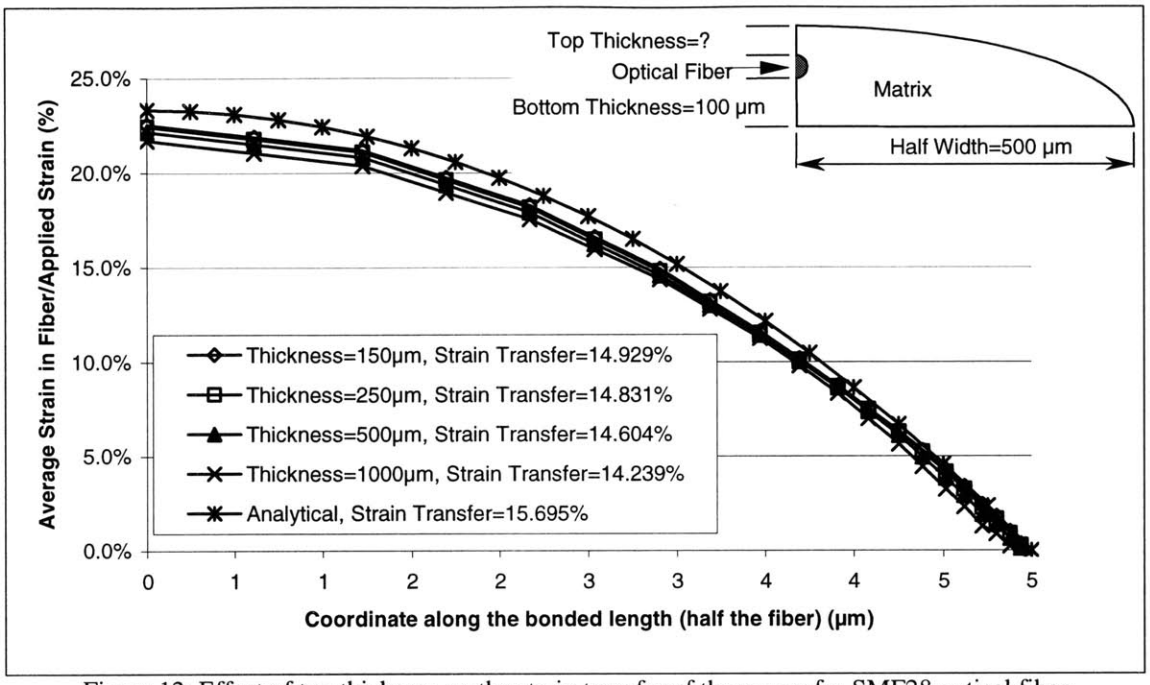

Figure 12: Effect of top thickness on the strain transfer of the sensor for SMF28 optical fiber

Table 3: Effect of top thickness on strain transfer for Interferometric sensor (bottom thickness=100µm and side width=0.5mm)

Top Thickness (µm)	Corning SMF28			3M (FS-SN-4224)			Bare-fiber		
	Ave. strain in fiber/ applied strain (%)	% Different from Analytical	% Change compared to previous thickness	Ave. strain in fiber/ applied strain (%)	% Different from Analytical	% Change compared to previous thickness	Ave. strain in fiber/ applied strain (%)	% Different from Analytical	% Change compared to previous thickness
Analy.	15.695	–	–	53.044	–	–	94.475	–	–
150	14.929	4.881	–	50.861	4.115	–	85.881	9.097	–
250	14.831	5.505	0.659	50.540	4.721	0.633	85.320	9.690	0.655
500	14.604	6.951	1.542	49.794	6.127	1.487	85.320	9.690	0.000
1000	14.239	9.277	2.531	48.619	8.342	2.388	85.320	9.690	0.000

Table 3, with bottom thickness=100µm and side width=500µm, gives a more quantitative indication of this transfer similarity. The column entitled "% Change compared to previous thickness" compares the transfer rate to the rate in the previous row. The changes are low. However, one will notice that the thickness on top jumping from 500µm to 1000µm does have the greatest change in decreasing the strain transfer

efficiency (it is also the largest incremental jump in thickness). This is the case for both of the coated fibers however for the bare-fiber there is no effect. Therefore, for coated optical fibers it is important to not let the top thickness become excessive as this may affect the strain transfer adversely.

2.3.3 Gage Length

The gage length of the strain sensor influences the strain transfer very directly. The longer the gage length the closer the transfer goes to near complete transfer. Figure 13, were the side width is 2000μm, the bottom thickness is 100μm and the top thickness is 150μm, graphically shows that as the gage length increases so does the transfer efficiency.

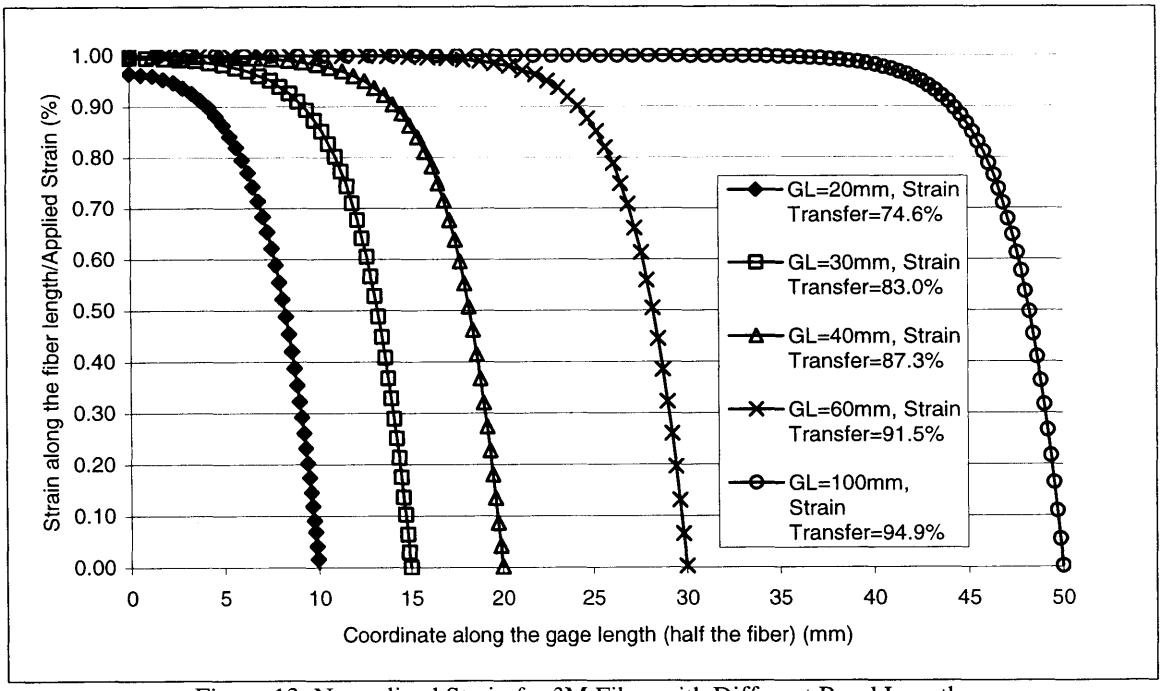

Figure 13: Normalized Strain for 3M Fiber with Different Bond Lengths

The stiffness of the coating on the fiber also influences the transfer effectiveness as seen in Table 4 (with the side width maintained at 2000μm, the bottom thickness held at 100μm and the top thickness is 150μm). The transfer in the bare-fiber is most efficient

and therefore the increase in the length (as shown in Table 4) does not create as dramatic of a strain transfer increase as in the coated fibers. This effect is illustrated in Figure 14 where it is clear that the bare-fiber is closer to reaching an asymptotic value of 100% whereas the other fibers are not as close.

Table 4: Influence of gage length on strain transfer for different fibers
(side width=2000μm, bottom thickness=100μm and top thickness=150μm)

Gage Length (mm)	Corning SMF28				3M (FS-SN-4224)				Bare-fiber			
	Ave. strain in fiber/ applied strain (%)	% Different from Previous	Analytical Transfer Prediction (%)	FEM Different from Analytical (%)	Ave. strain in fiber/ applied strain (%)	% Different from Previous	Analytical Transfer Prediction (%)	FEM Different from Analytical (%)	Ave. strain in fiber/ applied strain (%)	% Different from Previous	Analytical Transfer Prediction (%)	FEM Different from Analytical (%)
20	39.267	–	40.295	2.552	74.571	–	75.762	1.572	92.942	–	97.309	4.487
30	56.213	35.496	57.120	1.588	83.043	10.75	83.833	0.942	95.313	2.519	98.101	2.842
40	66.579	16.884	67.314	1.092	87.287	4.983	87.875	0.669	96.500	1.238	98.448	1.978
60	77.613	15.305	78.115	0.643	91.530	4.746	91.916	0.420	97.685	1.220	98.787	1.116
100	86.564	10.904	86.866	0.348	94.917	3.633	95.081	0.173	98.606	0.938	98.959	0.356

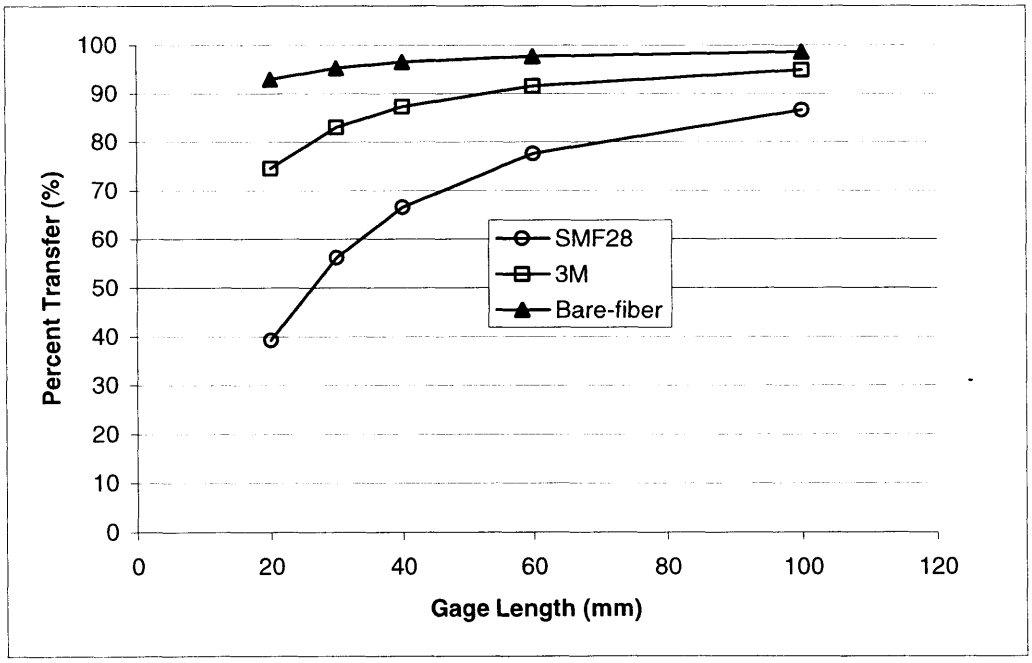

Figure 14: Comparison of the effect of gage length on strain transfer for different fibers

2.3.4 Bottom Thickness

The final geometric quantity to assess is the thickness of the glue beneath the sensor, referred to as the bottom thickness. Table 5 (side width=2mm, top width=150μm and gage length=10mm) shows the influence of the adhesive thickness with different fibers. The Corning SMF28 fiber which has the softest coating is the least affected by the bottom thickness while the bare-fiber which is very stiff is the most affected. As the coating stiffness become higher the adhesive matrix starts to influence the results more. If the coating is very soft then the strain transfer operates almost all in the fiber coating and therefore becomes less sensitive to the adhesive dimensions. In the case of the bare-fiber, since it is much more stiff than the adhesive, the dimensions of the matrix heavily influence the transfer.

Table 5: Analytical prediction compared to 3D FEM results for different coatings and bare-fiber (side width=2mm, top width=150μm and gage length=10mm)

Bottom Thickness (μm)	SMF28		3M		Bare-fiber	
	Ave. strain in fiber/ applied strain (%)	% Different from Analytical	Ave. strain in fiber/ applied strain (%)	% Different from Analytical	Ave. strain in fiber/ applied strain (%)	% Different from Analytical
Analy.	15.684	–	53.040	–	97.513	–
10	15.096	3.75	51.639	2.65	89.478	8.24
20	15.082	3.84	51.563	2.79	89.015	8.71
50	15.031	4.16	51.317	3.26	87.749	10.01
100	14.929	4.81	50.861	4.12	85.881	11.93
250	14.542	7.28	49.268	7.12	80.995	16.94
500	13.718	12.54	46.123	13.05	73.578	24.55
1000	11.657	25.68	38.740	26.97	59.437	39.05

Table 6 shows the influence of the bottom thickness combined with the gage length using the 3M optical fiber. This comparison is made while maintaining the side width at 2000μm and the top thickness at 150μm.

Table 6: Bottom thickness and gage length influence on the strain transfer in a 3M optical fiber sensor (side width=2000μm and top thickness=150μm)

Thickness (μm)	Gage Length (mm)											
	10		20		30		40		60		100	
	Ave. strain in fiber/ applied strain (%)	% Different from Analytical	Ave. strain in fiber/ applied strain (%)	% Different from Analytical	Ave. strain in fiber/ applied strain (%)	% Different from Analytical	Ave. strain in fiber/ applied strain (%)	% Different from Analytical	Ave. strain in fiber/ applied strain (%)	% Different from Analytical	Ave. strain in fiber/ applied strain (%)	% Different from Analytical
Analy	53.04	–	75.76	–	83.83	–	87.87	–	91.92	–	95.15	–
10	51.64	2.65	74.99	1.01	83.33	0.60	87.50	0.43	91.67	0.27	95.00	0.15
20	51.56	2.79	74.95	1.07	83.30	0.64	87.48	0.45	91.65	0.28	94.99	0.16
50	51.31	3.26	74.82	1.25	83.21	0.75	87.41	0.53	91.61	0.33	94.97	0.19
100	50.86	4.12	74.57	1.57	83.04	0.94	87.29	0.67	91.53	0.42	94.92	0.24
250	49.27	7.12	73.72	2.70	82.47	1.62	86.86	1.15	91.25	0.73	94.75	0.42
500	46.12	13.05	72.04	4.92	81.35	2.96	86.02	2.11	90.69	1.34	94.41	0.77
1000	38.74	26.97	67.98	10.28	78.64	6.19	83.99	4.43	89.33	2.81	93.60	1.63

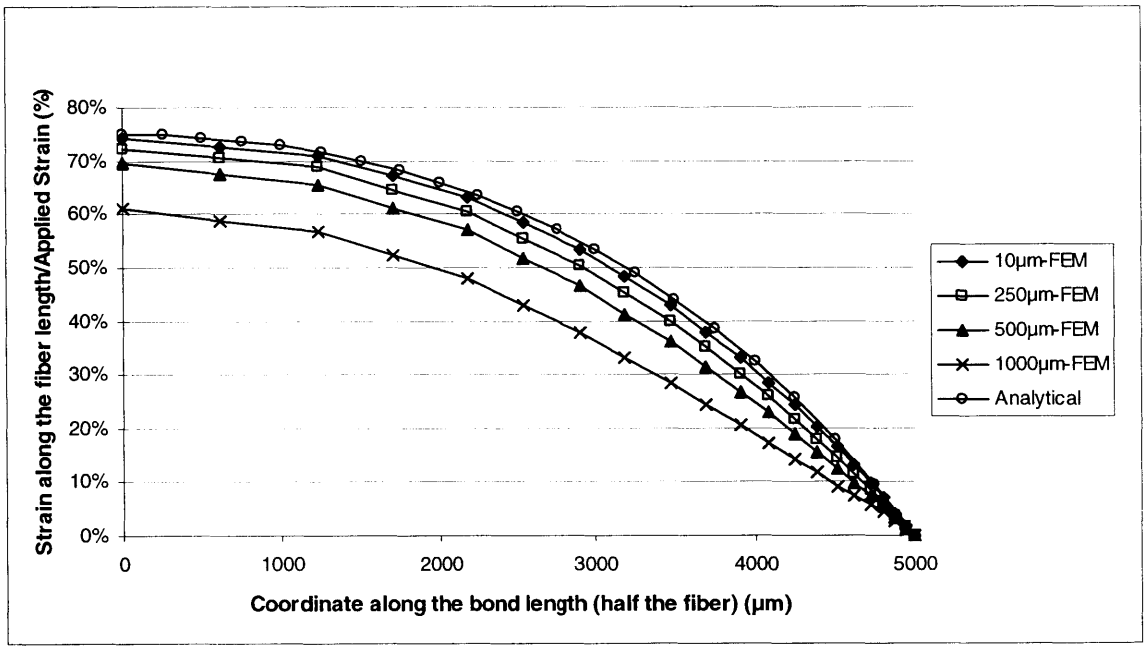

Figure 15: Influence of the adhesive thickness on the strain transfer of an optical strain sensor (3M single-layer acrylate fiber)

Table 5 and Table 6 compare the strain transfer calculated from the FEM model with the analytical model in the column "% Different from Analytical". Since the analytical model assumes the matrix adhesive to be rigid the strain transfer is very efficient however the adhesive does influence the strain transfer especially as it becomes greater in size. As

the thickness starts at 10μm it is only 2.65% different (for 10mm gage length) from the analytical solution however at 1mm thickness it is already 27% different. It changes from the 10μm thickness by 25%. Even though this trend is true for all gage lengths, as the length becomes longer the effect of the glue thickness greatly reduces. With a gage length of 100mm the strain transfer is in the mid-ninety percentile and the difference from the analytical is less than 2% even with a 1mm thickness. The change from the 10μm thickness is only 1.5%. This shows that with a long enough bond length the influence of the bottom thickness is greatly reduced.

2.3.5 Conclusions about sensor design from 3M FEM study

It is clear from the analysis that it is not a good idea to just assume that the strain transfer into an optical fiber sensor is 100% even for bare-fiber. Certainly, for coated optical fibers the strain transfer needs to be looked at in order to know what is being measured. The top thickness of the glue does not need to be controlled with great precision, however it should not be allowed to become excessive or the strain transfer effectiveness may be affected. The influence of the side thickness is not very great and does not need to be monitored closely. Albeit, the bottom thickness does exert a great influence on the transfer as does the gage length. The proper design of the sensor requires that these items be taken into consideration. Finally, the coating stiffness of the strain sensor also is very important in knowing the performance of the strain transfer.

Given the performance of the bare-fiber when compared to the coated fibers, it is the most efficient in strain transfer and would be a good choice except for the fact that bare-fiber is easily damaged by its environment and is not easily handled. Comparing the two fibers with coatings, Corning SMF28 and 3M (FS-SN-4224), the 3M fiber emerges as the

best choice in transfer efficiency. The 3M fiber exhibits almost the same geometric matrix insensitivity as the Corning fiber and it is much quicker to reach higher strain transfer rates. It should be noted that this comparison is only looking at the different coating systems not the actual fiber costs and related system costs. The Corning SMF28 fiber is at least 10 times cheaper than the 3M fiber (with current prices). Additionally, the Corning fiber operates at a 1310/1550nm wavelength and the equipment to run at this wavelength is generally cheaper than the 850nm wavelength equipment that the 3M fiber runs at. However, these considerations are beyond the present investigation.

2.4 Comparison of 3D FEM and analytical results

A comparison of the results for different coated fibers and bare-fiber to 3D FEM results illustrates the limitation of the analytical model in accurately predicting the strain in the bonded fiber. Figure 16 shows a comparison between a Corning SMF28 fiber with an acrylate dual-coating, a 3M fiber with an acrylate single-coating and a bare-fiber. The thickness of the adhesive between the fiber and the structural body was taken to be 250μm.

The analytical model cannot address the influence of the side, bottom and top thicknesses since the matrix is assumed to be rigid. However, the analytical solution is effective in predicting the strain transfer if the coating is much softer than the adhesive matrix and the bottom and top thicknesses are kept within the bounds mentioned in the previous sections. Additionally, the analytical model can show the effect of the gage length in the strain transfer.

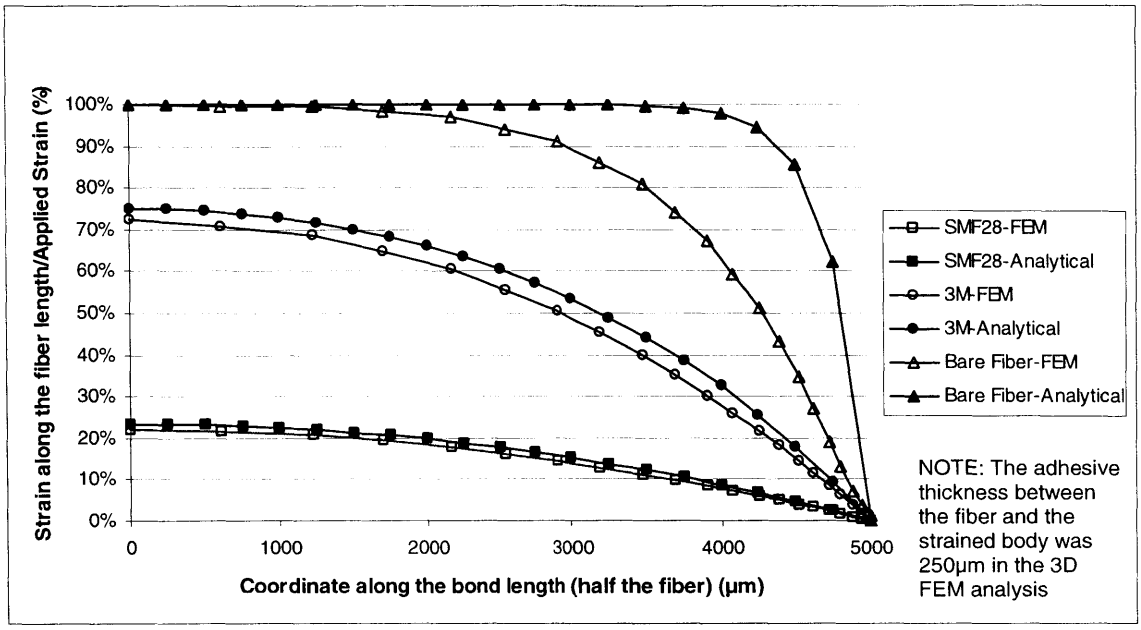

Figure 16: Comparison of analytical and 3D FEM analysis for different fiber coatings and bare-fiber

The comparison reveals that for the very soft acrylate coatings the analytical solution yields good results. However, with the bare-fiber the results are poor. The analytical solution does not accurately predict the strain transfer from the structure into the optical fiber. The assumptions of the analytical solution are no longer valid.

Table 2 compares the analytical solution to the FEM solution looking at the effect of the side width. For the soft coatings, comparison to the analytical solution is a fairly consistent 4-5% difference. However, for the bare-fiber it is a consistent 9% difference. This just reinforces that the assumptions of the analytical solution are not valid for the bare-fiber.

The top thickness comparison can be viewed in Table 3. Once again the softer coatings are more similar to the analytical prediction with a different around 5% and the bare-fiber is more different at about 9.5%. However, the difference does start to increase as the top

thickness increases for the coated fibers. For the bare-fiber, the increase in top thickness does not have an effect.

Table 4 shows that the increasing gage length for all of the fibers improves the correlation between the analytical and FEM models. The difference between the two different theoretical models decreases fastest with the bare-fiber as it was the largest difference at first and it comes down to almost the same as the coated fibers once it reaches 100mm gage length.

When looking at the bottom thickness (Table 5), the trend continues with the soft-coated fibers being much closer to the analytical solution than the bare-fiber. The Corning fiber strain transfer rate decreases with increasing bottom thickness at a rate of 3.45×10^{-3}%/μm while the 3M fiber decreases at a rate of 1.30×10^{-2}%/μm and the bare-fiber decreases at a rate of 3.02×10^{-2}%/μm. This further illustrates that the stiffer the coating material the more significant the bottom thickness becomes. Therefore, it is no surprise that as the coating material becomes stiffer the disagreement with the analytical solution becomes greater.

3. OPTICAL ANALYSIS

The mechanical information from the previous analysis gives an understanding of the strain field that is present in the fiber as it is transmitted from the body through the epoxy adhesive and the fiber coating(s) into the glass core. The optical analysis needs to correlate the strain in the body to the phase shift in the interferometer. When the fiber just undergoes axial stress, the relative phase change of a Mach-Zehnder Interferometer, $\Delta\phi$, is related to fiber strain in the direction of the fiber axis ε_{xx} by[6]

$$\Delta\phi = \frac{2\pi n_0}{\lambda}(1-c)\int_0^L \varepsilon_{xx} ds \qquad (15)$$

and

$$c = n_0^2[P_{12} - \upsilon_f (P_{11} + P_{12})]/2 \qquad (16)$$

where λ represent the light wavelength in free space, n_0 is the refractive index of the fiber in the unstrained state, L is the length of fiber mounted on the beam, P_{11} and P_{12} are strain optic constants, and ν_f is the Poisson's ratio of the fiber. The parameters, λ, n_0, ν_f, and L are known however P_{11} and P_{12} are not known. Some materials experience a change in their refractive index when strained. The photo-elastic strain optic constants relate the change in refractive index to the mechanical strain for a material. For an isotropic material it is only necessary to know the two constants, P_{11} and P_{12}, to complete the 6×6 Pockel matrix. Figure 17 shows the significance of the Pockel's coefficients.

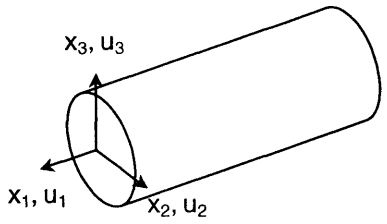

General Case for Strains in Sensor

$$e_1 = e_{11} = \frac{\partial u_1}{\partial x_1} \quad e_4 = \gamma_{23} = \frac{\partial u_3}{\partial x_2} + \frac{\partial u_2}{\partial x_3}$$

$$e_2 = e_{22} = \frac{\partial u_2}{\partial x_2} \quad e_5 = \gamma_{13} = \frac{\partial u_3}{\partial x_1} + \frac{\partial u_1}{\partial x_3}$$

$$e_3 = e_{33} = \frac{\partial u_3}{\partial x_3} \quad e_6 = \gamma_{12} = \frac{\partial u_2}{\partial x_1} + \frac{\partial u_1}{\partial x_2}$$

Isotropic Case with $\Delta T = 0$

$$P_{ij} = \begin{bmatrix} P_{11} & P_{12} & P_{12} & 0 & 0 & 0 \\ P_{12} & P_{11} & P_{12} & 0 & 0 & 0 \\ P_{12} & P_{12} & P_{11} & 0 & 0 & 0 \\ 0 & 0 & 0 & \frac{P_{11}-P_{12}}{2} & 0 & 0 \\ 0 & 0 & 0 & 0 & \frac{P_{11}-P_{12}}{2} & 0 \\ 0 & 0 & 0 & 0 & 0 & \frac{P_{11}-P_{12}}{2} \end{bmatrix}$$

$$e_4 = e_5 = e_6 = 0$$

$$\Delta n_{ave} = -\frac{n_o^3}{2}\left\{(P_{11} + P_{12})\left(\frac{e_2 + e_3}{2}\right) + P_{11}e_1\right\}$$

Figure 17: Pockel's Coefficients for Sensor in Isotropic Material and Effect on Refractive Index[8] (n_o is the refractive index in the sensor with no strain and n_{ave} is the refractive index under strain)

The 3M company could not provide the coefficients for the optical fiber used in the tests. These constants can be measured for the fiber by using Brillouin scattering in a preform.[6] This method can provide accurate results however it also requires expensive equipment. The coefficients for pure fused silica have been reported as $P_{11} = 0.121$ and $P_{12} = 0.270$.[6] Using this information along with $\nu_f = 0.17$ (commonly reported for fused silica) and $n_0 = 1.458$ (provided by the manufacturer of the fiber) then c is equal to 0.2163. Nevertheless, this value is for pure fused silica and not for a doped optical fiber and therefore would most likely be incorrect. A direct method for measuring the value of c has been proposed by Sirkis et al.[6] This involves calibrating the optical fiber readings with that of a resistive strain gage reading both measuring the same strain in a body. In order to carry out the measurement a bare-fiber optical fiber was embedded into epoxy and set-up as seen in Figure 19. Three different bond lengths were used for the measurement. A 3D FEM analysis was done for each of the three bond lengths to see the level of integrated strain that should be reached. A linear least square fit was used to find the best-fit slope of the interferometer strain (which already has taken into consideration the Pockel's effect) versus the strain gage readings as shown in the following equation:

$$\varepsilon_{\text{int erferometer}} = \left(\varepsilon_{strain\_gage} \cdot \beta_{FEM}\right) \qquad (17)$$

with β_{FEM} representing the percent transfer predicted by the 3D FEM model. Table 8, Table 9 and Table 10 show the results for this analysis for the three different bond lengths (Appendix II contains the data that was used to create these tables). Table 7 shows a summary of these results and the final result that was used for the calculations.

Table 7: Tabulation of Results for *c*

Gage Length (μm)	Calculated *c*
29,237 ± 3.731	0.19207
39,652 ± 3.991	0.18742
49,371 ± 4.234	0.19825
Average	0.19258
Standard Deviation	0.00543

Figure 18 graphically shows the three different results for the 3D FEM analysis that was carried out to find the amount of strain that should be transferred. Since bare-fiber was used in the tests it is not surprising that the predicted transfer is in the ninety percentile.

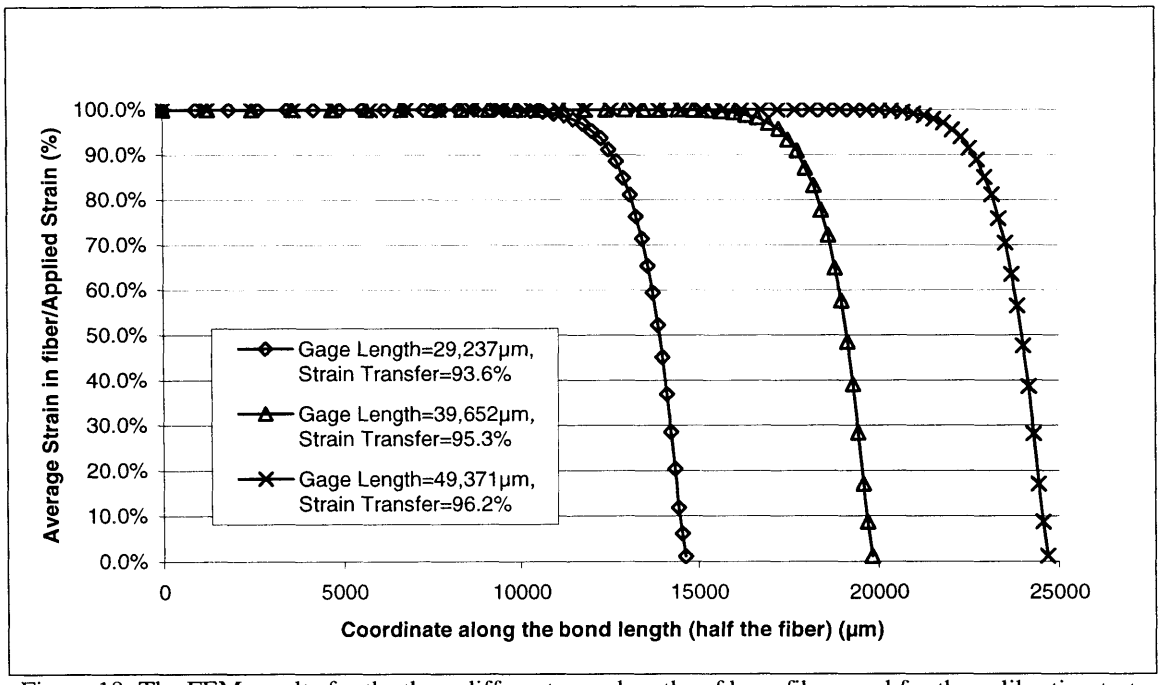

Figure 18: The FEM results for the three different gage lengths of bare-fiber used for the calibration tests

Table 8: Calculation of c for optical fiber, Gage Length=29,237μm

Load (N)	Test	Apparent Strain in Optical Fiber (μstrain)	Strain Gage Result (μstrain)	FEM prediction Transfer= 0.936408)	Results of Linear Regression
2000	1	48.222	67.808	63.496	
	2	50.208	68.589	64.227	
	3	49.950	67.808	63.496	
3000	1	75.468	102.707	96.175	
	2	78.124	103.488	96.907	
	3	76.873	102.186	95.688	
4000	1	102.190	135.655	127.029	
	2	103.637	135.004	126.419	$x_{slope}=$ 0.80175
	3	97.188	135.004	126.419	
8000	1	203.085	269.115	252.001	$r^2=$ 0.99990
	2	202.147	268.985	251.879	
	3	204.301	269.505	252.367	
12000	1	301.655	403.866	378.184	$c=1-x_{slope}=$ 0.19825
	2	302.144	404.778	379.037	
	3	302.199	405.168	379.402	
16000	1	401.233	537.913	503.706	
	2	403.143	537.523	503.340	
	3	403.499	537.001	502.852	
20000	1	505.888	671.655	628.943	
	2	502.470	671.655	628.943	
	3	503.580	672.307	629.553	

Table 9: Calculation of c for optical fiber, Gage Length=39,652μm

Load (N)	Test	Apparent Strain in Optical Fiber (μstrain)	Strain Gage Result (μstrain)	FEM prediction (Transfer= 0.953242)	Results of Linear Regression
2000	1	51.559	68.068	64.885	
	2	51.004	67.807	64.637	
	3	51.582	67.937	64.761	
3000	1	78.400	101.795	97.035	
	2	77.913	101.664	96.911	
	3	78.364	101.925	97.159	
4000	1	103.297	135.394	129.063	
	2	103.789	135.394	129.063	
	3	104.054	135.654	129.311	x_{slope}= 0.80793
8000	1	206.706	269.375	256.780	r^2= 0.99998
	2	206.597	269.506	256.904	
	3	207.756	268.985	256.408	$c=1-x_{slope}$= 0.19207
12000	1	312.230	403.738	384.860	
	2	309.758	402.827	383.991	
	3	309.761	403.348	384.488	
16000	1	412.001	537.657	512.517	
	2	414.267	537.136	512.021	
	3	413.634	537.267	512.145	
20000	1	516.074	671.273	639.886	
	2	516.544	670.491	639.140	
	3	515.082	670.752	639.389	

Table 10: Calculation of c for optical fiber, Gage Length=49,371μm

Load (N)	Test	Apparent Strain in Optical Fiber (μstrain)	Strain Gage Result (μstrain)	FEM prediction (Transfer= 0.962447)	Results of Linear Regression
2000	1	52.482	68.979	66.388	
	2	52.244	68.979	66.388	
	3	51.884	69.890	67.265	
3000	1	80.516	102.445	98.598	
	2	78.346	102.185	98.347	
	3	78.835	102.185	98.347	
4000	1	105.059	136.174	131.060	
	2	105.950	136.565	131.436	
	3	103.686	136.565	131.436	x_{slope}= 0.81258
8000	1	208.994	269.243	259.132	r^2= 0.99997
	2	209.399	269.504	259.383	
	3	209.366	269.634	259.508	$c=1-x_{slope}$= 0.18742
12000	1	315.162	404.647	389.451	
	2	315.617	405.557	390.327	
	3	315.696	403.604	388.448	
16000	1	420.615	539.607	519.342	
	2	420.183	537.131	516.960	
	3	419.522	538.694	518.464	
20000	1	523.125	672.178	646.935	
	2	523.171	671.787	646.559	
	3	523.807	671.265	646.057	

4. EXPERIMENTATION

4.1 Experimental set-up

For this study, a linear strain field was applied to a straight optical fiber. This was done by adhering a straight single-mode optical fiber to an aluminum beam as shown in Figure 19.

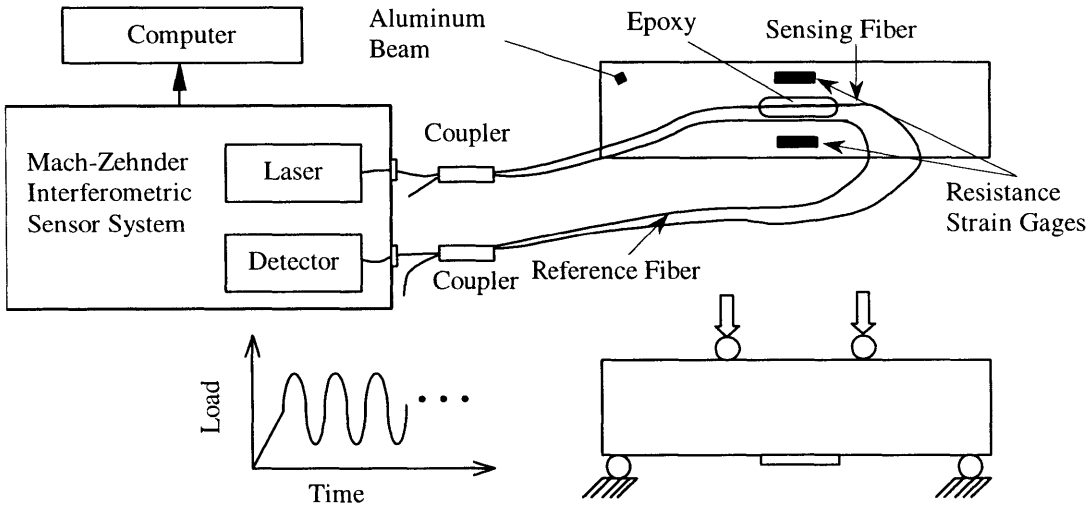

Figure 19: Schematic diagram showing the experimental set-up

The strain along the bottom of the beam between the inner supports is constant and the analytical solution is available. However, in these tests two strain gages were attached to the beam to measure the strain directly. The readings from the two strain gages were essentially the same. This is expected since the beam was carefully aligned in the testing machine and the sample was uniform. The beam was ramp loaded up to a set value and then a cyclic one hertz load was applied to the beam as shown in Figure 20 and Figure 21. Since the beam was preloaded the optical fiber was always in tension. The cyclic loading made it possible to find the displacements of the fiber for a certain load from the peaks of the oscillation. Since the oscillation occurred for a number of times a number of

peak-to-peak values could be found increasing the accuracy of the displacement values found.

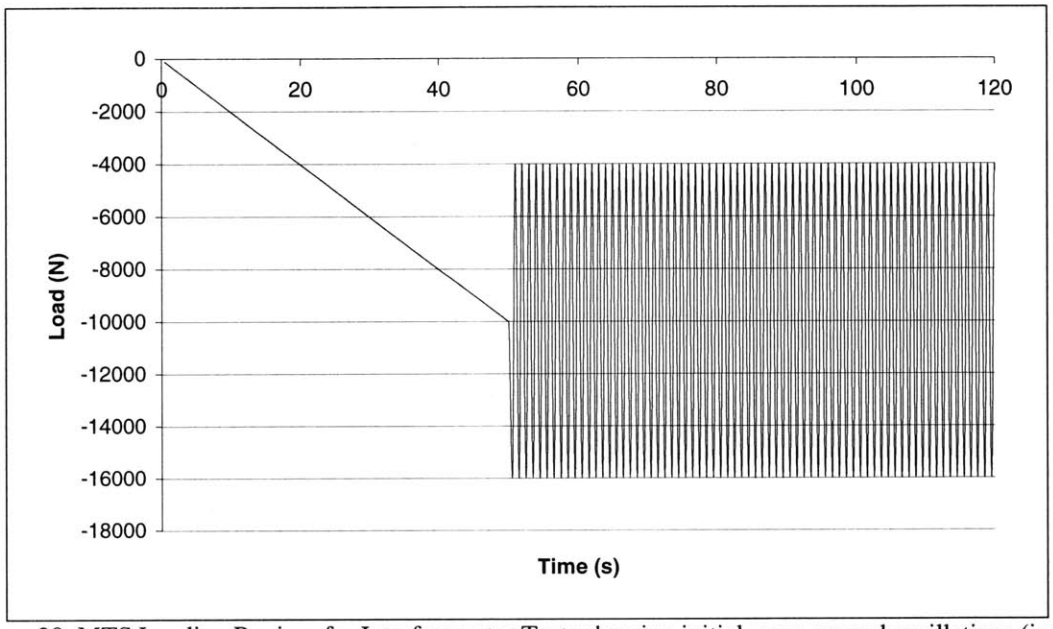

Figure 20: MTS Loading Regime for Interferometer Tests showing initial ramp-up and oscillations (in this example, ramp-up is to –10,000N, then a sinusoidal oscillation with from –4,000N to –16,000N with a mean of –10,000N, the loads are negative since the load cell was in compression)

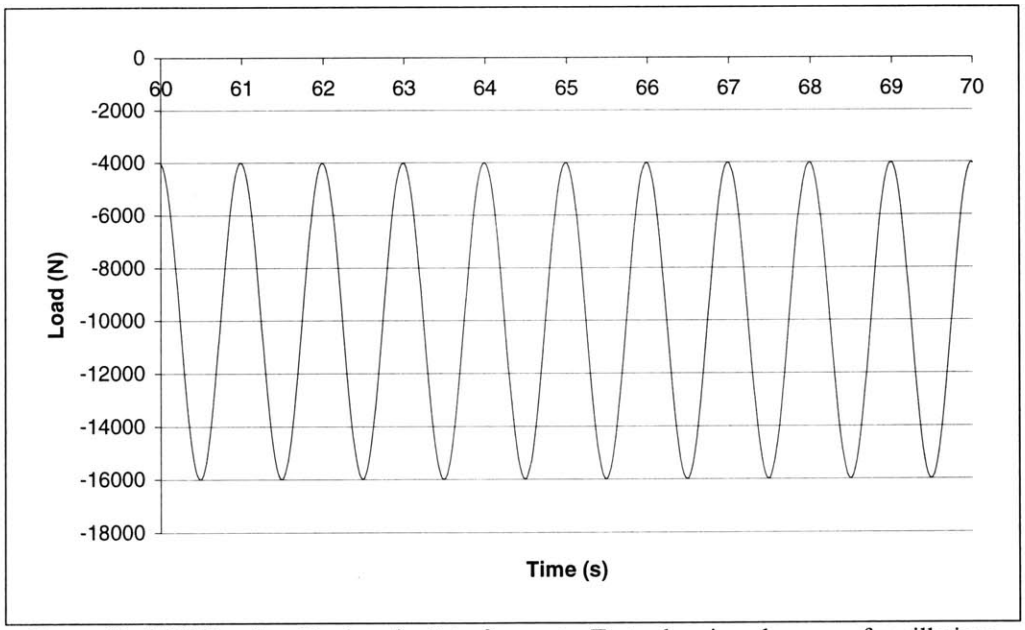

Figure 21: MTS Loading Regime for Interferometer Tests showing close-up of oscillations

4.1.1 Interferometric Sensor System

The interferometric system used to make the optical measurements was purchased from Precision-Dynamics, Inc. in Ontario, Canada and is called PD-1000 (please see Appendix III for additional details). The system works at a 780nm wavelength. The laser diode temperature is maintained within 0.1°C and has a drift of less than one part in 10^5 with the control current accurate to 1 microamp because the accuracy depends on the laser wavelength. The wavelength is confirmed by a monochromator which is itself calibrated from a multi-line low pressure mercury discharge lamp. With the interpolation of the space between fringes, nanometer resolution calibration is possible. An accuracy of 1nm over several millimeters range of displacement is attainable. The system used in the lab could be operated in two modes. It could be operated as a probe working on the Fizeau cavity principle or as a Mach-Zhender Interferometer. The experimental tests that were carried out used the Mach-Zhender Interferometer. However, the probe can be used to check that the system is operating properly. To carry out the check, the probe was placed inside an LVDT calibration system with a minimum indication of 1μm. By moving the calibration system to a certain displacement, the probe should also measure the same displacement. The PD-1000 system was found to be in good agreement with the LVDT calibrator. Since the interferometer should be able to accurately measure displacements smaller than one micrometer, this was only a rough check to ensure that the system was working.

4.1.2 MTS 810 Universal Testing Machine

The MTS testing machine is a well-known material testing system. The system that was used for the tests had a 100KN load cell that could be selected to operate in smaller load ranges such as 20KN. A smaller load range allows for better resolution of the loads

being measured. The machine had been calibrated and tuned so that it would function properly in generating a 1Hz loading. The MTS testing control program, TestWorks®, allows for the creation of a template that is used to run the system following a predefined loading, data recording and unloading plan. For these experimental tests, the system would first ramp up to a defined load and then oscillate with a 1Hz sinusoidal wave pattern (Figure 20 and Figure 21). To keep the sensor in tension during the entire experiment, the lower bound of the oscillation load does not go greater than zero (the load is negative because the load cell is in compression). Additionally, the program also records the time, crosshead movement, load, and the strain gage readings. This data could later be correlated with the PD-1000 by knowing the time at which the data was collected.

4.1.3 Sensor Configuration

The configuration of the beam used to run the tests is shown in Figure 22.

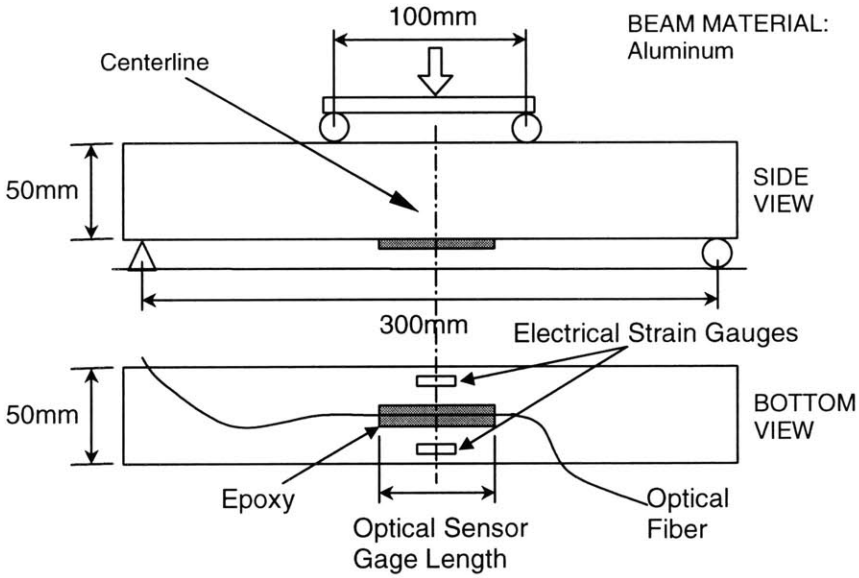

Figure 22: Experimental Set-up for Optical Sensor

A more detailed close-up of the sensor can be seen in Figure 23. The creation of a quality sensor required attention to detail. First the optical fiber was placed in the center of the beam and was attached with tape to the thin copper metal strips that had been previously attached to the beam. The optical fiber had a light tension applied to it before it was taped to ensure that it was straight. The purpose of the copper strips was to makes sure that the optical fiber was not resting on the aluminum beam but rather that it was a little suspended so that adhesive would be underneath the optical fiber.

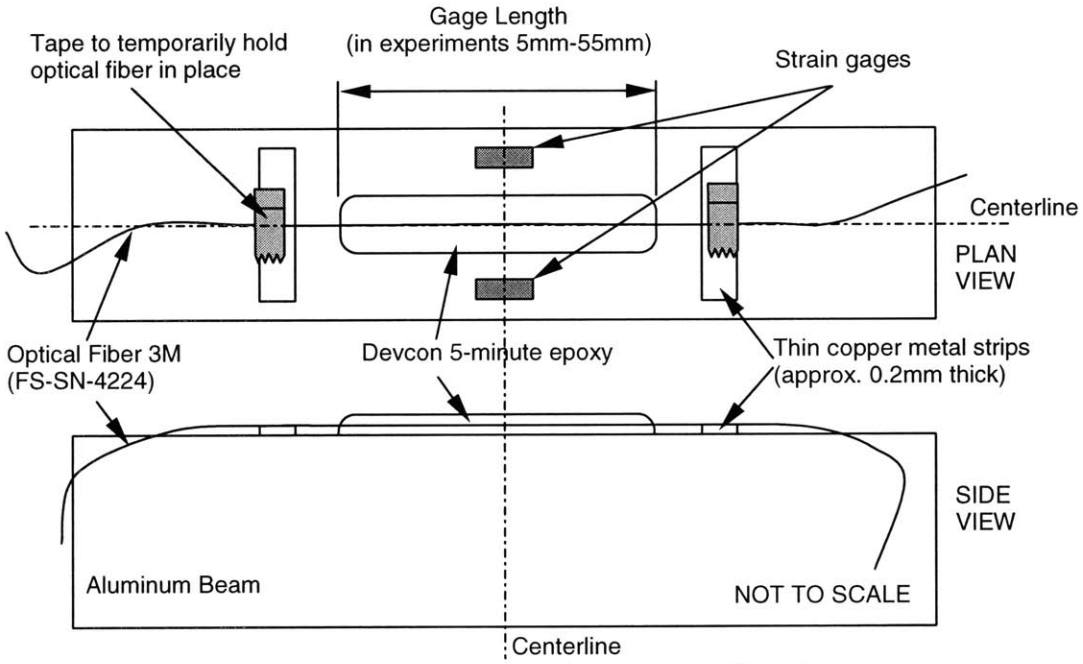

Figure 23: Close-up view of the sensor configuration

Once the fiber is in place epoxy (Devcon 5-minute epoxy) is carefully placed onto and around the optical fiber. The epoxy sets up in 5 minutes however it is not fully cured for at least one hour. Generally, 3 or more hours were allowed for the sample to fully cure.

After the tests were run the sensors were carefully removed from the aluminum beam and cut into sections using a diamond saw. Next the sections were examined underneath a powerful measuring optical microscope, Topcon model TMM-13OZ. The system had a

minimum indication of 1μm with an accuracy of (3 + 2.5 L/100) μm where L is the travel of the microscope stage in millimeters. The amount of adhesive between the optical fiber and the beam was measured and found to be consistently 250μm. This same system was used to measure the gage length of the sensor before it was tested.

4.1.4 Analytical Calculation

To verify that the strain gage readings made sense the analytical solution for the set-up was checked. Figure 24 shows the formulas for calculating the maximum strain at the center of the beam. These formulas and their derivation are available in many mechanics of materials and structural analysis books. For a four-point bending regime, the strain is constant between the two loading points. The strain gage readings were very close to the theoretical strain calculation.

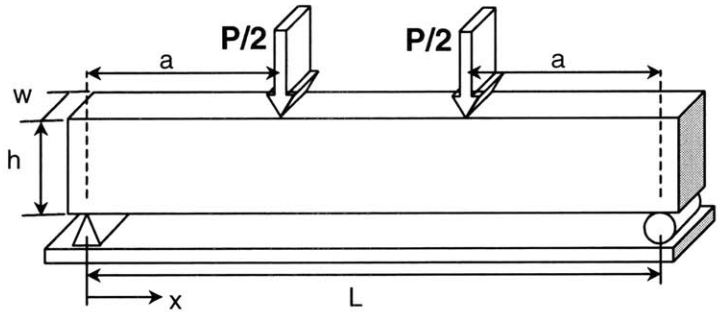

$$I = \frac{wh^3}{12}$$

$$y_{\max} = \frac{-Pa}{24EI}\left(3L^2 - 4a^2\right)$$

$$\varepsilon_{center} = \frac{Pah}{2EI}$$

Figure 24: Four-point bending formulas for calculating maximum deflection and maximum strain which both occur at the center of the beam.

4.2 Results

A comparison of the theoretically predicted values and the measured values can be seen in Table 11. In general as the gage length increases the difference between the theory and experimental values decreases as expected. Also, the longer the gage length the more complete is the strain transfer.

Table 11: Comparison of measured and predicted strain values

Gage Length (μm)	FEM Transfer Prediction	Analytical Transfer Prediction	Experimental Transfer	% Difference from FEM Prediction	% Difference from Analytical Prediction
5,016±3.125	0.20102	0.25006	0.63140 ± 0.06215	214.10182%	152.49901%
12,486±3.312	0.58415	0.61604	0.74077 ± 0.02447	26.81177%	20.24633%
23,089±3.577	0.77226	0.78997	0.85703 ± 0.00673	10.97768%	8.48932%
33,185±3.830	0.84156	0.85385	0.89291 ± 0.00391	6.10138%	4.57478%
43,639±4.091	0.87962	0.88886	0.90445 ± 0.00241	2.82218%	1.75388%
53,855±4.346	0.90241	0.90994	0.93920 ± 0.00692	4.07661%	3.21545%

Table 11 shows that there is some difference between the theoretical predictions and the experimental values especially as the gage length becomes smaller. Some of the error present can be explained by looking at some of the measured quantities. In actuality, there is a judgment call when determining the beginning and ending places of bonding for the fiber. The epoxy does not have a clean beginning and ending location, as shown diagrammatically in Figure 25.

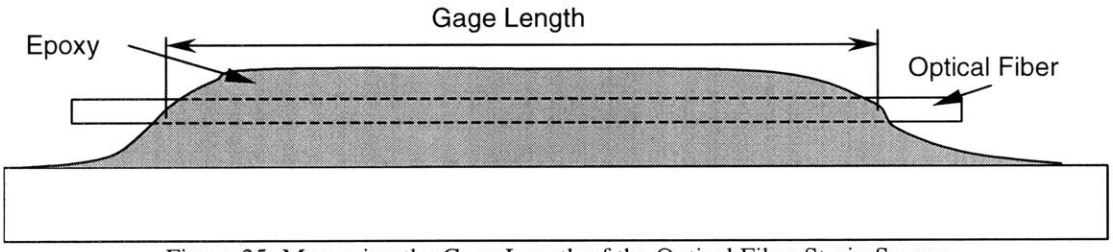

Figure 25: Measuring the Gage Length of the Optical Fiber Strain Sensor

Table 12: Effect of Gage Length Uncertainty on Difference between Experiment and Theory

Gage Length (μm)		Analytical Transfer Prediction	Experimental Transfer	% Difference from Analytical Prediction	% Change due to gage length uncertainty
5,016 ± 3.125	5012.875	0.24984	0.6314	152.720%	0.442%
	5016.000	0.25006		152.499%	
	5019.125	0.25028		152.278%	
12,486 ± 3.312	12482.688	0.61594	0.74077	20.266%	0.037%
	12486.000	0.61604		20.247%	
	12489.312	0.61614		20.228%	
23,089 ± 3.577	23085.423	0.78994	0.85703	8.494%	0.009%
	23089.000	0.78997		8.489%	
	23092.577	0.79000		8.485%	
33,185 ± 3.830	33181.170	0.85383	0.89291	4.577%	0.004%
	33185.000	0.85385		4.575%	
	33188.830	0.85386		4.573%	
43,639 ± 4.091	43634.909	0.88885	0.90445	1.755%	0.002%
	43639.000	0.88886		1.754%	
	43643.091	0.88887		1.753%	
53,855 ± 4.346	53850.654	0.90993	0.9392	3.216%	0.002%
	53855.000	0.90994		3.215%	
	53859.346	0.90995		3.215%	

Table 12 shows that when the gage length is shorter the error in the measurement is greatest. Additionally, as seen in Figure 26, the strain transfer efficiency increases at a much greater rate when the gage length is shorter as compared to when it becomes larger. Therefore, when the gage length is shorter, any error in the gage length would have a greater influence on the amount of transfer when compared to longer gage lengths when it becomes less important. Table 12 shows that even when looking only at the measurement error present in the measuring microscope (not including judgment error) the influence on the "% Change due to gage length uncertainty" is greater for short bond lengths and decreases significantly for longer bond lengths. It is interesting to note that when the bond length gets beyond 20,000μm, where it graphically can be seen to be reaching more of an asymptote in Figure 26, the difference between theory and experiment becomes much less.

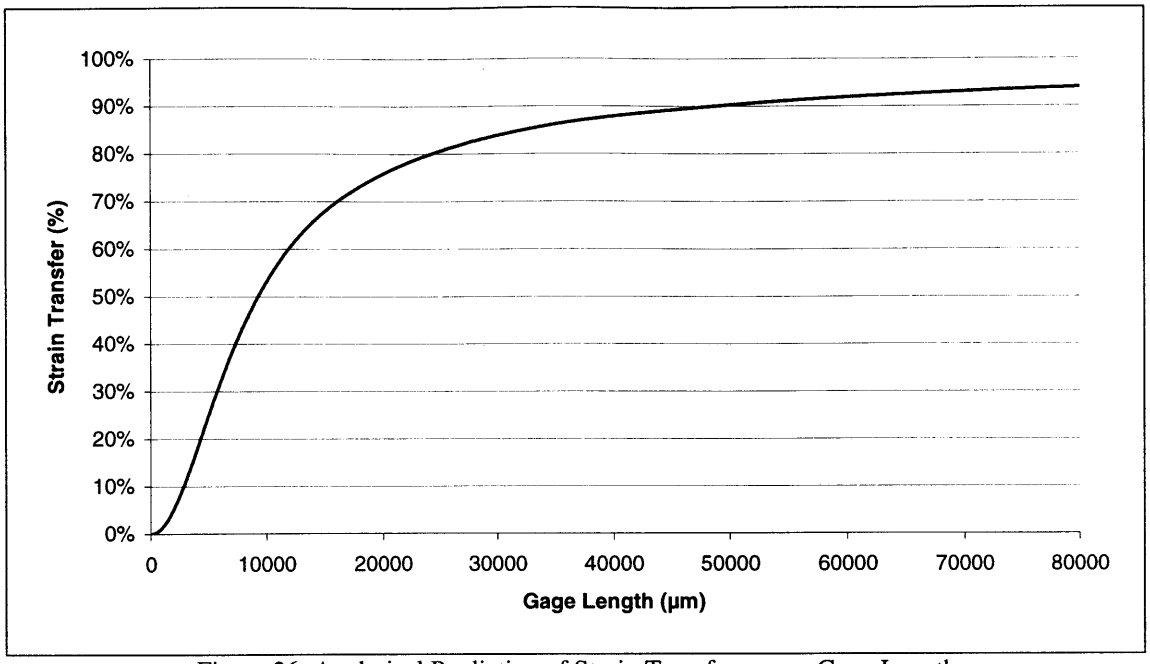

Figure 26: Analytical Prediction of Strain Transfer versus Gage Length

The results from the PD-1000 and the strain gages can be found in Appendix II. This data was used to create Table 13, Table 14, Table 15, Table 16, Table 17, and Table 18, which compare the experimental and theoretical transfer rates for different bond lengths.

Table 13: Comparison between experimental and theoretical analysis (sensor gage length is 5,016μm)

Load (N)	Test	Apparent Strain in Optical Fiber (μstrain)	Strain Gage Result (μstrain)	Strain reading corrected with FEM (Transfer= 0.201018)	Percent different from theory	Average & Standard Deviation per load	Average & Standard Deviation for all loads
8000	1	141.032	269.765	54.228	160.07%	217.99% ± 62.51%	214.10% ± 30.92%
	2	159.824	270.025	54.280	194.44%		
	3	219.706	269.114	54.097	306.14%		
	4	168.892	269.895	54.254	211.30%		
12000	1	260.941	403.475	81.106	221.73%	211.90% ± 8.56%	
	2	250.094	404.126	81.237	207.86%		
	3	248.516	403.866	81.184	206.11%		
16000	1	352.580	537.913	108.130	226.07%	216.79% ± 8.20%	
	2	339.435	538.173	108.183	213.76%		
	3	335.781	537.913	108.130	210.53%		
20000	1	434.677	671.786	135.041	221.89%	209.85% ± 9.18%	
	2	412.386	672.046	135.093	205.26%		
	3	420.339	671.135	134.910	211.57%		
	4	405.980	671.655	135.015	200.69%		

Table 14: Comparison between experimental and theoretical analysis (sensor gage length is 12,486μm)

Load (N)	Test	Apparent Strain in Optical Fiber (μstrain)	Strain Gage Result (μstrain)	Strain reading corrected with FEM (Transfer= 0.584146)	Percent different from theory	Average & Standard Deviation per load	Average & Standard Deviation for all loads
8000	1	188.645	268.318	156.737	20.36%	24.71% ± 4.18%	26.81% ± 4.19%
	2	201.953	268.651	156.931	28.69%		
	3	196.593	269.027	157.151	25.10%		
12000	1	290.746	402.563	235.155	23.64%	24.47% ± 0.74%	
	2	294.980	403.866	235.916	25.04%		
	3	293.340	402.563	235.155	24.74%		
16000	1	423.690	535.958	313.078	35.33%	27.98% ± 6.59%	
	2	384.120	536.348	313.306	22.60%		
	3	394.415	535.827	313.001	26.01%		
20000	1	496.557	652.759	381.307	30.22%	30.08% ± 1.50%	
	2	502.116	653.672	381.840	31.50%		
	3	490.604	653.540	381.763	28.51%		

Table 15: Comparison between experimental and theoretical analysis (sensor gage length is 23,089μm)

Load (N)	Test	Apparent Strain in Optical Fiber (μstrain)	Strain Gage Result (μstrain)	Strain reading corrected with FEM (Transfer= 0.772256)	Percent different from theory	Average & Standard Deviation per load	Average & Standard Deviation for all loads
8000	1	226.636	268.333	207.222	9.37%	10.22% ± 0.83%	10.98% ± 0.87%
	2	228.575	268.463	207.322	10.25%		
	3	230.205	268.463	207.322	11.04%		
12000	1	347.765	402.695	310.983	11.83%	11.43% ± 0.67%	
	2	344.138	402.695	310.984	10.66%		
	3	347.682	402.695	310.983	11.80%		
16000	1	459.098	535.962	413.899	10.92%	10.59% ± 0.30%	
	2	457.458	536.091	413.999	10.50%		
	3	457.052	536.351	414.200	10.35%		
20000	1	583.179	669.964	517.384	12.72%	11.67% ± 0.91%	
	2	573.947	669.313	516.881	11.04%		
	3	575.668	669.963	517.383	11.27%		

Table 16: Comparison between experimental and theoretical analysis (sensor gage length is 33,185μm)

Load (N)	Test	Apparent Strain in Optical Fiber (μstrain)	Strain Gage Result (μstrain)	Strain reading corrected with FEM (Transfer= 0.841561)	Percent different from theory	Average & Standard Deviation per load	Average & Standard Deviation for all loads
8000	1	240.835	268.994	226.375	6.39%	5.67% ± 0.77%	6.10% ± 0.46%
	2	236.563	268.068	225.596	4.86%		
	3	238.674	268.184	225.693	5.75%		
12000	1	359.502	403.730	339.763	5.81%	6.01% ± 0.23%	
	2	360.479	403.079	339.215	6.27%		
	3	359.990	403.730	339.763	5.95%		
16000	1	480.397	536.354	451.375	6.43%	6.35% ± 0.12%	
	2	480.682	536.744	451.703	6.42%		
	3	480.134	537.135	452.032	6.22%		
20000	1	599.404	670.629	564.367	6.21%	6.37% ± 0.16%	
	2	601.076	670.489	564.258	6.53%		
	3	600.658	670.879	564.586	6.39%		

Table 17: Comparison between experimental and theoretical analysis (sensor gage length is 43,639μm)

Load (N)	Test	Apparent Strain in Optical Fiber (μstrain)	Strain Gage Result (μstrain)	Strain reading corrected with FEM (Transfer= 0.879623)	Percent different from theory	Average & Standard Deviation per load	Average & Standard Deviation for all loads
8000	1	244.169	268.551	236.223	3.36%	2.76% ± 0.55%	2.82% ± 0.27%
	2	242.608	268.681	236.338	2.65%		
	3	242.227	269.260	236.847	2.27%		
12000	1	364.420	402.826	354.335	2.85%	2.80% ± 0.05%	
	2	364.865	403.737	355.136	2.74%		
	3	364.761	403.346	354.793	2.81%		
16000	1	484.791	537.003	472.360	2.63%	2.74% ± 0.12%	
	2	485.887	537.003	472.360	2.86%		
	3	485.983	537.784	473.047	2.73%		
20000	1	607.220	669.313	588.744	3.14%	2.98% ± 0.18%	
	2	606.550	670.876	590.118	2.78%		
	3	607.525	670.355	589.660	3.03%		

Table 18: Comparison between experimental and theoretical analysis (sensor gage length is 53,855μm)

Load (N)	Test	Apparent Strain in Optical Fiber (μstrain)	Strain Gage Result (μstrain)	Strain reading corrected with FEM (Transfer= 0.902412)	Percent different from theory	Average & Standard Deviation per load	Average & Standard Deviation for all loads
8000	1	249.580	268.855	242.618	2.87%	3.29% ± 1.16%	4.08% ± 0.77%
	2	248.807	269.245	242.970	2.40%		
	3	252.923	267.943	241.795	4.60%		
12000	1	380.456	402.826	363.515	4.66%	4.40% ± 0.39%	
	2	378.112	403.086	363.750	3.95%		
	3	379.448	402.044	362.809	4.59%		
16000	1	503.432	536.874	484.481	3.91%	4.40% ± 0.61%	
	2	508.124	535.832	483.541	5.08%		
	3	504.184	536.092	483.776	4.22%		
20000	1	631.574	669.315	603.998	4.57%	4.21% ± 0.31%	
	2	629.100	669.706	604.351	4.10%		
	3	628.008	669.315	603.998	3.98%		

5. CONCLUSION

A further investigation into the shear transfer behavior of strain optical fiber sensors shows that it is indeed an important consideration when designing the strain sensors. The 3D FEM model presented gives insight into the importance of the adhesive thickness between the structural body and the fiber in order to have good shear transfer. Additionally, an analytical model shows good agreement with the 3D FEM model when the coating stiffness is low. However, for bare-fiber the analytical model does not match the 3D FEM results. Determining the photo-elastic coefficients with some calibration tests proved essential to getting good results. The experimental results show close agreement with the theoretical prediction for larger bond length. The analysis presented can aid the sensor designer in knowing what parameters are most important for a good effective design.

6. REFERENCES

1. K. O. Hill, Y. Fujii, D. C. Johnson, and B. S. Kawasaki, "Photo-sensitivity in optical fiber waveguides: Application to reflection filter fabrication," *Appl. Phys. Lett.,* vol. 32, pp. 647–649, 1978.
2. R. M. Measures, *Structural Monitoring with Fiber Optic Technology*, San Diego, CA: Academic Press, 2001.
3. K. O. Hill and G. Meltz, "Fiber Bragg Grating Techonology Fundamentals and Overview," *J. of Ltwave. Tech.* **15**, No. 8, pp. 1263-1276, 1997.
4. C. K. Y. Leung and D. Darmawangsa, "Interfacial changes of optical fibers in the cementitious environment," *J. Mat. Sci.* **35**, pp. 6197-6208, 2000.
5. C. K. Y. Leung, X. Wang and N. Olson, "Debonding and Calibration Shift of Optical Fiber sensors in Concrete", *J. Engrg. Mech*, ASCE **126**, No. 3, pp. 300-307, 2000.
6. J. S. Sirkis and H. W. Haslach, Jr. "Interferometric Strain Measurement by Arbitrarily Configured, Surface-Mounted, Optical Fibers," *J. of Ltwave. Tech.* **8**, No. 10, pp. 1497-1503, 1990.
7. F. Ansari and L. Yuan, "Mechanics of Bond and Interface Shear Transfer in Optical Fiber Sensors," *J. Engrg. Mech.*, ASCE **124**, No. 4, pp. 385-394, 1998.
8. K. S. Kim, L. Kollár and G. S. Springer, "A Model of Embedded Fiber Optic Fabry-Perot Temperature and Strain Sensors," *Journal of Composite Materials*, **27**, No. 17, pp. 1618-1662, 1993.

Chapter 5

Conclusion

1. SUMMARY

Monitoring structural integrity and performance is important for safer structures that efficiently meet the needs of the users. The strain and crack sensors that have been developed and investigated in this thesis are good tools that can be used to measure and observe structural behavior. In strain and crack sensing, the change in optical output is related to the mechanical deformation of the fiber and the effect of fiber deformation on the characteristics of the light signal. To design optical sensors and to properly interpret the results, it is important to understand both the mechanical and optical behavior of the optical fiber.

1.1 Measuring Optical Fiber Coating Stiffness

To understand the performance of a sensor it is important to know the characteristics of the constituent materials. Quite often engineering material handbooks can offer the information that is needed to characterize the materials being used, however that is not always the case. With the coatings on an optical fiber, the available information is very scarce. The NANO INDENTER II® procedure outlined in Chapter 2 provides a method that can be applied to measure the mechanical properties of the coating directly on the optical fiber. Just like the coating properties are not available in standard manuals, the standard indenter testing procedures are not proficient in finding the material properties. The sample preparation and material testing required new non-standard techniques. While these new techniques are not revolutionary, they are a careful extension of existing

methods that succeed in the required purpose. Traditionally, samples are often of one material, frequently metal. However, the optical fiber contains multiple materials with very dissimilar mechanical properties. Hence, the preparation process required a method that could deal well with polishing both soft and very stiff materials simultaneously. Such a technique was developed and outlined in detail in Chapter 2. With an acceptable sample surface created, some adjustments were needed to test the soft materials. Finding the surface of the sample turned out to be the biggest obstacle. Carefully adjusting some of the surface finding capabilities of the machine made it possible to judiciously select the correct contact point manually. Finally, the actual indentation could take place yielding acceptable results.

1.2 Crack Sensing

The novel distributed optical fiber crack sensor that has been further developed in Chapter 3, can detect cracks without prior knowledge of crack location. This has been demonstrated experimentally for the first time. A concrete beam with a crack sensor attached to it was broken in two locations. The crack sensor correctly identified the existence of the cracks as well as their locations. Additionally, a theoretical model has been developed to give insight into the performance of the crack fiber sensor. The model combines the mechanical analysis of fiber deformation with the optical analysis of light loss in a curved waveguide. Several approaches were investigated to find the best mechanical model for the fiber deformation. Likewise, different ways for calculating the optical loss due to the bent waveguide were also studied. The optical analysis investigation was not only done for single-mode fibers but for multimode fibers as well. The crack sensor loss theory allows the optimization of sensitivity and loss which governs the number of cracks that can be monitored by a single fiber. The inclusion of

multimode fibers increases the potential applications for the crack sensor by giving the designer additional choices in fiber selection while reducing the cost. The verification of the theoretical models has also been carried out with the use of the crack simulating *Epoxy Blocks*. The crack simulators along with the specially designed testing machine provided the experimental data for such a confirmation. Reasonable agreement between predicted and measured sensor performance has been obtained. Validation of the single-mode model has been more substantial than with the multimode model. While more verification will be useful in fine-tuning the models, especially the multimode, the basic analytical structure is present.

1.3 Strain Sensing

Strain measurement using optical fibers offers many possibilities beyond traditional electrical strain gages. However, to simply utilize these sensors like traditional strain gages would be a mistake. For an electrical strain gage it is generally safe to assume that the transfer of the strain from the monitored member into the gage is very close to 100%. The work done in this thesis clearly shows that it is not safe to make this assumption in regards to optical fiber strain sensors. The geometry of the sensor, the manner in which it is attached to the structure, and whether coated or uncoated optical fiber is used all influence the efficiency of the strain transfer. Chapter 4 has looked at the different ways in which the different factors influence the strain transfer in a linear strain field. The thickness of the adhesive between the structure being monitored and the optical fiber was found to be very important in the stress transfer, as was the gage length of the embedded optical fiber. The coating stiffness was also influential in the strain transfer efficiency. Bare-fiber which is not easy to handle because it breaks easily, was found to have the best strain transfer efficiency. However the bare-fiber was also found to be the most

sensitive to the thickness of the adhesive underneath the optical fiber. While some previous studies have looked at the influence of fiber coatings, they have not carried out as complete a verification of the shear lag theory. This study performs the experiments with coated fiber to show that the model is in agreement with the strain measurements. This is done while using independently measured coating properties and Pockel's constants. Measuring the coating properties has been covered exclusively in Chapter 2 while the procedure for determining the Pockel's effect has been included in Chapter 3. This information will aid the engineer in properly utilizing this promising strain measuring technique in a judicious manner.

As the continuing efforts by engineers to design and build safer, more efficient and user-friendly structures increases, structural monitoring will also grow in importance. Nonetheless, for the sensors to be utilized well they must be built upon a sure foundation by having a thorough understanding of the manner in which they will perform.

2. ORIGINAL CONTRIBUTIONS

This thesis presents many contributions to the field of crack and strain sensing using optical fibers. The major contributions are:

1. <u>A practical and reliable method for the measurement of the coating stiffness</u>

   In the past, some investigators simply took values for the coating stiffness from material handbooks which is not good since the polymers used in the coatings are greatly effected by the coating process and therefore the value is different than that reported in a manual. Other methods for measuring the coating stiffness were indirect or highly susceptible to noise. The nano-

indentation method provides a reliable method that can directly measure the coating stiffness. Since the coating is an important phase, governing strain and deformation transfer between the structure and an attached optical fiber, knowledge of the coating stiffness allows proper performance characterization of fiber optic sensors.

2. Further development of a mechanical model for the optical fiber crack sensor

   Various approaches to model the crack sensor were tried until the one that best matched the experimental results was found. This analysis included the development of a 3D FEM model for the sensor.

3. Optical analysis for single mode fiber crack sensor

   Different optical analyses were investigated, including the Beam Propagation Method and the different analytical solutions for a fixed radius as proposed by various authors such as Marcuse and Snyder. Since the crack sensor does not create a single fixed radius it is necessary to find which method can best be applied to the analysis. Furthermore, many of the analysis solutions do not account for small radii like are found in the crack sensor and an appropriate correction factor has to be applied.

4. Optical analysis for the multimode fiber crack sensor

   The multimode analysis as suggested by Snyder and Love was used since it is straightforward and quick which is important so that it can serve as a good design guide. However, the theory is for a fixed radius whereas the crack sensor produces many different radii. Careful application of the theory was

necessary to account for the different radii from the crack sensor. Comparison with the experimental values is good when attention is given to the launching condition of the light into the fiber.

With contributions 2, 3 and 4, a framework is now available for predicting the signal loss versus crack opening relation for both single mode and multimode fibers. With this theoretical framework, the effect of various design parameters on the signal loss can be predicted. For specific design requirements (e.g., sensitivity at small crack openings, maximum loss at large opening, etc), the optimal combination of design parameters can hence be selected.

5. Mechanical modeling of the strain transfer for optical fiber strain sensors

A full 3D FEM model was developed to investigate the shear lag effect in optical fiber sensors. This investigation centered on coated optical fibers. Coated fibers are more easily handled than bare fibers but have a more pronounced influence from the shear lag effect. With the analysis, the effect of coating properties on strain transfer efficiency and consistency of the calibration factor for the strain sensor can be studied.

6. An analytical model for strain sensing

This solution provides a much quicker way for determining the strain transfer efficiency for a specific setup. The limitations of the analysis have also been studied in Chapter 4.

With contributions 5 and 6, a theoretical framework is developed for the selection of fiber coating stiffness to provide a good compromise between high strain transfer efficiency, and low sensitivity of the calibration factor to the gluing process of the fiber sensor (which affects the thickness of adhesive between the sensor and the member to which it is attached).

3. RECOMMENDED FUTURE WORK

To understand the behavior of optical fiber sensors, knowledge of the mechanical properties of the fiber coating is very important. The testing procedure presented in the thesis gives a way by which this information can be obtained. With technology advancing at high rates it is likely that more sensitive and improved indentation equipment will become available. However, the concepts involved in preparing the sample and in finding the sample surface as presented here will still be pertinent. Hence, additional fiber coatings can be tested which will further enhance the available knowledge of the mechanical performance characteristics of optical fibers.

Implementation of the theoretical models in designing crack sensors for actual structures would be beneficial for the progression of the crack sensor in making the transition from the laboratory to the real world. A significant amount of work has been done to develop the crack sensor to the level presented and it would now be beneficial to implement the sensor to actually monitor a structure. This would provide information that cannot be gathered in the lab and would enhance the commercial potential of the sensor. Oftentimes when things are used in their intended environment issues that may have been overlooked in the development become obvious. Therefore, actually modeling a sensor

to be used in a structure and then implementing that design might bring to light some deficiencies that could then be fixed.

In addition, the crack sensor concept can be expanded to measure more information about the crack opening. Using multiple fibers at different orientations within the crack sensor has the potential to measure not only the crack opening but also any shearing that has occurred between the crack faces. It may also be possible to gather the same information without the addition of more fibers by using different wavelengths within the same single-mode optical fiber. Should these new ideas work they would increase the potential applications for the crack sensor.

The strain sensing analysis has thus far been limited to linear strain fields. The next step is to see how the strain sensors function in non-linear strain fields. An assessment about whether the numerical and analytical models still are valid should be made. Additionally, those factors that are important to the strain transfer, such as bond length, can also be found. Furthermore, the shear lag analysis presented here has been focused on interferometric strain sensors. The effect of the strain would be different with a Fiber Bragg Grating. For an FBG the gage length is the length of the Bragg Grating (assuming that the bond length is greater than the grating length) not the entire length of the bonded fiber. However, if the bond length of the FBG were very close to the Bragg Grating length there obviously would be an issue with the strain transfer. Furthermore, besides the measurement of average strain, FBGs can also be designed for the measurement of the actual strain distribution used in distributed sensing configurations in which case accurate knowledge of the strain transfer would be necessary. This becomes even more obvious when considering non-linear strain fields. To properly measure the desired

information the design engineer would need to know the strain transfer trend to make judicious decisions on sensor location and geometry.

Appendix I

Mechanical Drawings-Sensor Sheet

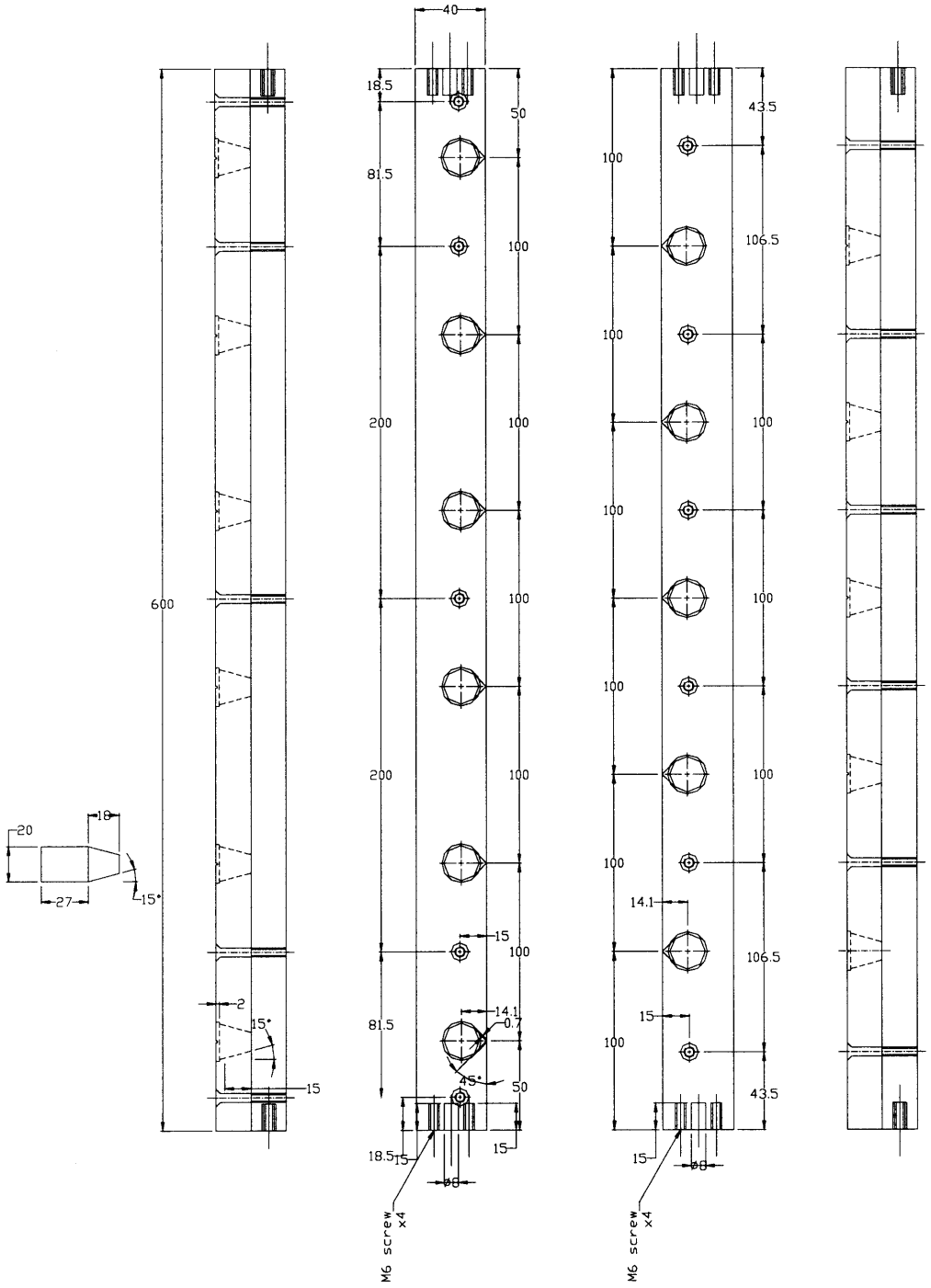

Please note that the linear measurements are in millimeters and the angle measurements are expressed in degrees.

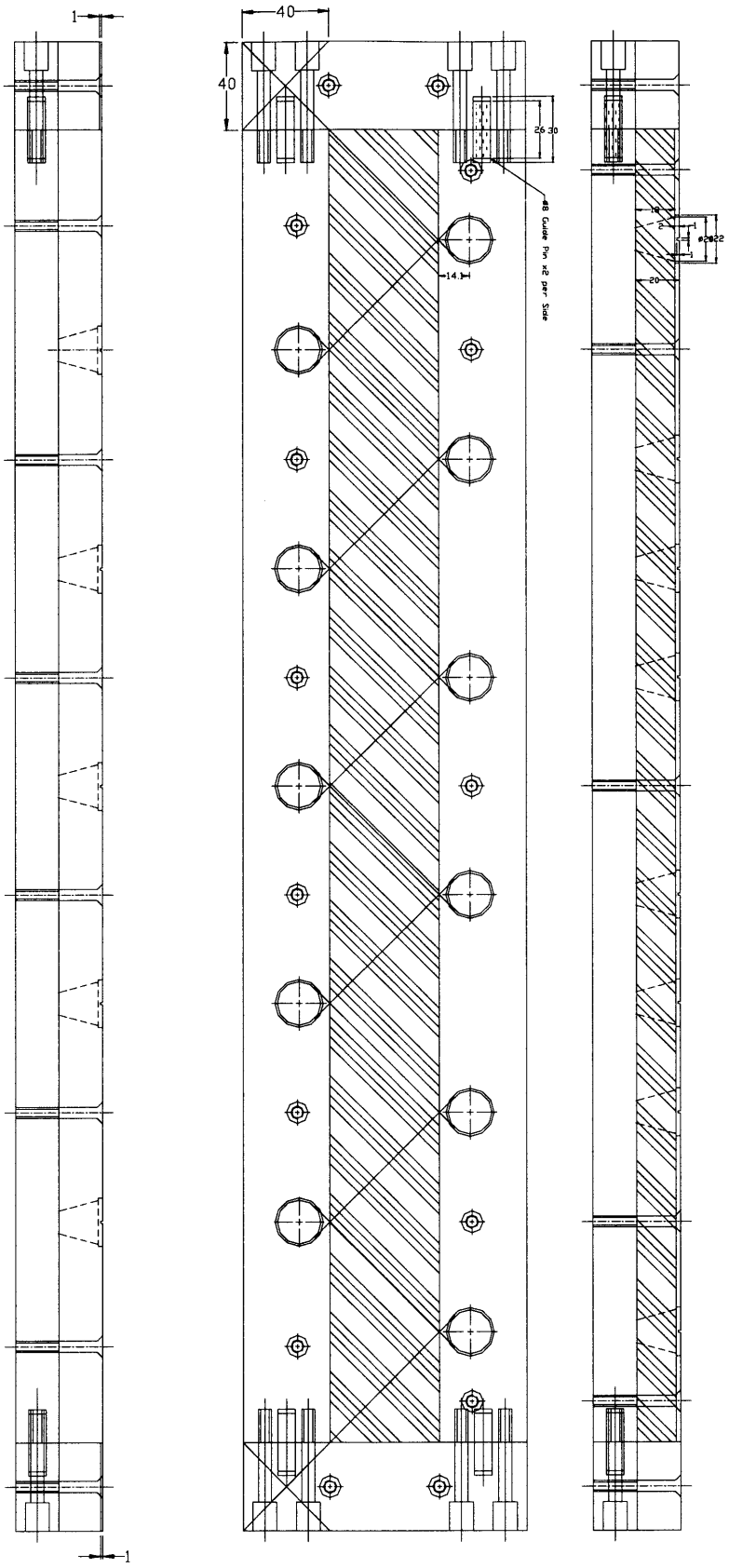
40
40
26.30
14.1
20

Appendix II

Experimental Data-Strain Sensor

1. INTRODUCTION

The data contained in this Appendix refers to the information presented in chapter 4. The data here shows how the strain readings were obtained from the original data. Figure 1 illustrates the meaning of the different table headings. The tables show the results from the PD-1000 interferometer tests and from the Strain gages.

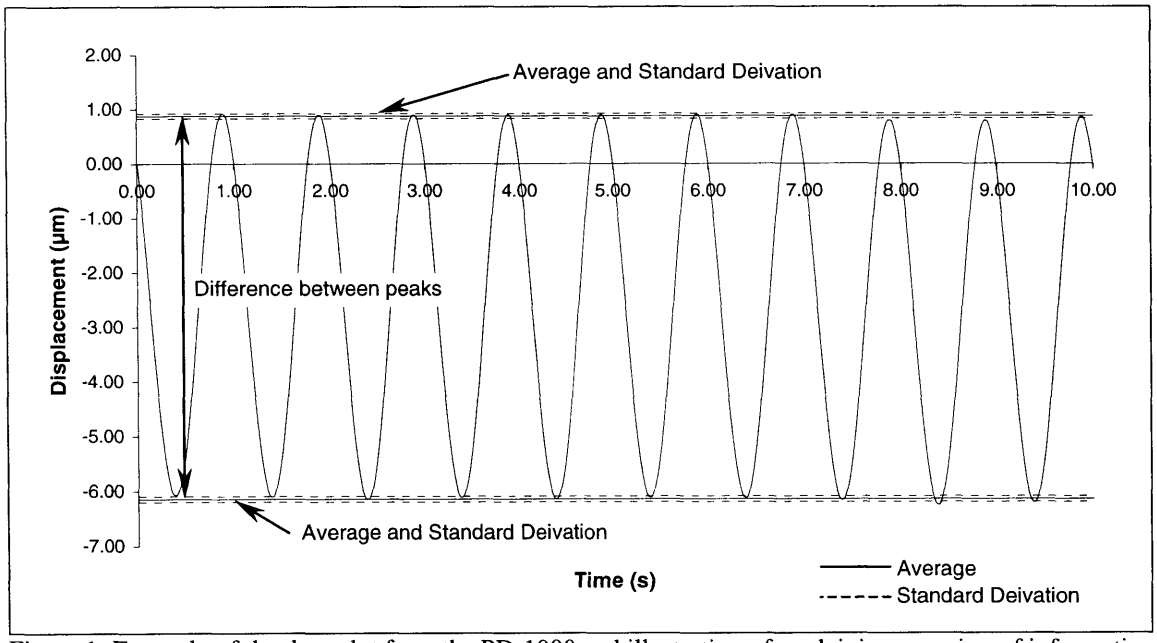

Figure 1: Example of the data plot from the PD-1000 and illustration of explaining meaning of information in the tables. It also applies to tables with MTS results except that the y-axis is "Strain".

The tables with the PD-1000 data show a "Corrected Difference..." column. The reason for the correction term is that the interferometer software provided by the manufacturer incorrectly calculates the displacement as if it were a Fizeau cavity rather than a Mach-Zhender interferometer. Appendix III further addresses this issue.

Table 1: Data from the PD-1000, Gage Length=29,237μm

Load (N)	Test	Average Min. Peak Value (μm)	Standard Deviation (μm)	Average Max. Peak Value (μm)	Standard Deviation (μm)	Difference between peaks (μm)	Corrected Difference ($2/n_{core}$ =2/1.458)	Apparent Strain in Optical Fiber (μstrain)
2000	1	-0.69912	0.34534	0.32867	0.36281	1.02779	1.410	48.22196
	2	-0.94033	0.19029	0.12979	0.19577	1.07012	1.468	50.20803
	3	0.08839	0.13299	1.15302	0.11427	1.06463	1.460	49.95011
3000	1	-1.58690	0.51782	0.02160	0.52976	1.60851	2.206	75.46795
	2	0.41401	0.46919	2.07913	0.43979	1.66513	2.284	78.12444
	3	-1.02895	0.38767	0.60951	0.38878	1.63845	2.248	76.87289
4000	1	0.14328	0.42546	2.32132	0.46908	2.17805	2.988	102.18973
	2	-0.39812	0.56640	1.81078	0.56822	2.20890	3.030	103.63712
	3	-1.67934	0.38806	0.39210	0.36833	2.07144	2.841	97.18787
8000	1	-4.88400	0.60665	-0.55548	0.66660	4.32852	5.938	203.08547
	2	-3.88167	0.13591	0.42685	0.11992	4.30852	5.910	202.14707
	3	-3.36414	0.53854	0.99029	0.51687	4.35442	5.973	204.30098
12000	1	-6.31686	0.21193	0.11253	0.18781	6.42940	8.819	301.65455
	2	-2.77937	0.19921	3.66046	0.18919	6.43983	8.834	302.14393
	3	-3.67132	0.17313	2.76968	0.17688	6.44099	8.835	302.19868
16000	1	-2.78448	0.20406	5.76730	0.22005	8.55178	11.731	401.23267
	2	-0.27266	0.16854	8.31983	0.16351	8.59249	11.787	403.14259
	3	-1.29830	0.17489	7.30179	0.19202	8.60009	11.797	403.49900
20000	1	-7.36454	0.21271	3.41784	0.18690	10.78238	14.791	505.88794
	2	-9.94622	0.36655	0.76331	0.39645	10.70953	14.691	502.47005
	3	-10.69914	0.07783	0.03404	0.08932	10.73318	14.723	503.57961

Table 2: Data from the Strain Gages, Optical Fiber Gage Length=29,237μm

Load (N)	Test	Average Min. Peak Value (μstrain)	Standard Deviation (μstrain)	Average Max. Peak Value (μstrain)	Standard Deviation (μstrain)	Strain Gage Result (μstrain)
2000	1	137.439	1.257	205.247	1.072	67.808
	2	136.918	1.196	205.507	0.739	68.589
	3	137.179	0.672	204.987	0.920	67.808
3000	1	204.596	0.823	307.303	0.961	102.707
	2	203.945	0.629	307.433	1.196	103.488
	3	203.685	0.686	305.871	0.868	102.186
4000	1	239.090	1.072	374.745	0.961	135.655
	2	239.350	0.739	374.354	0.910	135.004
	3	238.699	1.399	373.703	0.739	135.004
8000	1	203.292	1.027	472.407	0.686	269.115
	2	203.292	0.823	472.277	0.672	268.985
	3	202.772	0.910	472.277	0.672	269.505
12000	1	134.313	0.823	538.179	0.868	403.866
	2	133.793	1.257	538.570	0.629	404.778
	3	133.272	1.063	538.440	1.197	405.168
16000	1	133.662	0.878	671.575	0.911	537.913
	2	134.053	0.910	671.575	0.673	537.523
	3	133.923	1.265	670.924	0.961	537.001
20000	1	167.109	0.868	838.765	1.381	671.655
	2	166.979	0.412	838.634	0.673	671.655
	3	166.979	0.960	839.286	0.740	672.307

Table 3: Data from the PD-1000, Gage Length=39,652μm

Load (N)	Test	Average Min. Peak Value (μm)	Standard Deviation (μm)	Average Max. Peak Value (μm)	Standard Deviation (μm)	Difference between peaks (μm)	Corrected Difference ($2/n_{core}$ =2/1.458)	Apparent Strain in Optical Fiber (μstrain)
2000	1	-1.39741	0.04219	0.09296	0.03261	1.49037	2.044	51.55877
	2	-1.68356	0.10495	-0.20922	0.09452	1.47434	2.022	51.00402
	3	-0.11753	0.09397	1.37351	0.08345	1.49105	2.045	51.58214
3000	1	0.05474	0.14379	2.32100	0.08593	2.26626	3.109	78.40003
	2	0.07084	0.10075	2.32303	0.08707	2.25219	3.089	77.91337
	3	0.27051	0.22761	2.53573	0.20563	2.26522	3.107	78.36420
4000	1	-0.15602	0.19132	2.82991	0.19187	2.98592	4.096	103.29664
	2	-0.09560	0.28569	2.90455	0.29920	3.00015	4.115	103.78870
	3	-0.90517	0.13621	2.10264	0.12453	3.00781	4.126	104.05381
8000	1	-0.81291	0.34879	5.16219	0.34395	5.97510	8.196	206.70567
	2	-5.32672	0.20290	0.64522	0.14146	5.97195	8.192	206.59662
	3	-5.62157	0.14985	0.38388	0.18251	6.00545	8.238	207.75573
12000	1	-8.00239	0.37196	1.02303	0.37679	9.02542	12.381	312.23008
	2	-1.46037	0.20142	7.49358	0.19918	8.95395	12.283	309.75777
	3	-3.40467	0.52873	5.54939	0.56265	8.95406	12.283	309.76128
16000	1	-3.33952	0.33314	8.56990	0.34866	11.90942	16.337	412.00057
	2	-3.09289	0.19219	8.88203	0.13108	11.97492	16.427	414.26669
	3	-4.19753	0.16662	7.75909	0.19129	11.95662	16.401	413.63375
20000	1	-9.03218	0.27305	5.88562	0.26759	14.91780	20.463	516.07406
	2	-4.42282	0.20671	10.50856	0.20853	14.93138	20.482	516.54404
	3	-3.73237	0.38231	11.15675	0.40868	14.88913	20.424	515.08230

Table 4: Data from the Strain Gages, Optical Fiber Gage Length=39,652μm

Load (N)	Test	Average Min. Peak Value (μstrain)	Standard Deviation (μstrain)	Average Max. Peak Value (μstrain)	Standard Deviation (μstrain)	Strain Gage Result (μstrain)
2000	1	131.673	0.549	199.741	0.920	68.068
	2	131.543	0.739	199.350	0.823	67.807
	3	131.283	0.960	199.220	0.412	67.937
3000	1	200.782	0.629	302.577	0.921	101.795
	2	200.262	1.140	301.926	0.000	101.664
	3	200.522	0.739	302.447	0.672	101.925
4000	1	236.056	1.098	371.450	1.098	135.394
	2	236.187	0.920	371.580	0.686	135.394
	3	235.926	0.879	371.580	0.921	135.654
8000	1	203.385	0.878	472.761	0.824	269.375
	2	203.385	0.629	472.891	0.879	269.506
	3	203.516	0.672	472.500	1.063	268.985
12000	1	136.879	1.027	540.617	0.879	403.738
	2	137.269	1.265	540.096	0.961	402.827
	3	137.399	1.097	540.747	0.911	403.348
16000	1	137.920	0.868	675.577	0.961	537.657
	2	138.050	0.739	675.186	0.911	537.136
	3	138.050	0.739	675.317	0.879	537.267
20000	1	173.580	0.672	844.853	1.346	671.273
	2	173.580	1.257	844.071	0.824	670.491
	3	173.710	1.106	844.462	0.687	670.752

Table 5: Data from the PD-1000, Gage Length=49,371μm

Load (N)	Test	Average Min. Peak Value (μm)	Standard Deviation (μm)	Average Max. Peak Value (μm)	Standard Deviation (μm)	Difference between peaks (μm)	Corrected Difference ($2/n_{core}$ =2/1.458)	Apparent Strain in Optical Fiber (μstrain)
2000	1	-0.61157	0.10183	1.27733	0.10605	1.88890	2.59108	52.48177
	2	-0.84801	0.10677	1.03233	0.11036	1.88034	2.57934	52.24406
	3	-0.96468	0.07008	0.90272	0.07731	1.86740	2.56159	51.88445
3000	1	-0.02833	0.30943	2.86956	0.13802	2.89789	3.97516	80.51606
	2	-2.38992	0.16987	0.42988	0.19323	2.81979	3.86803	78.34613
	3	-2.23901	0.11321	0.59837	0.09952	2.83739	3.89216	78.83498
4000	1	-3.48802	0.24019	0.29320	0.25403	3.78121	5.18685	105.05864
	2	-3.47656	0.25327	0.33675	0.27738	3.81331	5.23088	105.95038
	3	-3.22700	0.17641	0.50482	0.17397	3.73182	5.11909	103.68621
8000	1	-6.45044	0.21938	1.07157	0.25350	7.52201	10.31826	208.99426
	2	-7.38718	0.18439	0.14942	0.20585	7.53659	10.33826	209.39948
	3	-2.62328	0.19923	4.91211	0.18819	7.53539	10.33661	209.36596
12000	1	-5.14029	0.19860	6.20284	0.17501	11.34312	15.55984	315.16157
	2	-2.31333	0.32656	9.04617	0.31692	11.35951	15.58231	315.61674
	3	-3.58570	0.33215	7.77666	0.33210	11.36236	15.58622	315.69588
16000	1	-11.95319	0.19481	3.18536	0.18131	15.13855	20.76619	420.61514
	2	-15.18693	0.16118	-0.06391	0.18460	15.12302	20.74488	420.18346
	3	-3.21182	0.23832	11.88739	0.28704	15.09921	20.71222	419.52207
20000	1	-7.56437	0.66309	11.26366	0.64185	18.82803	25.82720	523.12496
	2	-13.47219	0.38970	5.35750	0.38306	18.82969	25.82948	523.17109
	3	-18.61702	0.10919	0.23557	0.09673	18.85259	25.86089	523.80737

Table 6: Data from the Strain Gages, Optical Fiber Gage Length=49,371μm

Load (N)	Test	Average Min. Peak Value (μstrain)	Standard Deviation (μstrain)	Average Max. Peak Value (μstrain)	Standard Deviation (μstrain)	Strain Gage Result (μstrain)
2000	1	131.580	1.945	200.559	0.879	68.979
	2	131.840	0.739	200.819	0.739	68.979
	3	131.190	1.959	201.080	0.960	69.890
3000	1	199.387	1.344	301.833	2.397	102.445
	2	198.997	0.920	301.182	1.227	102.185
	3	198.476	0.412	300.661	0.672	102.185
4000	1	232.839	1.762	369.013	1.433	136.174
	2	232.709	2.229	369.274	0.879	136.565
	3	232.188	0.614	368.753	0.961	136.565
8000	1	199.127	0.910	468.370	0.672	269.243
	2	200.299	1.106	469.803	0.921	269.504
	3	199.518	0.739	469.151	1.063	269.634
12000	1	132.882	0.878	537.528	1.107	404.647
	2	131.450	2.469	537.007	0.739	405.557
	3	132.621	1.406	536.226	1.266	403.604
16000	1	133.402	1.139	673.009	2.764	539.607
	2	133.272	1.227	670.403	0.921	537.131
	3	133.142	1.432	671.836	1.099	538.694
20000	1	168.021	1.072	840.198	3.465	672.178
	2	168.021	0.878	839.807	0.922	671.787
	3	167.890	0.910	839.156	0.869	671.265

Table 7: Data from PD-1000 for Optical Sensor Gage Length=5,016μm

Load (N)	Test	Average Min. Peak Value (μm)	Standard Deviation (μm)	Average Max. Peak Value (μm)	Standard Deviation (μm)	Difference between peaks (μm)	Corrected Difference ($2/n_{core}$)	Strain including P_{11} and P_{12} (μstrain)	Apparent Strain in Optical Fiber (μstrain)
8000	1	0.3347	0.7751	0.7511	0.7543	0.4164	0.5712	0.7074	141.0319
	2	-0.7528	0.2407	-0.2809	0.2449	0.4719	0.6473	0.8017	159.8236
	3	0.8936	1.5599	1.5423	1.5574	0.6487	0.8898	1.1020	219.7061
	4	-0.3195	0.2058	0.1792	0.2075	0.4986	0.6840	0.8472	168.8918
12000	1	-0.2448	0.2020	0.5256	0.1947	0.7704	1.0568	1.3089	260.9407
	2	-0.2020	0.1260	0.5364	0.1304	0.7384	1.0129	1.2545	250.0935
	3	0.3102	0.3035	1.0440	0.3052	0.7337	1.0065	1.2466	248.5157
16000	1	0.3085	0.6702	1.3495	0.6641	1.0410	1.4280	1.7685	352.5800
	2	-0.2978	0.2458	0.7044	0.2282	1.0022	1.3747	1.7026	339.4347
	3	-0.7746	0.0782	0.2168	0.0705	0.9914	1.3599	1.6843	335.7805
20000	1	-1.1865	0.4371	0.0969	0.5136	1.2834	1.7604	2.1803	434.6769
	2	0.4592	0.3172	1.6767	0.3427	1.2176	1.6702	2.0685	412.3863
	3	-0.4134	0.5529	0.8276	0.5622	1.2410	1.7024	2.1084	420.3391
	4	-0.4001	0.3888	0.7985	0.4183	1.1986	1.6442	2.0364	405.9802

Table 8: Data from Electrical Strain Gages for Optical Sensor Gage Length=5,016μm

Load (N)	Test	Average Min. Peak Value (μstrain)	Standard Deviation (μstrain)	Average Max. Peak Value (μstrain)	Standard Deviation (μstrain)	Strain Gage Result (μstrain)
8000	1	200.971	0.960	470.736	0.961	269.765
	2	200.971	0.960	470.996	1.236	270.025
	3	201.622	0.910	470.736	0.739	269.114
	4	201.362	0.549	471.257	0.686	269.895
12000	1	133.684	0.823	537.159	1.433	403.475
	2	133.684	0.549	537.810	0.911	404.126
	3	133.424	1.063	537.289	1.027	403.866
16000	1	133.554	0.412	671.467	0.824	537.913
	2	133.033	1.071	671.206	0.869	538.173
	3	133.424	0.868	671.337	0.740	537.913
20000	1	167.391	0.739	839.177	1.141	671.786
	2	167.131	1.140	839.177	0.412	672.046
	3	168.042	0.672	839.177	0.962	671.135
	4	167.001	0.549	838.656	0.687	671.655

Table 9: Data from PD-1000 for Optical Sensor Gage Length=12,486μm

Load (N)	Test	Average Min. Peak Value (μm)	Standard Deviation (μm)	Average Max. Peak Value (μm)	Standard Deviation (μm)	Difference between peaks (μm)	Corrected Difference ($2/n_{core}$)	Strain including P_{11} and P_{12} (μstrain)	Apparent Strain in Optical Fiber (μstrain)
8000	1	0.8651	0.5981	2.2515	0.6171	1.3864	1.9018	2.3554	188.6445
	2	-0.8005	0.1492	0.6837	0.1686	1.4842	2.0360	2.5216	201.9533
	3	-0.8648	0.1845	0.5800	0.1797	1.4448	1.9819	2.4547	196.5933
12000	1	-0.8492	0.2570	1.2876	0.2890	2.1368	2.9311	3.6303	290.7460
	2	-1.0428	0.2481	1.1251	0.2459	2.1679	2.9738	3.6831	294.9797
	3	-1.8381	0.2244	0.3178	0.2199	2.1559	2.9573	3.6626	293.3405
16000	1	0.5233	1.0064	3.6371	0.7141	3.1138	4.2714	5.2902	423.6897
	2	-0.5500	0.3710	2.2730	0.3780	2.8230	3.8725	4.7961	384.1200
	3	-2.3528	0.4983	0.5459	0.4801	2.8987	3.9763	4.9247	394.4150
20000	1	-3.1078	0.1685	0.5416	0.1522	3.6494	5.0060	6.2000	496.5569
	2	-3.6284	0.1660	0.0618	0.2644	3.6902	5.0620	6.2694	502.1159
	3	-3.2435	0.1495	0.3621	0.1226	3.6056	4.9460	6.1257	490.6041

Table 10: Data from Electrical Strain Gages for Optical Sensor Gage Length=12,486μm

Load (N)	Test	Average Min. Peak Value (μstrain)	Standard Deviation (μstrain)	Average Max. Peak Value (μstrain)	Standard Deviation (μstrain)	Strain Gage Result (μstrain)
8000	1	201.438	1.196	469.756	0.783	268.318
	2	201.829	1.784	470.480	1.855	268.651
	3	201.308	1.629	470.335	0.921	269.027
12000	1	132.980	0.823	535.542	1.098	402.563
	2	133.370	0.686	537.236	2.535	403.866
	3	132.850	1.294	535.412	1.236	402.563
16000	1	132.980	1.344	668.938	1.028	535.958
	2	132.589	1.886	668.938	0.824	536.348
	3	132.720	0.613	668.547	0.687	535.827
20000	1	166.817	1.027	819.577	53.317	652.759
	2	167.078	1.098	820.750	53.781	653.672
	3	165.516	1.921	819.055	53.117	653.540

Table 11: Data from PD-1000 for Optical Sensor Gage Length=23,089μm

Load (N)	Test	Average Min. Peak Value (μm)	Standard Deviation (μm)	Average Max. Peak Value (μm)	Standard Deviation (μm)	Difference between peaks (μm)	Corrected Difference ($2/n_{core}$)	Strain including P_{11} and P_{12} (μstrain)	Apparent Strain in Optical Fiber (μstrain)
8000	1	-1.9389	0.6564	1.1412	0.6625	3.0801	4.2251	5.2328	226.6361
	2	-1.1140	0.2024	1.9924	0.2116	3.1064	4.2612	5.2776	228.5752
	3	-3.0908	0.4569	0.0377	0.4515	3.1286	4.2916	5.3152	230.2048
12000	1	-3.1554	0.5390	1.5708	0.5722	4.7262	6.4832	8.0295	347.7646
	2	-0.3568	0.2013	4.3202	0.2222	4.6770	6.4156	7.9458	344.1381
	3	-3.3357	0.3739	1.3895	0.3792	4.7251	6.4817	8.0276	347.6822
16000	1	-0.4864	0.3352	5.7529	0.3614	6.2393	8.5587	10.6001	459.0981
	2	-0.8022	0.1847	5.4149	0.1961	6.2170	8.5282	10.5623	457.4582
	3	-1.7029	0.4339	4.5086	0.4150	6.2115	8.5206	10.5529	457.0518
20000	1	-3.3988	0.6611	4.5268	0.6749	7.9256	10.8719	13.4650	583.1791
	2	-4.5219	0.3675	3.2783	0.3590	7.8001	10.6998	13.2519	573.9465
	3	-0.2922	0.4163	7.5314	0.4284	7.8235	10.7319	13.2916	575.6676

Table 12: Data from Electrical Strain Gages for Optical Sensor Gage Length=23,089μm

Load (N)	Test	Average Min. Peak Value (μstrain)	Standard Deviation (μstrain)	Average Max. Peak Value (μstrain)	Standard Deviation (μstrain)	Strain Gage Result (μstrain)
8000	1	202.832	0.739	471.165	0.549	268.333
	2	202.311	0.629	470.774	0.412	268.463
	3	202.181	0.910	470.644	0.824	268.463
12000	1	135.154	0.739	537.849	0.911	402.695
	2	135.284	1.196	537.979	0.687	402.695
	3	134.894	0.960	537.588	1.027	402.695
16000	1	136.195	1.294	672.157	1.266	535.962
	2	135.414	1.071	671.505	0.614	536.091
	3	135.154	0.739	671.505	0.869	536.351
20000	1	169.382	0.910	839.346	0.549	669.964
	2	169.772	0.878	839.085	0.673	669.313
	3	168.861	0.868	838.825	0.673	669.963

Table 13: Data from PD-1000 for Optical Sensor Gage Length=33,185μm

Load (N)	Test	Average Min. Peak Value (μm)	Standard Deviation (μm)	Average Max. Peak Value (μm)	Standard Deviation (μm)	Difference between peaks (μm)	Corrected Difference ($2/n_{core}$)	Strain including P_{11} and P_{12} (μstrain)	Apparent Strain in Optical Fiber (μstrain)
8000	1	-5.1106	0.1850	-0.4063	0.2378	4.7042	6.4530	7.9921	240.8350
	2	-2.0328	0.3038	2.5880	0.3104	4.6208	6.3385	7.8503	236.5626
	3	-0.0035	0.1214	4.6585	0.1120	4.6620	6.3951	7.9204	238.6744
12000	1	-6.1441	0.0535	0.8780	0.0480	7.0221	9.6326	11.9301	359.5017
	2	-5.6201	0.1444	1.4211	0.1405	7.0412	9.6588	11.9625	360.4794
	3	-2.6562	0.1861	4.3754	0.1812	7.0317	9.6456	11.9463	359.9900
16000	1	-7.8165	0.1503	1.5671	0.1679	9.3836	12.8718	15.9420	480.3967
	2	-3.0177	0.2235	6.3715	0.2284	9.3891	12.8795	15.9514	480.6818
	3	-7.3123	0.2781	2.0661	0.2695	9.3784	12.8648	15.9332	480.1337
20000	1	-10.7404	0.3872	0.9678	0.4149	11.7081	16.0605	19.8912	599.4044
	2	-3.4127	0.2518	8.3281	0.2545	11.7408	16.1053	19.9467	601.0762
	3	-11.0775	0.1603	0.6552	0.1788	11.7326	16.0941	19.9328	600.6579

Table 14: Data from Electrical Strain Gages for Optical Sensor Gage Length=33,185μm

Load (N)	Test	Average Min. Peak Value (μstrain)	Standard Deviation (μstrain)	Average Max. Peak Value (μstrain)	Standard Deviation (μstrain)	Strain Gage Result (μstrain)
8000	1	194.050	1.106	463.044	1.208	268.994
	2	194.831	0.739	462.899	0.651	268.068
	3	194.570	0.739	462.754	0.783	268.184
12000	1	127.024	1.063	530.754	1.295	403.730
	2	127.024	0.868	530.103	1.400	403.079
	3	126.764	0.823	530.494	0.412	403.730
16000	1	137.242	0.910	673.595	1.107	536.354
	2	137.111	1.406	673.856	1.236	536.744
	3	136.721	0.549	673.856	0.879	537.135
20000	1	171.730	0.412	842.349	0.869	670.619
	2	171.990	0.629	842.479	0.962	670.489
	3	171.470	0.960	842.349	0.869	670.879

Table 15: Data from PD-1000 for Optical Sensor Gage Length=43,639μm

Load (N)	Test	Average Min. Peak Value (μm)	Standard Deviation (μm)	Average Max. Peak Value (μm)	Standard Deviation (μm)	Difference between peaks (μm)	Corrected Difference ($2/n_{core}$)	Strain including P_{11} and P_{12} (μstrain)	Apparent Strain in Optical Fiber (μstrain)
8000	1	-3.8675	0.1332	2.4043	0.1180	6.2718	8.6033	10.6553	244.1693
	2	-1.8344	0.1071	4.3973	0.0900	6.2317	8.5483	10.5872	242.6076
	3	-0.0354	0.1139	6.1865	0.1174	6.2219	8.5349	10.5706	242.2272
12000	1	-8.9345	0.2477	0.4261	0.2529	9.3606	12.8403	15.9029	364.4199
	2	-6.5398	0.0635	2.8323	0.0583	9.3720	12.8560	15.9224	364.8652
	3	-2.5951	0.1774	6.7742	0.1834	9.3693	12.8523	15.9178	364.7605
16000	1	-11.7580	0.1498	0.6945	0.1564	12.4525	17.0816	21.1558	484.7914
	2	-6.5908	0.1325	5.8899	0.1346	12.4806	17.1202	21.2036	485.8869
	3	-9.5694	0.1434	2.9137	0.1558	12.4831	17.1236	21.2078	485.9830
20000	1	-4.1124	0.1823	11.4849	0.1241	15.5972	21.3954	26.4985	607.2202
	2	-14.7284	0.0855	0.8516	0.1255	15.5800	21.3717	26.4692	606.5500
	3	-4.1926	0.3440	11.4125	0.3524	15.6051	21.4061	26.5118	607.5254

Table 16: Data from Electrical Strain Gages for Optical Sensor Gage Length=43,639μm

Load (N)	Test	Average Min. Peak Value (μstrain)	Standard Deviation (μstrain)	Average Max. Peak Value (μstrain)	Standard Deviation (μstrain)	Strain Gage Result (μstrain)
8000	60	203.611	0.910	472.161	0.651	268.551
	90	203.481	0.629	472.161	0.651	268.681
	120	203.481	1.072	472.740	1.018	269.260
12000	60	135.803	1.379	538.628	1.236	402.826
	90	135.282	0.960	539.019	1.373	403.737
	120	135.412	0.868	538.759	0.824	403.346
16000	90	135.022	0.878	672.025	0.412	537.003
	120	134.892	0.910	671.894	0.869	537.003
	150	134.501	0.629	672.285	0.629	537.784
20000	90	170.031	1.098	839.344	0.922	669.313
	120	169.250	0.868	840.126	1.296	670.876
	150	169.250	0.000	839.605	1.236	670.355

Table 17: Data from PD-1000 for Optical Sensor Gage Length=53,855μm

Load (N)	Test	Average Min. Peak Value (μm)	Standard Deviation (μm)	Average Max. Peak Value (μm)	Standard Deviation (μm)	Difference between peaks (μm)	Corrected Difference ($2/n_{core}$)	Strain including P_{11} and P_{12} (μstrain)	Apparent Strain in Optical Fiber (μstrain)
8000	1	-6.0651	1.0492	1.8465	1.0027	7.9116	10.8526	13.4411	249.5803
	2	-5.2965	0.2629	2.5906	0.4492	7.8870	10.8190	13.3995	248.8066
	3	-5.2204	0.5363	2.7972	0.5816	8.0175	10.9980	13.6212	252.9234
12000	1	-4.0763	0.4867	7.9840	0.4208	12.0603	16.5436	20.4895	380.4564
	2	-5.8260	0.5961	6.1599	0.5913	11.9860	16.4416	20.3632	378.1119
	3	-6.2645	0.3649	5.7638	0.3474	12.0283	16.4997	20.4352	379.4480
16000	1	-8.7731	0.3332	7.1854	0.3581	15.9585	21.8910	27.1123	503.4318
	2	-8.9341	1.0620	7.1732	1.0159	16.1073	22.0950	27.3650	508.1237
	3	-15.3412	0.2517	0.6412	0.2381	15.9824	21.9237	27.1528	504.1843
20000	1	-11.9169	0.8345	8.1037	0.7821	20.0206	27.4631	34.0134	631.5744
	2	-1.3571	0.9230	18.5850	0.9202	19.9421	27.3555	33.8802	629.0998
	3	-2.7389	0.5331	17.1686	0.5223	19.9075	27.3080	33.8214	628.0079

Table 18: Data from Electrical Strain Gages for Optical Sensor Gage Length=53,855μm

Load (N)	Test	Average Min. Peak Value (μstrain)	Standard Deviation (μstrain)	Average Max. Peak Value (μstrain)	Standard Deviation (μstrain)	Strain Gage Result (μstrain)
8000	1	203.678	1.235	472.533	1.345	268.855
	2	202.897	1.072	472.142	1.407	269.245
	3	203.808	1.757	471.751	1.027	267.943
12000	1	136.260	1.106	539.086	0.412	402.826
	2	135.740	0.960	538.826	0.879	403.086
	3	136.000	0.878	538.044	1.433	402.044
16000	1	136.260	1.866	673.134	1.197	536.874
	2	136.651	1.820	672.483	1.236	535.832
	3	136.391	1.646	672.483	0.879	536.092
20000	1	171.009	1.344	840.324	0.962	669.315
	2	171.139	0.629	840.845	2.150	669.706
	3	171.009	0.823	840.324	1.296	669.315

Appendix III

PD-1000 Fundamental Principles

1. INTRODUCTION

The basic operating principle of the PD-1000, manufactured by Canadian Instrumentation and Research Limited, will be discussed in this appendix. The manufacturer specially modified the PD-1000 to include an additional detector port so that it could be used with a Mach-Zhender interferometer in addition to the standard Extrinsic Fizeau Interferometer probe. It should be noted that the manufacturer did not provide any information concerning the operating principles of the system and would not provide such information upon request. Therefore, the information given in this section has been gathered from the patent[1].

1.1 Basic Principles

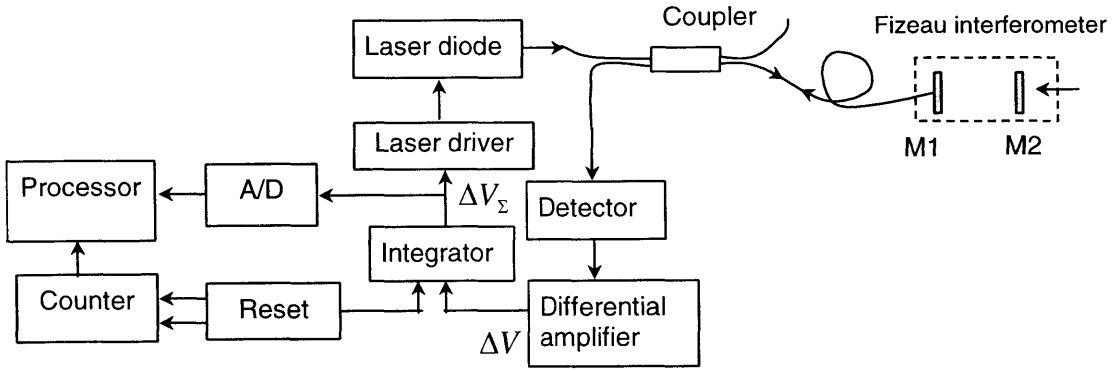

Figure 1: Schematic diagram for detecting the interference signal

The interference signal detection system is based on a closed loop fringe tracking servo system (Figure 1). The intensity of the light at the photo detector is given by the interference of the two beams going through two different optic paths. One beam comes

from the reflector M1 (please see Figure 1) while the other beam comes from the reflector M2. Reflector M2 is moveable with the external displacement. The intensity is:

$$I_L = I_0(1 + a\cos\phi) \qquad (1)$$

with I_0 and a dependent on the light intensity of the laser diode and the splitting ratio of the coupler and ϕ is the phase difference of the two optic paths. It is related with the distance of the two mirrors L as:

$$\phi = \frac{2\pi}{\lambda} * 2L \qquad (2)$$

where λ is the wavelength of the laser light. If there is a very small displacement ΔL, the intensity at the photo detector is:

$$I_{L+\Delta L} = I_0\left[1 + a\cos\left(\frac{2\pi}{\lambda} * 2(L + \Delta L)\right)\right] \qquad (3)$$

The photo detector converts this optical signal to voltage $V_{L+\Delta L}$. After being amplified by a differential amplifier, the servo error voltage $\Delta V = V_L - V_{L+\Delta L}$ is cumulated on the integrator as the output signal as well as the servo control signal ΔV_Σ. As the servo control signal, this voltage is applied to the voltage controlled current driver. This causes the laser diode to adjust wavelength λ to $\lambda + \Delta\lambda$, let $L/\lambda = (L + \Delta L)/(\lambda + \Delta\lambda)$, then, $I_{L+\Delta L}$ returns back to I_L, $\Delta V = 0$. If I_L is set to be on the steepest part of the coherent fringe slope at the half peak height, ΔV_Σ is in proportion to ΔL in a certain range. So

ΔV_Σ is representative of ΔL as the output signal from the integrator. ΔV_Σ is input to the A/D conversion circuit , then is sent to the processor.

If ΔL becomes larger and gets to $k\frac{\lambda}{2}$, the reset circuit lets the output of the integrator be zero and generates a pulse to up/down the counter while at the same time, $\lambda + \Delta\lambda$ returns to λ. The processor performs a summation and applies a scaling factor, to display the ΔL in appropriate units.

In the realized detection system of the PD-1000, the fringe-tracking servo is based on a synchronous detection system[1]. The laser diode is also modulated by current at a frequency of 100KHz about a bias current corresponding to a mean or base wavelength. The amplitude of the modulation frequency is chosen to cause I_L to be on the steepest part of the fringe slope at the half peak height.

1.2 The features of the optic system in PD-1000

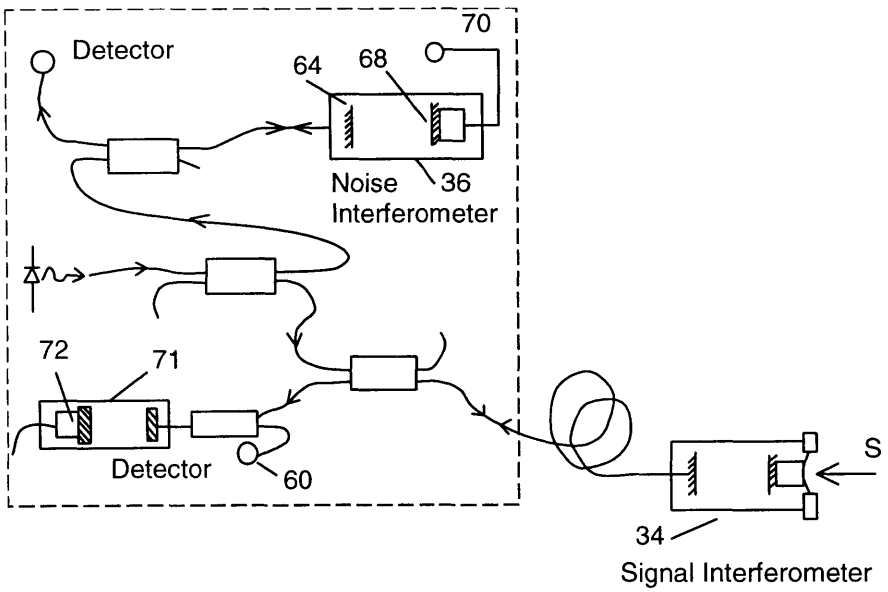

Figure 2: Schematic diagram of the optical system in PD-1000.

A disadvantage of the laser diodes that the PD-1000 uses is that they are sensitive to external cavity feed back, which is manifest as mode hopping and wavelength jitter. In the past, optical isolators have been used to prevent feedback, but optical isolators tend to be expensive.

In the PD-1000, a noise measuring interferometer (number 36 in Figure 2) is used to measure noise in the laser. This interferometer has an optical path length controlled by motion of a mirror driven by a piezoelectric positioning device (number 70 in Figure 2). A second fringe-tracking servo is used with additional feedback from the first signal fringe-tracking servo described in the first portion, as a means of removing signal information from the noise measuring interferometer. Thus, the interference signal from this noise measuring interferometer is then only the noise associated with the wavelength jitter of the laser diode. In the difference between the outputs of the signal interferometer and the noise measuring interferometer, the noise component is eliminated from the signal. The detailed steps for the signal processing are in the patent[1].

Because the optical path difference $2L$ in the Fizeau interferometer, which is around 40mm, exceeds the coherent length of the laser light, which is within 10mm, there may be a compensating Fizeau interferometer (number 71, Figure 2). This may be used to read out the interference signal from the signal interferometer and the same device may be used to read the noise from the noise measuring interferometer (which is not shown in Figure 2). The compensating Fizeau interferometer (number 71, Figure 2) and piezoelectric positioning device (number 72, Figure 2) are not shown in the PD-1000 patent. So the optical path difference that contributes to the interference signal is not $2L$

but 2(L-L'), where L' is the distance between the two mirrors in the compensating Fizeau interferometer (number 71, Figure 2).

1.3 Working process of the PD-1000

1.3.1 Calibration

Before calibration, the signal interferometer must be stable. Then, calibration over the sub wavelength distance is performed to confirm the actual optical path distance 2(L-L'). Next adjust the light wavelength of the laser from λ_1 to λ_2, if the reduced number of fringes is k, then:

$$\frac{2(L-L')}{\lambda_2} = \frac{2(L-L')}{\lambda_1} - k \qquad (4)$$

So,
$$2(L-L') = k\lambda_1\lambda_2 /(\lambda_1 - \lambda_2) \qquad (5)$$

If L' is known according to the control signal of the piezoelectric positioning device 72 in Figure 2, L can be given.

Next, it drives the piezoelectric positioning device 70 in Figure 2 to set the distance between the two mirrors 64 and 68 (Figure 2) of the noise measuring interferometer L.

It drives the piezoelectric positioning device 72 (Figure 2), adjusts the optical path difference L' from about L'-10mm to about L'+10mm, counts the fringes to confirm the external displacement tolerance of signal interferometer 34 (Figure 2). Then it returns the optical path difference back to L'. Then it sets the initial value for every circuit.

1.3.2 Testing

The signal detecting is based on the synchronous detection system. The oscillator supplies a 100KHz triangle waveform to the control sample and hold circuit. The laser diode is also modulated by a 100KHz frequency current. The bias current corresponding to the mean wavelength and the amplitude of the modulation frequency are chosen so that when there isn't displacement, the servo error signal ΔV is zero.

If there is a displacement ΔL applied on the signal interferometer 34 (see Figure 2), the interference optical fringe arises and is detected and converted to voltage by photo detector 60 (Figure 2). The output of the differential amplifier is the servo error signal ΔV (see Figure1), which now is not zero. The servo error signal ΔV, is integrated by the integrator to give a servo control signal ΔV_{Σ}. The servo control signal is applied to the programmable gain amplifier, the output of which is applied to the voltage controlled current driver along with a bias voltage. This causes the laser diode to adjust the wavelength from the initial λ to $\lambda + \Delta\lambda$, and lets ΔV reduce to zero. ΔV_{Σ} is in proportion to ΔL, so it is representative of ΔL. ΔV_{Σ} does not just represent the displacement ΔL but also includes the noise N of the laser source.

At the same time, the laser noise N is applied to the noise measuring interferometer 36 (Figure 2), that gives the corresponding interference signal. By another set of closed loop fringe tracking servos similar to that mentioned above, the voltage signal ΔV_{Σ}' that represents the laser noise N is obtained. Then, the noise N is eliminated by subtracting ΔV_{Σ}' from ΔV_{Σ}.

If ΔL is large enough to let ΔV_Σ exceeding the reset voltage of the reset circuit, the reset circuit generates a counting pulse to the up/down counter, at the same time, resets ΔV_Σ to be zero. The count is input to a processor.

Input $\Delta V_\Sigma - \Delta V_\Sigma$' to an A/D converter, which generates a digital representation of the fractional part of the displacement between resets. This digital signal is also input to the processor. The processor performs a summation and applies a scaling factor, to display the displacement in appropriate units.

1.4 Some further comments

(a). The above discussion refers to the Fizeau interferometer. For the Mach Zhender (MZ) interferometer, the working principle is the same, but the compensating interferometer 71 (Figure 2) and the noise measuring interferometer 36 (Figure 2) should be changed to the same MZ interferometers.

(b). The relationship between the displacement and the interference signal when the PD-1000 is used with the MZ interferometer is different from that when used with the Fizeau interferometer. This should be adjusted in the software. However, the software for the PD-1000 does not offer an option to use the correct algorithm. From experimental testing, it was found that when the PD-1000 is used with a MZ interferometer the testing result should be adjusted as:

$$\Delta L_{MZ} = \Delta L \times \frac{2}{n} \qquad (6)$$

where ΔL_{MZ} is the real displacement applied on the MZ interferometer, ΔL is the measured result produced by the PD-1000.

2. REFERENCE

1. M. Failes, "Noise compensated interferometric measuring device and method using signal and reference interferometers", United States Patent: 5,598,264

Appendix IV

List of Symbols

CHAPTER 2

S	Sample Stiffness
P	Load
h	Displacement
a	Radius of the cylinder
G	Shear Modulus
ν	Poisson's Ratio
A	Area of Contact
E	Young's Modulus
K	Spring Stiffness
E_r	Reduced Modulus
β	Geometric Indenter Shape Factor
K_s	Indenter Support Springs Stiffness
m	Indenter Column Mass
K_f	Load Frame Stiffness
C_i	Capacitive Displacement Gauge Damping Coefficient
ω	Forcing Frequency
ϕ	Phase Angle
E_i,	Indenter elastic modulus
ν_i	Indenter Poisson's Ratio
$C_1 \ldots C_8$	Fitting Constants for indenter area function

CHAPTER 3

E	Elastic modulus
ν	Poisson's Ratio
L	Crack Opening Size
R,r	Bend radius
y_1,y_2	Distance from neutral axis
$d\theta$	Incremental angle between node points
dS	Incremental distance between node points
ε_1, ε_2	Strain at node points
a	Core radius
λ	Wavelength of light
n_1	Core refractive index
n_2	Cladding refractive index
k	Free-space propagation constant
V	Normalized frequency parameter of an optical fiber

J_ν	Bessel function of the first kind
K_ν	Modified Bessel function of the second kind
b	Normalized propagation constant
β, κ, γ	Propagation characteristics of optical fiber
α	Loss coefficient
P_c	Cumulative optical signal loss
H	Hankel Function
w	Mode Field Diameter/2
$E(\omega, x, y, z)$	Transverse component of electric field (BPM)
NA	Numerical Aperture
θ	Fiber angle inclination in crack sensor
θ_c	Complement of the critical angle
α_c	Complement of the critical angle (3D only)
$\gamma(\phi)$	Power attenuation coefficient (multimode analysis)
T_i	Ray incident power lost by reflection
$\Delta\phi_i$	Angular separation between successive reflections
ϕ_p	Angular separation
N	Number of reflections in the section
θ_ϕ	Complement of incident angle (outer interface)
θ_ϕ'	Complement of incident angle (inner interface)
ϕ_m	Angle displacement
R_m	Curvature radius
$\gamma_m(r_m, \theta_{zm}, R_m)$	Ray power attenuation coefficient

CHAPTER 4

$\tau(x,r)$	Shear stress at any point in the fiber coating
$\tau_f(x)$	Shear stress at the glass/polymer interface
r_f	Radius of the glass fiber
x	Coordinate along fiber axis
r	Radial distance from fiber center
u_f	Displacement of glass fiber relative to rigid matrix
G_c, G_{c2}	Shear moduli of the coatings
u_m	Axial displacement in matrix
σ_f	Normal stress in fiber
$\Delta\phi$	Relative phase change
ε_{xx}	Fiber strain in direction of the fiber axis
λ	Wavelength of light in free space
n_0	Refractive index of fiber unstrained
L	Length of the fiber
P_{11}, P_{12}	Strain optic constants for isotropic material (Pockel's Constants)
ν_f	Poisson's Ratio of the fiber
β_{FEM}	Percent of strain transfer predicted by 3D FEM model